NASA/TP-20220008270

Semispan Test Results of a Conventional High-Lift Common Research Model in Landing Configuration

John C. Lin, LaTunia P. Melton, Judith A. Hannon, Mehti Koklu, and Marlyn Y. Andino
Langley Research Center, Hampton, Virginia

August 2022

NASA STI Program Report Series

Since its founding, NASA has been dedicated to the advancement of aeronautics and space science. The NASA scientific and technical information (STI) program plays a key part in helping NASA maintain this important role.

The NASA STI program operates under the auspices of the Agency Chief Information Officer. It collects, organizes, provides for archiving, and disseminates NASA's STI. The NASA STI program provides access to the NTRS Registered and its public interface, the NASA Technical Reports Server, thus providing one of the largest collections of aeronautical and space science STI in the world. Results are published in both non-NASA channels and by NASA in the NASA STI Report Series, which includes the following report types:

- TECHNICAL PUBLICATION. Reports of completed research or a major significant phase of research that present the results of NASA Programs and include extensive data or theoretical analysis. Includes compilations of significant scientific and technical data and information deemed to be of continuing reference value. NASA counterpart of peer-reviewed formal professional papers but has less stringent limitations on manuscript length and extent of graphic presentations.

- TECHNICAL MEMORANDUM. Scientific and technical findings that are preliminary or of specialized interest, e.g., quick release reports, working papers, and bibliographies that contain minimal annotation. Does not contain extensive analysis.

- CONTRACTOR REPORT. Scientific and technical findings by NASA-sponsored contractors and grantees.

- CONFERENCE PUBLICATION. Collected papers from scientific and technical conferences, symposia, seminars, or other meetings sponsored or co-sponsored by NASA.

- SPECIAL PUBLICATION. Scientific, technical, or historical information from NASA programs, projects, and missions, often concerned with subjects having substantial public interest.

- TECHNICAL TRANSLATION. English-language translations of foreign scientific and technical material pertinent to NASA's mission.

Specialized services also include organizing and publishing research results, distributing specialized research announcements and feeds, providing information desk and personal search support, and enabling data exchange services.

For more information about the NASA STI program, see the following:

- Access the NASA STI program home page at http://www.sti.nasa.gov

- Help desk contact information:

https://www.sti.nasa.gov/sti-contact-form/
and select the "General" help request type.

NASA/TP-20220008270

Semispan Test Results of a Conventional High-Lift Common Research Model in Landing Configuration

John C. Lin, LaTunia P. Melton, Judith A. Hannon, Mehti Koklu, and Marlyn Y. Andino
Langley Research Center, Hampton, Virginia

National Aeronautics and
Space Administration

Langley Research Center
Hampton, VA 23681

August 2022

Acknowledgments

This R&D effort was sponsored by the High Aspect Ratio Wing Subproject under the NASA Advanced Air Transport Technology (AATT) Project. The effort involved many people who provided valuable contributions through their hard work that made a successful test possible. The authors would like to acknowledge and thank all those involved for their great support throughout this investigation. Some key personnel are as follows.

Model design: Jared Fell (design team lead), Sandy Webb, Miranda Snyder, Christopher Laws, Reggie Kidd, John Mulvaney, Mark Cagle, David Lewis, Nigel Schneider, Dave Castle, Douglas Weber, William Langford, and Ray Rhew, as well as NASA interns Jacob Ganzak and Steven Call.

Model fabrication: Stephen Geissinger, Christopher McLain, Danny Lovaglio, Robert Andrews, and Thomas Hall.

14x22 air supply system and AFC plumbing: Joe Giuliana and Robert Kyle.

14x22 managerial staff: Frank Quinto (Facility Manager), Ashley Dittberner (Operation Manager), William Krieger (Facility Safety Head), Joseph Burton (Facility Coordinator).

14x22 test engineers: James Byrd (Lead), Abigail Cayton, Jeremy Ulanday, and Samantha Zauber.

14x22 technician and supporting staff:

Lead technician - Ronald Hunter
Mechanical technicians - Kyle Deaver (Lead), Joshua Beasley, Marvin Le Gendre, Andrew Sawyer, Cassandra Stevens, and Patricia Christian
Instrumentation technicians - Andrew Harrison, Benjamin Lester, and Neil Coffey
Electrical technicians - Stuart Dale Bennett and Leon Adams
Data system - Andy Boney (Manager), Benjamin Trower, and Charlotte Teague
Facility equipment specialist - Karl Maddox
Environmental coordinator - Joseph Burton, Jr.
High pressure air support - Michael Henshaw and Robert Askew

CRM-HL photogrammetry data: Felecia Berry, Harriett Dismond, Michael Carmine, Scott Bartram, and Richard Schwartz (Vidi Support)

CRM-HL CFD data: Veer Vatsa, David Lockard and Melissa Rivers

CRM-HL unsteady pressure instrumentation and measurement: Keith Paschal

CRM-HL consultation: Douglas Lacy of Boeing Commercial Airplanes.

Available from:

NASA Center for AeroSpace Information
7115 Standard Drive
Hanover, MD 21076-1320
443-757-5802

Abstract

A 10%-scale high-lift version of the Common Research Model (CRM-HL) was tested in the 14- by 22-Foot Subsonic Tunnel at the NASA Langley Research Center. This research was aimed at providing a representative reference case for comparison with an Active Flow Control (AFC) enabled version of the CRM-HL and to increase the existing experimental database for CFD high-lift prediction. The test was conducted mostly at a freestream Mach number of 0.20. The effects of the engine nacelle, nacelle chine, tufts, small variations in Mach number, hysteresis-associated increasing/decreasing angle of attack, and incoming floor boundary-layer thickness (i.e., thinning by activation of the floor boundary layer removal system) were examined. A prestall lift performance degradation for the CRM-HL configuration was resolved with a properly placed nacelle chine. Surface pressure results are presented in detail for three key variants of the CRM-HL — baseline (nacelle on), nacelle off, and nacelle with the most effective chine installation. The presented aerodynamic forces and surface pressures include both with and without the wall correction using the Transonic Wall Interference Correction System (TWICS) method. A limited set of photogrammetry results is also presented to document the model deformation under test conditions.

Nomenclature

b	=	wing semispan; 115.7 inches
C_D	=	drag coefficient; (drag force)/($S \cdot q_\infty$)
$C_{D,u}$	=	drag coefficient without wall correction; (drag force,$_u$)/($S \cdot q_{\infty,u}$)
C_L	=	lift coefficient; (lift force)/($S \cdot q_\infty$)
$C_{L,u}$	=	lift coefficient without wall correction; (lift force,$_u$)/($S \cdot q_{\infty,u}$)
C_p	=	pressure coefficient; $(p - p_\infty)/q_\infty$
C_m	=	pitching moment coefficient; (pitching moment)/($S \cdot c_r \cdot q_\infty$)
$C_{m,u}$	=	pitching moment coefficient without wall correction; (pitching moment,$_u$)/($S \cdot c_r \cdot q_{\infty,u}$)
c_{MAC}	=	mean aerodynamic chord; 27.6 inches
L/D	=	lift-to-drag ratio
$L/D,_u$	=	lift-to-drag ratio without wall correction
M_∞	=	freestream Mach number
$M_{\infty,u}$	=	freestream Mach number without wall correction
p	=	pressure
p_∞	=	freestream static pressure
q_∞	=	freestream dynamic pressure
$q_{\infty,u}$	=	freestream dynamic pressure without wall correction
Re	=	unit Reynolds number; per foot
$Re,_u$	=	unit Reynolds number per foot without wall correction
Re_{MAC}	=	Reynolds number based on mean aerodynamic chord (c_{MAC})
S	=	semispan wing reference area; 2,973.6 in^2
x, y, z	=	coordinates along the model's longitudinal axis, lateral axis, and normal axis, respectively
α	=	angle of attack
α_u	=	angle of attack without wall correction
Δ	=	differential value
$\Delta\alpha_{wc}$	=	α minus α_u
$\Delta q_{\infty,wc}$	=	q_∞ minus $q_{\infty,u}$
η	=	normalized spanwise location; y/b
θ	=	azimuth angle

Acronyms

3D	three dimensional
AFC	active flow control
AR	aspect ratio
AATT	Advanced Air Transport Technology
BLRS	boundary layer removal system
CFD	computational fluid dynamics
CRM-HL	high-lift version of the Common Research Model
CRM-SHL-AFC	AFC-enabled simplified high-lift version of the Common Research Model
ESP	electronic scanned pressure
LaRC	Langley Research Center
ME	main element
MRC	moment reference center
NASA	National Aeronautics and Space Administration
R&D	research and development
SHL	simplified high lift
TWICS	transonic wall interference correction system
WUSS	wing under slat surface

Introduction

A modern transport airplane typically takes advantage of the aerodynamic properties of slotted flows on the wing leading and trailing edges to achieve the necessary high-lift performance [1]. NASA has a history of interest in high-lift research relevant to commercial transport airplanes [2–5]. Under the sponsorship of the NASA Advanced Air Transport Technology (AATT) Project, a 10%-scale conventional high-lift model based on the transonic Common Research Model (CRM) [6,7] was successfully built and tested at the NASA Langley Research Center (LaRC) during the fall of 2018. The design and geometry of the High-Lift Common Research Model (CRM-HL) was first reported by Lacy and Sclafani [8]. Similar to the transonic CRM, the low-speed CRM-HL is also an open source geometry to be used for high-lift research, computational fluid dynamics (CFD) code verification, and tunnel-to-tunnel comparisons.

The primary objective of the current research was to provide a representative reference case for comparison with an Active Flow Control (AFC) enabled simplified high-lift (SHL) version of the CRM-HL equipped with highly deflected (≥ 50°) simple-hinged flaps (CRM-SHL-AFC) [9–15]. A secondary objective was to increase the existing experimental database for the CFD High-Lift Prediction Workshop [16–21]. The model could also be used for high-lift flow physics experiments, rigging studies [22], and aeroacoustics investigations [23,24]. The current test was conducted in the NASA Langley 14- by 22-Foot Subsonic Tunnel (14x22) mostly at a freestream Mach number of 0.20 and Reynolds number of ~3.3 x 10^6 based on the mean aerodynamic chord.

As companion documentation to previous CRM-HL publications [9–15], this paper provides the 14x22 test results of the CRM-HL in greater detail for the initial (or nominal) landing configuration as described in Ref. [8]. The presented aerodynamic dataset includes lift, drag, and moment coefficients as a function of angle of attack. The aerodynamic effects of the engine nacelle, nacelle chine, tufts, small variations in Mach number, hysteresis-associated with increasing/decreasing angle of attack, and incoming floor boundary-layer thickness (i.e., thinning by activation of the floor boundary layer removal system [BLRS]) were examined. The aerodynamic effects of the tufts are included because the model was tested without boundary layer trip devices. Surface pressure distributions are shown for the high-lift wing, fuselage, and nacelle for three key variants of the CRM-HL — baseline (nacelle on), nacelle off, and nacelle with the most effective chine installation. Note variant refers to versions or configurations of the 10% scale CRM-HL. The baseline configuration, one variant of the CRM-HL, in this paper is defined to be the case where the nacelle/pylon is installed without a nacelle chine.

The test data presented include results with and without wind tunnel wall corrections applied. Note that if a CFD simulation performed on the CRM-HL was done without modeling the tunnel walls, then the results should be compared against the test data with the wall corrections. However, if a CFD simulation models the tunnel walls, e.g., as reported by Vatsa et al. [12,15], then the results should be compared against the data without the wall correction.

Wind Tunnel Test

The 14x22 wind tunnel is an atmospheric, closed return wind tunnel with a 14.5 ft high, 21.75 ft wide, and 50 ft long test section [25]. A schematic of the tunnel circuit is shown in Figure 1. When testing in the closed-wall configuration, a maximum freestream velocity of 338 ft/s and a dynamic pressure (q_∞) of 144 psf can be achieved. The unit Reynolds number ranges from 0 to 2.2×10^6 per foot. As previously mentioned, most of the recent tests were performed at a freestream Mach number (M_∞) of 0.2 and a corresponding q_∞ of approximately 60 psf. The turbulence intensity, which varies with dynamic pressure and test section location, is between 0.07% and 0.08% at a dynamic pressure of 60 psf [26]. A few lower speed runs were made at M_∞ of 0.175, 0.15, and 0.125. The following four subsections provide the description of (A) CRM-HL model, (B) measurement uncertainty and wall correction method used, (C) pressure tap layout, and (D) photogrammetry.

A. CRM-HL Model

The 10%-scale NASA CRM-HL model has a half-body fuselage, a semispan wing, a set of inboard and outboard slats, an engine nacelle/pylon, and a set of inboard and outboard single-element Fowler flaps with flap track fairings. All model surfaces have a finish of 32 microinches. A photograph and two sketches of the CRM-HL in the 14x22 are shown in Figure 2. Key model components such as the slats, wing under slat surface (WUSS), wing trailing edge (spoiler), wing outboard region (aileron) beyond the outboard flap, and flaps are all modular and replaceable (see Figure 3 for the location of these components). Provisions were made for interchangeable model pieces for regions at the wingtip as well as flap and slat side edges. The wind tunnel model includes slat and flap brackets (not included in the geometry of Ref. [8]) to deploy the control surfaces to their takeoff and landing positions. There are three inboard and 12 outboard slat brackets to hold the inboard and outboard slats in position, respectively. One internal (inside the fuselage) and one external flap bracket are used to hold the inboard flap in place, whereas two external flap brackets are used to hold the outboard flap in position. Each of the three external flap brackets is covered with a flap track fairing (see Figure 3). A rigging study was not performed. Rather fixed brackets were used to replicate the nominal landing configuration of Ref. [8]. The nominal landing configuration of Ref. [8] had 30° slat and 37° trailing edge flap deflection angles. The as-designed gap and overhang values at the most inboard and outboard brackets of the inboard and outboard slats are provided in Table 1. As-designed gap and overhang values measured at the outboard bracket of the inboard flap and the inboard and outboard brackets of the outboard flap are provided in Table 2.

The model spar is hollow to allow for routing of instrumentation and AFC plumbing. A wing/fuselage strake, designed by Boeing, was installed on the CRM-HL to represent a typical transport airplane (Figure 4). A 6.25-inch-long by 1.86-inch-tall nacelle chine (designed by Boeing), shown in Figure 4, could be installed on the engine nacelle to resolve the prestall lift degradation issue as needed. The engine nacelle/pylon was removeable to permit testing of a CRM-HL variant with clean wing, as shown in Figure 5. When the nacelle was not installed, a slat filler piece connected the inboard and outboard slats to provide a continuous slat, and the adjacent wing leading edge piece was replaced by a WUSS insert to ensure a continuous WUSS. The model was tested without any boundary-layer transition tripping and the transition location was not documented. Correct scaling and simulation of boundary layer flows over three-dimensional swept high-lift wings are strongly dependent on the type and location of transition [1]. Since transition location was not measured, model surface finish (32 microinches) and freestream turbulence levels (0.07%–0.08% at q_∞ = 60 psf) of the facility are provided.

The semispan model was installed on top of a 3.5 inch peniche (left image of Figure 2), and together the model and its peniche covered 68% of the tunnel span in the vertical direction. The model fuselage is

20.59 feet in length; therefore, it extended past the turntable and past the end of the model cart (right image of Figure 2). The peniche is nonmetric and attached to the turntable, whereas the fuselage is metric and connected to the force balance below the model. A labyrinth seal provided the interface between the fuselage and the peniche.

Model coordinate information (e.g., moment reference center and fuselage nose location) is provided in the airplane coordinate system [8], where the spanwise origin (y = 0) is at the centerline of the fuselage. The CRM-HL wing was straightened in a spanwise sense to represent a wing in a tool supported position compared to the original CRM wing, which represented a wing under cruise flight loading [8]. Simplification of the design, build, and testing of the CRM-HL wing with high-lift hardware were factors influencing the decision to straighten the wing. While the design of the NASA 10% scale CRM-HL model was based on Ref. [8], the slat upper and lower surface trailing edge thicknesses were 0.01 inches instead of 0.02 inches.

Key model geometric reference parameters are listed below and summarized in Table 3:

- Mean aerodynamic chord (c_{MAC}) = 27.6 inches at y = 46.9 inches (η = 0.41)
- Wing semispan (b) = 115.7 inches
- Reference area of the semispan model (S) = 2,973.6 in^2, based on Wimpress area
- Aspect ratio = 9
- Sweep angle of the wing quarter chord = 35°
- Moment reference center (MRC): x = 132.6 inches, y = 0 inches, z = 17.8 inches
- Fuselage nose location: x = 9.3 inches, y = 0 inches, z = 19.8 inches
- Reynolds Number based on mean aerodynamic chord, $Re_{MAC} \approx 3.3\times10^6$ for the landing configuration at M_∞ = 0.20
- Wing dihedral angle: 5°
- Wing twist = 6.72° at η = 0; wing twist = -3.75° at η =1

B. Measurement Uncertainty and Wall Correction

The experimental measurements included forces and moments using the NASA MC-110 balance, surface static pressures using pressure taps connected to electronically scanned pressure (ESP) modules, model deformation using photogrammetry, and flow visualization using tufts [11,14]. This paper documents the results of the force balance and surface pressure measurements in detail. Based on the balance accuracy, angle of attack (α), and dynamic pressure (q_∞), the expected instrumentation uncertainty is estimated to be ±0.007 to ±0.008 for the lift coefficient (C_L), ±0.0022 to ±0.0036 for the drag coefficient (C_D), and ±0.004 for the pitching moment coefficient (C_m). The uncertainty of the first two quantities is also a function of α (i.e., a greater uncertainty is associated with higher angles of attack).

The primary data presented in this paper have been corrected for interference from the tunnel walls using the Transonic Wall Interference Correction System (TWICS) method [27–29]. TWICS works for the subsonic flow regime of the 14x22. This wall correction method uses measured wall pressures and factors in solid body blockage, separation wake blockage, and lift interference correction for a semispan model. The application of TWICS typically increased the angle of attack for the lift curve by ~0.2° to 1.1° and decreased the maximum lift coefficient by ~0.01 to 0.06 [13]. Tunnel flow angularity correction was not applied to the data.

Note that the CRM-HL test results presented in Refs. [9–11,14] had no wall corrections applied, and the CFD results reported in Ref. [12,15] used the test data without the wall correction for comparison because the tunnel walls were simulated in the predictions. The CRM-HL test results presented in Ref. [13] had the TWICS wall correction method applied.

C. Pressure Tap Layout

A schematic of the pressure tap locations, indicated by circular dots, is shown in Figure 6. Most of the pressure taps on the high-lift wing are in streamwise arrays at eight spanwise locations (butt lines) with three rows across the inboard flap span, three rows across the outboard flap span, and two rows across the aileron region (i.e., η = 0.15, 0.24, 0.33, 0.42, 0.55, 0.69, 0.82, and 0.91). Note the Yehudi break that separates the inboard and outboard flaps is located at η = 0.37. Furthermore, there are six pressure taps near the wing tip and 18 taps around the inboard and outboard flap edge surfaces (three each on the upper, side-edge, and lower surfaces surrounding the two flap side edges). Additionally, six spanwise arrays are on the upper wing surface with one row on the slat, three rows on the main wing, and two rows on the flap (Figure 6(a)). A total of 609 pressure taps were installed on the wing.

There are 56 pressure taps on the fuselage, covering streamwise rows at three different heights (waterline locations) and circumferential rows at six fuselage stations around the wing root, as shown in Figure 6(b). Additionally, there are 63 pressure taps on the nacelle/pylon, covering four streamwise rows on both the interior and the exterior of the nacelle at the 12, 3, 6, and 9 o'clock positions (facing downstream). Pressure taps are on an exterior circumferential row covering 180° of the nacelle upper surface (between 3 and 9 o'clock) at $x \approx 99.8$ inches. There is also a circumferential row of pressures taps covering 360° of the interior inner nacelle surface at $x \approx 106.6$ inches. Finally, there is a row of pressure taps on the nacelle pylon at $x = 109.2$ inches (Figure 6(c)).

The measured pressure tap coordinates for the wing main element (ME) as well as the slats and flaps in both the stowed and the (baseline) deployed positions are listed in Table A1 under Appendix A. The pressure taps coordinates for the WUSS filler piece (for the full-span slat without nacelle/pylon), fuselage, and the nacelle/pylon are provided in Tables A2 to A4, respectively, in the same appendix. The associated datafile channels and bad pressure taps are identified in these tables as well. Some bad pressure taps may be fixed for future tests.

D. Photogrammetry

A limited set of photogrammetry data was taken to document the model deformation under test conditions at $M_\infty = 0.2$. The measurement performed is similar to that described by Kushner et al. [30]. The photogrammetry data were recorded using a seven-camera, commercial off-the-shelf system. The cameras were positioned to capture data over the angle of attack range (-4° to 22°) of the model. For the current data, the images were acquired at a framerate of approximately 100 images per second and at least 1000 frames were acquired for each condition.

Fifty-seven adhesive retroreflective circular dots or targets, 0.375 inches in diameter and ~0.004 inches thick, were applied along the upper surface of the model to measure model deformation. These targets were added to the model at the beginning of the test and remained in place throughout the duration of the test. No data were acquired to quantify the effects of the presence of the targets on flow transition, stall, and model forces and moments since the targets were always on the model. Photographs of the targets on the model are shown in Figure 7(a) and the target layout is shown in Figure 7(b). The target layout allows for a one-to-one comparison between wind-off to wind-on deformation at the same locations on the model. The photogrammetry data were processed to determine the spatial locations of the targets, which were converted to obtain deflection and angular information. Wind-off polars were used to calibrate the measurement system.

The spanwise wing bending distributions were calculated using data-reduction procedures described in Burner et al. [31] and Liu et al. [32]. Typically, a minimum of two targets at approximately the same spanwise location were chosen for the analysis. The two targets were examined at wind off for several angles of attack. In all cases, the two targets predict α within ±0.03°. As a result, the twist and wing bending calculation should be reasonably accurate. The uncertainty at the wingtip spanwise station should be minimal because the two targets cover most of the wing chord there.

Results and Discussion

A total of 21 test runs made on the aforementioned CRM-HL model are summarized in Table 4. The corresponding figures and aerodynamic data tables for these runs are also provided in the table. The wind tunnel test results and discussion are presented in the following three subsections: (A) aerodynamic data for all test runs, (B) surface pressures for the three key CRM-HL variants (baseline, nacelle with the best evaluated chine position based on lift recovery near stall, and nacelle off), and (C) photogrammetry data for the baseline CRM-HL configuration (Run 212).

A. Aerodynamic Performance Data

The aerodynamic performance data with the application of TWICS for all CRM-HL test runs at the baseline landing configuration (i.e., 30° slat deflection and 37° flap deflection) are tabulated in Tables B**1** to B21 under Appendix B. Appendix C contains all the data corresponding to Appendix B without the wall correction.

Test results on data repeatability as well as the effects of hysteresis, floor BLRS, small M_∞ variations (nominal $M_\infty = 0.2$), tufts, nacelle chine, and nacelle off are provided in the following discussion and presented in Figures 8 to 15. For reference purpose, the corresponding aerodynamics plots without the wall correction are also provided in Figures D1–D7 under Appendix D.

Repeatability

There were five repeat runs (Runs 200, 208, 212, 221, and 227) made for the baseline CRM-HL configuration. This was done to account for any unknown variations in the model or tunnel setup as the test progressed. These repeat runs also provide an opportunity to assess the variability of the data. Note that Run 227 is the last run after a model change at the end of the test. Figure 8 shows the aerodynamic plots (drag, pitching moment, and lift coefficients versus angle of attack) for these runs with TWICS applied. For reference, the corresponding plots without the wall correction are shown in Figure D1. The lift curves indicate a prestall lift degradation between $\alpha = 13°$ and 18° that was repeatable. The C_m is negative for all angles of attack, which indicates the wing pitches in the nose-down direction consistent with a typical high-lift wing [3]. In general, the repeatability seems to be excellent with little or no variation. Since there is negligible difference between repeat runs, Run 208 was chosen to represent the baseline CRM-HL case for the comparisons in the following discussion.

For a closer examination, Figure 16 shows variations in ΔC_D, ΔC_m and ΔC_L as a function of α for the five baseline repeat runs. All differential values (ΔC_D, ΔC_m and ΔC_L) were calculated with respect to the corresponding average values of the five repeat runs. The variations in ΔC_L were within the measurement uncertainty of ±0.007 to ±0.008 for most angles of attack, except near stall (i.e., $16° \leq \alpha \leq 17°$) where larger variations in inboard wing loading were also observed in the static pressure results. The variations in ΔC_m were well within the measurement uncertainty of ±0.004 for most of angles of attack, except $\alpha > 19°$ (poststall). The variations in ΔC_D were also within the measurement uncertainty of ±0.0022 to ±0.0036 for most angles of attack, except at $\alpha = 17.6°$ (maximum lift). The data for Run 200 show several outliers for ΔC_L and ΔC_D.

Hysteresis effects

Hysteresis effects associated with increasing and decreasing angle of attack were examined (Runs 201 and 202, respectively). Figure 9 shows the aerodynamic plots for the hysteresis runs with TWICS applied. The corresponding plots without the wall correction are shown in Figure D2. The results indicate little or no hysteresis due to increasing and/or decreasing angle of attack for the lift and moment curves. However, there is a slight increase in drag for decreasing angle of attack (Run 202) between $\alpha = 18°$ and 14°. Examination of the C_p distributions indicate that the nacelle did not fully reattach during the decreasing angle of attack sweep until around $\alpha = 9°$.

Floor BLRS effects

The 14x22 test section floor has a boundary-layer removal system (BLRS) [5] located at its entrance (see lower right image of Figure 2). The system is often used when testing semispan models to reduce the size of the tunnel floor boundary layer. While not measured in this test, previous studies have indicated that the floor boundary layer thickness is approximately 5 inches with the BLRS inactive and is reduced by approximately 50% when the BLRS is active based on surveys performed at tunnel station 7.87 feet with

q_∞ = 60 psf. At the beginning of the test, data were acquired with and without the BLRS active to determine the effects of the incoming boundary layer height on the aerodynamic performance of the CRM-HL model. Figure 10 shows the aerodynamic plots with TWICS applied for runs with and without the activation of the floor BLRS (Runs 203 and 208, respectively). The corresponding plots without the wall correction are shown in Figure D3. The results indicate little or no difference due to the activation of BLRS on the lift and drag curves. However, there is a slight increase in pitching moment for $\alpha \geq 4°$. The change in pitching moment without a change in lift is surprising. The pitching moment difference could be due to a thinner boundary layer produced by the activation of BLRS and its close proximity to the fuselage. Because of the desire to minimize the BLRS-generated noise and to simplify CFD simulations, the rest of the test was performed with the floor BLRS inactive. The BLRS is known to introduce some tunnel nonuniformity that would need to be modeled in CFD simulations.

M_∞ effects

Several runs were made with M_∞ lower than 0.2 to provide a performance reference for comparison with the CRM-SHL-AFC configuration at these conditions. Figure 11 shows the aerodynamic plots with TWICS applied for runs at M_∞ = 0.125, 0.15, 0.175, and 0.2 (Runs 209, 210, 211, and 208, respectively). The corresponding plots without the wall correction are shown in Figure D4. Because the variation in M_∞ and Re_{MAC} are relatively small, there is little or no difference in the aerodynamic curves, with the exception of slightly higher drag at $\alpha \approx 16°$ to 18° for the M_∞ = 0.125 case.

Tuft effects

Tufts were installed on the main wing and the flaps to diagnose the prestall lift degradation observed between $\alpha \approx 13°$ and 18° for the baseline CRM-HL [11,14]. The tufts, visible in the upper and lower images on the right side of Figure 3 were made from thin sewing thread. Tuft effects are included to illustrate the effects of the model geometry changes due to the tufts on the force and moment results since the model did not have boundary layer tripping devices installed. Figure 12 shows the aerodynamic plots with TWICS applied for runs with tufts (Runs 219 and 220) and without tufts (Run 208). The corresponding plots without the wall correction are shown in Figure D5. Installation of tufts marginally reduced the lift and slightly increased the pitching moment for angles of attack up to the maximum lift. For $\alpha \leq 16°$, the tufts-induced ΔC_L is between -0.01 to -0.02 and ΔC_m is between 0.004 and 0.006, which are just beyond the measurement uncertainty of ±0.01 for C_L and ±0.0035 for C_m. There is no observable change in drag due to tufts. The ΔC_D is between 0.001 and -0.002 for $\alpha \leq 16°$, which is well within the measurement uncertainty of ±0.0030 to ±0.0040. Perhaps an expected slight increase in drag due to tufts was offset by a marginal reduction in drag due to lift.

Nacelle chine effects

A nacelle chine was added to the model to eliminate the prestall lift degradation between α = 13° and 18° (C_L curves of Figs. 8–12) that was deemed unacceptable for practical applications. It is hypothesized that this lift degradation is due to the flow separation that is caused by the interaction of the nacelle/pylon vortex system with the adverse pressure gradient at higher angles of attack [9].

The vortices generated at the nacelle/pylon region and their effect on the aerodynamic performance were investigated in detail using tuft flow visualization and numerical simulations [11,14]. The surface flow visualization with tufts (Figure 13(a)) clearly shows flow separation on the inboard wing as well as on the inboard flap at α = 16°. The CFD simulations (not shown) are in line with the tuft flow visualization and predict flow separation at higher angles of attack.

The flow separation caused by the nacelle/pylon vortex system is controlled by a nacelle chine as shown in Figures 3 and 4. One important parameter of the nacelle-chine application is the location of the chine. Three nacelle chine locations were investigated [14]. Chine position 1, 2, and 3 correspond to the installation of a chine on the nacelle inboard side at azimuthal angles of 56°, 51°, and 45°, respectively, where the 3 o'clock position (facing downstream) is $\theta = 0°$ (see Figure 4 for θ convention). Note that positive θ is defined to be in the counterclockwise direction, which is a different convention than Ref. [14]. The surface tuft visualization demonstrates the effectiveness of the nacelle chine at $\alpha = 16°$ (Figure 13(b)). When compared to the baseline case in Figure 13(a), the nacelle chine eliminates the flow separation over the inboard wing. The tufts exhibit unsteady flow over the main wing downstream of the pylon without any sign of separated flow. Flow separation control over the main wing also affects the flow over the inboard flap where the tufts appear to be more streamlined due to the attached flow. Figure 14 shows the aerodynamic plots with TWICS applied for chine positions 1, 2, and 3 and chine position 3 repeat runs (Runs 215, 216, 217, and 218, respectively). The corresponding plots without the wall correction are shown in Figure D6. Based on the lift curves and tuft visualization [14], all chine positions were effective in attenuating the localized flow separation. The chine position 3 configuration (Figures 3 and 4) was shown to be the most effective in eliminating the prestall lift degradation, and therefore, providing the necessary lift recovery between $\alpha = 13°$ and 18°, as shown in Figure 14. Excellent repeatability is observed for the chine position 3 results.

For a closer examination, Figure 17 shows variations in ΔC_D, ΔC_m and ΔC_L as a function of α for the three nacelle chine positions. All differential values were calculated with respect to the corresponding values of the baseline case without chine (Run 208). All three chine positions produced a slight decrease in lift (ΔC_L up to ~0.02) for $\alpha < 10°$, however, they also generated a significant lift increase for $\alpha > 12°$. A maximum ΔC_L of nearly 0.1 was achieved with chine position 3 at $\alpha \approx 16°$, but the ΔC_L dropped to nearly zero at $\alpha \approx 19°$ and was followed by a second ΔC_L increase that took place poststall. A reduction of the azimuthal angle from 56° (chine position 1) to 45° (chine position 3) produced a corresponding increase in ΔC_L. A slight increase in pitching moment (ΔC_m up to ~0.008) was observed for all chine positions for $\alpha \leq 14°$, however, there is a steep decrease in pitching moment (or increase in negative pitching moment) at $\alpha \approx 19°$, which corresponds to a steep decline in the ΔC_L. No significant variation in ΔC_D was observed for $\alpha < 10°$. The steep increase in ΔC_D for $\alpha > 12°$ is similar to the corresponding increase in ΔC_L. The only difference is the steep drop in ΔC_D occurred at $\alpha = 18°$ instead of 19° observed for ΔC_L. The results of the chine position 3 case repeat very well with little variability.

Note that the aerodynamic results for the CRM-HL variant with chine position 3 was selected for comparison with the CRM-SHL-AFC configuration. The associated lift performance also establishes the goal for the CRM-SHL-AFC cases to match or exceed.

Nacelle off

For completeness of the dataset, the model was tested with the nacelle removed (see Figure 5). Note that the CAD files for the CRM-HL nominal landing configuration without the nacelle, the wing/fuselage strake, the 15 slat brackets, and the three flap track fairings can be downloaded from the Third AIAA High-Lift Prediction Workshops [19] website.

Figure 15 shows the aerodynamic plots with TWICS applied for runs with the nacelle off (Runs 222, 224 (with tufts), 225 (repeat), and 226 (repeat)). The nacelle-on variant (Run 208) is also provided for comparison. The corresponding plots without wall corrections are shown in Figure D7. As expected, the nacelle-off case produced lower drag than the nacelle-on case for $\alpha > 0°$. The nacelle-off variant also exhibited slightly lower lift at lower angles of attack than the nacelle-on variant as the presence of the nacelle could contribute a small amount of lift (Figure 15). The pronounced effect of the nacelle is most clearly seen in the C_m versus α plot. The C_m for the nacelle-off case has a significantly flatter (minimal change with increasing angle of attack) slope between $\alpha = 0°$ and 16° compared to the nacelle-on case. The C_m for the nacelle-on variant shows a greater change with angle of attack between $\alpha = 0°$ and ~18°. The repeatability is excellent for the nacelle-off results.

B. Surface Pressure Data

As a result of the analysis of the aerodynamics performance data, three key variants of the CRM-HL — baseline (Run 208), nacelle off (Run 222), and nacelle with the chine in position 3 (Run 217) — were chosen for further comparison of surface pressures (Figures 18–56). A special case showing the effect of the BLRS on the streamwise fuselage pressure distribution at z = 32 inches (upper waterline location) is shown in Figure 57. The pressure distribution plots are presented for these cases at five angles of attack of $\alpha = 4.7°$, 8.9°, 13°, 17.1°, and 19.1°. For clarity, an image showing the location of the pressure row highlighted in red accompanies each figure.

High-lift wing: streamwise

The streamwise surface pressure distributions for the eight spanwise (butt line) locations plus the wingtip (Figure 6), corresponding to $\eta = 0.15$, 0.24, 0.33, 0.42, 0.55, 0.69, 0.82, 0.91, and 1.0, are shown in Figures 18–26. Note that the pressure tap x locations for the slats and flaps are given in deflected coordinates. Also note that the spanwise positions of the orifices on the slats and flaps are not aligned with the streamwise orifices on the main element. However, the η locations shown in all the inset images show them as being so (for illustration purpose only). The lower angle of attack cases ($4.7° \leq \alpha \leq 8.9°$) correspond to typical landing approach flight conditions, whereas $\alpha = 13°$, 17.1°, and 19.1° correspond to typical prestall, stall, and poststall conditions, respectively. Generally speaking, the expected trends were observed: as the angle of attack increased, the suction pressure on the leading edge of the slat and the main wing also increased, whereas the suction pressure on the leading edge of the flap decreased.

For inboard flap locations $\eta = 0.15$, 0.24 and 0.33 (Figures 18, 19, and 20, respectively), the flow is mostly attached on the flap for the three CRM-HL variants tested up to the stall angle ($\alpha \approx 17.1°$). The exception is the nacelle-on case (Run 208), where flow separation occurred near the trailing edge of the main wing and at approximately 30% of the flap chord for the $\eta = 0.24$ location (downstream from the inboard side of the nacelle) at $\alpha = 17.1°$ (Figure 19). The installation of the nacelle chine (Run 217) significantly reduced the flow separation and increased the suction pressures at these locations. The pressure on the lower surface of the main wing shows more variation at the two most inboard locations ($\eta = 0.15$ and 0.24) for different angles of attack.

Near stall, at the spanwise location just inboard of the nacelle ($\eta = 0.24$), the nacelle-off variant (Run 222) has the highest suction peak around the main wing leading edge at the spanwise location just inboard of the nacelle ($\eta = 0.24$); however, the presence of the nacelle resulted in higher suction pressures on the slat than that of the nacelle-off case (Figure 19). At the spanwise location aligned with the nacelle ($\eta = 0.33$), the pressure distribution on the wing leading edge is quite different for the nacelle-off variant because it has a slat filler piece connecting the inboard and outboard slat edges; however, there were no pressure taps on the slat filler piece (Figure 20). At the spanwise location just outboard of the nacelle ($\eta = 0.42$), the nacelle-off variant has the highest suction peak on the slat and main wing leading edge for the five angles of attack shown (Figure 21). Notice that the maximum suction peak on the slat at $\eta = 0.42$ for the nacelle-off variant is nearly twice that of the nacelle-on variants.

The presence of the engine nacelle does not significantly affect the flow over the outboard locations ($\eta \geq 0.55$), as the difference in the C_p distributions for the three CRM-HL variants are negligible for the five angles of attack shown (Figures 22–26). At the mid-outboard flap span of $\eta = 0.55$, the pressure distributions indicate the existence of three-dimensional flow separation at ~60% of the flap chord for all CRM-HL variants, and the separation seems more severe at lower angles of attack (Figure 22). Tuft flow visualization confirmed the existence of a 3D separation in this region [11].

For stall and poststall conditions ($\alpha = 17.1°$ and 19.1°, respectively), the outboard slat at $\eta = 0.69$ carried significantly higher suction pressure than that of the inboard slat at $\eta = 0.24$ (i.e., $C_p \approx -13$ versus -7, in Figures 23 and 19, respectively), indicating higher flow circulation on the slat at the outboard location.

For the outboard wing locations ($\eta = 0.82$ and 0.91), the suction pressures remained fairly high on the slat and the wing leading edge, despite the fact that there is no flap at these spanwise locations to enhance the flow circulation. The pressure distributions indicate there could be a small amount of flow separation near the wing trailing edge at $\alpha = 17.1°$ and 19.1°, as shown in Figures 24 and 25.

The streamwise pressure distributions for the wingtip location ($\eta = 1.0$) are shown in Figure 26. Even with only five working pressure taps at the wingtip, there is an indication of a strong tip vortex, as evidenced by the higher suction pressures upstream of the trailing edge, at stall and poststall conditions ($\alpha = 17.1°$ and 19.1°, respectively).

High-lift wing: spanwise

The spanwise surface pressure distributions along eight chordwise locations across the midslat, wing leading edge, midwing, wing spoiler trailing edge, flap leading edge, flap trailing edge, ~72% wing chord beyond the outboard flap, and wing trailing edge beyond the outboard flap are shown in Figures 27–34, respectively. For clarity, a transparent planform image showing the location of the corresponding spanwise pressure row, highlighted in red, and the relative location of key wing components accompanies the first five figures.

At the midslat row, the maximum spanwise suction pressure occurred at $\eta = 0.51$ for the nacelle-off variant and at $\eta = 0.55$ for the nacelle-on variants (with and without nacelle chine), as shown in Figure 27. All CRM-HL variants show very similar spanwise pressure distributions across the mid-slat for $\eta \geq 0.7$ (Figure 27). The effect of the nacelle/pylon is clearly shown in the C_p distributions for the wing leading-edge row (Figure 28). The drop in the suction pressure at $0.2 \leq \eta \leq 0.5$ with the nacelle/pylon present is due in part to this region being located immediately downstream of the slat cutout required to integrate the nacelle. The vortex system generated by the nacelle/pylon may also be influencing the C_p distributions. The footprint of the nacelle/pylon vortex system is not as evident by the midwing row, as shown in Figure 29, but the spanwise C_p distributions appear slightly skewed toward the outboard direction. At the mid-wing row, the increasing strength of the wingtip vortex as angle of attack increased is especially noticeable. All CRM-HL variants show very similar spanwise pressure distributions over the midwing for $\eta \geq 0.5$ (Figure 29).

To better identify any localized effects on the wing spoiler trailing edge and on the leading edge of the flaps, the locations of the Yehudi break and the outboard flap edge are indicated by dotted, vertical lines in Figures 30 and 31. In addition, the locations of the flap track fairings are also added in Figure 31 to help identify the source of 3D flows on the flap leading edge. The effect of the nacelle vortex system seems to reemerge on the wing spoiler trailing edge for the nacelle-on variant (Run 208) for $\alpha \geq 13°$, as shown in Figure 30, which decreases the suction pressure on the flap leading edge (Figure 31). Note that the wake from the inboard flap track fairing might also contribute to this reduction of suction pressure on the flap leading edge for $\alpha \geq 13°$. Tuft flow visualization results reported by Koklu et al. [14] at $\alpha = 8°$ illustrate the influence on the flap fairing wakes on the flow over the flap. Vatsa et al. [33] performed a computational study exploring the use of AFC to reduce the influence of the flap fairing wakes on the takeoff configuration of the CRM-HL. Additionally, more subtle reduction of suction pressure could be seen on the outboard flap leading edge due the outboard flap track fairings at all angles of attack, as shown in Figure 31. With the exception of $\alpha = 4.7°$ and 19.1°, the spanwise pressure distributions on the flap trailing edge indicate more attached flow (pressure recovery) on the inboard flap than that on the outboard (Figure 32).

Additional localized spanwise pressure rows on the main wing beyond the outboard flap at ~72% wing chord and the wing trailing edge are shown in Figures 33 and 34, respectively. These two locations correspond to the pressure taps on the flap leading-edge and flap trailing-edge rows in their respective stowed positions. Higher suction pressures near the wingtip ($\eta = 1$) and near the outboard flap edge ($\eta = 0.73$) in Figure 33 are due to the strong vortices generated at these regions. With the exception of $0.9 < \eta < 0.95$ at $\alpha = 4.7°$, there are indications of flow separation near the wing trailing edge (Figure 34).

Flap edges

The 18 pressure taps on the inboard and outboard flap edges (three each on the upper, side-edge, and lower surfaces surrounding the two flap side edges) were installed mainly for future aeroacoustics analysis associated with flap edge noise generation [23]. The chordwise pressure distributions on the inboard flap upper, side-edge, and lower surfaces, as well as on the outboard flap upper, side-edge, and lower surfaces are shown in Figures 35–40, respectively.

Figures 38–40 indicate a much stronger and more coherent flap-edge vortex generated around the outboard flap edge than that produced by the inboard flap edge, as shown in Figures 33–37. This phenomenon is more apparent near maximum lift (stall and poststall) conditions. The pressure distributions are fairly insensitive to CRM-HL variants and changes in angle of attack on the lower flap edge surfaces where $\Delta C_p \leq 0.1$ for the inboard flap (Figure 37) and $\Delta C_p \leq 0.2$ for the outboard flap (Figure 40).

Fuselage

The streamwise pressure distributions for the fuselage waterline locations of middle, upper, and lower rows (corresponding to z = 23, 32, and 10 inches) are shown in Figures 41–43, respectively. Note that z = 32 and 10 inches share the same spanwise location of $\eta = 0.06$. With the exception of the fuselage station near the nose, the z = 23 inches waterline location corresponds to $\eta = 0.11$.

The streamwise pressure distributions at z = 23 inches (middle waterline location) has the highest suction peak pressure at x = 106.4 inches, corresponding to the third tap from the leading edge of the wing root (Figure 41). Note that the nacelle-on variant without the chine has the lowest suction pressure for the poststall condition ($\alpha = 19.1°$) at x = 132.5 inches, corresponding to the fifth tap from the leading edge of the wing root.

At z = 32 inches (upper waterline location), the streamwise suction peak level is approximately half the level at the middle waterline location. The peak location moved downstream to x = 121.2 inches, corresponding to the fourth tap from the leading edge of the wing root (Figure 42). At z = 10 inches (lower waterline location), the streamwise pressure distributions indicate increasing pressure near the wing root, due to the highly deflected inboard flap as the flow passed underneath the wing root hump (Figure 43).

The circumferential pressure distributions on the fuselage around the wing root region at x = 99.7, 106.4, 132.5, 142.5, 149.5, and 156.5 inches are shown in Figures 44–49, respectively.

Around the leading edge of the wing root hump, the first two circumferential pressure distributions at x = 99.7 and 106.4 inches both have distinct suction peaks at z = 20 and 23 inches, respectively (Figures 44 and 45). For the four circumferential pressure distributions around the trailing edge of the wing root hump at x = 132.5, 142.5, 149.5, and 156.5 inches, the suction peak is not as distinguishable. The suction pressure levels reduce steadily with increasing fuselage station toward the hump trailing edge (Figures 46–49). There are signs of poststall flow separation on the fuselage surface pressures for the four circumferential fuselage stations around the trailing edge of the wing root hump (132.5 inches $\leq x \leq$ 156.5 inches).

Nacelle

The C_p distributions on the nacelle/pylon for two variants (baseline (nacelle on) and nacelle with the most effective chine installation) of the CRM-HL at five angles of attack are shown in Figures 50–56. Chine position 3 installed at the $\theta = 45°$ location as shown in Figure 4 was the most effective and is used for the comparisons in this section.

The streamwise pressure distributions covering both the interior and the exterior of the nacelle for the 12, 3, 6, and 9 o'clock positions (facing downstream) are shown in Figures 50–53, respectively. At the 12 o'clock position, the nacelle leading edge produced the highest suction pressures for prestall and stall angles of attack (Figure 50). The internal nacelle pressure distributions are fairly insensitive to the CRM-HL variants and changes in angle of attack. The nacelle with chine case produced only a marginal increase in suction pressure at $\alpha = 17.1°$ and $19.1°$ (stall and poststall conditions). The streamwise pressure distributions between the 3 and 9 o'clock positions are somewhat similar in shape but differ in pressure levels (Figures 51 and 53, respectively). The latter has more than double the peak suction of the former, indicating possible localized spanwise flows toward the outboard direction.

At the 6 o'clock position, the nacelle interior behaved as the suction surface and the external side acted as the pressure surface (Figure 52). Compared to the 12 o'clock position, the maximum suction pressures were reduced by a factor of 5 for the 9 and 6 o'clock positions, whereas the maximum suction pressures were reduced by a factor of 13 for the 3 o'clock position. No noticeable difference in pressure distributions was observed for variants with and without the nacelle chine at the 3, 6, and 9 o'clock positions (Figures 51–53).

Exterior circumferential pressure distributions covering 180° of the nacelle upper surface (between 3 and 9 o'clock in the counterclockwise direction) at $x \approx 99.8$ inches are shown in Figure 54. Although the nacelle chine was installed at the $\theta = 45°$ location, its maximum impact in terms of suction pressure enhancement occurs at $\theta = 135°$ ($\Delta\theta = 90°$) for the poststall condition of $\alpha = 19.1°$. The increased suction pressure due to the nacelle chine can clearly be seen between $45° \leq \theta \leq 157.5°$ for $\alpha = 17.1°$, and to a lesser extent for $\alpha = 13°$ (Figure 54).

Interior circumferential pressure distributions covering the full circumference of the inner nacelle surface at $x \approx 106.6$ inches are shown in Figure 55. The internal circumferential pressures are positive and sinusoidal, with the lowest pressures occurring at $\theta = 270°$ (or at the 6 o'clock position). The variant with the nacelle chine has slightly lower pressures than the variant without the chine, but the difference is marginal (i.e., $C_p \leq 0.01$).

Pressure distributions on the nacelle pylon at $x = 109.2$ inches are shown in Figure 56. The ΔC_p variation between the three spanwise (η) locations on the pylon is less than 0.3. The nacelle with chine variant produced higher suction pressure than the case without chine for $\alpha = 13°$ and 17.1°. However, the trend is reversed at $\alpha = 19.1°$ (poststall) for $\eta < 0.33$.

Special case: effect of BLRS on fuselage

In addition to the three variants of CRM-HL, a special case of fuselage streamwise pressure distributions at $z = 32$ inches (upper waterline location) is presented in Figure 57 to examine the effect of BLRS. The BLRS was active for select runs and these results are included for completeness. The figure compares the C_p distributions with and without activation of the BLRS (Runs 203 and 208, respectively). Generally speaking, activation of the BLRS slightly increased the streamwise suction pressure along the fuselage stations with the most noticeable changes occurring around the wing root hump region (93 inches $\leq x \leq 157$ inches). The maximum suction pressure increase occurred at $x \approx 121$ inches. No significant difference in C_p distributions was detected at the other two waterline locations of $z = 10$ and 23 inches. This increase in localized suction pressure on the fuselage occurs upstream and above the moment reference center (at $x = 132.6$ inches and $z = 17.8$ inches, respectively) and could explain the slight increase in pitching moment with the activation of BLRS that is shown in Figure 10.

Effect of wall correction on parameters affecting C_p values

For completeness, the effect of wall correction on parameters affecting the C_p values is illustrated here. Figure 58 shows the variations of $\Delta q_{\infty,wc}$ and $\Delta \alpha_{wc}$ as a function of uncorrected α due to the application of TWICS wall corrections for the three CRM-HL variants (Runs 208, 217, and 222). Since activation of floor BLRS could affect the q_∞ of the wind tunnel test, the BLRS-on case (Run 203) is also included in the figure for examination.

Figure 58(a) shows that the wall correction increased $\Delta \alpha_{wc}$ by approximately 0.2° to 1.1°, where the shape of the $\Delta \alpha_{wc}$ curves resemble that of the lift curves as it even captured the prestall lift degradation observed for Runs 203 and 208. Figure 58(b) shows that the wall correction increased $\Delta q_{\infty,wc}$ by approximately 0.5 psf (0.8%) up to $\alpha \approx 12°$ for Runs 208, 217, and 222, and then more steeply thereafter for the two nacelle-on cases (Runs 208 and 217). For the BLRS-on case (Run 203), the shape of the $\Delta q_{\infty,wc}$ curve parallels that of the three CRM-HL variants (Runs 208, 217, and 222) but $\Delta q_{\infty,wc}$ is approximately 0.3 psf (0.5%) less than when BLRS is inactive (Runs 208, 217, and 222). Since q_∞ is in the denominator of C_p equation, the relatively small increase in q_∞ for the wall correction case led to a slight decrease in the pressure coefficient magnitude (i.e., $|\Delta C_p| < 0.15$) compared to the case without the wall correction.

C. Photogrammetry Data

The photogrammetry data presented were obtained using data from a wind-off α sweep (Run 207) and a wind-on α sweep at $M_\infty = 0.2$ (Run 212). As a reminder, the photogrammetry targets were on the model during the entire test. The measurements were performed on the CRM-HL variant with the nacelle but without the chine. Prior to analyzing the wind-on results, the wind-off run was analyzed to determine if the target positions were adequate to produce reasonable results. A transformation of the wind-off data at various angles of attack using $\alpha = 0°$ as a reference accurately predicted wing angles of attack, providing confidence in the measurements.

The change in z position (Δz) in inches between wind-off and wind-on cases for each target was computed and a contour of Δz is shown in Figure 59 for the highest model deflection case at α = 19.1°, which corresponds to α = 18° without TWICS applied. Circular dots, indicating photogrammetry target locations, are also shown in the figure for reference. The contours show that the 3D Δz patterns on the model could be separated into three regions of deflection: up to ~0.4 inches across the inboard flap, up to ~0.8 inches across the outboard flap, and up to ~1.1 inches beyond the outboard flap. As expected, the contours indicate that the maximum deflection occurs at the wing tip.

The maximum model deflection in z occurred at the most outboard location (wingtip target 1051). Model deflection at the wingtip target is tabulated in Table 5 for angles of attack with and without TWICS applied. Corresponding Δz versus α curves are plotted in Figure 60. The shape of the deflection curves is similar to the lift curves, indicating that the model deflection in z is proportional to the aerodynamic loading. A maximum deflection in z of 1.16 inches is detected at the wingtip.

Photogrammetry results are typically processed to compute wing twist, which can be thought of as local variations in wing angle of attack. Using the methods described in Ref. [31] wing twist was computed at the wing tip. At the maximum angle of attack of 19.1° (18° without TWICS), the wingtip twist was calculated to be ~0.25°.

Conclusions

A 10%-scale CRM-HL with 30º inboard and outboard slats, a removable engine nacelle, and a set of 37° inboard and outboard single-element Fowler flaps was successfully tested in the NASA Langley Research Center 14- by 22-Foot Subsonic Tunnel. Three variants of the CRM-HL model— baseline (nacelle on), nacelle off, and nacelle with the most effective chine location were investigated. Some key findings from this wind tunnel investigation are as follows:

1) Results for the CRM-HL model with best chine placement studied were chosen as a reference case for comparison and to set the lift performance goals for the AFC-enabled version of the CRM-HL (CRM-SHL-AFC).
2) Effects of the tufts (Figure 12), lower Mach numbers (Figure 11), hysteresis associated with increasing/decreasing angle of attack (Figure 9), and activation of the floor BLRS (Figure 10) were found to be either negligible or marginal.
3) Placement of a chine on the nacelle inboard side at an azimuthal angle of 45° above the 3 o'clock position looking downstream eliminated the localized separation on the trailing edge of the main element and on the inboard flap downstream from the nacelle, and therefore, provided lift recovery between α = 13° and 17° (Figure 14).
4) Nacelle-on variant produced a prestall lift degradation between α = 13° and 17°, nacelle-off variant did not (Figure 15).
5) Presence of the engine nacelle did not seem to significantly affect the flow over the outboard portion of the wing ($\eta \geq 0.55$) (Figures 22–26).
6) Signs of poststall flow separation on the fuselage stations near the trailing edge of the wing root hump (Figures 46–49) were evident.
7) The highest suction pressures for prestall and stall angles of attack were produced at the nacelle leading edge at the 12 o'clock position (C_p ~ -7.8) when compared to pressures measured on the nacelle at the 3, 6, and 9 o'clock positions (C_p ~ -0.6, -1.5, -1.6, respectively) (Figures 50–52).
8) A nacelle chine increased the suction pressure on the nacelle between 45° ≤ θ ≤ 157.5° for α = 13° (~6% maximum increase) and 17.1°(~12% maximum increase) (Figure 54).
9) Photogrammetry results indicated a maximum deflection of 1.16 inches (or 1% of the wing span) (Figure 60) and twist of approximately 0.25° at the wingtip for the maximum angle of attack of 19.1°.

With the successful development and testing of the CRM-HL, an "open" geometry high-lift model is now available for future R&D efforts. These efforts can include (but are not limited to) AFC, airframe noise, flow physics, CFD validation, certification by analysis, and icing studies associated with a modern commercial transport airplane.

References

[1] Van Dam, C. P., "The Aerodynamic Design of Multi-Element High-Lift Systems for Transport Airplanes," *Progress in Aerospace Sciences*, Vol. 38, 2002, pp. 101–144. doi: 10.1016/S0376-0421(02)00002-7

[2] Lin, J. C. and Dominik, C. J., "Parametric Investigation of a High-Lift Airfoils at High Reynolds Numbers," *Journal of Aircraft*, Vol. 34, No. 4, July–August 1997, pp. 485-491. doi: 10.2514/2.2217

[3] Gatlin, G. M. and McGhee, R. J., "Experimental Investigation of Semispan Model Testing Techniques," *Journal of Aircraft*, Vol. 34, No. 4, July–August 1997, pp. 500-505. doi: 10.2514/2.2219

[4] Storms, B. L., James, K. D., Satran, D. R., Arledge, T., K., Burnside, N, J., Horne, W. C., and Driver, D. M., "Aerodynamics of a 26%-Scale Semi-Span Model of the Boeing 777 in the NASA Ames 40- by 80-Foot Wind Tunnel," NASA/TP–2005-212829, January 2005.

[5] Hannon, J. A., Washburn, A. W., Jenkins, L. N., and Watson, R. D., "Trapezoidal Wing Experimental Repeatability and Velocity Profiles in the 14- by 22-Foot Subsonic Tunnel," *50th AIAA Aerospace Sciences Meeting*, AIAA Paper 2012-0706, 2012. doi: 10.2514/6.2012-0706

[6] Vassberg, J. C., DeHaan, M. A., Rivers, M. S., and Wahls, R. A., "Retrospective on the Common Research Model for Computational Fluid Dynamics Validation Studies," *Journal of Aircraft*, Vol. 55, No. 4, pp. 1325-1337, July–Aug. 2018. doi: 10.2514/1.C034906

[7] NASA Common Research Model, September 2019. http://commonresearchmodel.larc.nasa.gov

[8] Lacy, D. S. and Sclafani, A. J., "Development of the High Lift Common Research Model (HL-CRM): A Representative High Lift Configuration for Transonic Transports," *54th AIAA Aerospace Sciences Meeting*, AIAA Paper 2016-0308, 2016. doi: 10.2514/6.2016-0308

[9] Lin, J. C., Melton, L. P., Hannon, J. A., Andino, M. Y., Koklu, M., Paschal, K. B., and Vatsa, V. N., "Wind Tunnel Testing of Active Flow Control on the High Lift Common Research Model," *AIAA AVIATION 2019 Forum*, AIAA Paper 2019-3723, 2019. doi: 10.2514/6.2019-3723

[10] Melton, L. P., Lin, J. C., Hannon, J. A., Andino, M. Y., Koklu, M., and Paschal, K. B., "Sweeping Jet Flow Control on the Simplified High-Lift Version of the Common Research Model," *AIAA AVIATION 2019 Forum*, AIAA Paper 2019-3726, 2019. doi: 10.2514/6.2019-3726

[11] Koklu, M., Lin, J. C., Hannon, J. A., Melton, L. P., Andino, M. Y., Paschal, K. B., and Vatsa, V. N., "Surface Flow Visualization of the High-Lift Common Research Model," *AIAA AVIATION 2019 Forum*, AIAA Paper 2019-3727, 2019. doi: 10.2514/6.2019-3727

[12] Vatsa, V. N., Duda, B., Lin, J. C., Melton, L. P., Lockard, D. P., O'Connell, M., and Hannon, J. A., "Comparative Study of Active Flow Control Strategies for Lift Enhancement of a Simplified High-Lift Configuration," *AIAA AVIATION 2019 Forum*, AIAA Paper 2019-3724, 2019. doi: 10.2514/6.2019-3724

[13] Lin, J. C., Melton, L. P., Hannon, J. A., Andino, M. Y., Koklu, M., Paschal, K. B., and Vatsa, V. N., "Wind Tunnel Testing of High Efficiency Low Power (HELP) Actuation for Active Flow Control," *AIAA SciTech 2020 Forum*, AIAA Paper 2020-0783, 2020. doi: 10.2514/6.2020-0783

[14] Koklu, M., Lin, J. C., Hannon, J. A., Melton, L. P., Andino, M. Y., Paschal, K. B., and Vatsa, V. N., "Mitigation of Nacelle/Pylon Wake on the High-Lift Common Research Model Using a Nacelle Chine," *AIAA SciTech 2020*, AIAA Paper 2020-0786, 2020. doi: 10.2514/6.2020-0786

[15] Vatsa, V. N., Lin, J. C., Melton, L. P., Lockard, D. P., and Ferris, R., "CFD and Experimental Data Comparisons for Conventional and AFC-Enabled CRM High-Lift Configurations," *AIAA AVIATION 2020 Forum*, AIAA Paper 2020-2939, 2020. doi: 10.2514/6.2020-2939

[16] Rumsey, C. L., Slotnick, J. P., Long, M., Stuever, R. A., and Wayman, T. R., "Summary of the First AIAA CFD High-Lift Prediction Workshop," *Journal of Aircraft*, Vol. 48, No. 6, November-December 2011, pp. 2068–2079. doi: 10.2514/1.C031447

[17] Rumsey, C. L. and Slotnick, J. P., "Overview and Summary of the Second AIAA High-Lift Prediction Workshop," *Journal of Aircraft*, Vol. 52, No. 4, July–August 2015, pp. 1006-1025. doi: 10.2514/1.C032864

[18] Rumsey, C. L., Slotnick, J. P., and Sclafani, A. J., "Overview and Summary of the Third AIAA High Lift Prediction Workshop," *Journal of Aircraft*, Vol. 56, No. 2, pp. 621-644, March–April 2019. doi: 10.2514/1.C034940

[19] Third AIAA CFD High Lift Prediction Workshop, NASA HL-CRM Geometry Files, July 2016. https://hiliftpw.larc.nasa.gov/Workshop3/geometries.html

[20] Lacy, D. and Clark, A. M., "Definition of Initial Landing and Takeoff Reference Configurations for the High Lift Common Research Model (CRM-HL)," *AIAA AVIATION 2020 Forum*, AIAA Paper 2020-2771, 2020. doi: 10.2514/6.2020-2771

[21] Clark, A. M., Slotnick, J. P., Taylor, N., and Rumsey, C. L., "Requirements and Challenges for CFD Validation within the High-Lift Common Research Model Ecosystem," *AIAA AVIATION 2020 Forum*, AIAA Paper 2020-2772, 2020. doi: 10.2514/6.2020-2772

[22] Evans, A., Lacy, D., Smith, I., and Rivers, M., "Test Summary of the NASA Semi-Span High-Lift Common Research Model at the QinetiQ 5-Metre Low-Speed Wind Tunnel," *AIAA AVIATION 2020 Forum*, AIAA Paper 2020-2770, 2020. doi: 10.2514/6.2020-2770

[23] Lockard, D. P., Choudhari, M. M., Vatsa, V. N., and O'Connell, M. D., "Noise Simulations of the High-Lift Common Research Model," *23rd AIAA/CEAS Aeroacoustics Conference*, AIAA Paper 2017-3362, 2017. doi: 10.2514/6.2017-3362

[24] Lockard, D. P., O'Connell, M. D., Vatsa, V. N., and Choudhari, M. M., "Assessment of Aeroacoustic Simulations of the High-Lift Common Research Model," *25th AIAA/CEAS Aeroacoustics Conference*, AIAA Paper 2019-2460, 2020. doi: 10.2514/6.2019-2460

[25] Gentry, G. L., Quinto, F. P., Gatlin, G. M., Applin, Z. T. "The Langley 14- by 22-Foot Subsonic Tunnel: Description, Flow Characteristics, and Guide for Users," NASA-TP-3008, September 1990. https://ntrs.nasa.gov/search.jsp?R=19900018333

[26] Neuhart, D. H. and McGinley, C. B., "Free-Stream Turbulence Intensity in the Langley 14- by 22-Foot Subsonic Tunnel," NASA TP 213247, August 2004. https://ntrs.nasa.gov/citations/20040120956

[27] Ulbrich, N., "The Real-Time Wall Interference Correction System of the NASA Ames 12-Foot Pressure Wind Tunnel," NASA/CR – 1998-208537, July 1998. https://ntrs.nasa.gov/citations/19980223963

[28] Ulbrich, N. and Boone, A. R., "Real-Time Wall Interference Correction System of the 12-Foot Pressure Wind Tunnel," *36th AIAA Aerospace Sciences Meeting*, AIAA Paper 98-0707, 1998. doi: 10.2514/6.1998-707

[29] Iyer, V., Kuhl, D. D., and Walker, E. L., "Improvements to Wall Corrections at the NASA Langley 14X22-Foot Subsonic Tunnel," *21st AIAA Applied Aerodynamics Conference*, AIAA Paper 2003-3950, 2003. doi: 10.2514/6.2003-3950

[30] Kushner, L. K., Drain, B. A., Schairer, E. T., Heineck, J. T., and Bell, J. H., "Model Deformation and

Optical Angle of Attack Measurement System in the NASA Ames Unitary Plan Wind Tunnel," *55th AIAA Aerospace Sciences Meeting*, AIAA Paper 2017-1052, 2017. doi: 10.2514/6.2017-1052

[31] Burner, A. W., Wahls, R. A., and Goad, W. K., "Wing Twist Measurements at the National Transonic Facility," NASA TM 110229, February 1996. https://ntrs.nasa.gov/citations/19960016773

[32] Liu, T., Radetzsky, R., Garg, S., and Cattafesta, L., "A Videogrammetric Model Deformation System and its Integration with Pressure Paint," *37th AIAA Aerospace Sciences Meeting*, AIAA Paper 1999-0568, 1999. doi: 10.2514/6.1999-568

[33] Vatsa, V. N., Lin, J. C., Melton, L. P., Lockard, D. P., and Ferris, R., "CFD Simulations of Landing and Takeoff CRM High-Lift Configurations," *AIAA AVIATION 2021 Forum*, AIAA Paper 2021-2499, 2021. doi: 10.2514/6.2021.2499

Table 1. Slat gap and overhang settings (as-designed) for the landing configuration.

Slat Bracket Number	Slat Gap (inches)	Slat Overhang (inches)	Gap/local chord (%)	Overhang/local chord (%)	η location	Local chord (inches)
1	0.317	-0.282	0.758	-0.675	0.175	41.7971
3	0.255	-0.214	0.738	-0.619	0.281	34.5705
4	0.233	-0.189	0.824	-0.669	0.381	28.2604
15	0.234	-0.231	1.973	-1.948	0.961	11.8590

Table 2. Flap gap and overhang settings (as-designed) for the landing configuration.

Flap Bracket Number	Flap Gap (inches)	Flap Overhang (inches)	Gap/local chord (%)	Overhang/local chord (%)	η location	Local chord (inches)
2	0.355	0.268	1.242	0.938	0.307	28.5786
3	0.361	0.137	1.380	0.524	0.455	26.1551
4	0.305	0.057	1.454	0.272	0.639	20.9703

Table 3. Summary of key model parameters.

Parameter	**Value**
c_{MAC}	27.6 inches at y=46.9 (η = 0.41)
b	115.7 inches
S	2973.6 in^2
Aspect Ratio	9
Sweep angle of the wing quarter chord	35°
MRC	x = 132.6 inches, y = 0 inches, z = 17.8 inches
Fuselage nose location	x = 9.3 inches y = 0 inches z = 19.8 inches
Re_{MAC}	≈ $3.3x10^6$ at M_∞ = 0.20
Wing dihedral angle	5°
Wing twist	6.72° at η = 0 -3.75° at η = 1

Table 4. Test summary (Runs 200 to 227).

Run No.	M_∞	Re_{MAC} (x 10^6)	Nacelle (on/off)	Chine (on/off)	Tufts (on/off)	With TWICS		Without TWICS		Comments
						Fig. No.	Table No.	Fig. No.	Table No.	
200	0.2	3.27	On	Off	Off	8	B1	D1	C1	CRM-HL baseline configuration
201	0.2	3.27	On	Off	Off	9	B2	D2	C2	Increasing α, hysteresis check
202	0.2	3.27	On	Off	Off	9	B3	D2	C3	Decreasing α, hysteresis check
203	0.2	3.27	On	Off	Off	10	B4	D3	C4	Floor BLRS activated
208*	0.2	3.27	On	Off	Off	8 to 15	B5	D1 to D7	C5	Repeat of baseline run
209	0.125	2.04	On	Off	Off	11	B6	D4	C6	Lower Mach number run
210	0.15	2.45	On	Off	Off	11	B7	D4	C7	Lower Mach number run
211	0.175	2.86	On	Off	Off	11	B8	D4	C8	Lower Mach number run
212 ‡	0.2	3.27	On	Off	Off	8	B9	D1	C9	Repeat of baseline run, photogrammetry data collected
215	0.2	3.27	On	On	On	14	B10	D6	C10	Chine position 1
216	0.2	3.27	On	On	On	14	B11	D6	C11	Chine position 2
217*	0.2	3.27	On	On	On	14	B12	D6	C12	Chine position 3
218	0.2	3.27	On	On	On	14	B13	D6	C13	Repeat of Run 217 (chine position 3)
219	0.2	3.27	On	Off	On	12	B14	D5	C14	Tufts on wing and fuselage
220	0.2	3.27	On	Off	On	12	B15	D5	C15	Tufts on wing and fuselage
221	0.2	3.27	On	Off	Off	8	B16	D1	C16	Repeat of baseline run
222*	0.2	3.27	Off	Off	Off	15	B17	D7	C17	Nacelle off run
224	0.2	3.27	Off	Off	On	15	B18	D7	C18	Nacelle off with tufts on wing and fuselage
225	0.2	3.27	Off	Off	Off	15	B19	D7	C19	Repeat of nacelle off run
226	0.2	3.27	Off	Off	Off	15	B20	D7	C20	Repeat of nacelle off run
227	0.2	3.27	On	Off	Off	8	B21	D1	C21	Repeat of baseline run

* Pressure data are used for comparative plots: Figure 18 to Figure 57 (with TWICS).

‡ Photogrammetry data are presented.

Table 5. Model aeroelastic deflection at the wingtip.

α (deg) without TWICS	α (deg) with TWICS	Δz (inches)
0.0	0.5	0.47
2.0	2.6	0.58
4.0	4.7	0.68
6.0	6.8	0.76
7.0	7.8	0.80
8.0	8.9	0.84
9.0	9.9	0.88
10.0	10.9	0.96
11.0	12.0	0.97
12.0	13.0	1.00
13.0	14.0	1.02
14.0	15.0	1.07
15.0	16.1	1.07
15.5	16.6	1.09
16.0	17.1	1.12
16.5	17.6	1.11
17.0	18.1	1.14
17.5	18.6	1.13
18.0	19.1	1.16
18.5	19.5	1.13
19.0	20.0	1.10

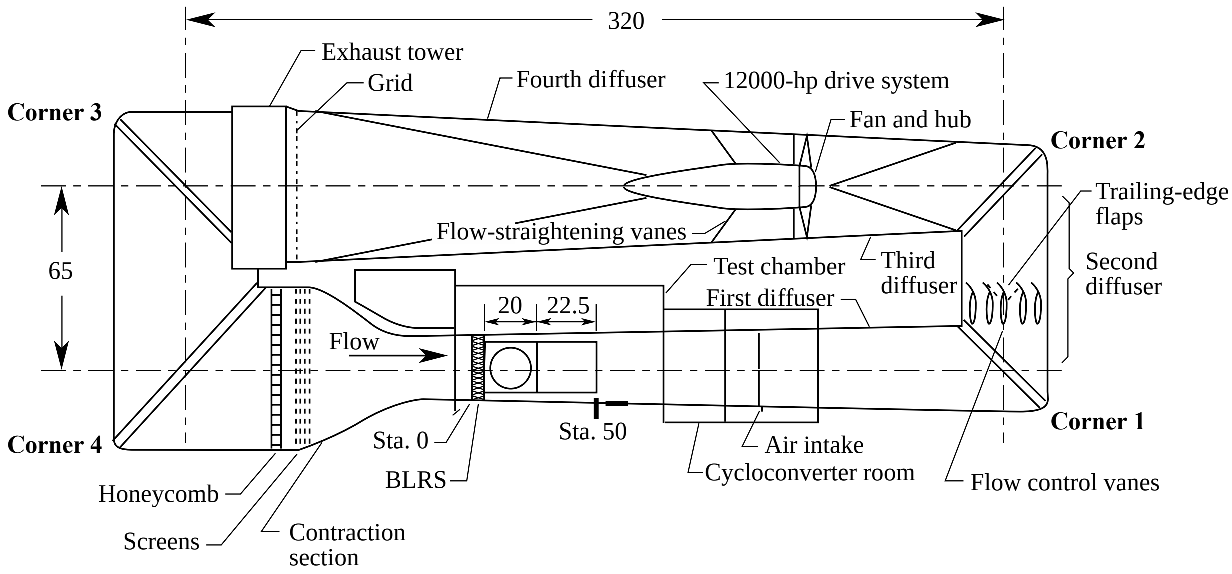

Figure 1. Schematic of the 14x22 tunnel circuit. Dimensions are given in feet.

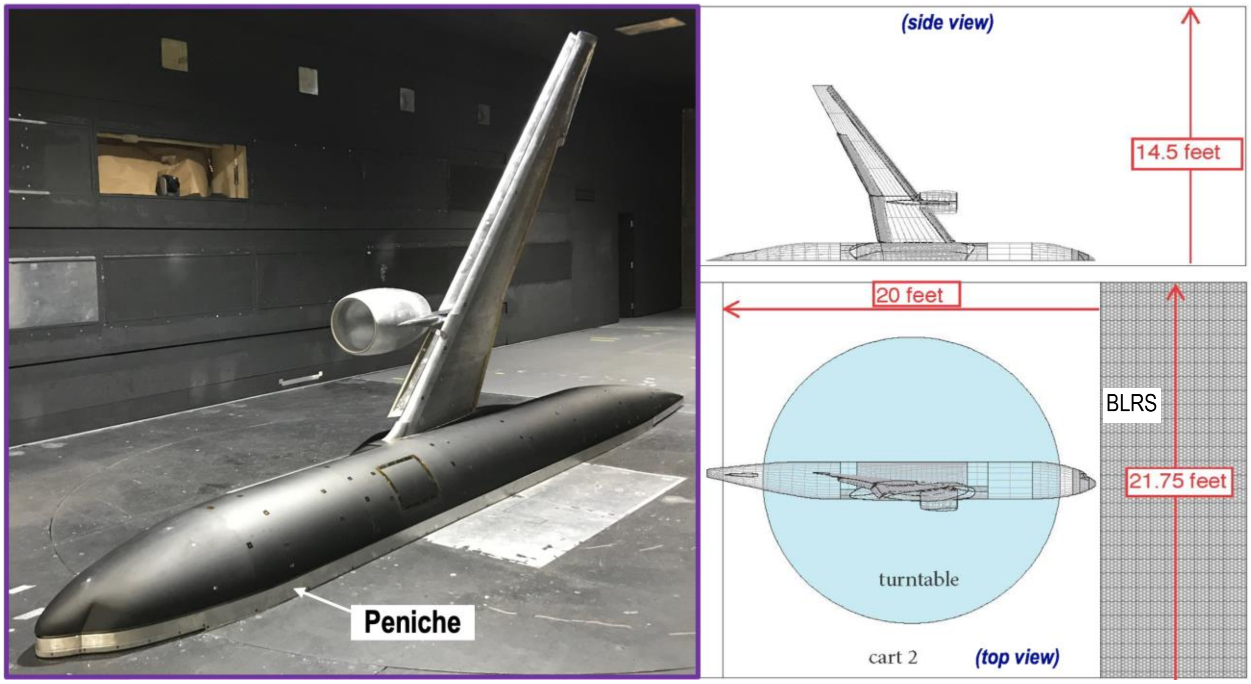

Figure 2. Semispan CRM-HL in the 14x22.

Figure 3. Photographs of CRM-HL model with the engine nacelle (baseline, left) and with nacelle chine installed (upper right). A close-up view of the nacelle chine is on lower right.

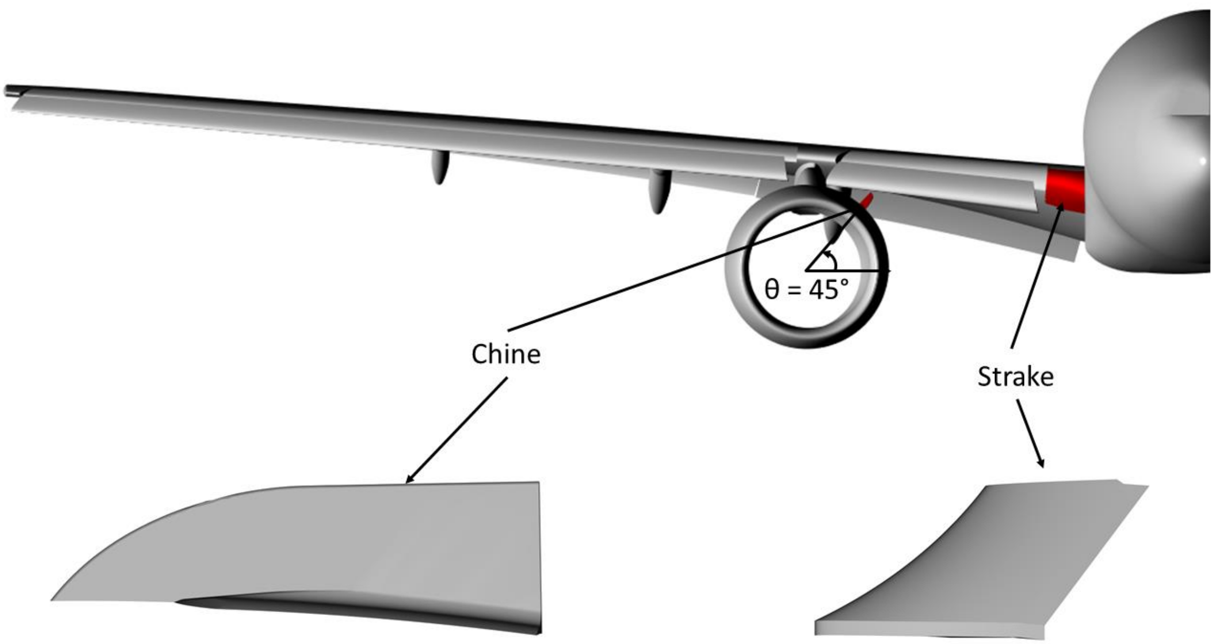

Figure 4. Planform view of the strake and nacelle chine and their locations on the CRM-HL CAD model.

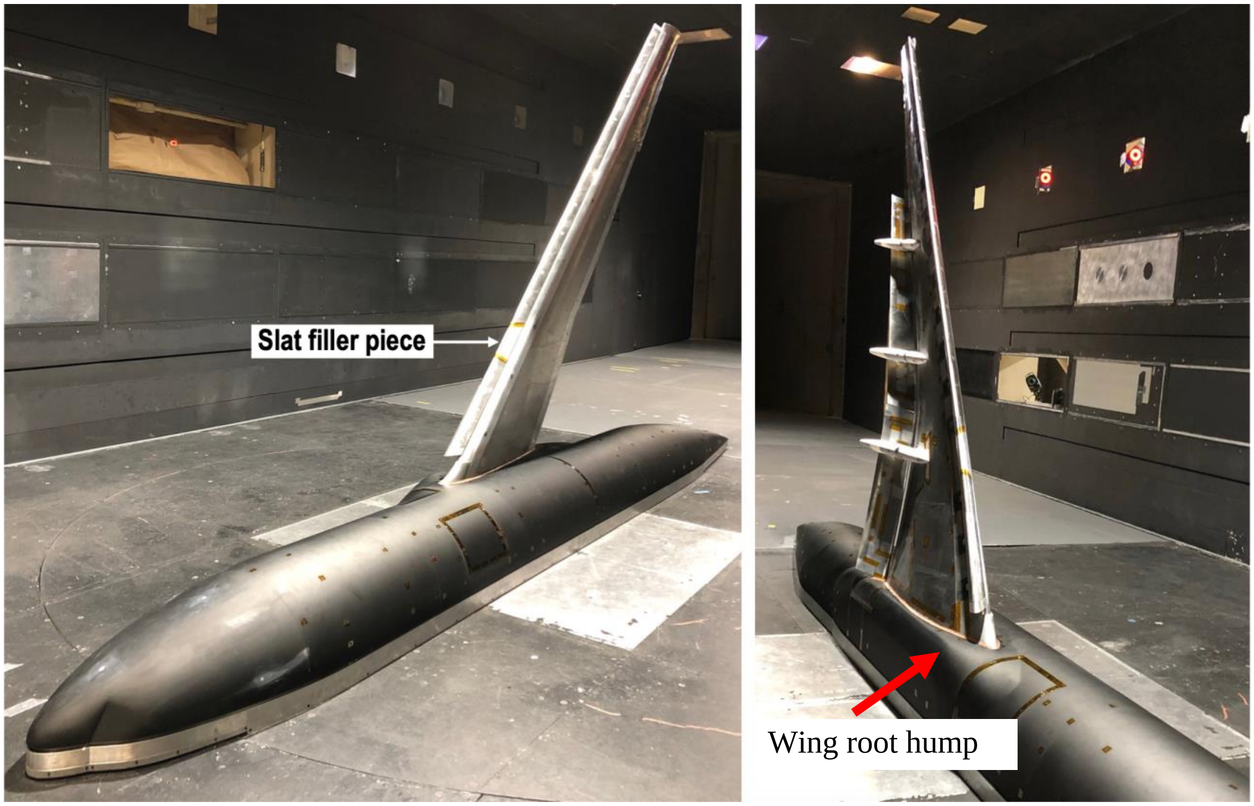

Figure 5. Photographs of CRM-HL model without engine nacelle: upper surface frontal view (left) and lower surface frontal view (right).

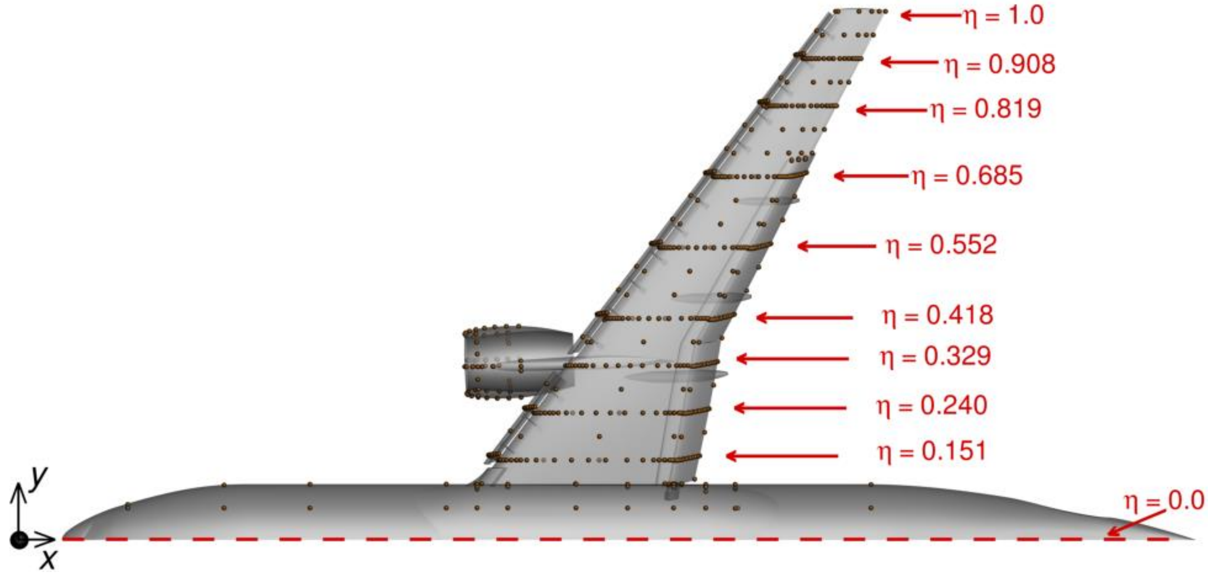

(a) Pressure tap layout on wing

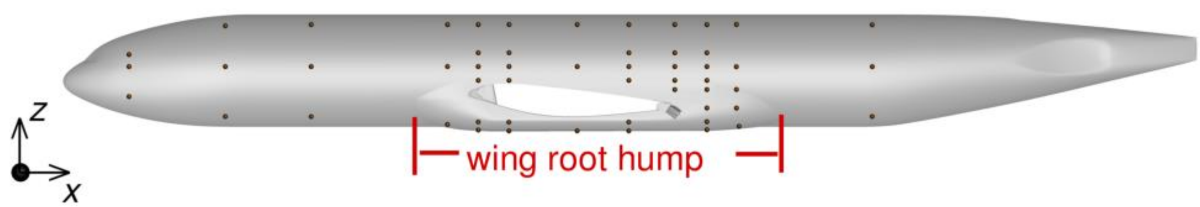

(b) Pressure tap layout on fuselage (image flipped horizontally for consistency).

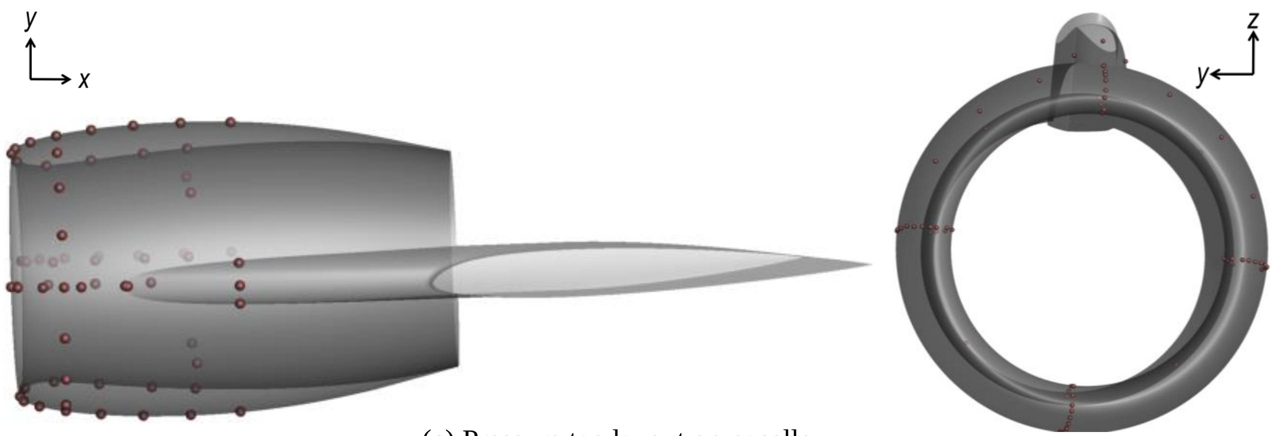

(c) Pressure tap layout on nacelle.

Figure 6. CRM-HL pressure port layout. Origin of coordinate system shown by (●) in (a) and (b).

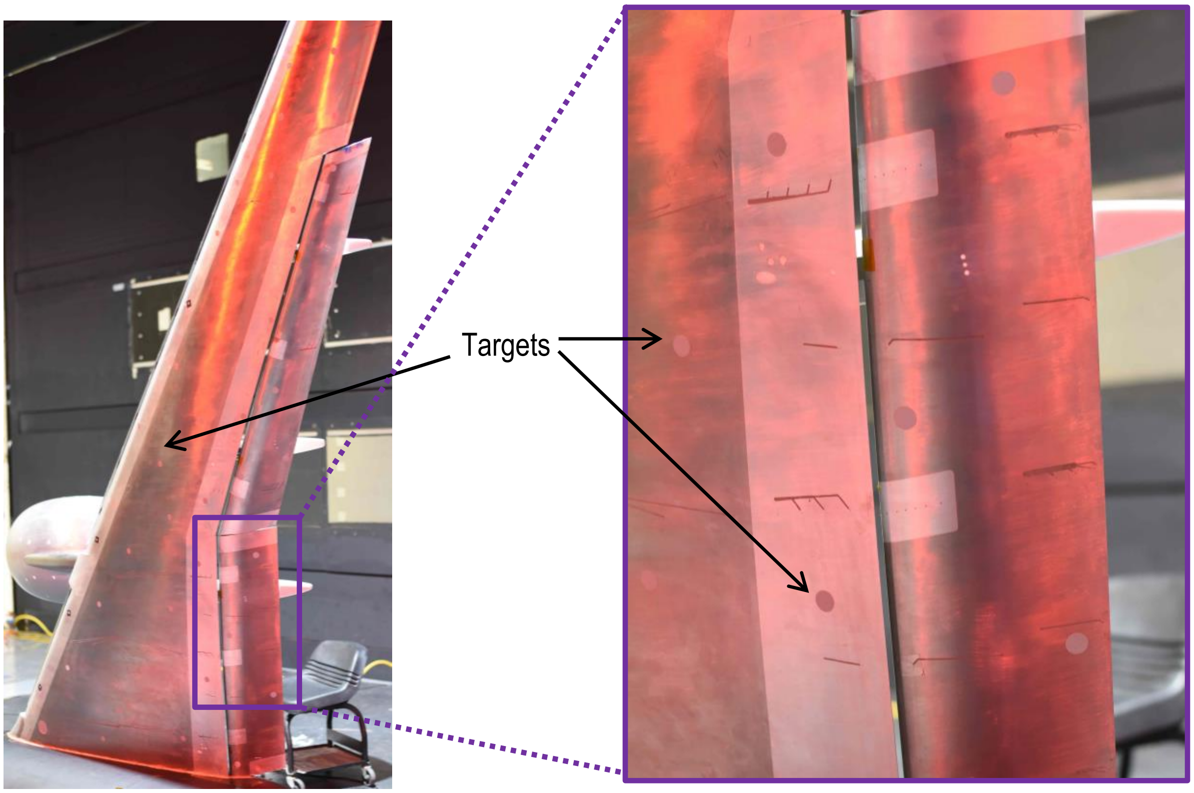

(a) Photographs of targets on the CRM-HL.

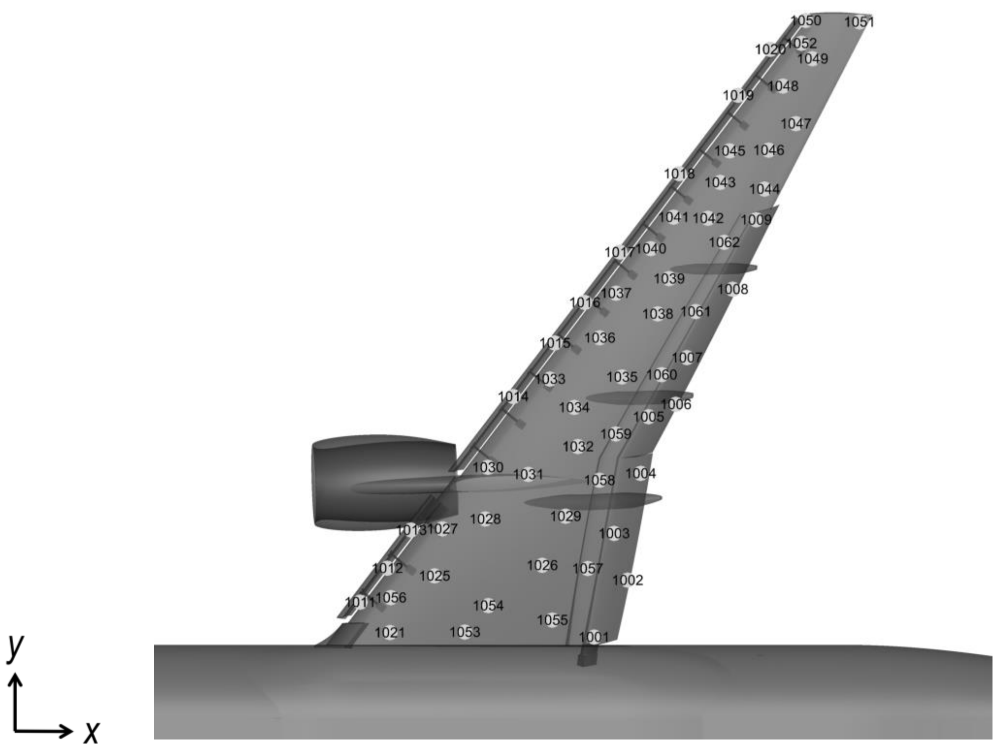

(b) Target ID and locations.

Figure 7. Photogrammetry targets on CRM-HL.

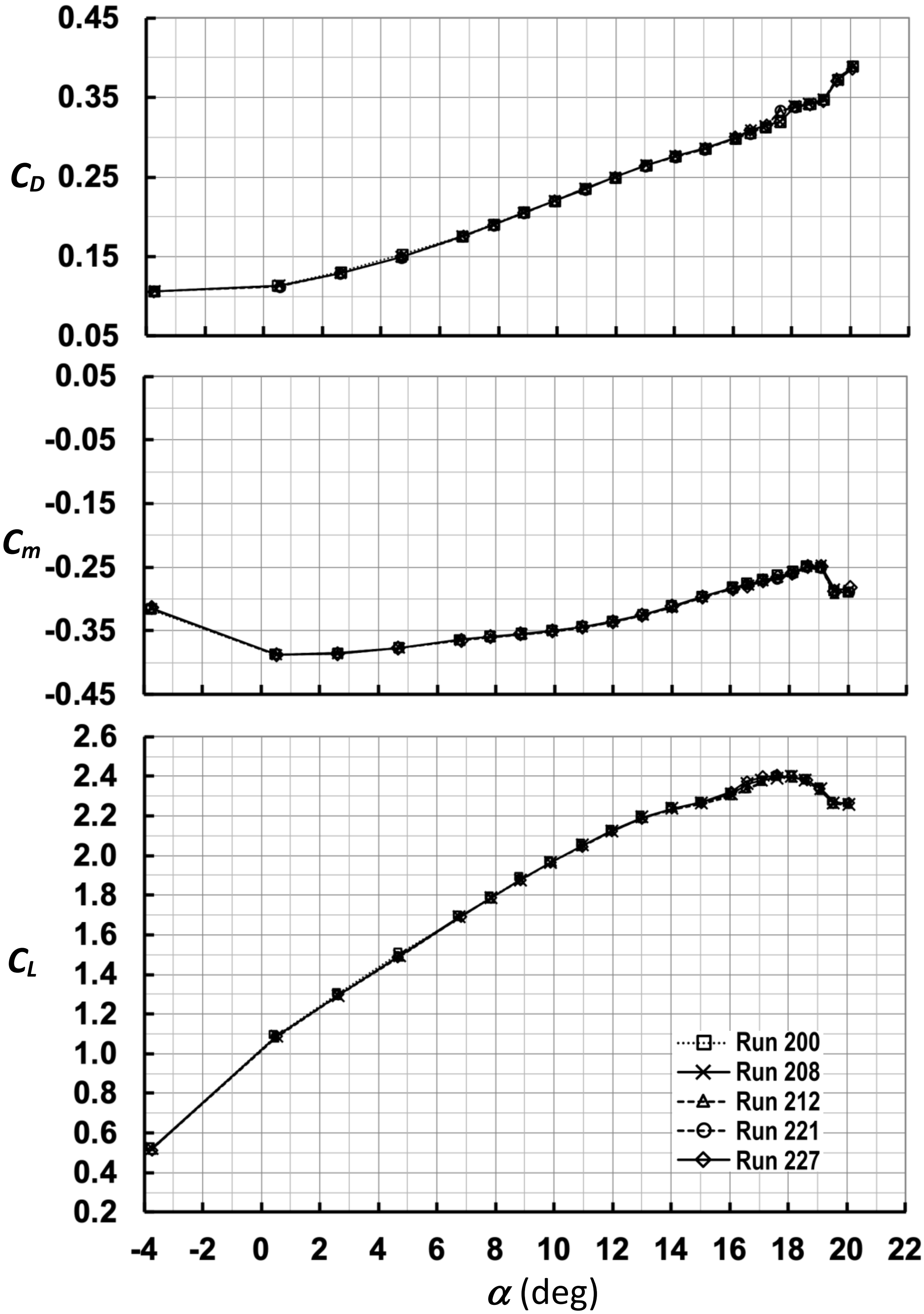

Figure 8. C_D, C_m and C_L vs. α plots for CRM-HL baseline repeat runs ($M_\infty = 0.2$, with TWICS).

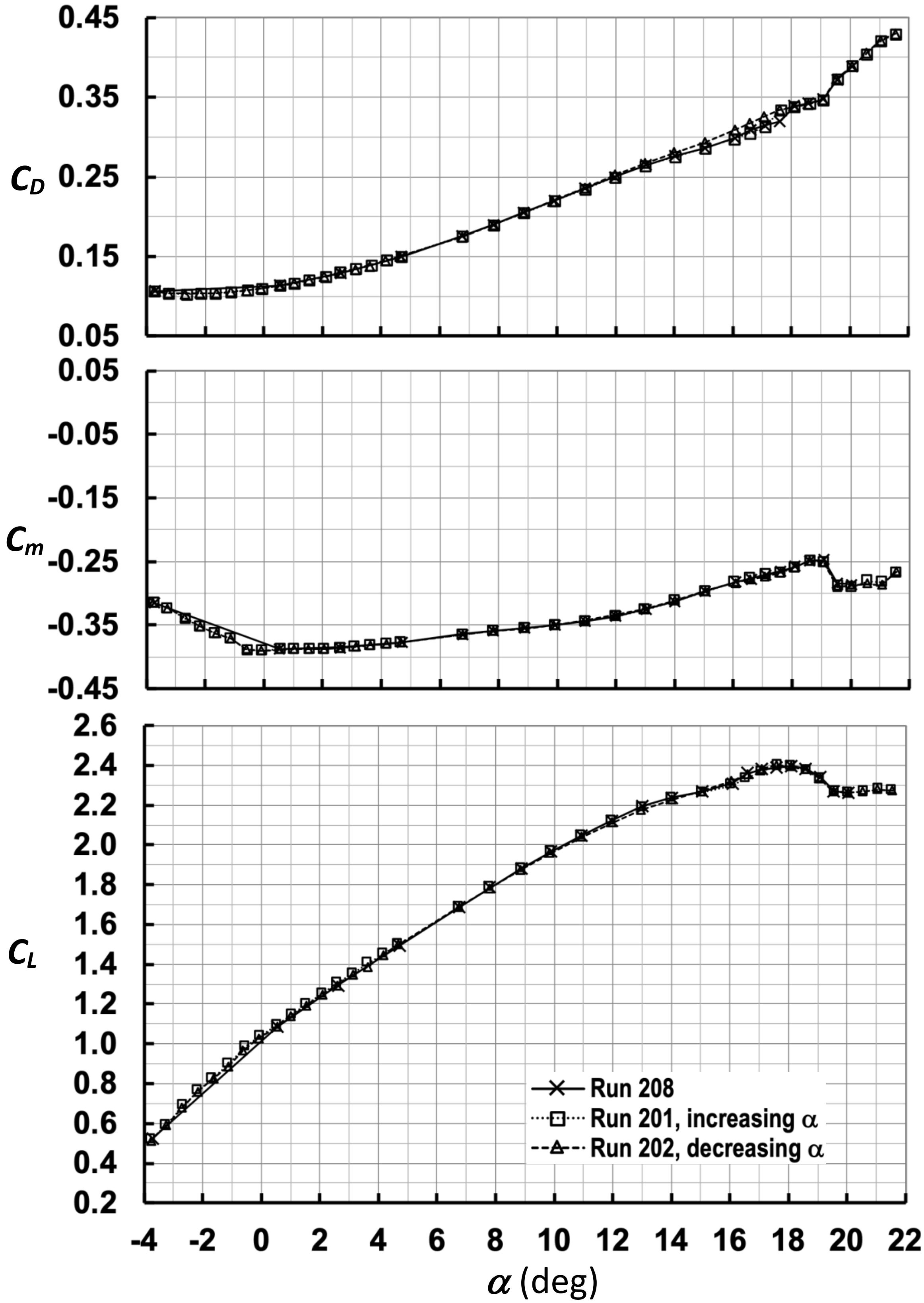

Figure 9. C_D, C_m and C_L vs. α plots for increasing/decreasing α showing hysteresis (M_∞ = 0.2, with TWICS).

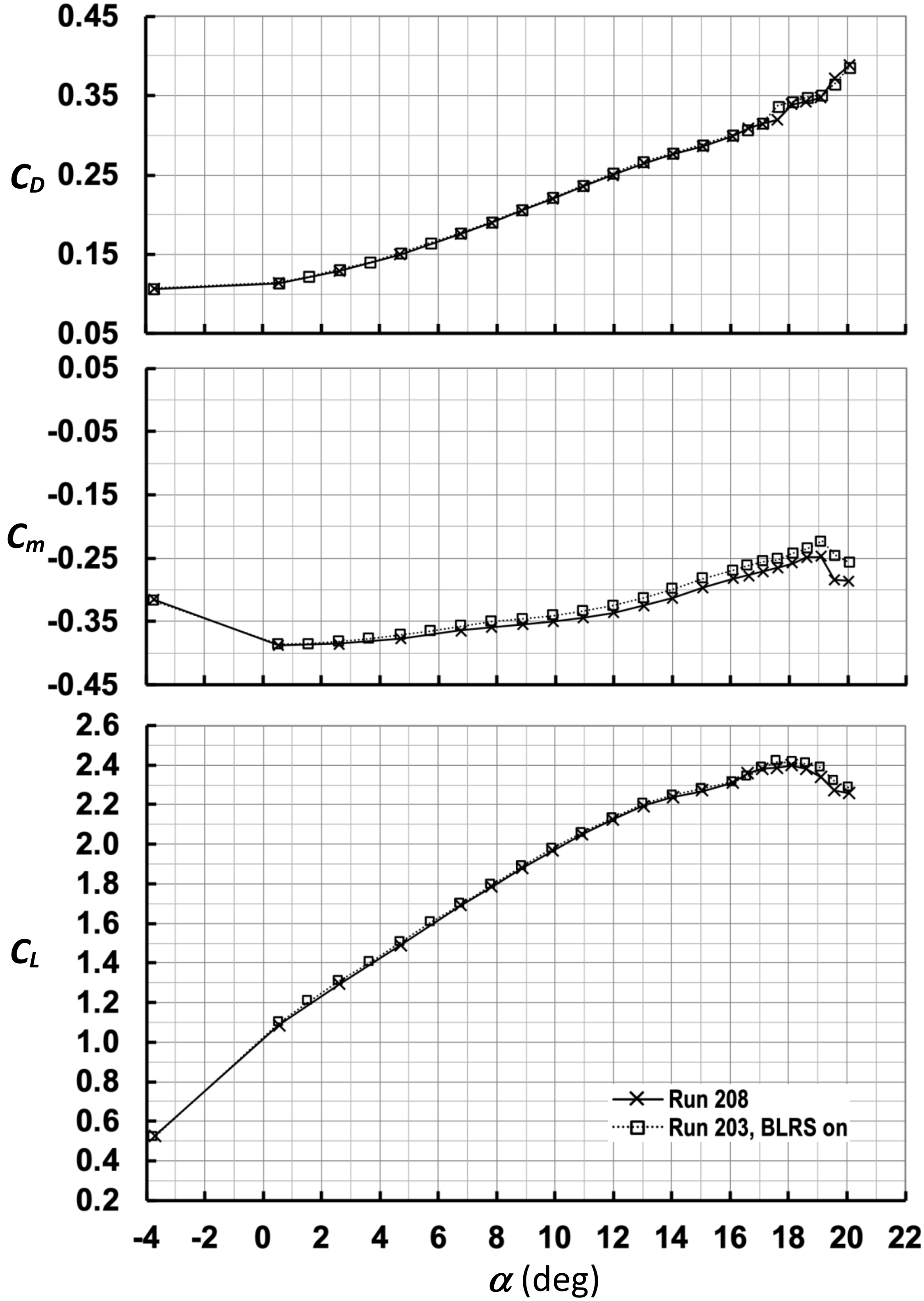

Figure 10. Effects of floor BLRS on C_D, C_m and C_L vs. α plots ($M_\infty = 0.2$, with TWICS).

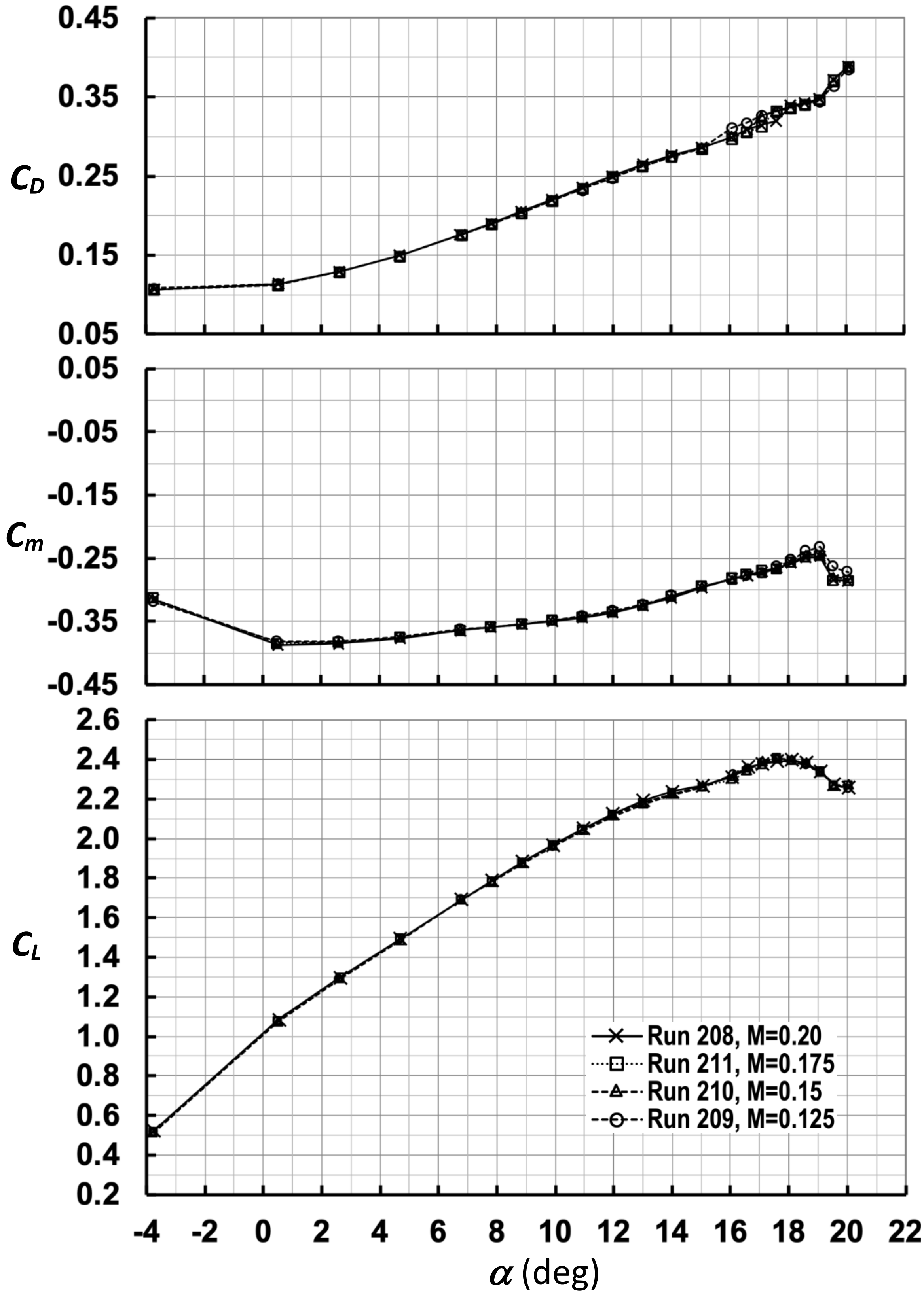

Figure 11. Effects of lower $M_¥$ on C_D, C_m and C_L vs. a plots (with TWICS).

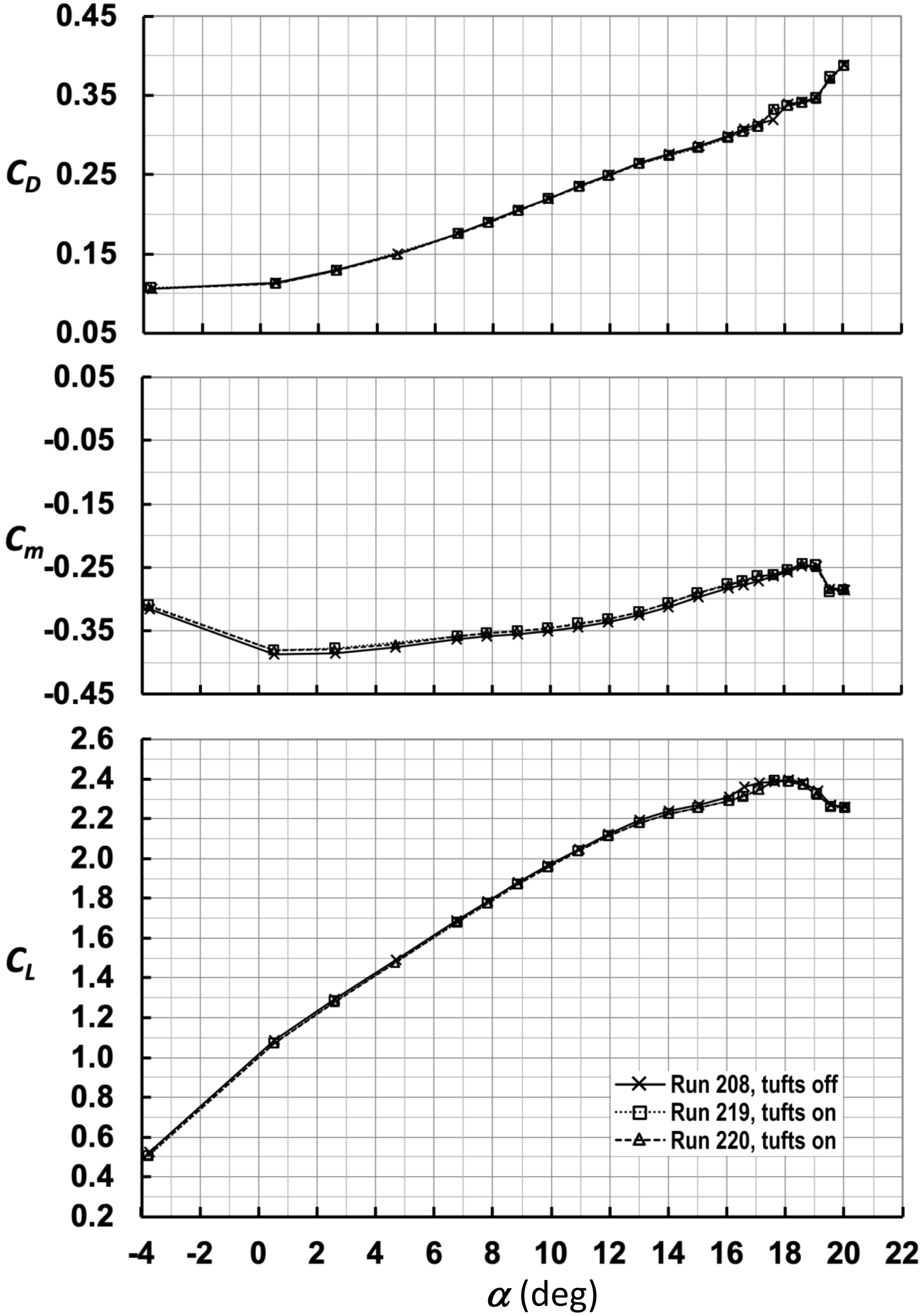

Figure 12. Effects of tufts on C_D, C_m and C_L vs. α plots ($M_\infty = 0.2$, with TWICS).

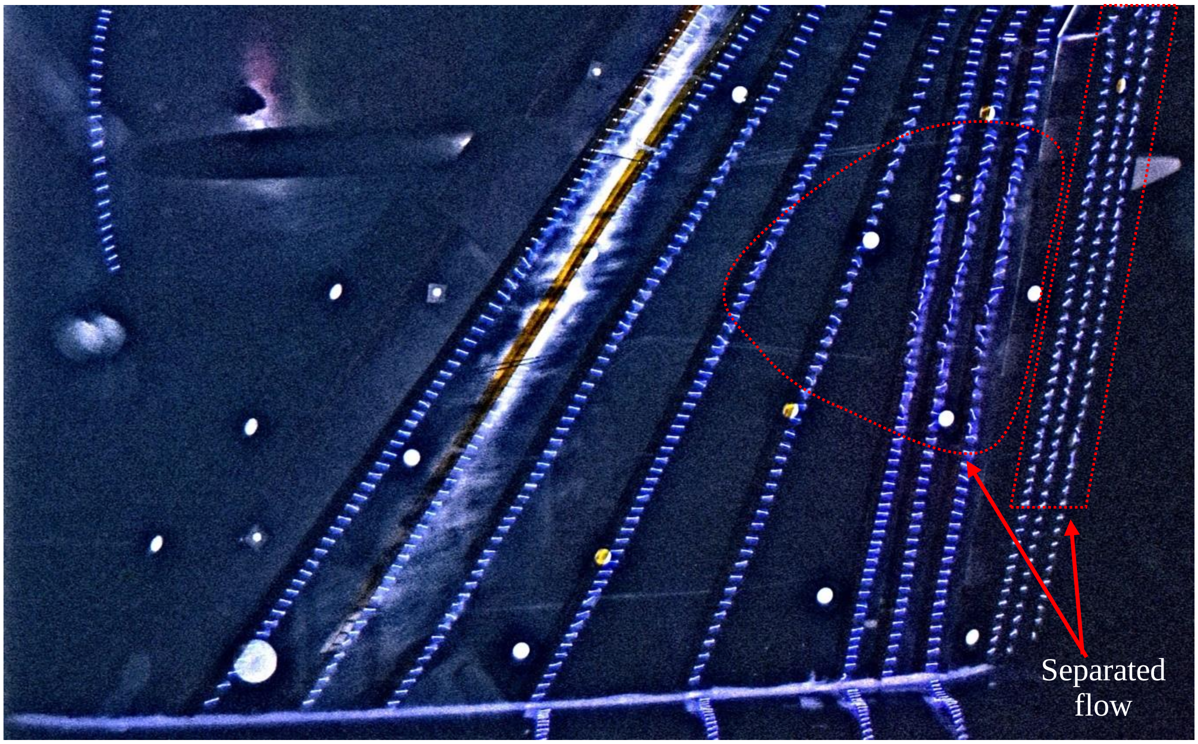

(a) Baseline case

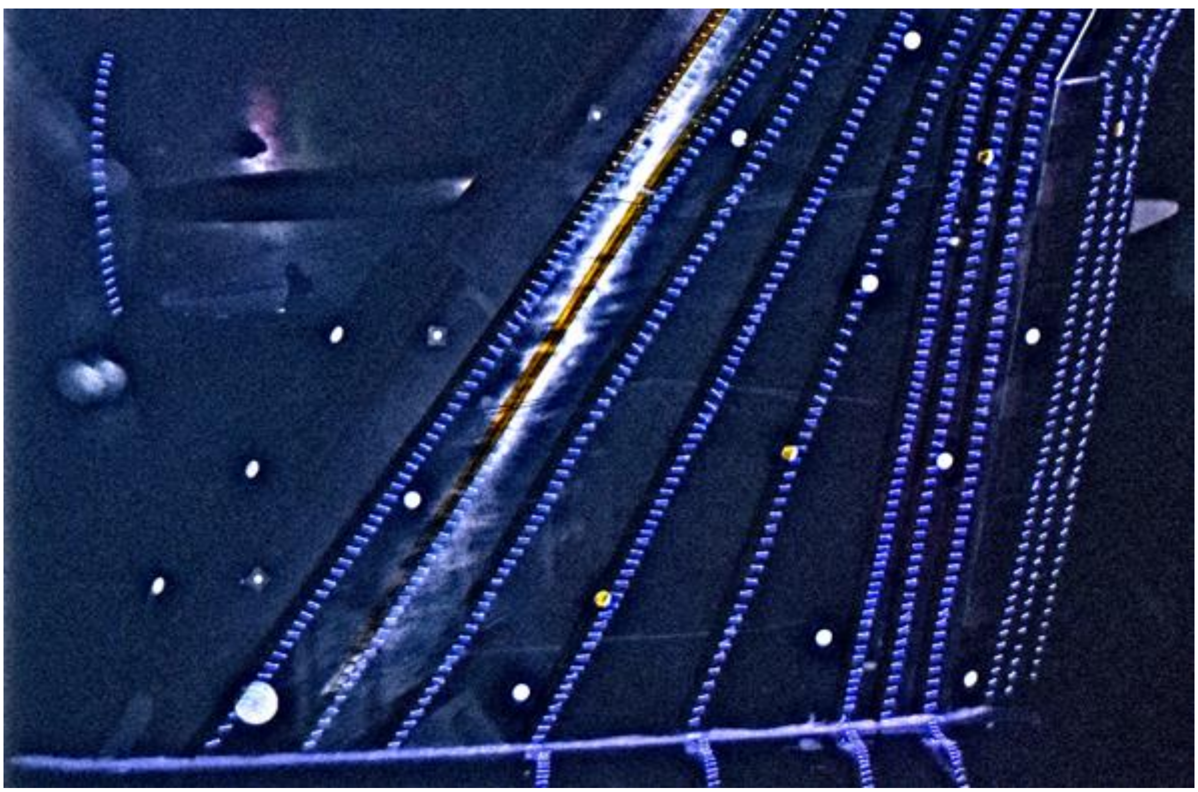

(b) Nacelle chine case

Figure 13. Surface tuft flow visualization at α = 16°.

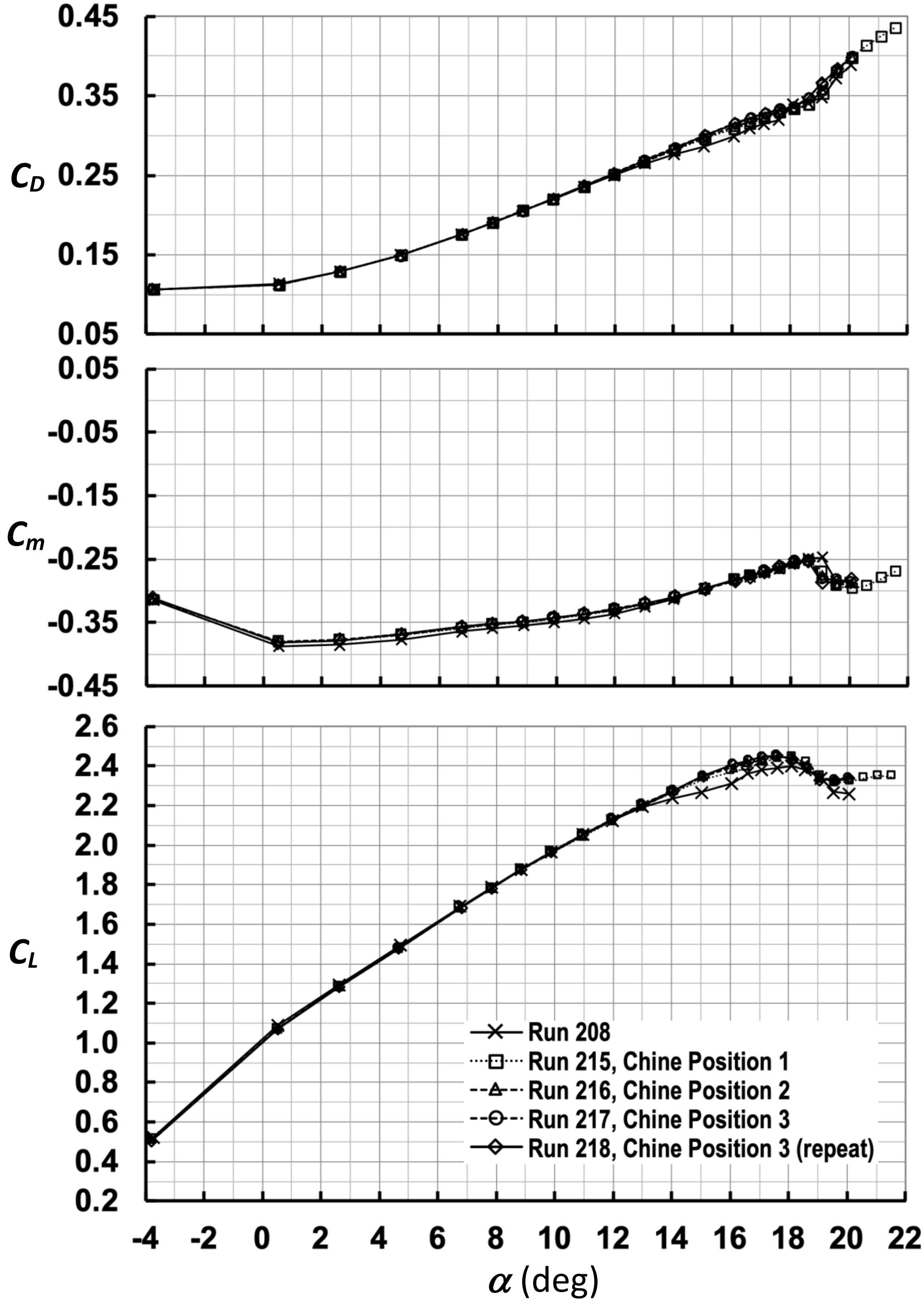

Figure 14. Effects of nacelle chine on C_D, C_m and C_L vs. α plots ($M_\infty = 0.2$, with TWICS).

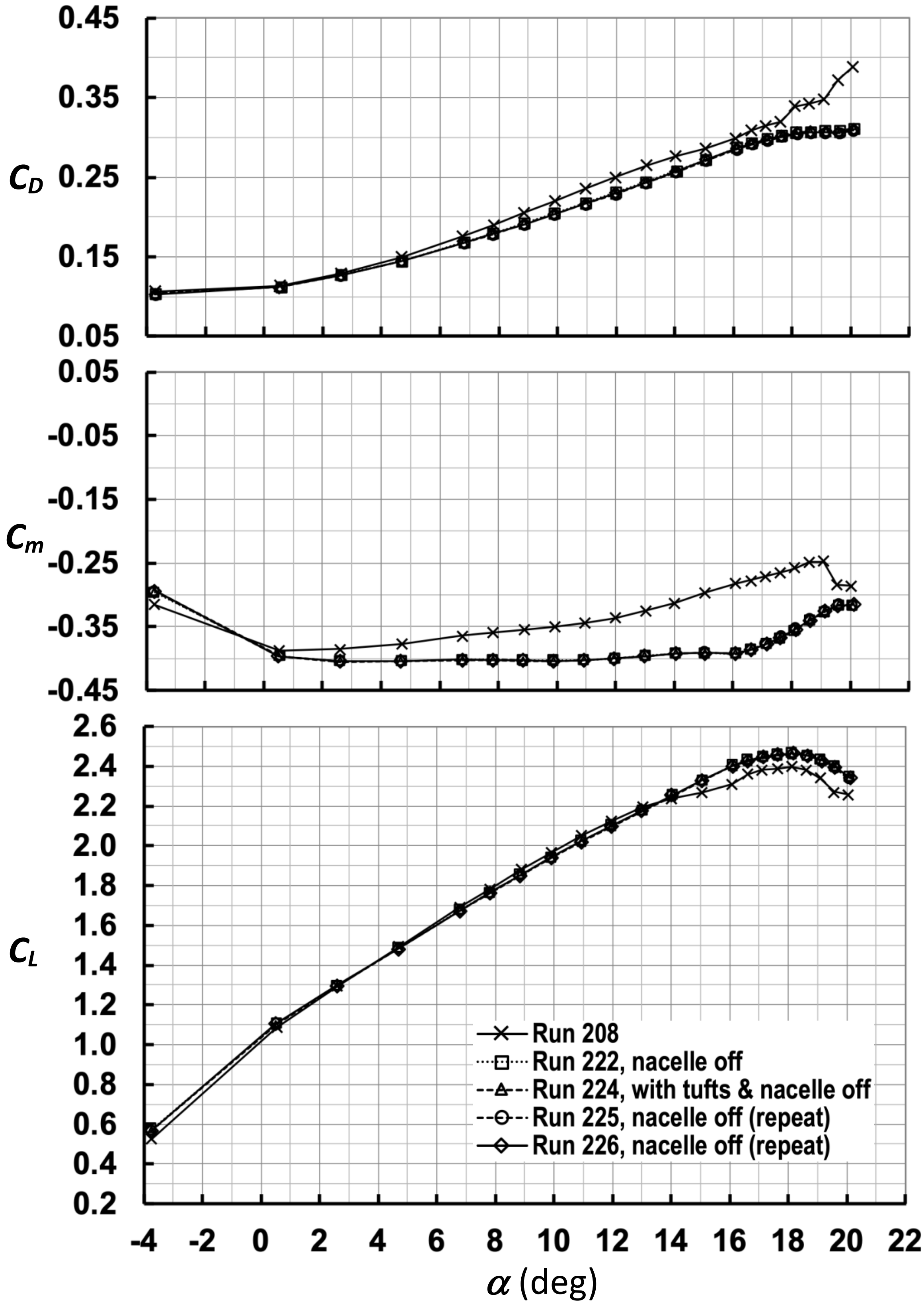

Figure 15. Effects of nacelle on C_D, C_m and C_L vs. α plots ($M_\infty = 0.2$, with TWICS).

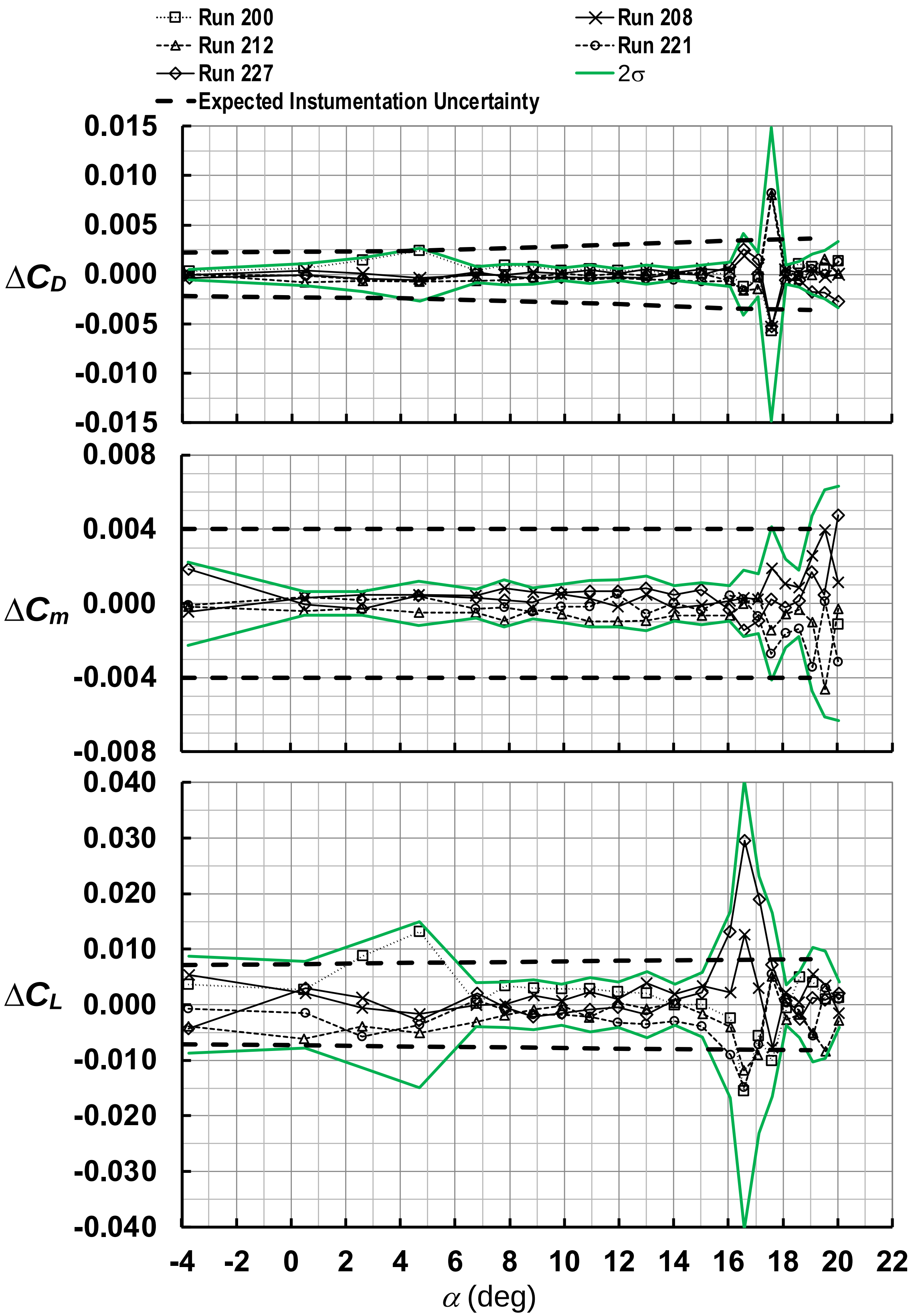

Figure 16. ΔC_D, ΔC_m and ΔC_L vs. α plots for CRM-HL baseline repeat runs ($M_\infty = 0.2$, with TWICS).

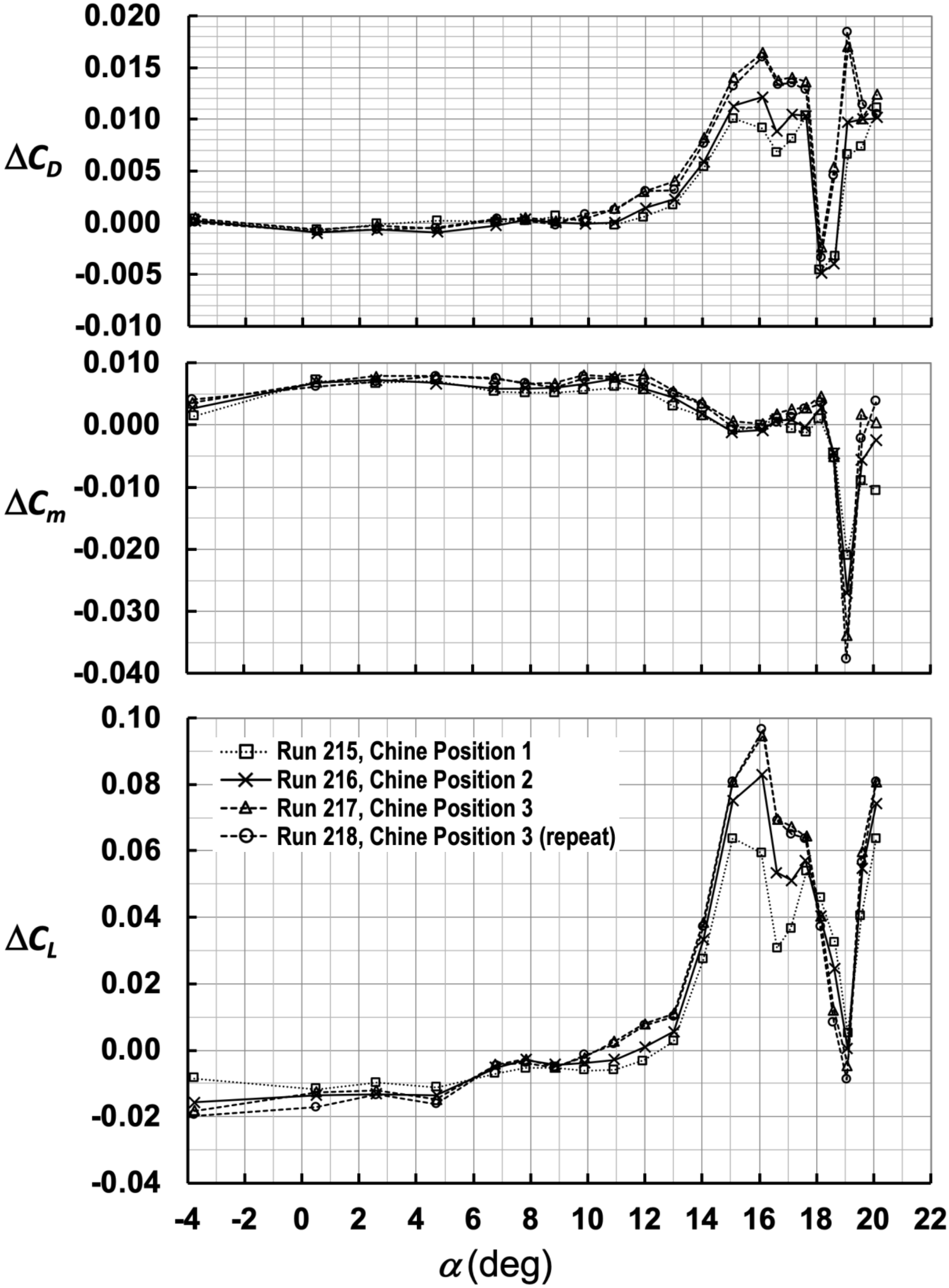

Figure 17. ΔC_D, ΔC_m and ΔC_L vs. α plots for CRM-HL with nacelle chine ($M_\infty = 0.2$, with TWICS).

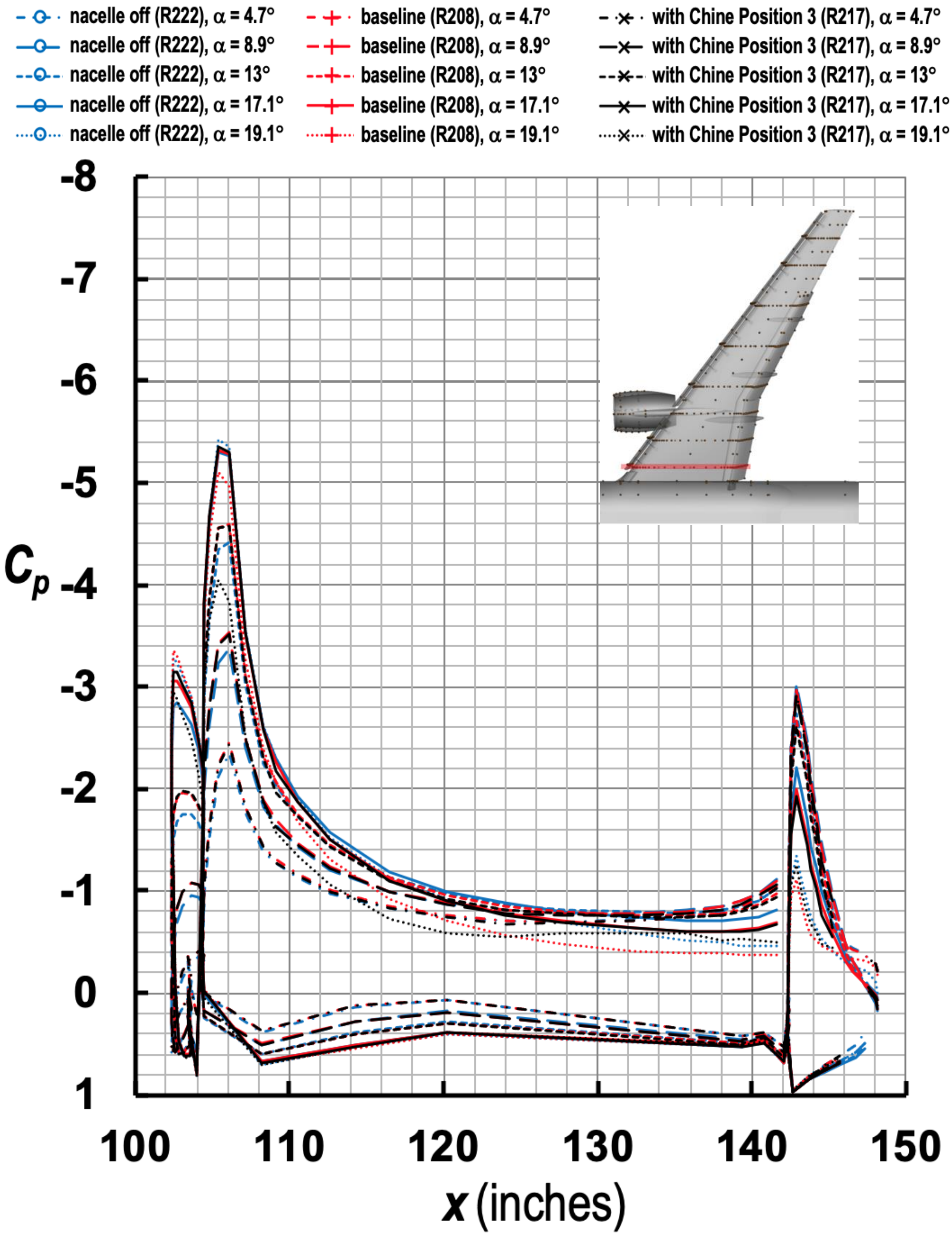

Figure 18. Streamwise C_p distributions at $\eta = 0.15$ for three variants of CRM-HL at five angles of attack ($M_\infty = 0.2$, with TWICS).

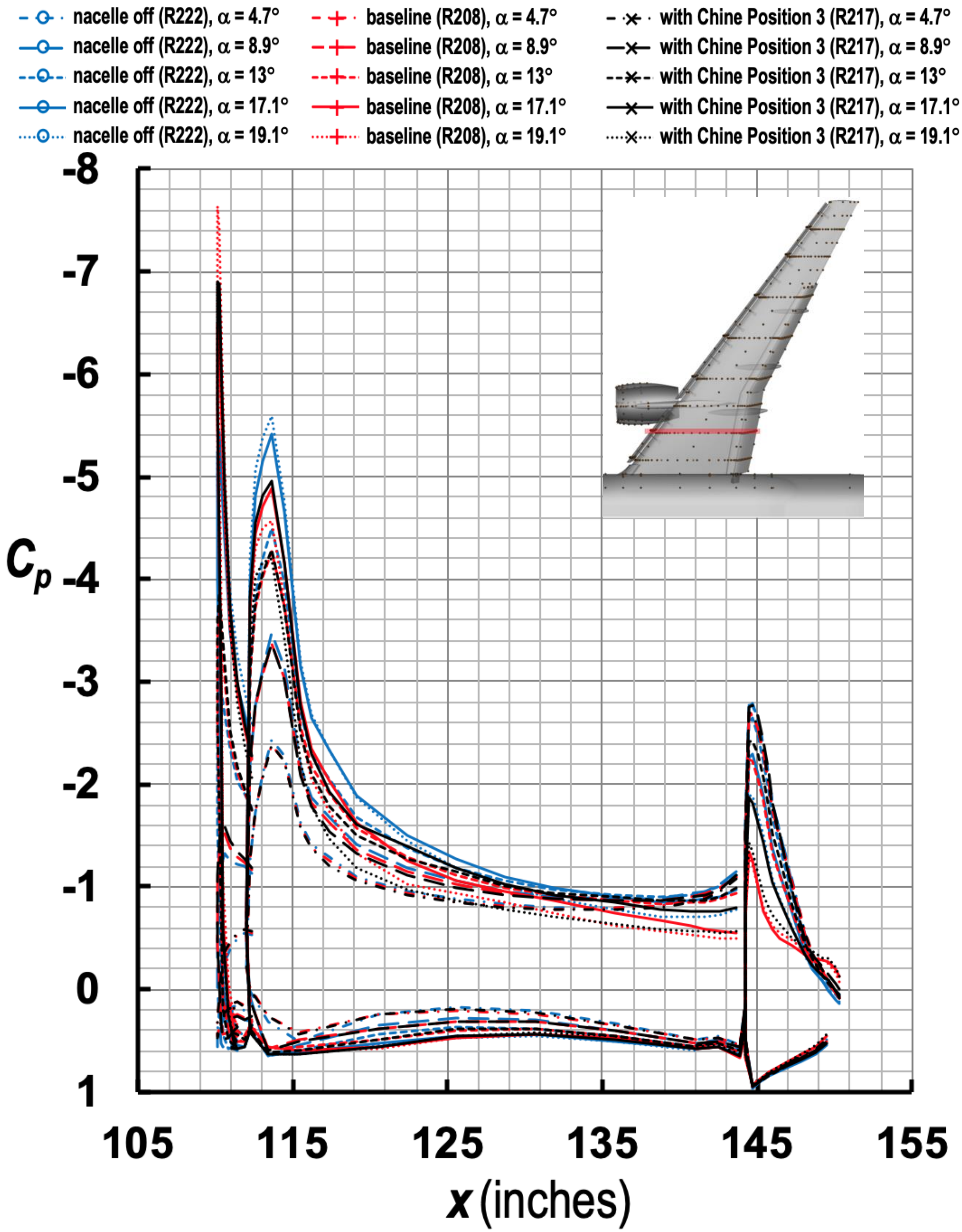

Figure 19. Streamwise C_p distributions at $\eta = 0.24$ for three variants of CRM-HL at five angles of attack ($M_\infty = 0.2$, with TWICS).

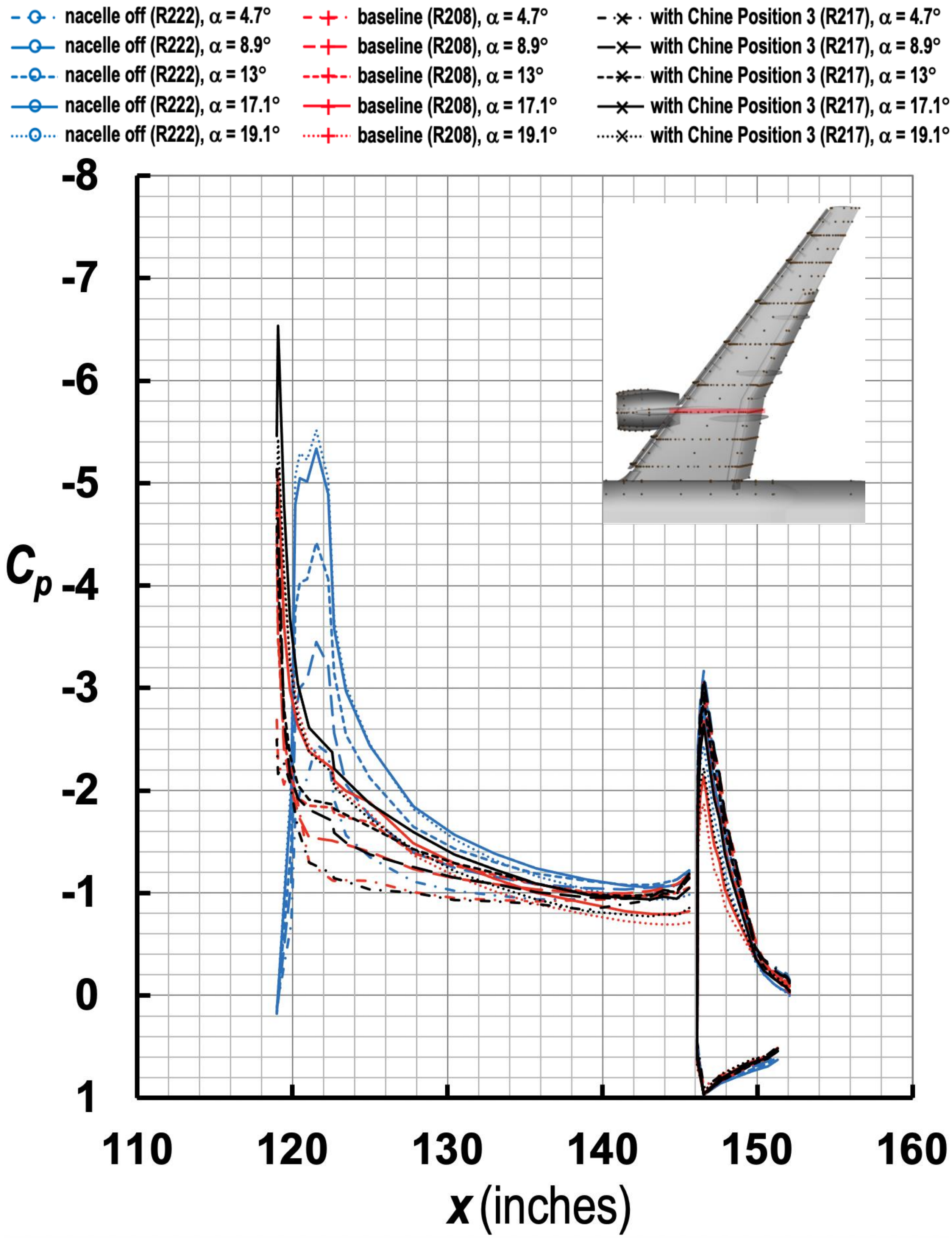

Figure 20. Streamwise C_p distributions at $\eta = 0.33$ for three variants of CRM-HL at five angles of attack ($M_\infty = 0.2$, with TWICS).

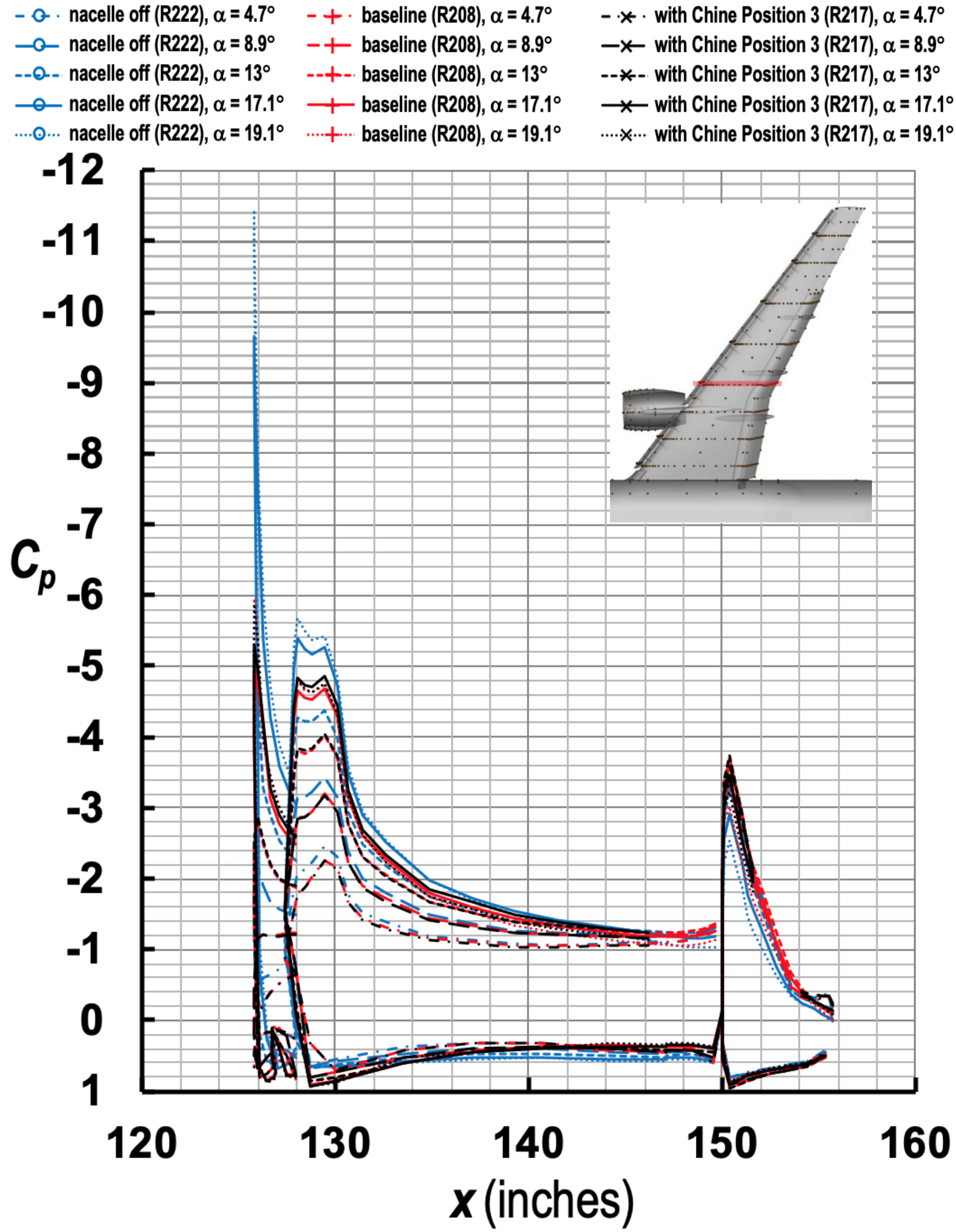

Figure 21. Streamwise C_p distributions at $\eta = 0.42$ for three variants of CRM-HL at five angles of attack ($M_\infty = 0.2$, with TWICS).

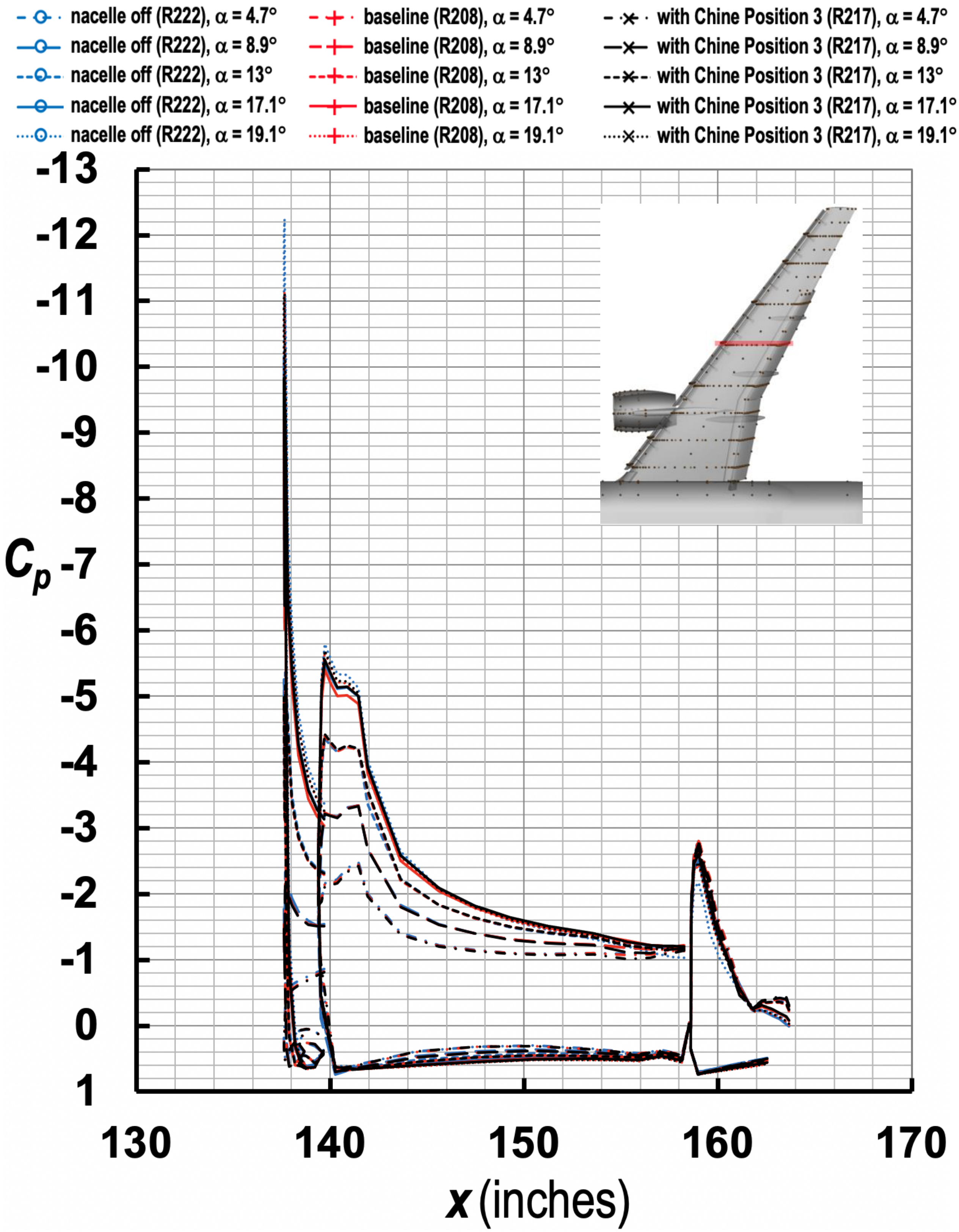

Figure 22. Streamwise C_p distributions at η = 0.55 for three variants of CRM-HL at five angles of attack (M_∞ = 0.2, with TWICS).

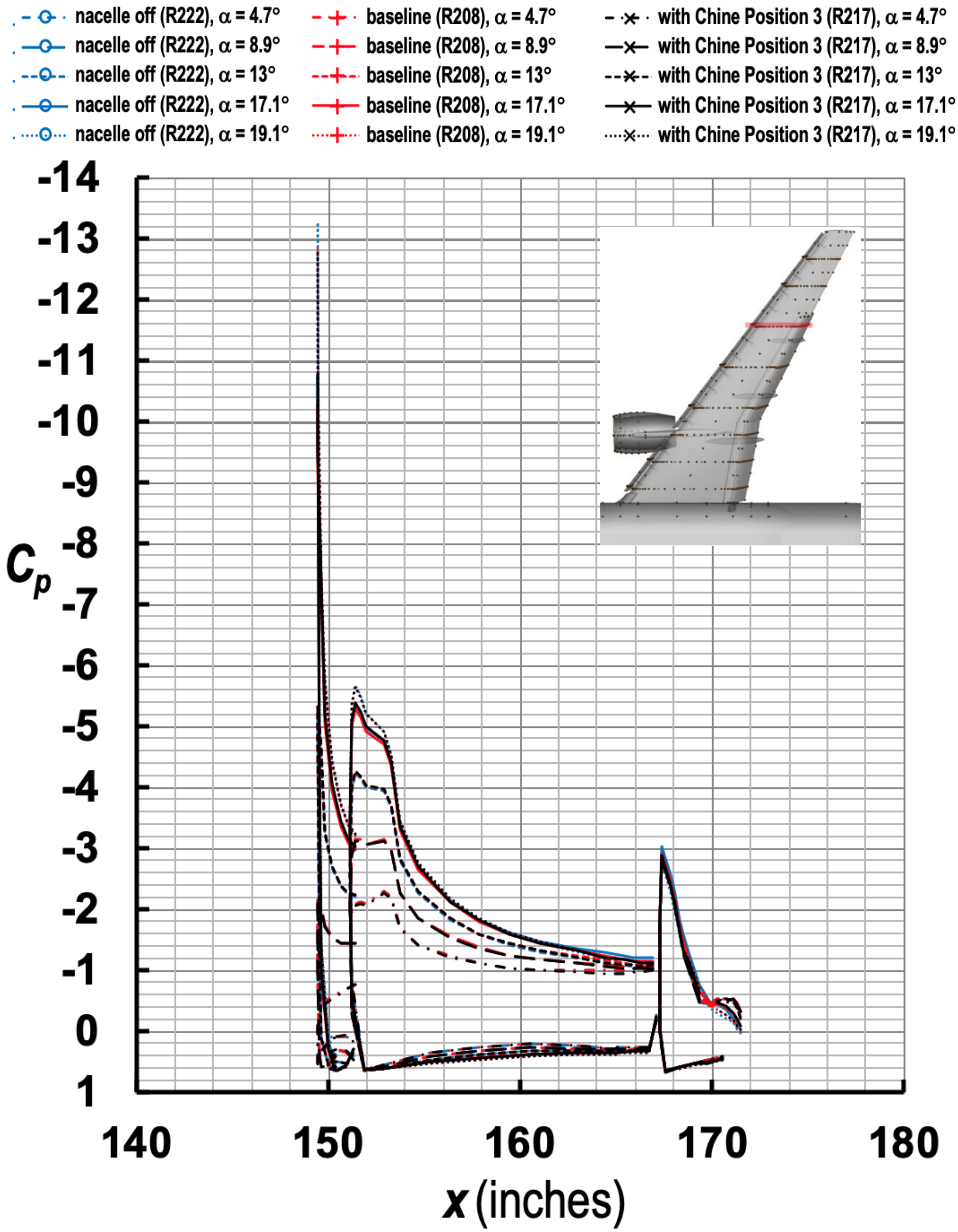

Figure 23. Streamwise C_p distributions at $\eta = 0.69$ for three variants of CRM-HL at five angles of attack ($M_\infty = 0.2$, with TWICS).

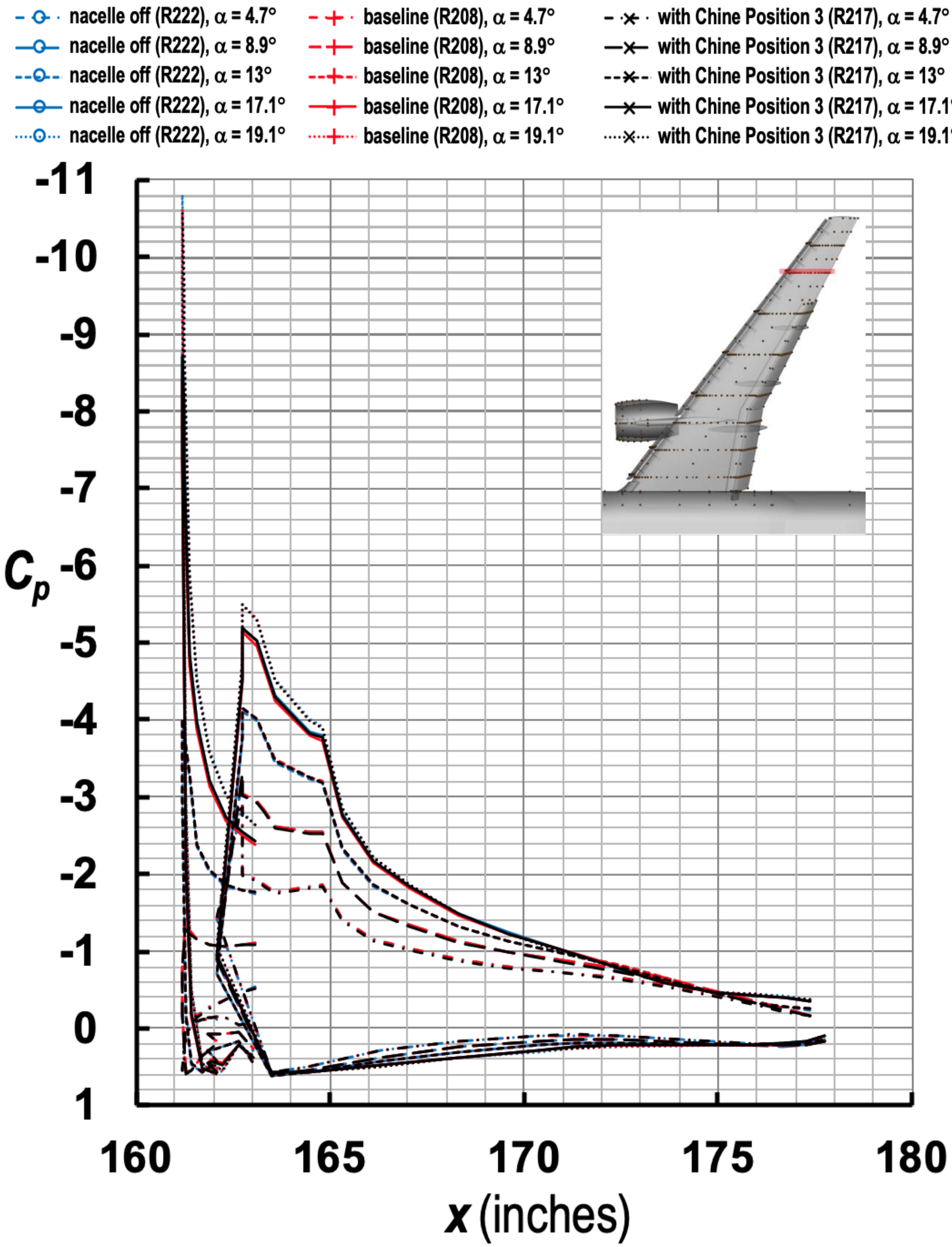

Figure 24. Streamwise C_p distributions at η = 0.82 for three variants of CRM-HL at five angles of attack (M_∞ = 0.2, with TWICS).

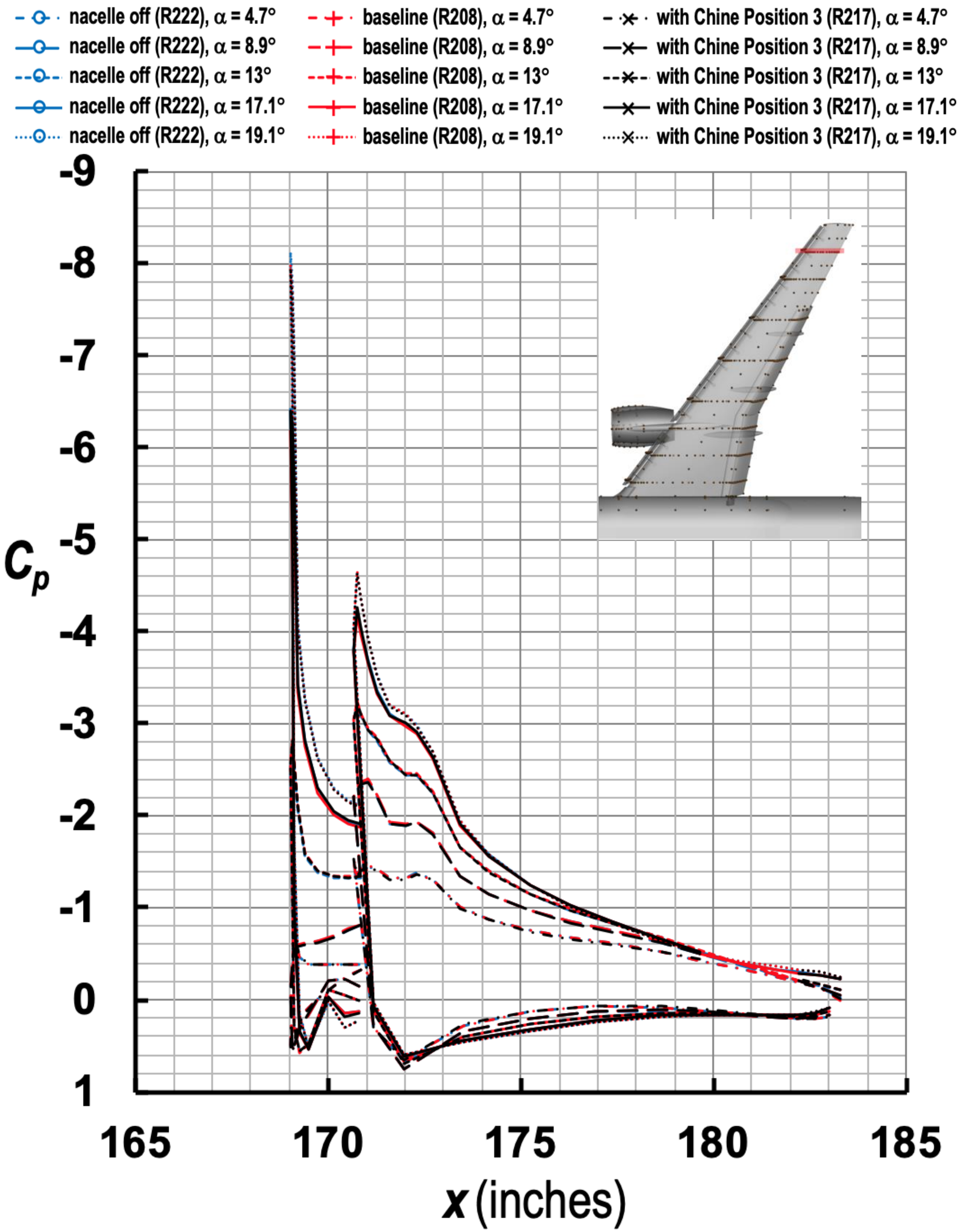

Figure 25. Streamwise C_p distributions at $\eta = 0.91$ for three variants of CRM-HL at five angles of attack ($M_\infty = 0.2$, with TWICS).

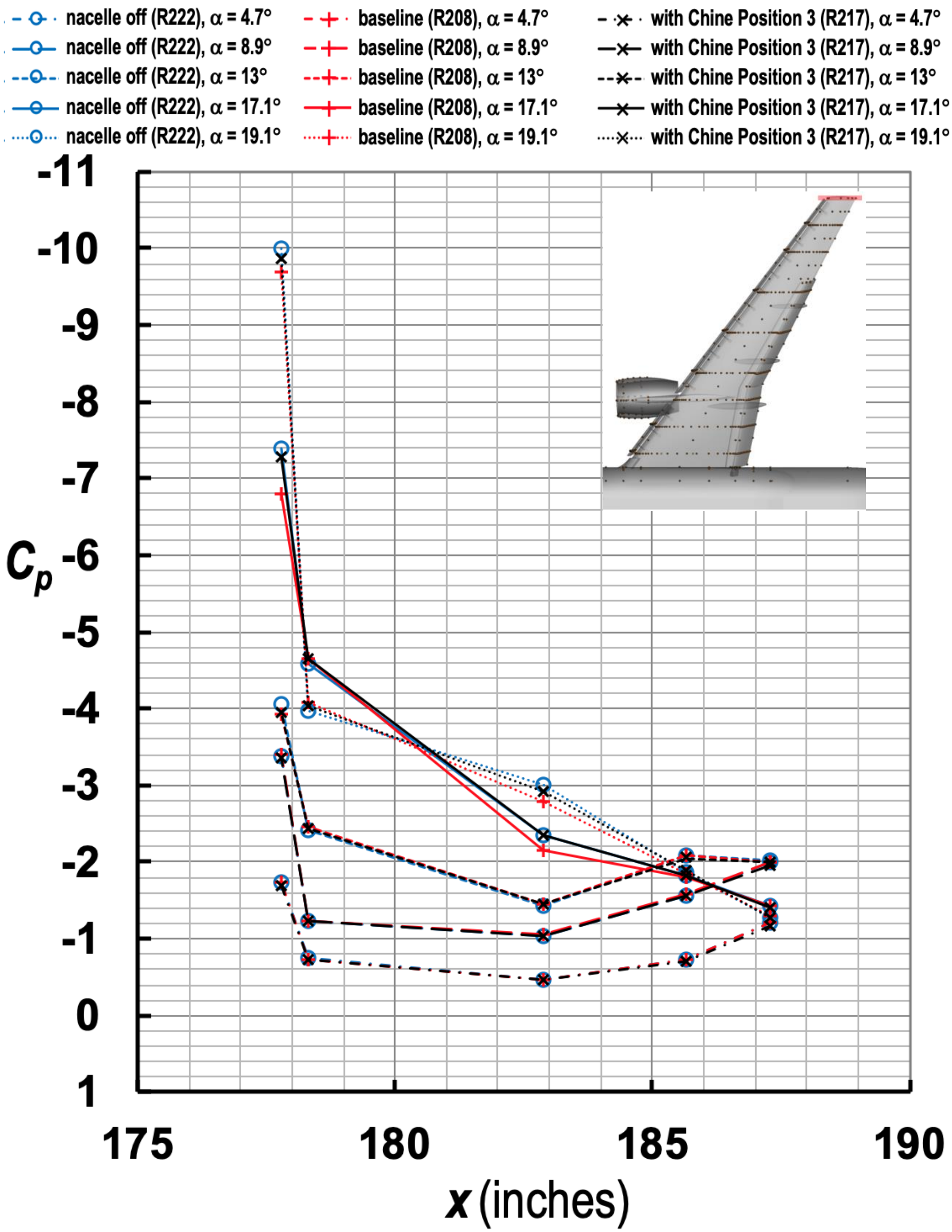

Figure 26. Streamwise C_p distributions at $\eta = 1.0$ (wingtip) for three variants of CRM-HL at five angles of attack ($M_\infty = 0.2$, with TWICS).

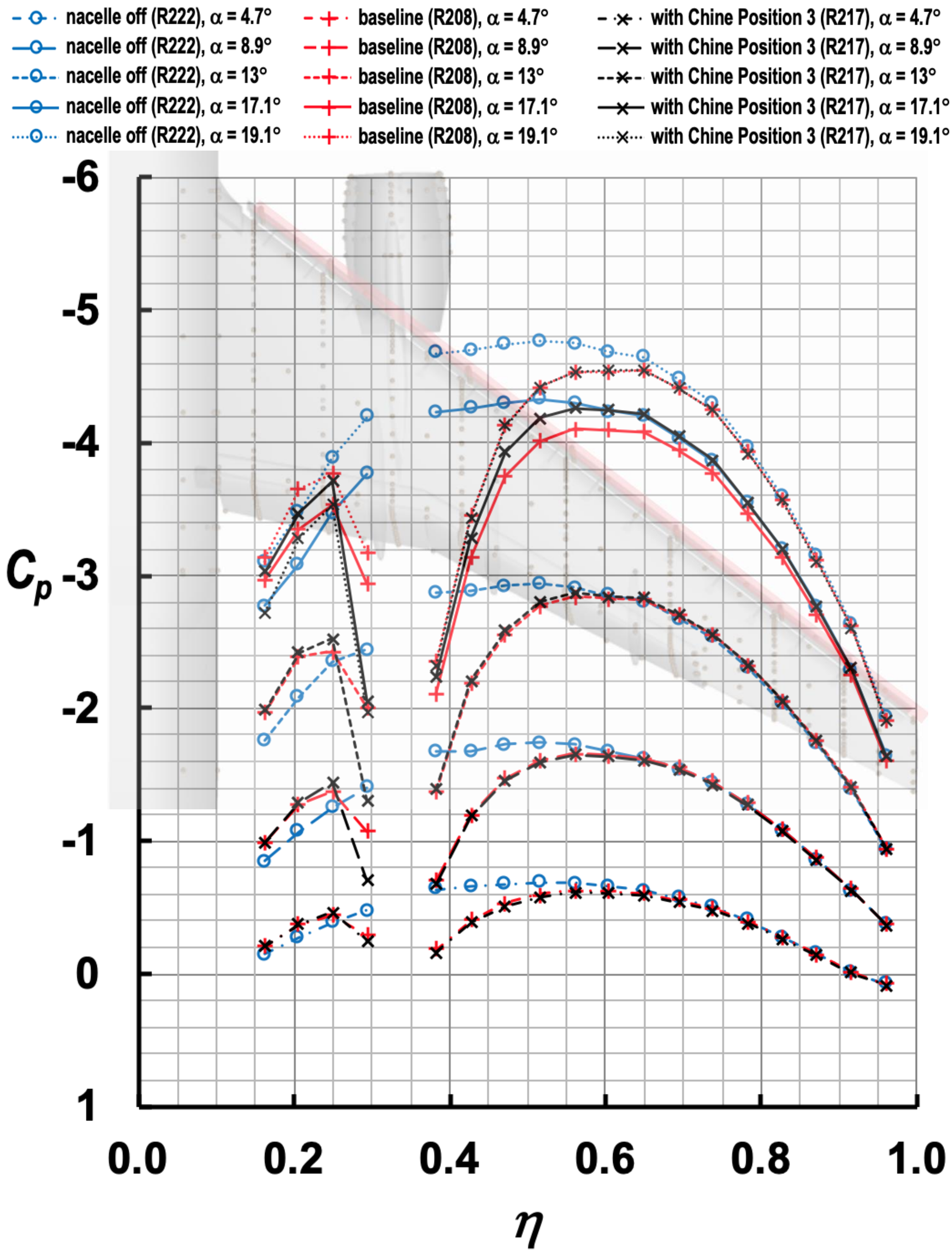

Figure 27. Spanwise C_p distributions along the midslat upper surface for three variants of CRM-HL at five angles of attack (M_∞ = 0.2, with TWICS).

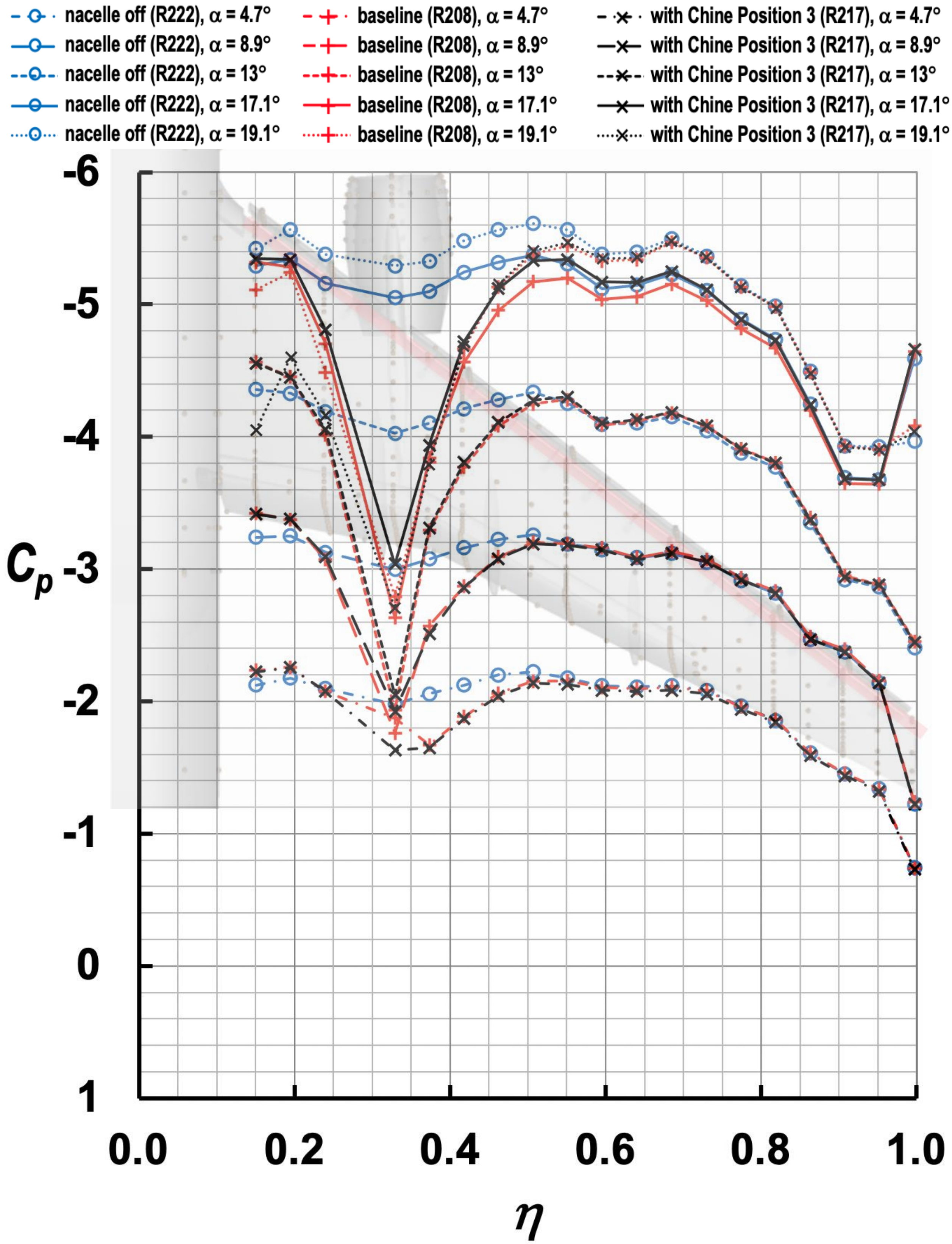

Figure 28. Spanwise C_p distributions along the wing leading edge for three variants of CRM-HL at five angles of attack (M_∞ = 0.2, with TWICS).

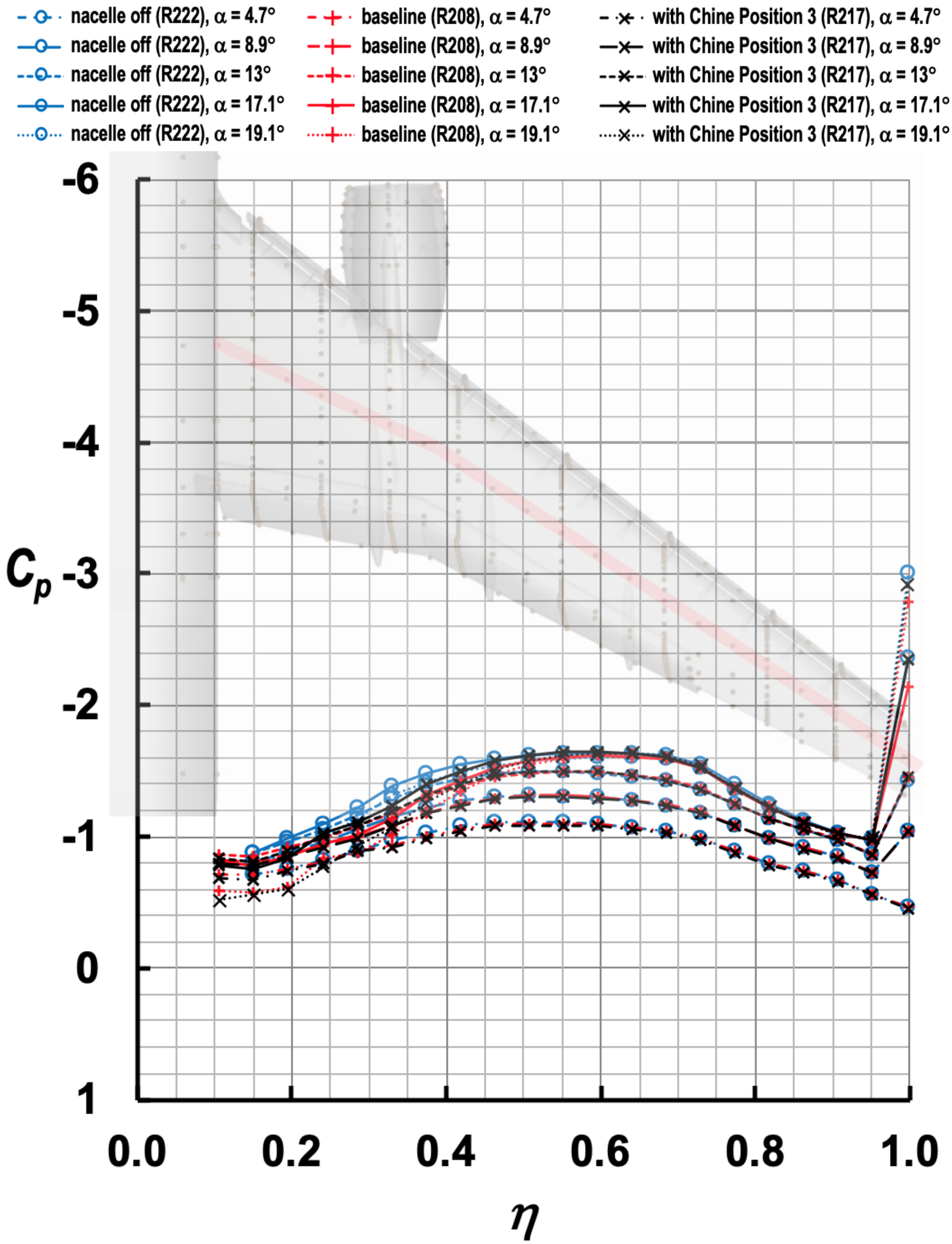

Figure 29. Spanwise C_p distributions along the midwing upper surface for three variants of CRM-HL at five angles of attack ($M_\infty = 0.2$, with TWICS).

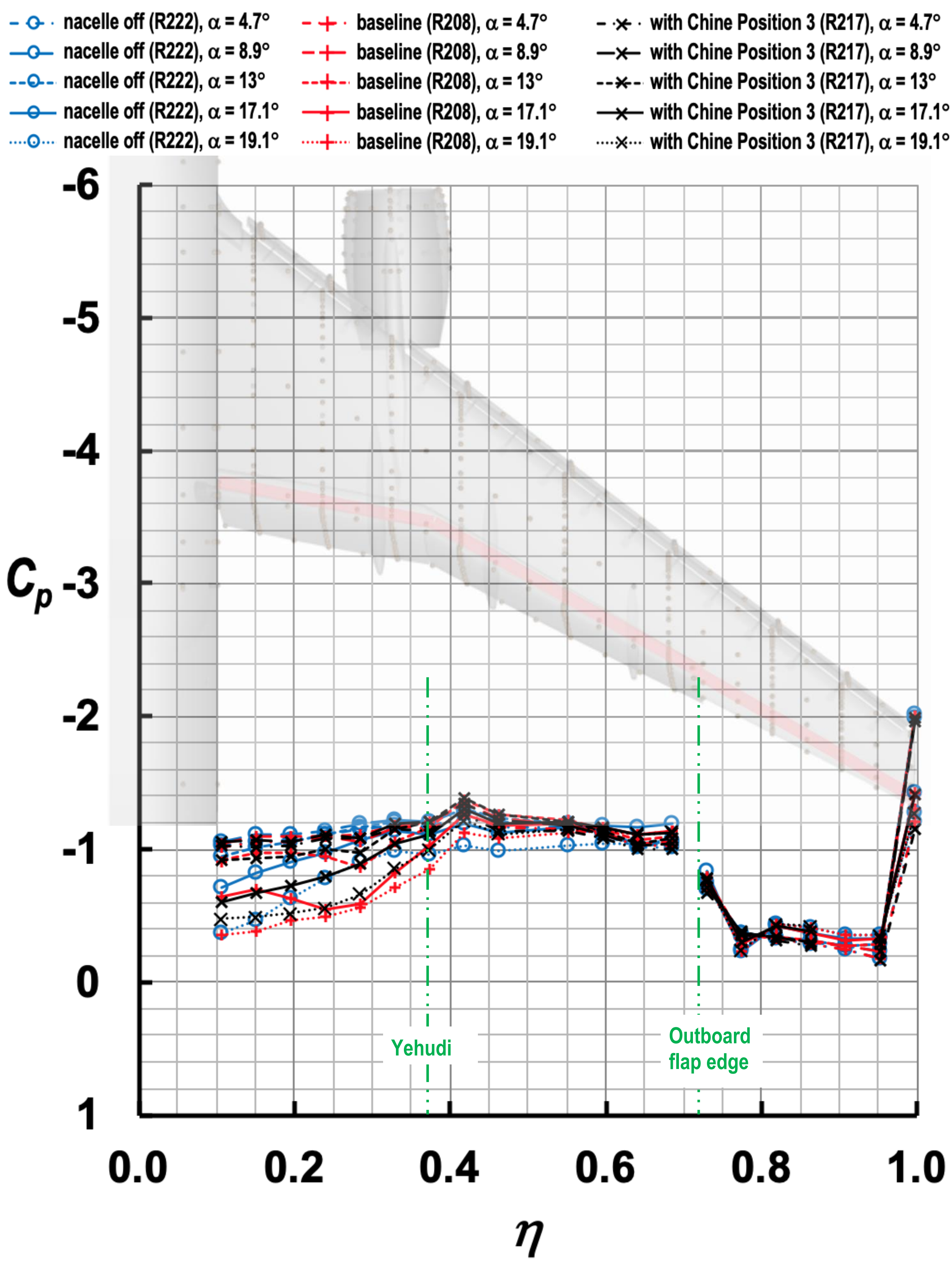

Figure 30. Spanwise C_p distributions along the wing spoiler trailing edge for three variants of CRM-HL at five angles of attack ($M_\infty = 0.2$, with TWICS).

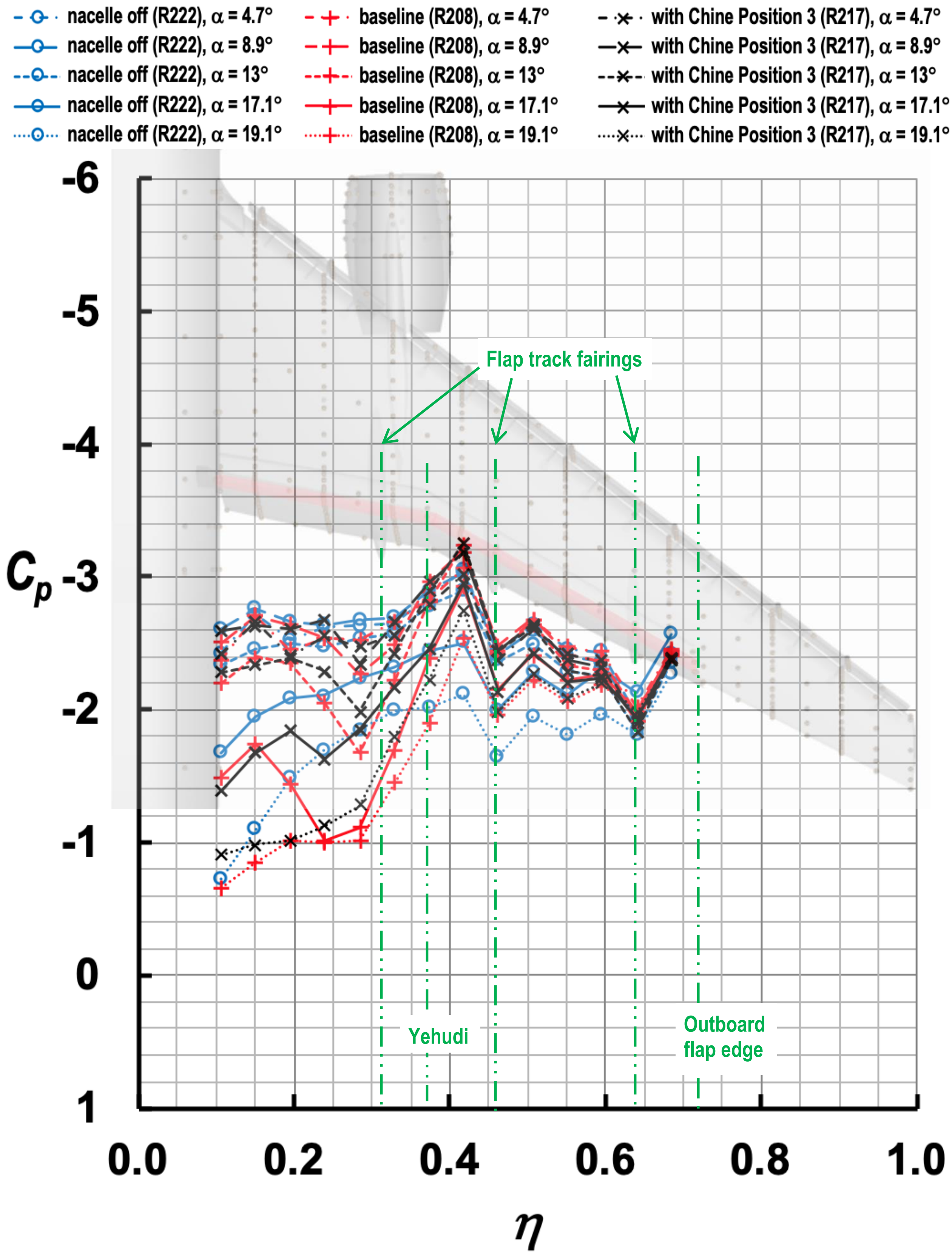

Figure 31. Spanwise C_p distributions along the flap leading edge for three variants of CRM-HL at five angles of attack ($M_\infty = 0.2$, with TWICS).

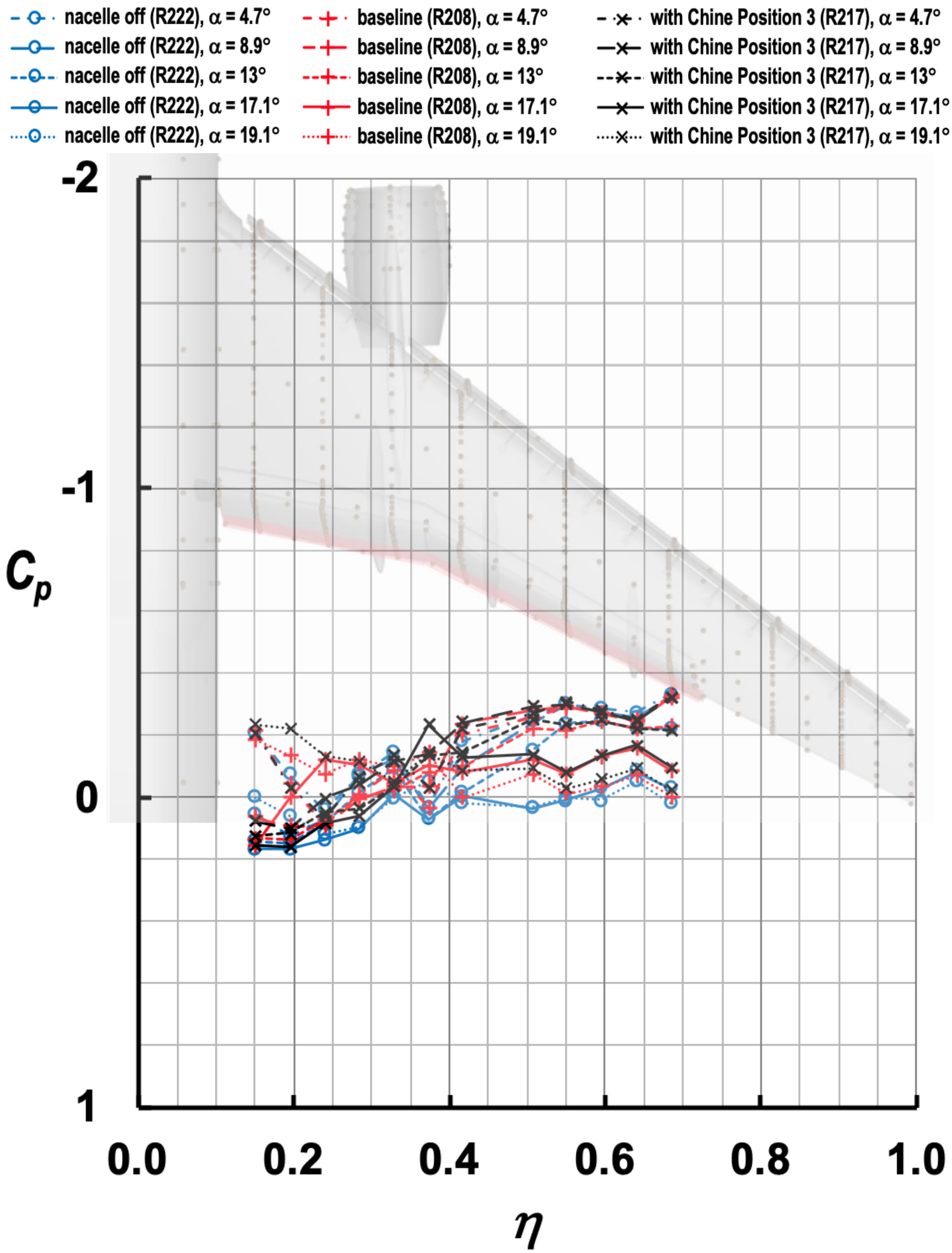

Figure 32. Spanwise C_p distributions along the flap trailing edge for three variants of CRM-HL at five angles of attack ($M_\infty = 0.2$, with TWICS).

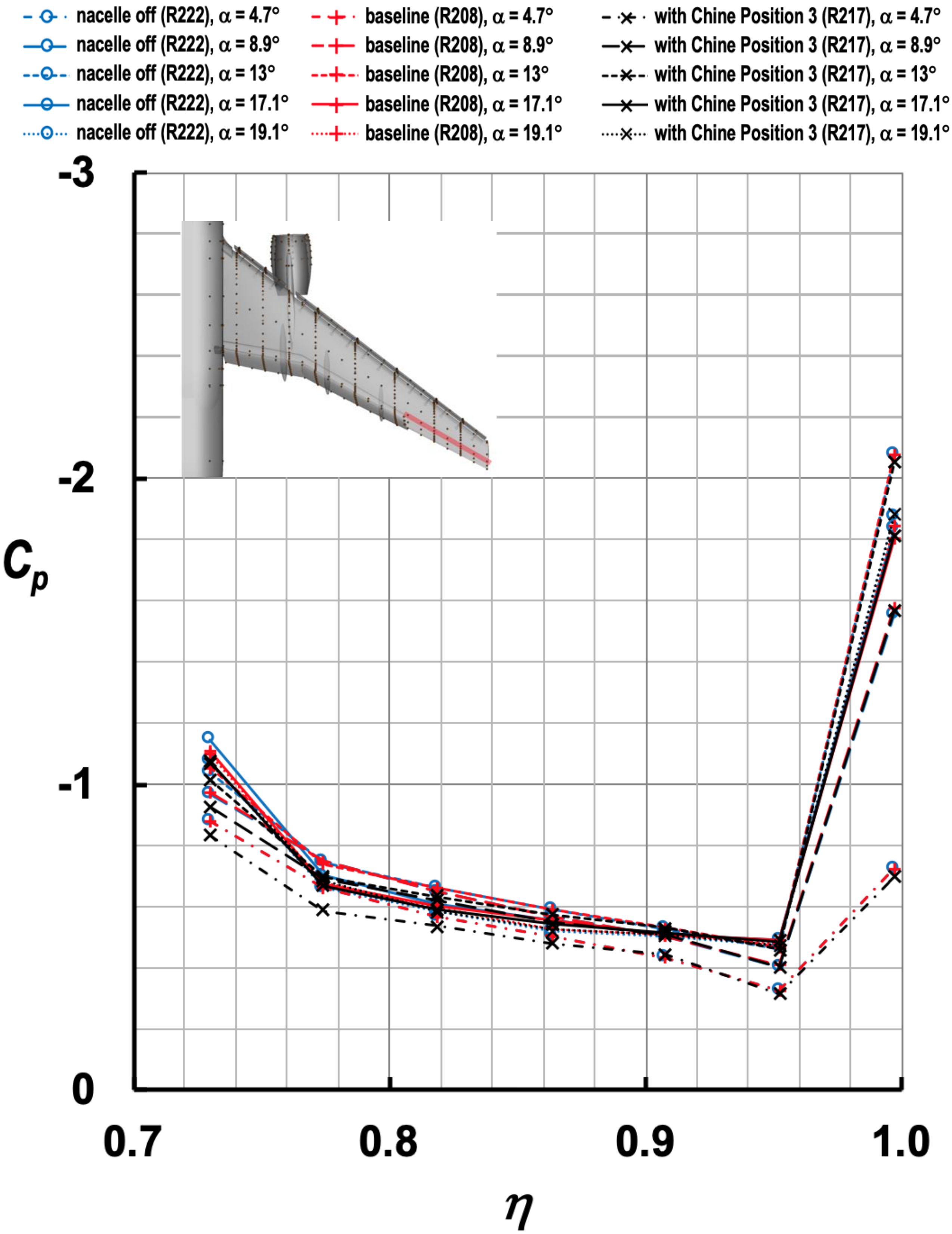

Figure 33. Spanwise C_p distributions along the ~72% wing chord upper surface beyond the outboard flap for three variants of CRM-HL at five angles of attack ($M_\infty = 0.2$, with TWICS).

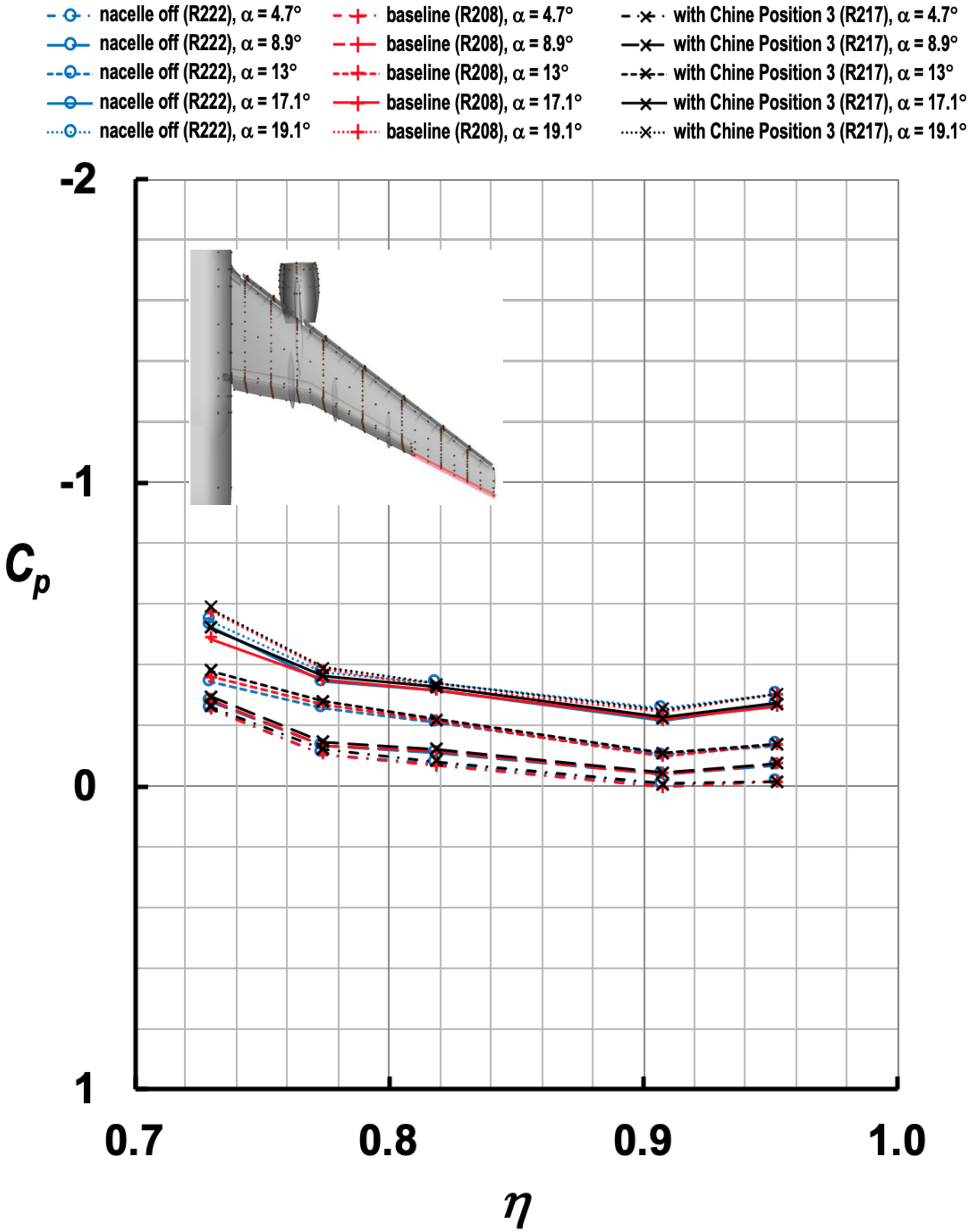

Figure 34. Spanwise C_p distributions along the wing trailing edge beyond the outboard flap for three variants of CRM-HL at five angles of attack ($M_\infty = 0.2$, with TWICS).

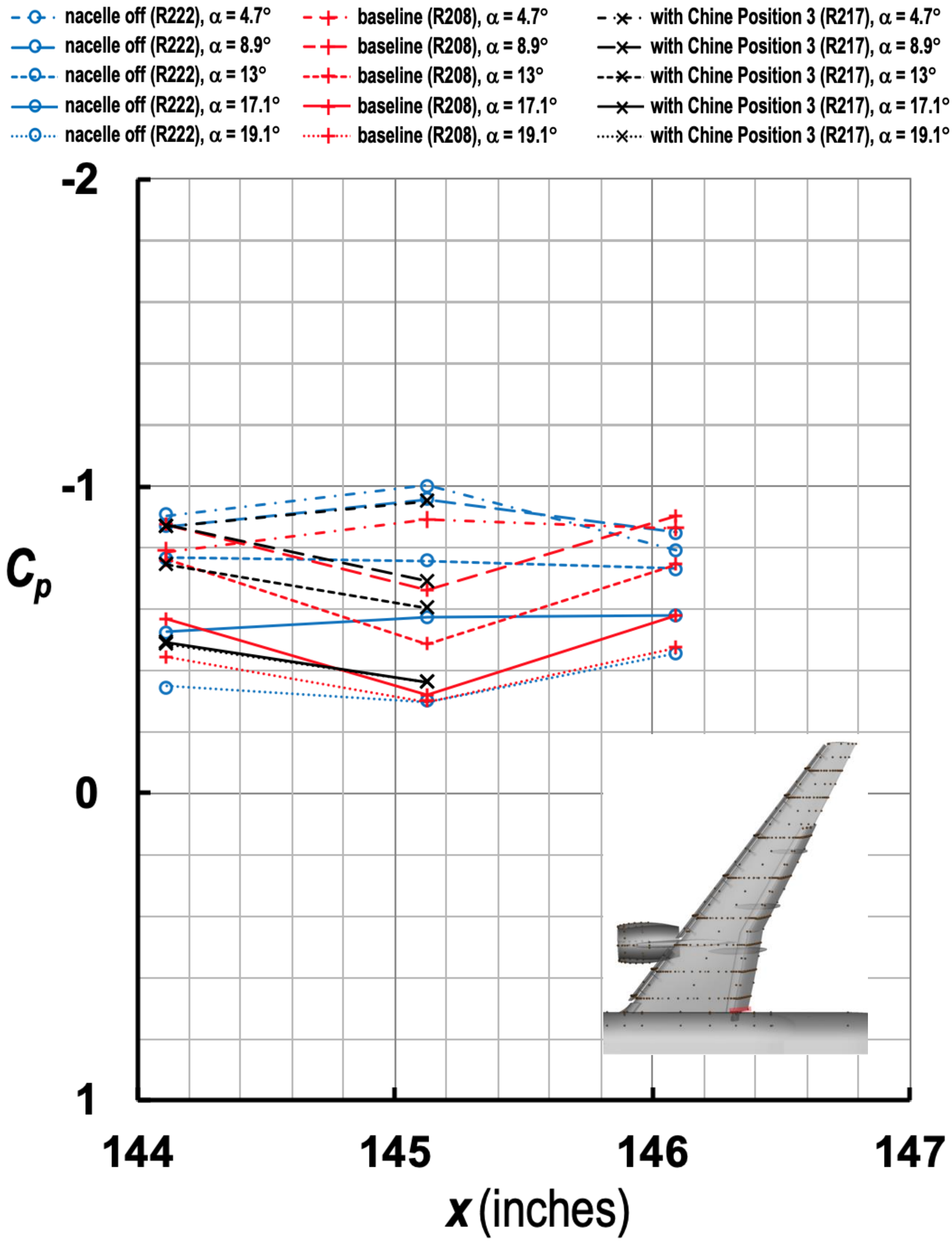

Figure 35. Streamwise C_p distributions along the upper surface of the inboard flap edge for three variants of CRM-HL at five angles of attack ($M_\infty = 0.2$, with TWICS).

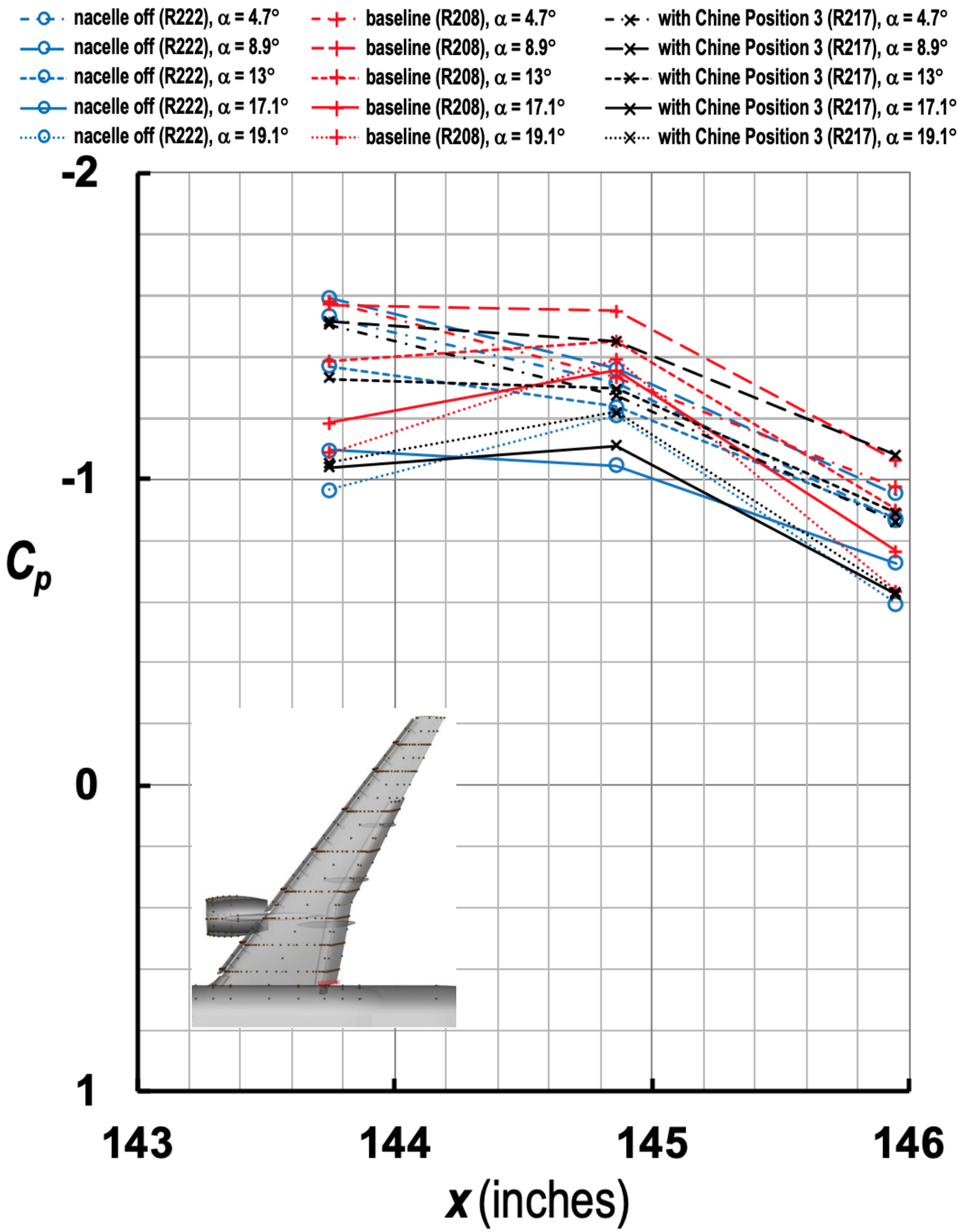

Figure 36. Streamwise C_p distributions along the side-edge surface of the inboard flap edge for three variants of CRM-HL at five angles of attack ($M_\infty = 0.2$, with TWICS).

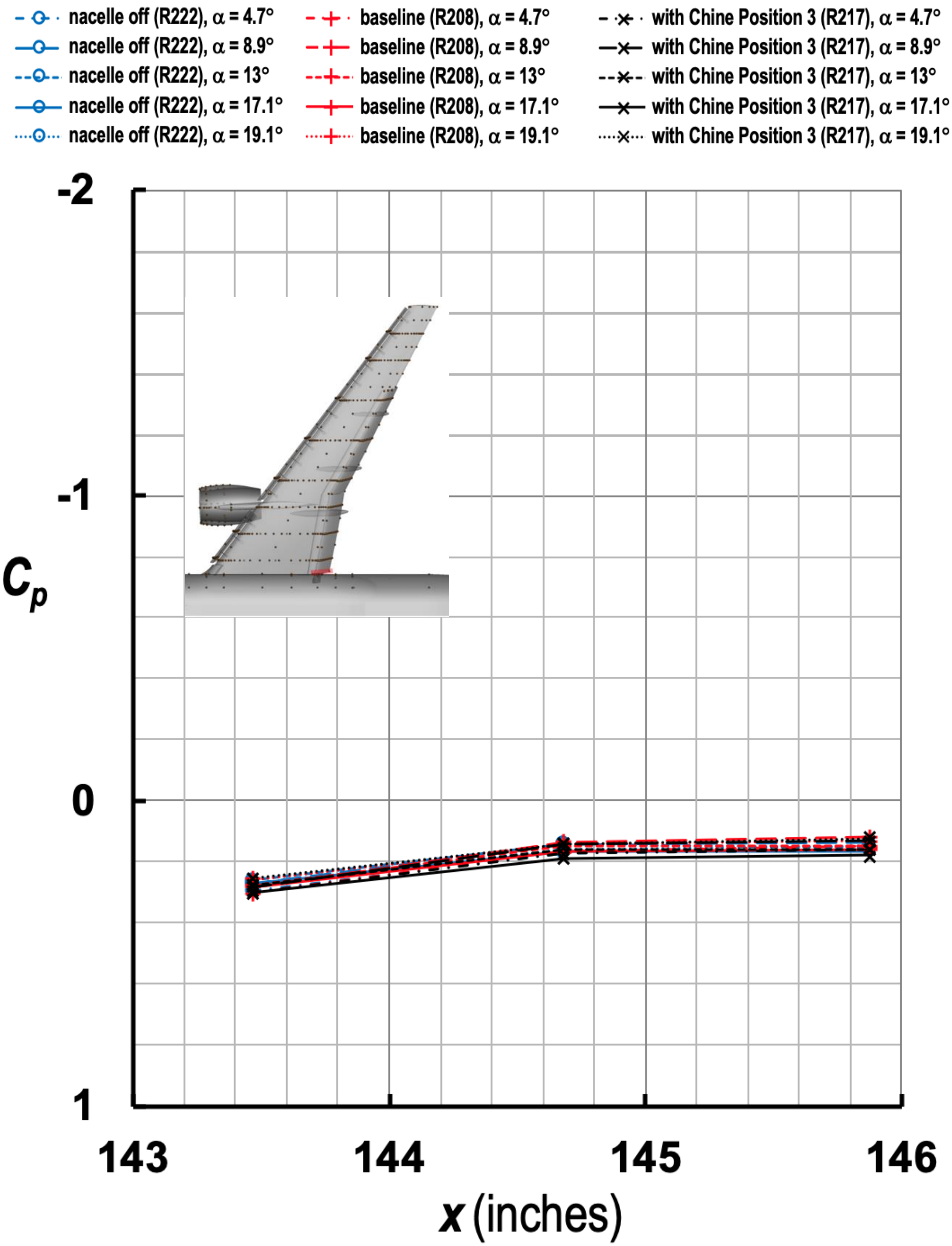

Figure 37. Streamwise C_p distributions along the lower surface of the inboard flap edge for three variants of CRM-HL at five angles of attack ($M_\infty = 0.2$, with TWICS).

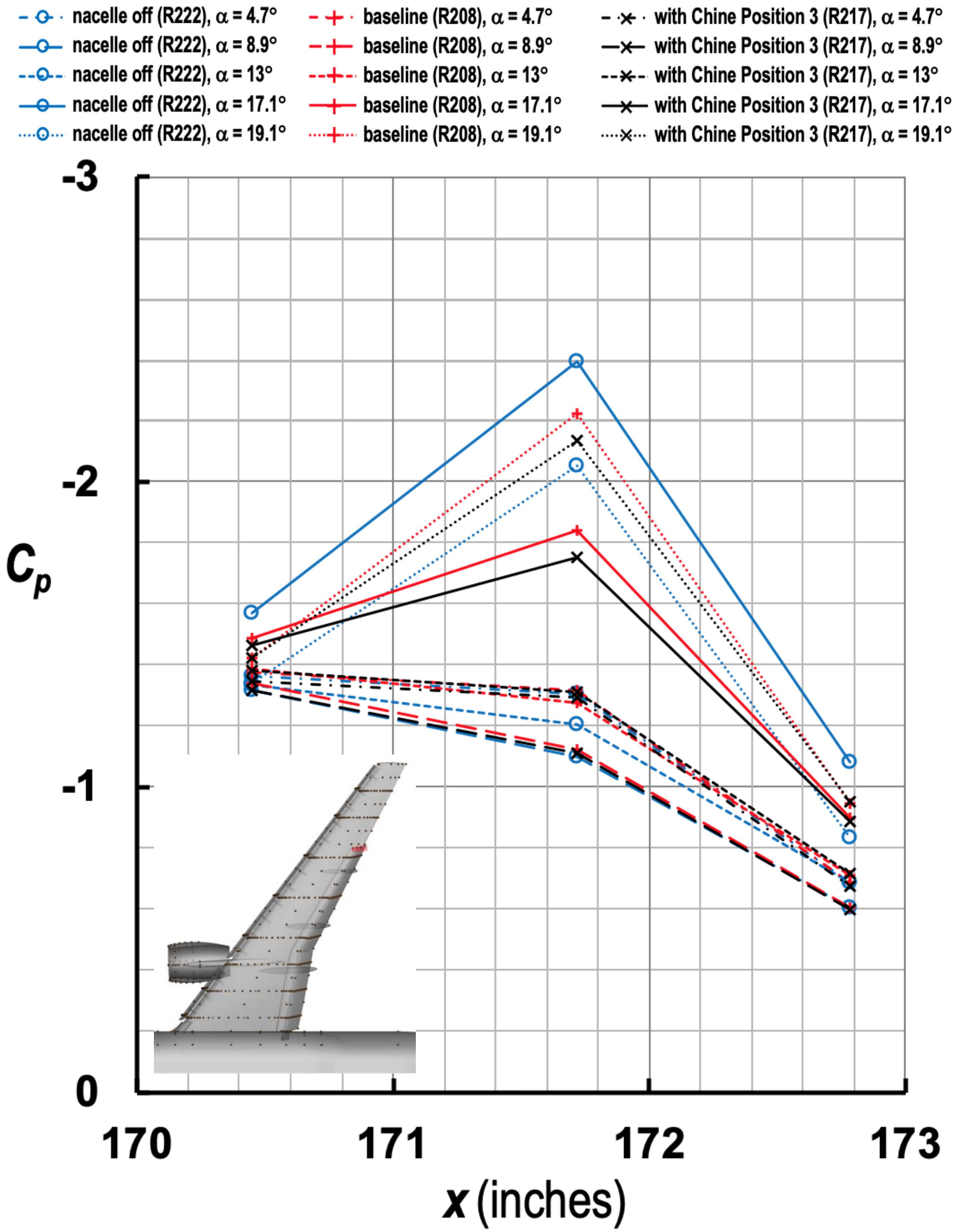

Figure 38. Streamwise C_p distributions along the upper surface of the outboard flap edge for three variants of CRM-HL at five angles of attack (M_∞ = 0.2, with TWICS).

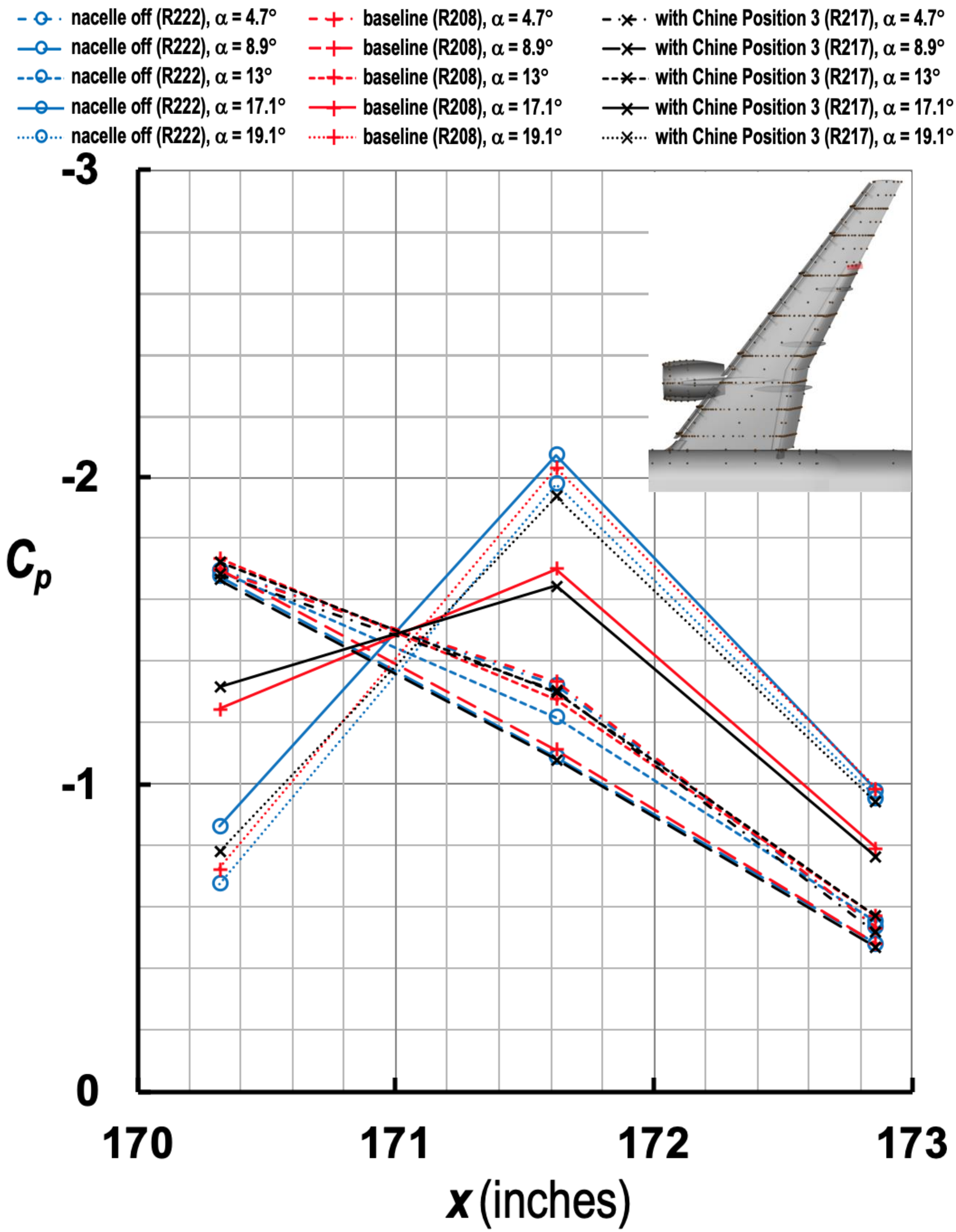

Figure 39. Streamwise C_p distributions along the side-edge surface of the outboard flap edge for three variants of CRM-HL at five angles of attack ($M_\infty = 0.2$, with TWICS).

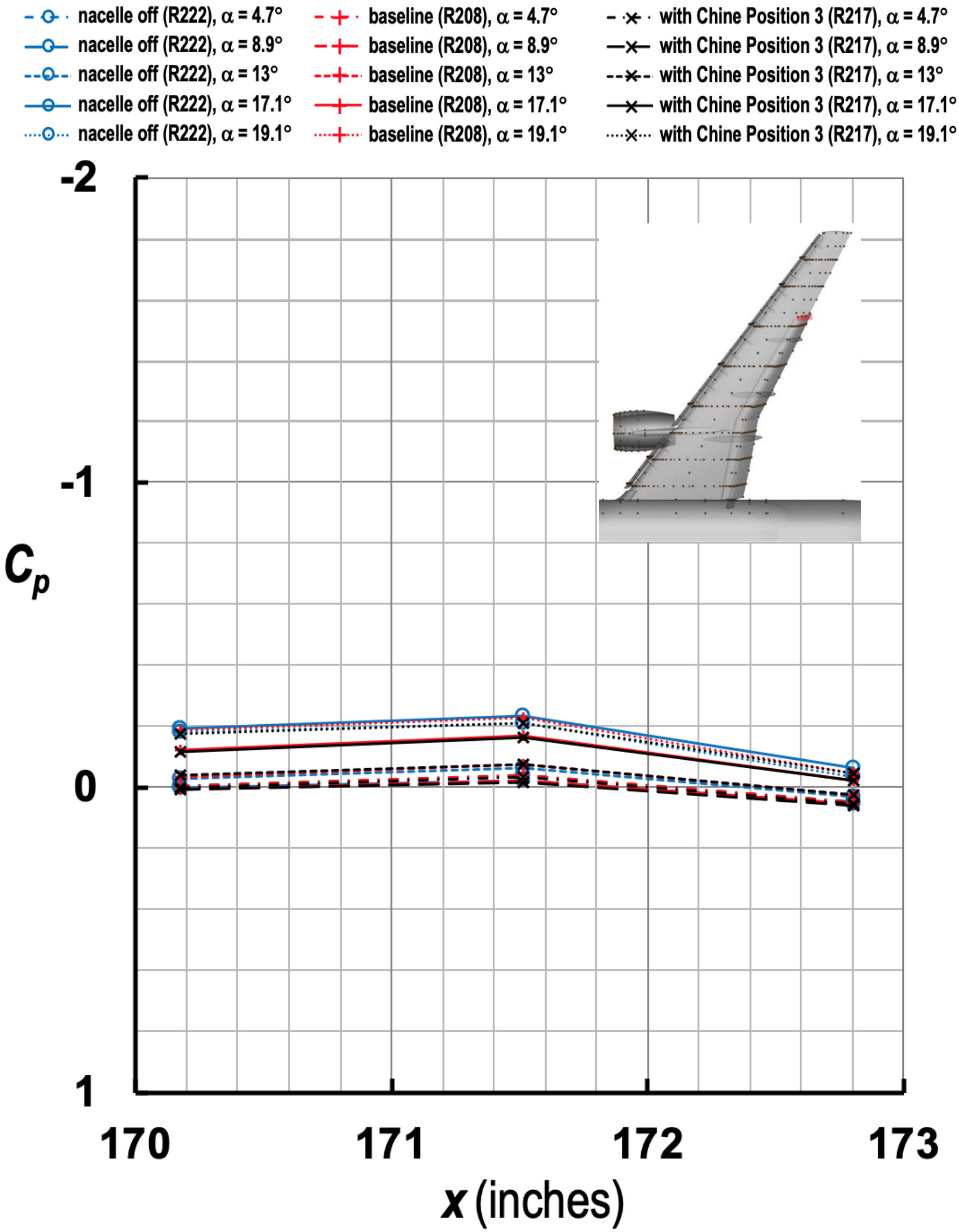

Figure 40. Streamwise C_p distributions along the lower surface of the outboard flap edge for three variants of CRM-HL at five angles of attack ($M_\infty = 0.2$, with TWICS).

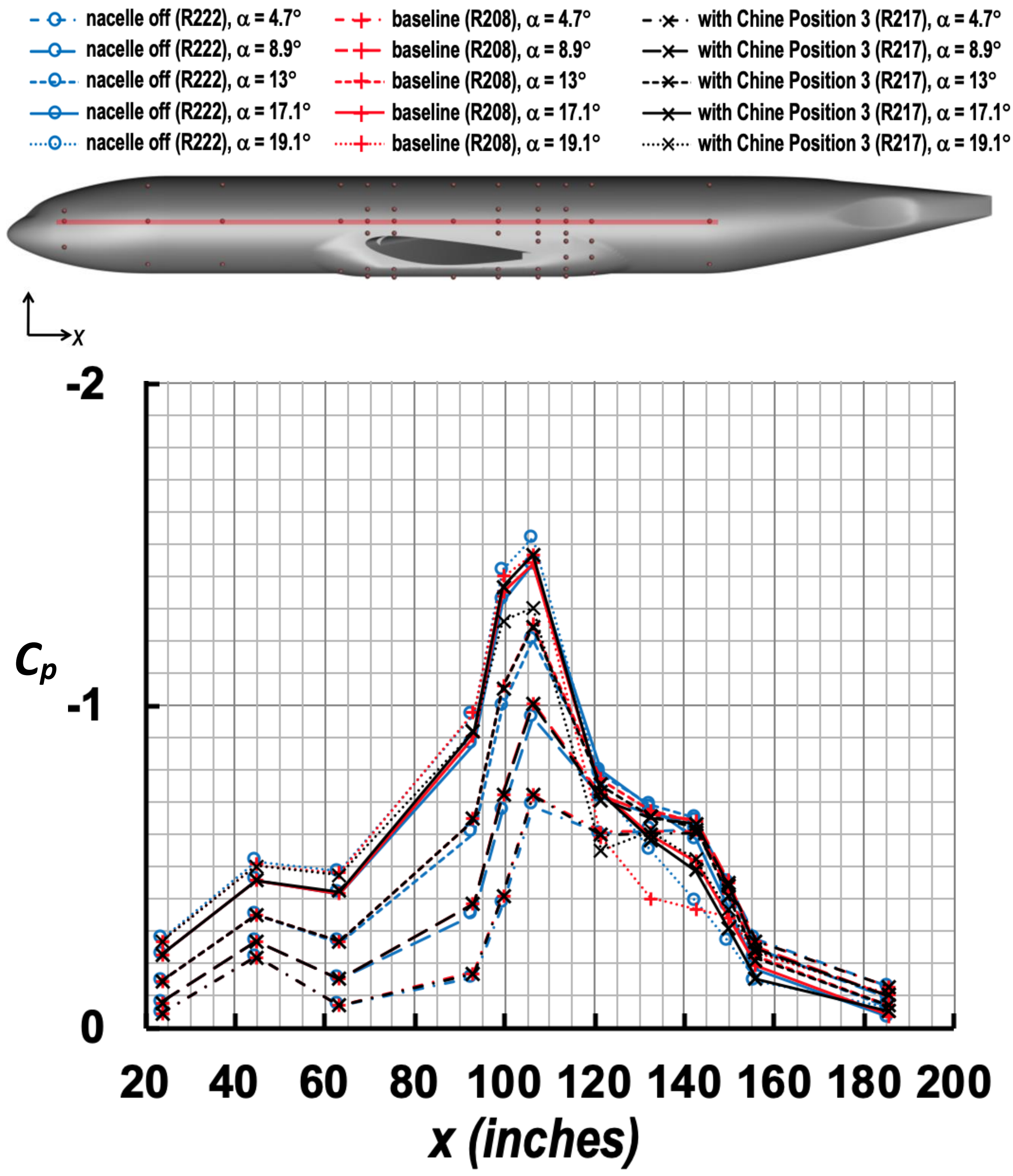

Figure 41. Streamwise C_p distributions at z = 23 inches on the fuselage for three variants of CRM-HL at five angles of attack (M_∞ = 0.2, with TWICS).

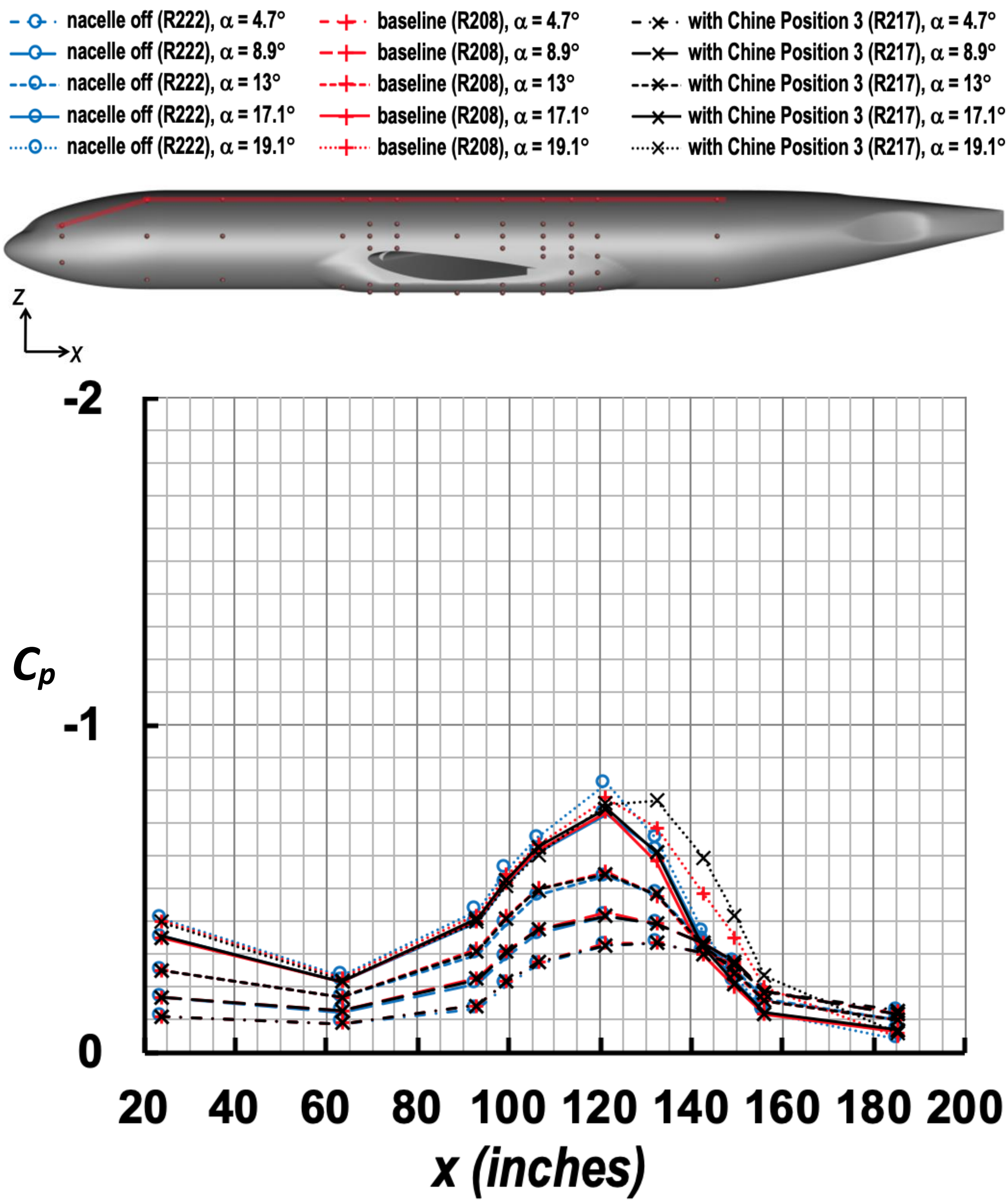

Figure 42. Streamwise C_p distributions at z = 32 inches (x > 23.6 inch station) on the fuselage for three variants of CRM-HL at five angles of attack (M_∞ = 0.2, with TWICS).

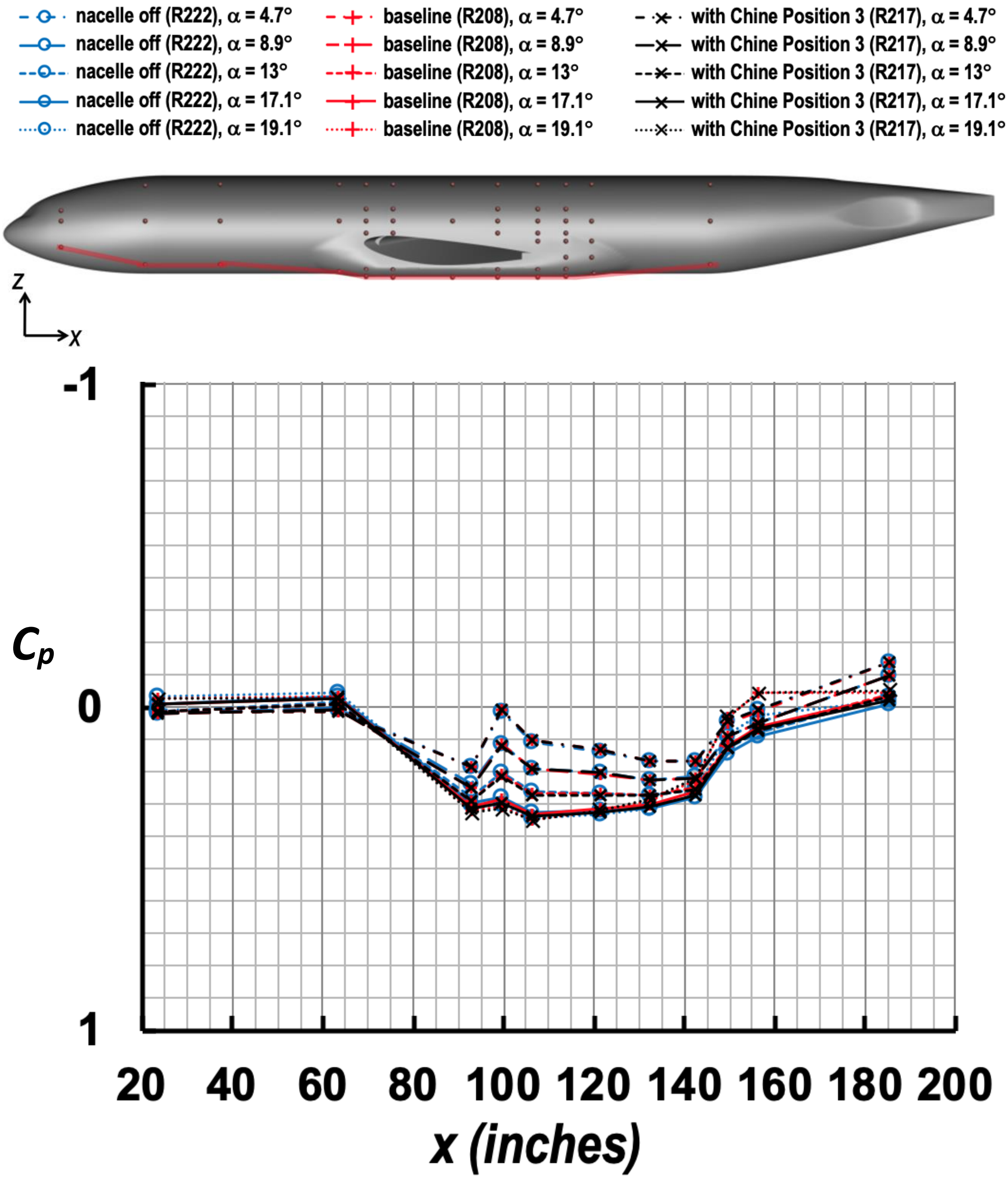

Figure 43. Streamwise C_p distributions at $z \sim 9$ inches ($106.4 \leq x \leq 142.6$) on the fuselage for three variants of CRM-HL at five angles of attack ($M_\infty = 0.2$, with TWICS).

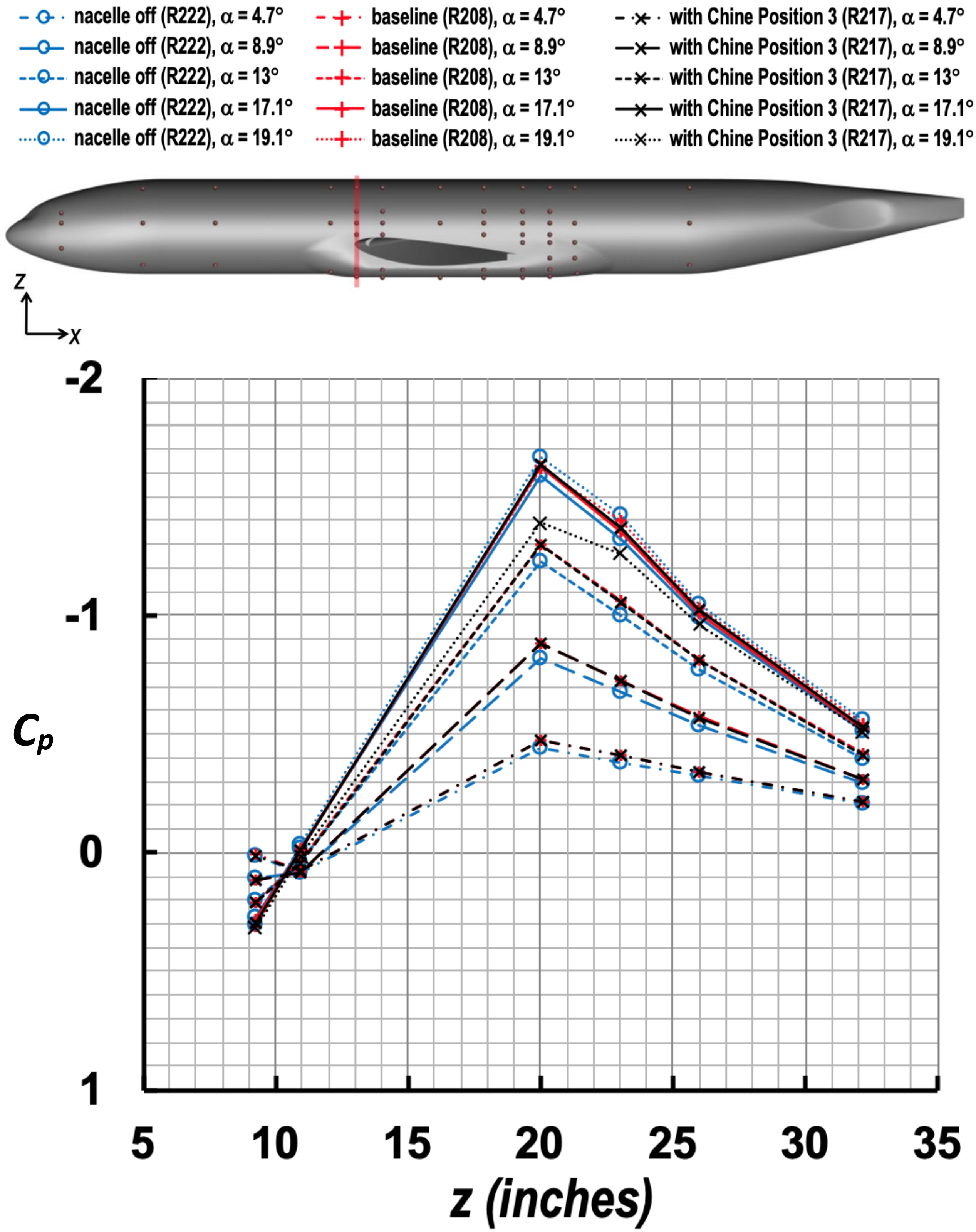

Figure 44. Circumferential C_p distributions at x = 99.7 inches on the fuselage for three variants of CRM-HL at five angles of attack (M_∞ = 0.2, with TWICS).

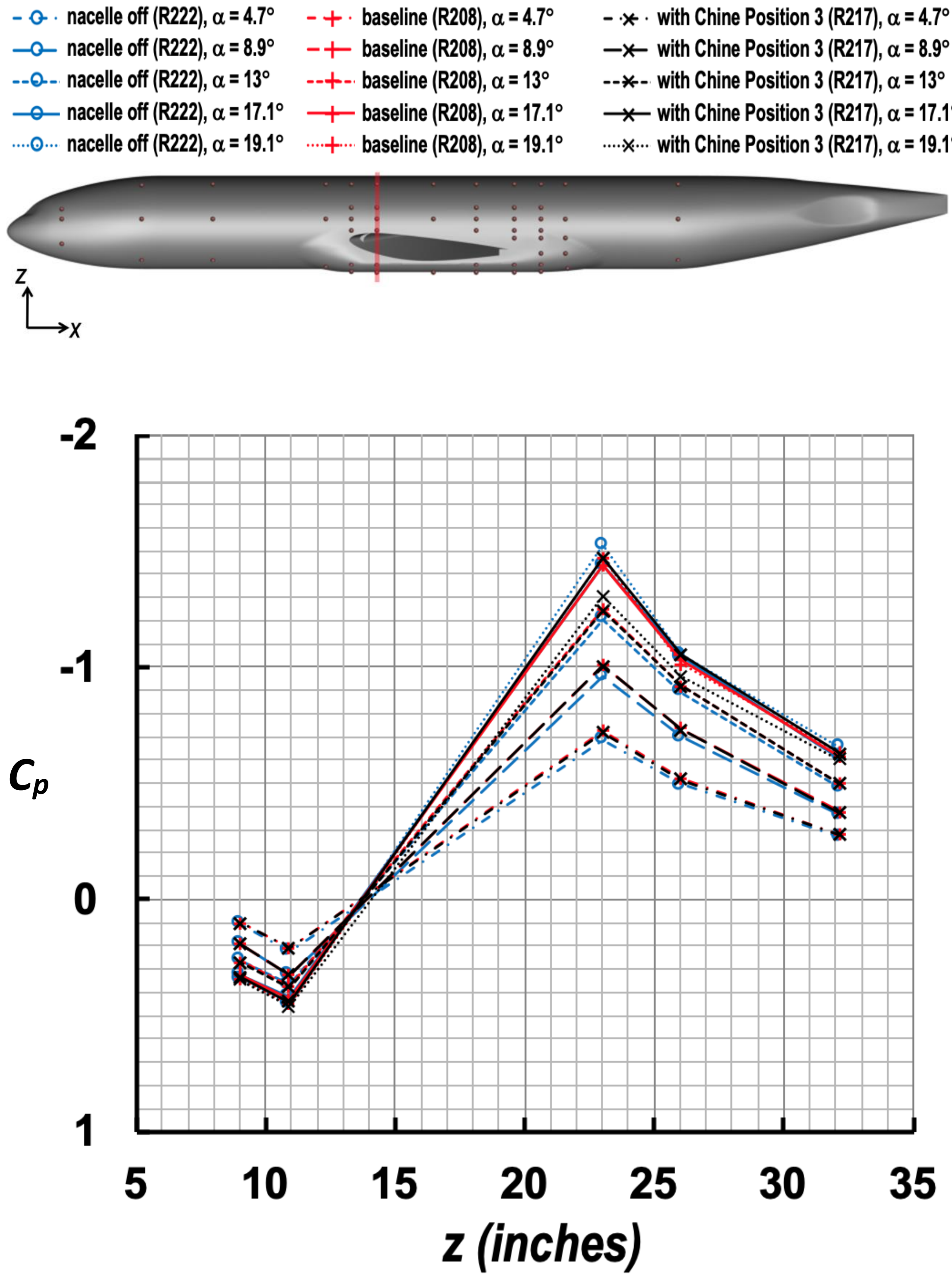

Figure 45. Circumferential C_p distributions at x = 106.4 inches on the fuselage for three variants of CRM-HL at five angles of attack (M_∞ = 0.2, with TWICS).

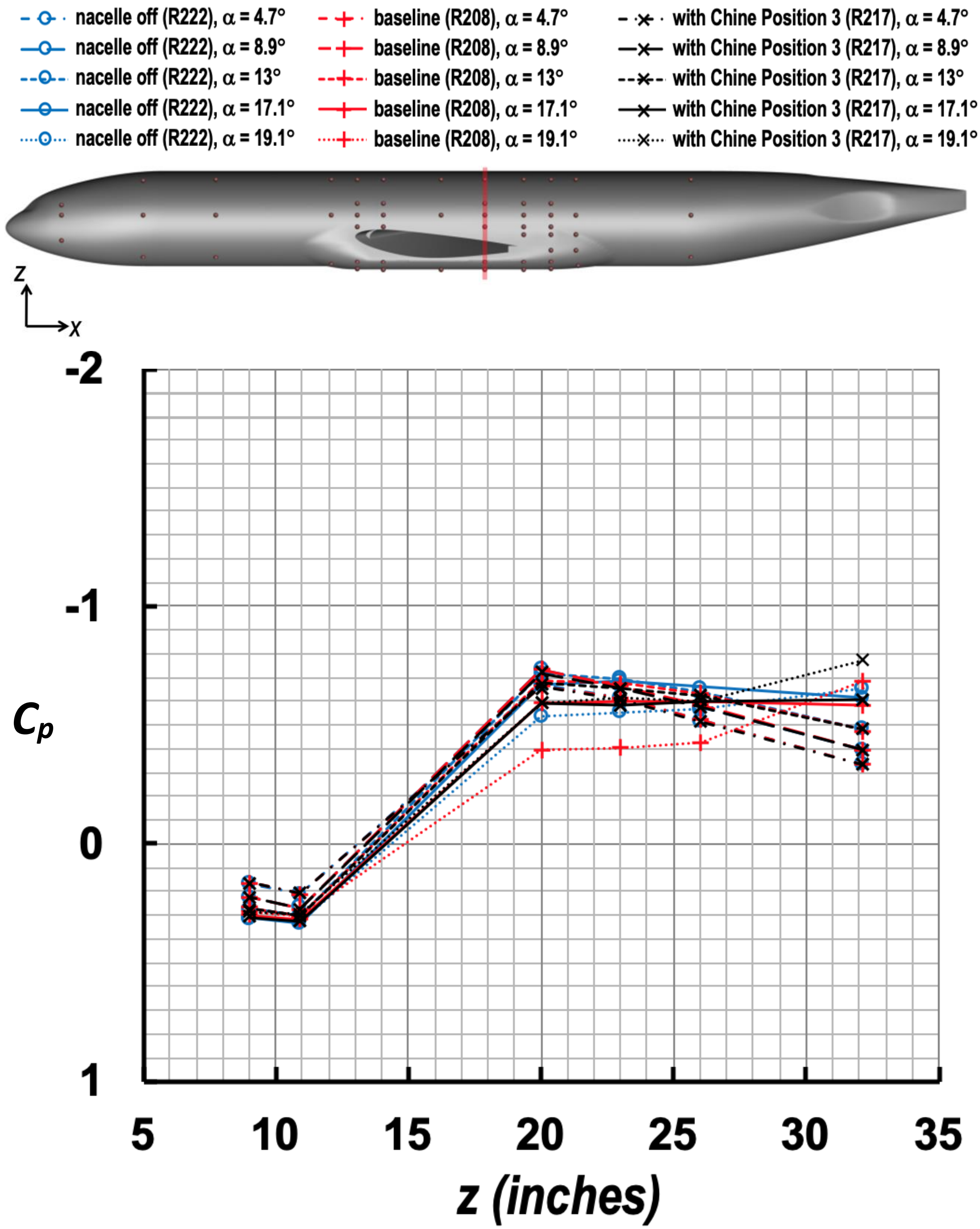

Figure 46. Circumferential C_p distributions at x = 132.5 inches on the fuselage for three variants of CRM-HL at five angles of attack (M_∞ = 0.2, with TWICS).

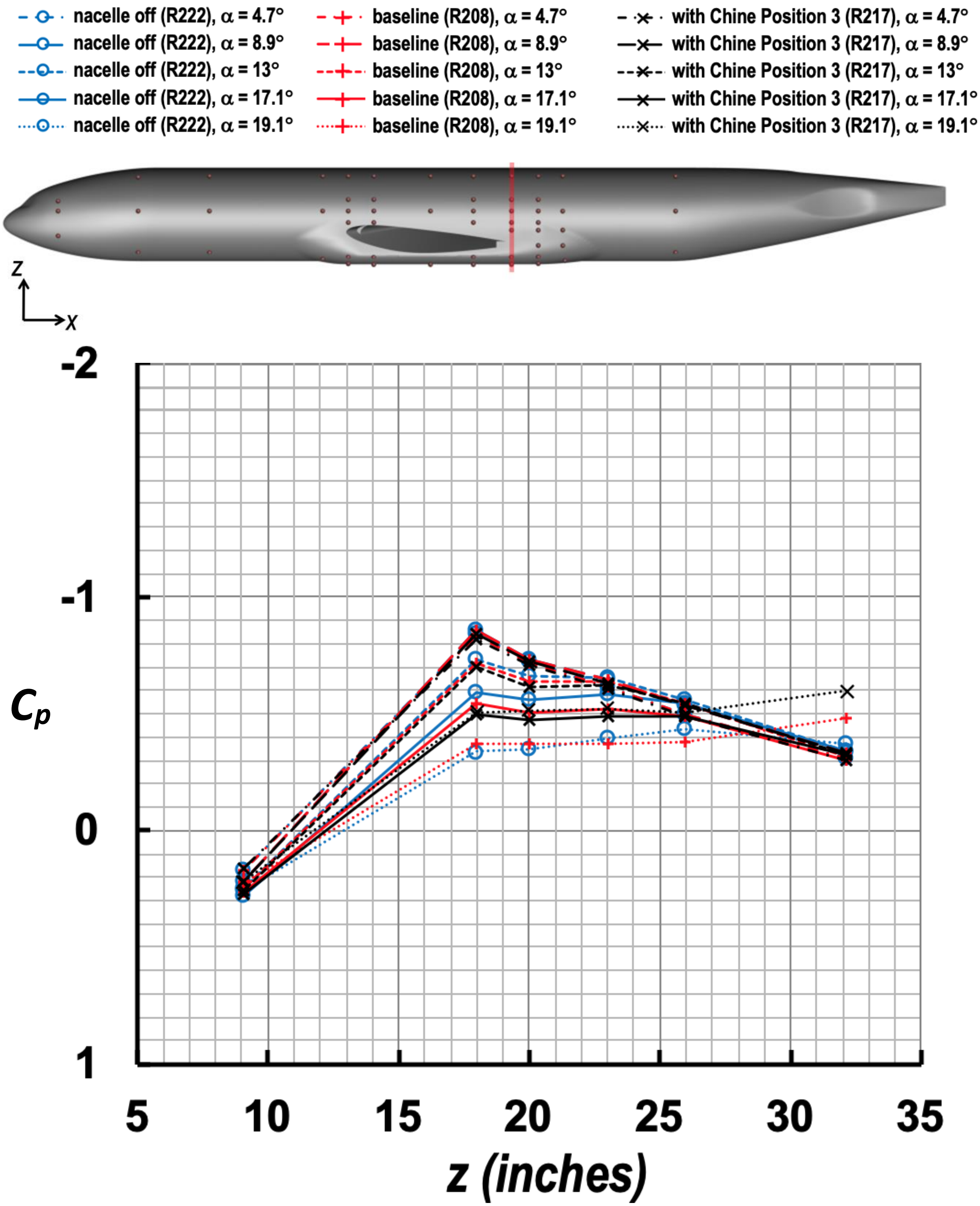

Figure 47. Circumferential C_p distributions at x = 142.5 inches on the fuselage for three variants of CRM-HL at five angles of attack (M_∞ = 0.2, with TWICS).

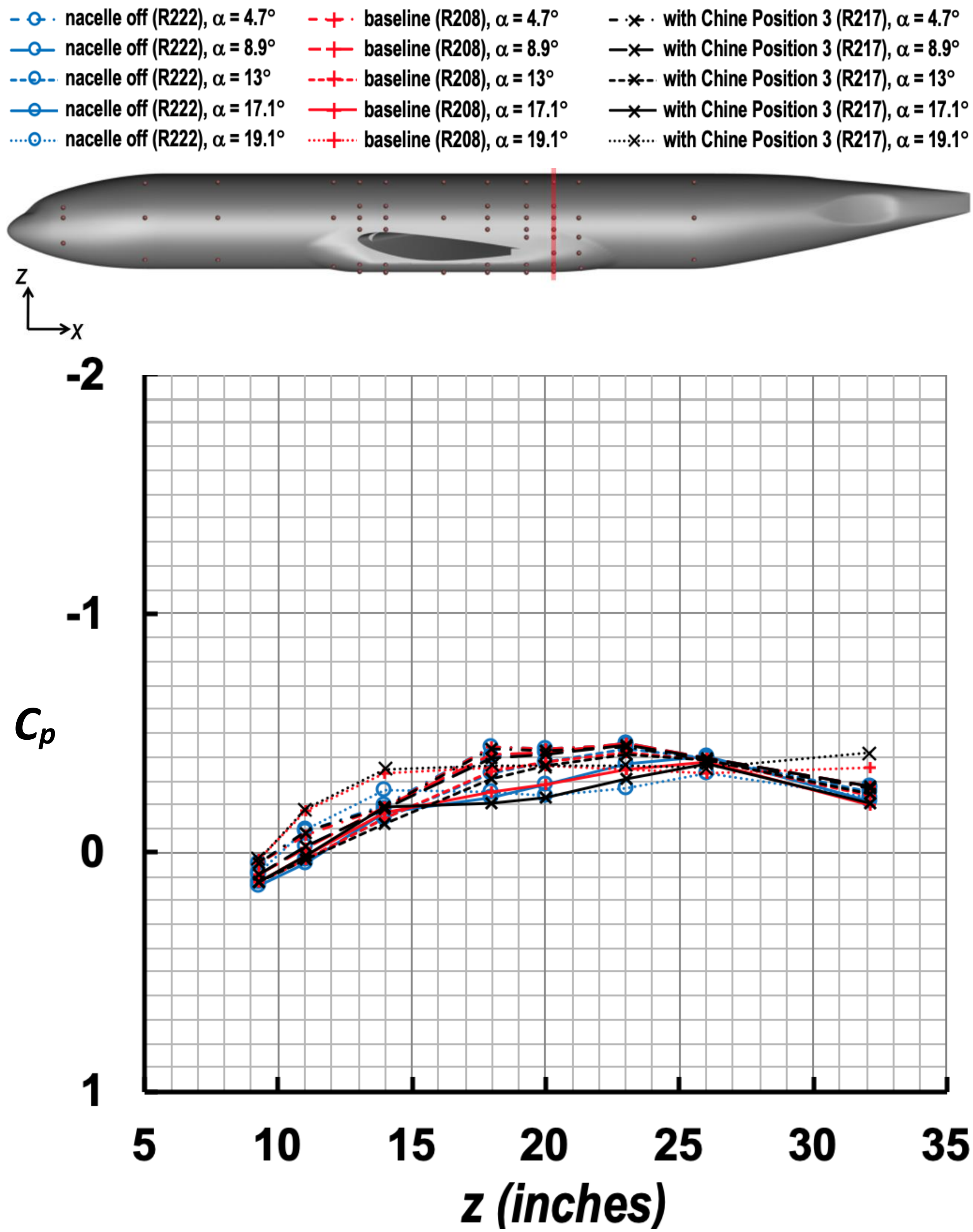

Figure 48. Circumferential C_p distributions at x = 149.5 inches on the fuselage for three variants of CRM-HL at five angles of attack (M_∞ = 0.2, with TWICS).

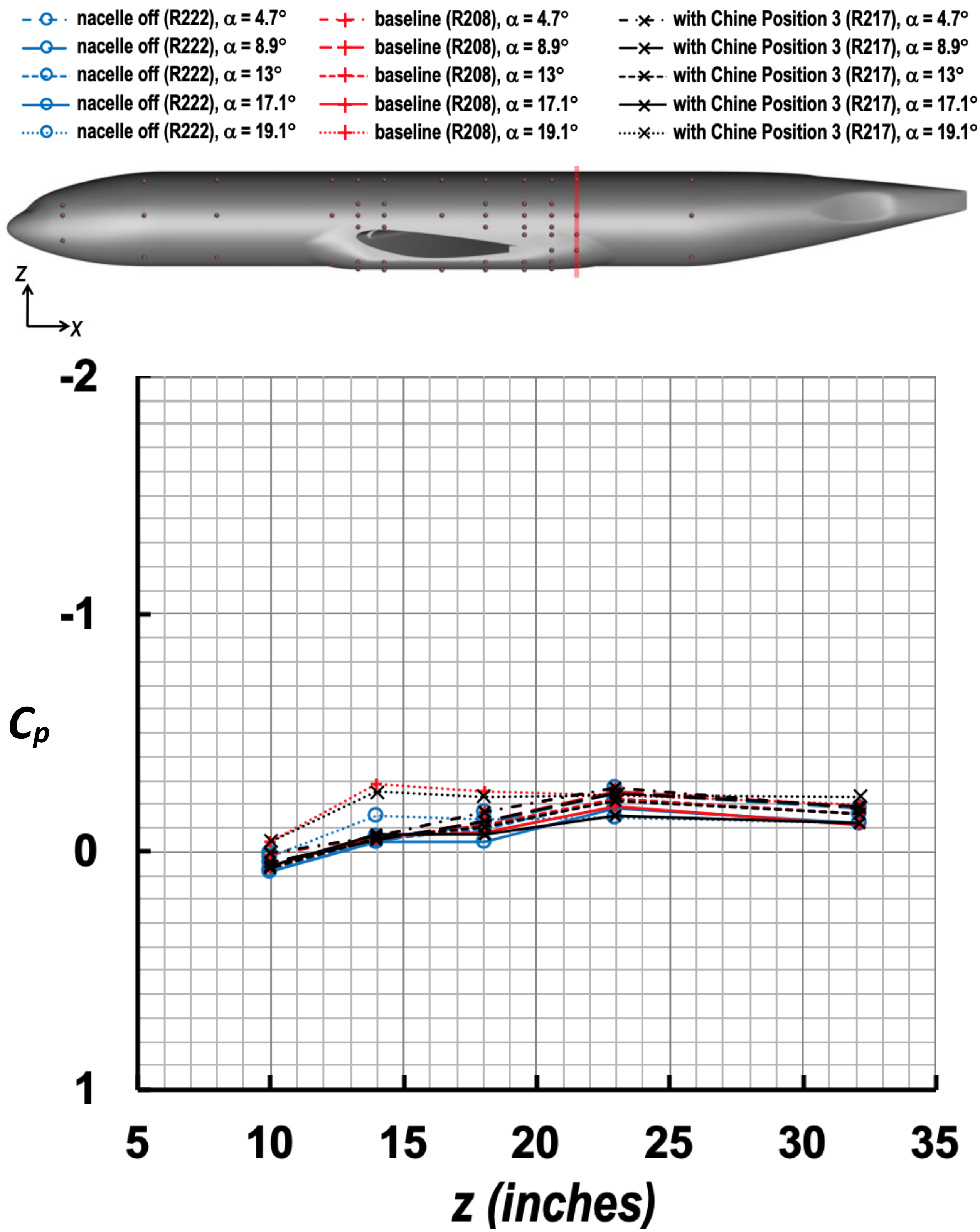

Figure 49. Circumferential C_p distributions at x = 156.5 inches on the fuselage for three variants of CRM-HL at five angles of attack (M_∞ = 0.2, with TWICS).

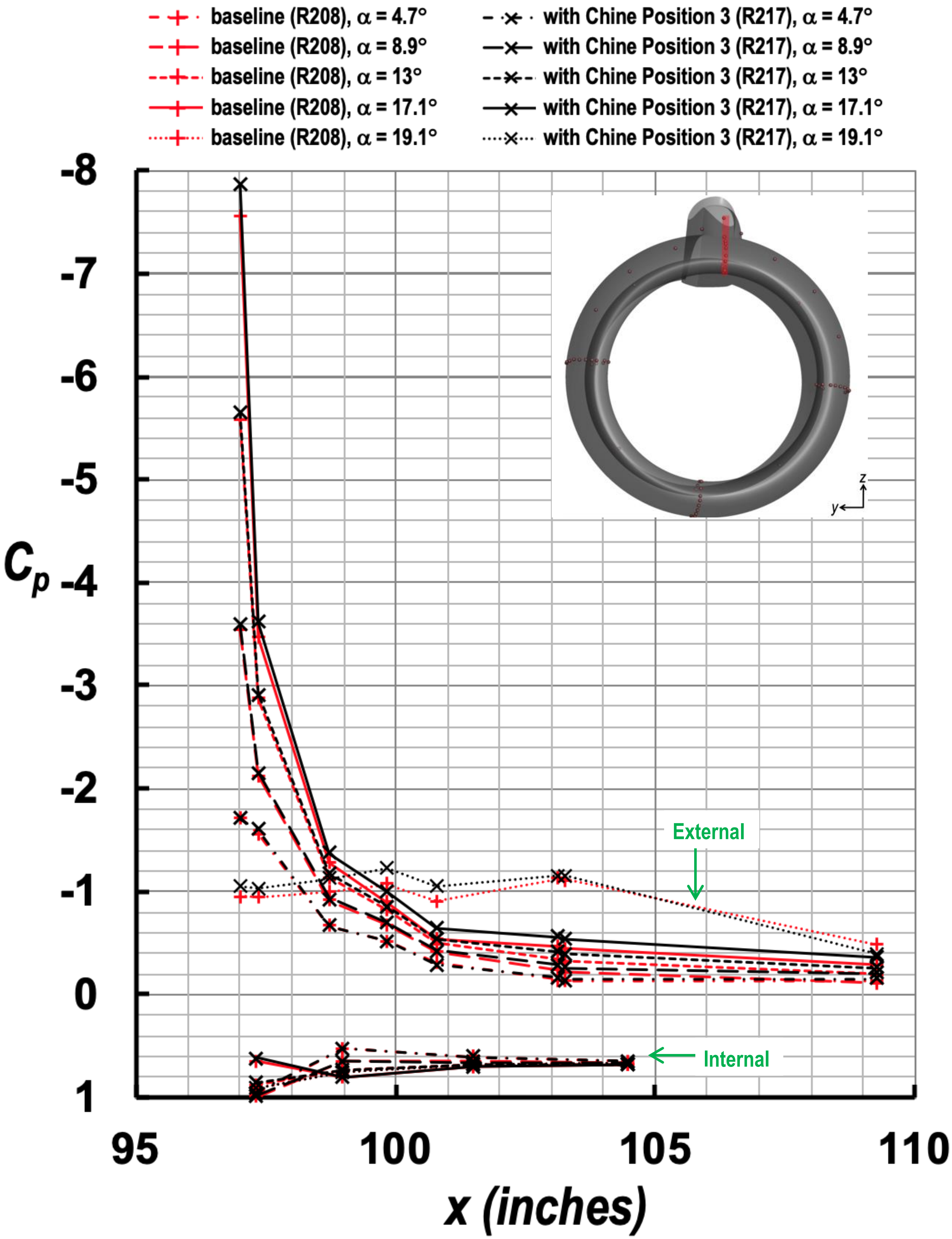

Figure 50. Streamwise C_p distributions of the 12 o'clock row (facing downstream) on the nacelle for two variants of CRM-HL at five angles of attack ($M_\infty = 0.2$, with TWICS).

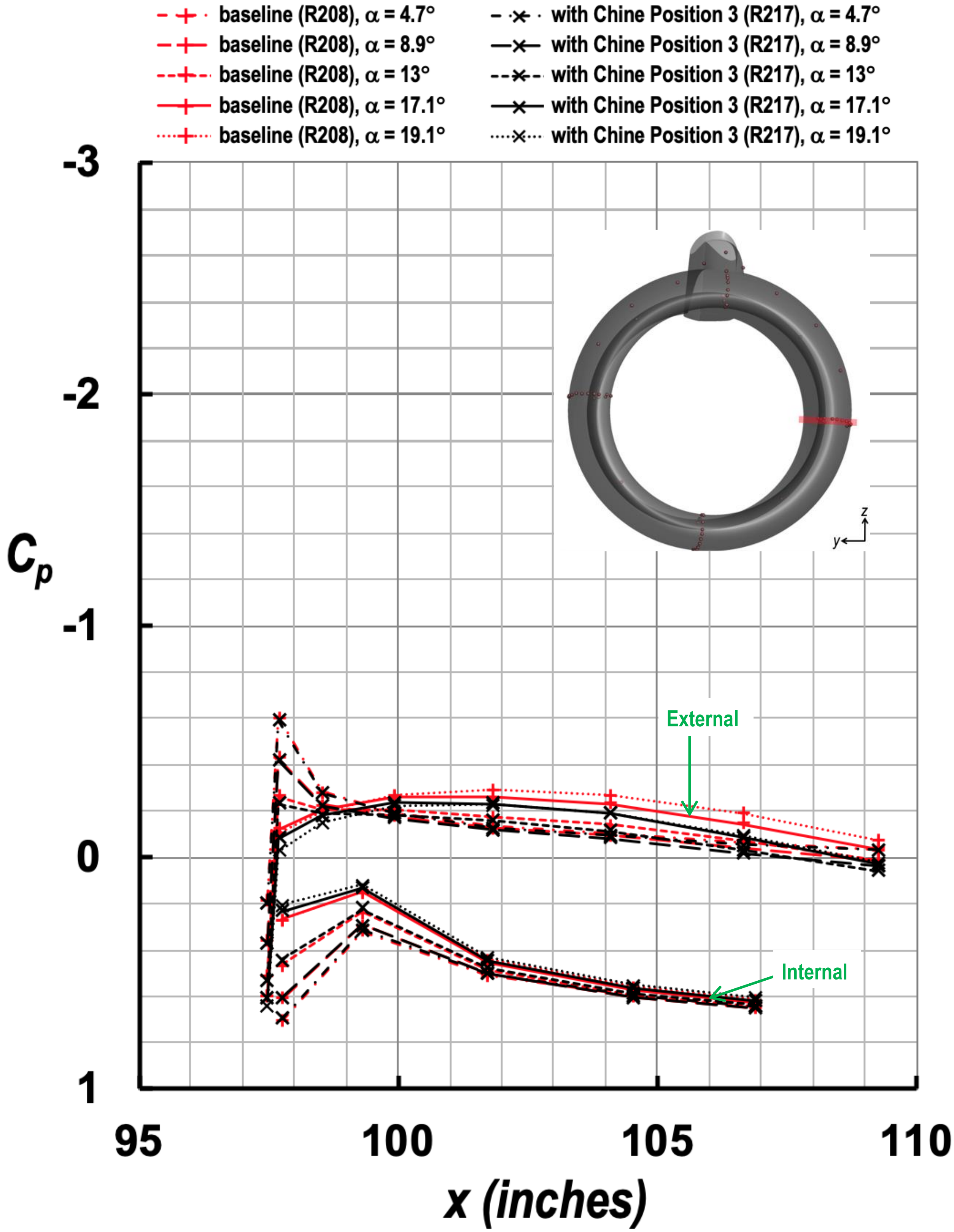

Figure 51. Streamwise C_p distributions of the 3 o'clock row (facing downstream) on the nacelle for two variants of CRM-HL at five angles of attack (M_∞ = 0.2, with TWICS).

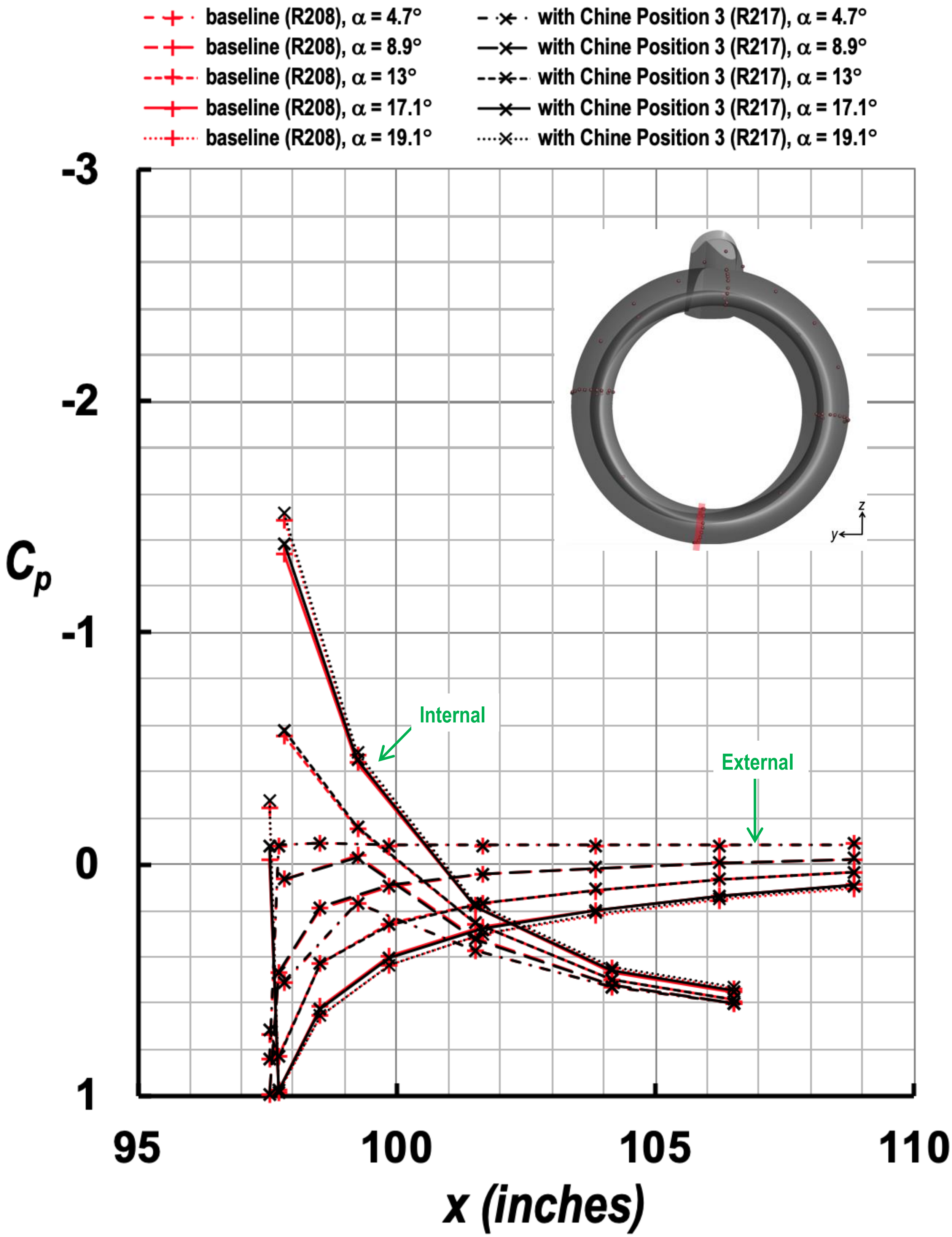

Figure 52. Streamwise C_p distributions of the 6 o'clock row (facing downstream) on the nacelle for two variants of CRM-HL at five angles of attack ($M_\infty = 0.2$, with TWICS).

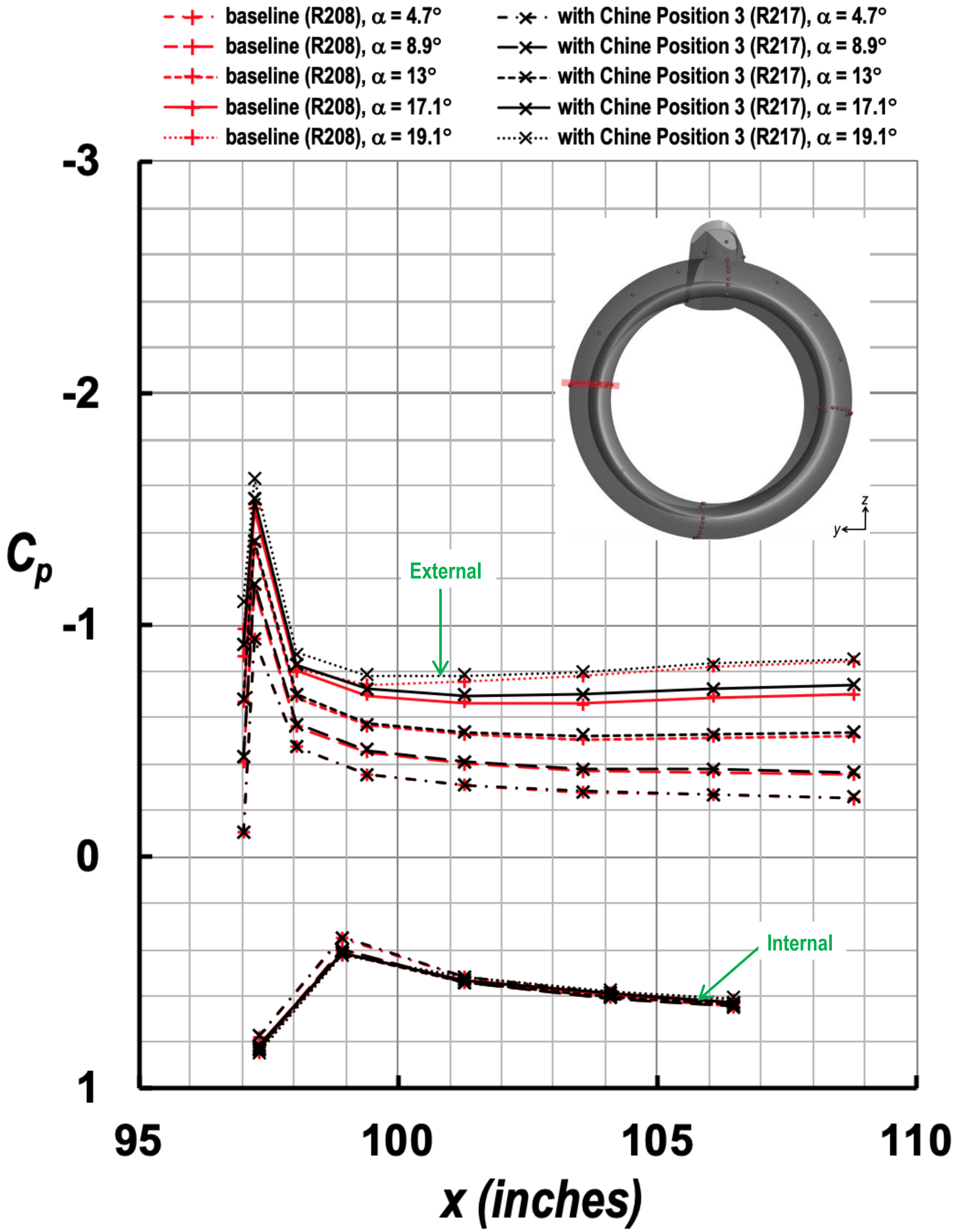

Figure 53. Streamwise C_p distributions of the 9 o'clock row (facing downstream) on the nacelle for two variants of CRM-HL at five angles of attack (M_∞ = 0.2, with TWICS).

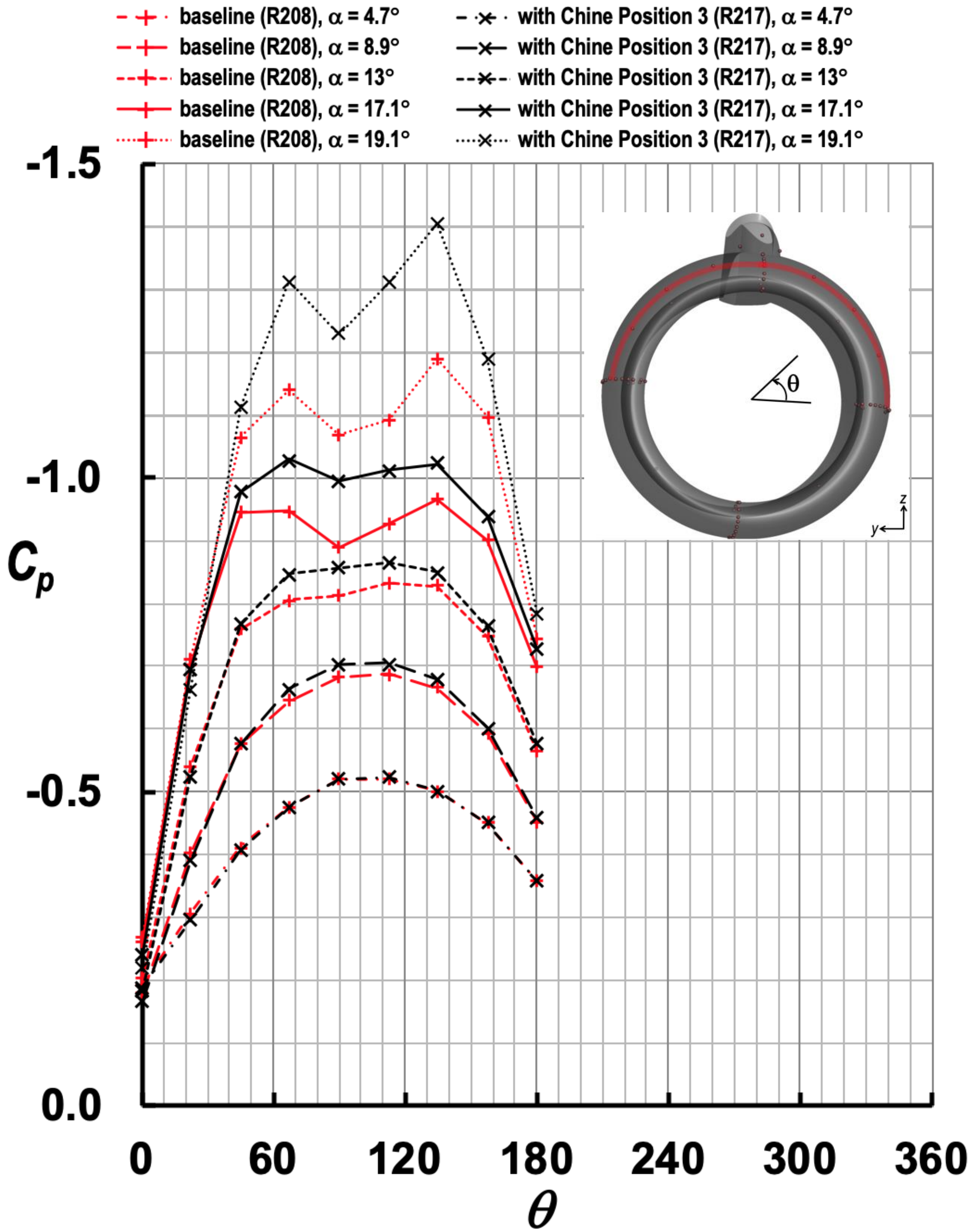

Figure 54. Circumferential C_p distributions at $x \approx 99.8$ inches on the nacelle exterior for two variants of CRM-HL at five angles of attack ($M_\infty = 0.2$, with TWICS).

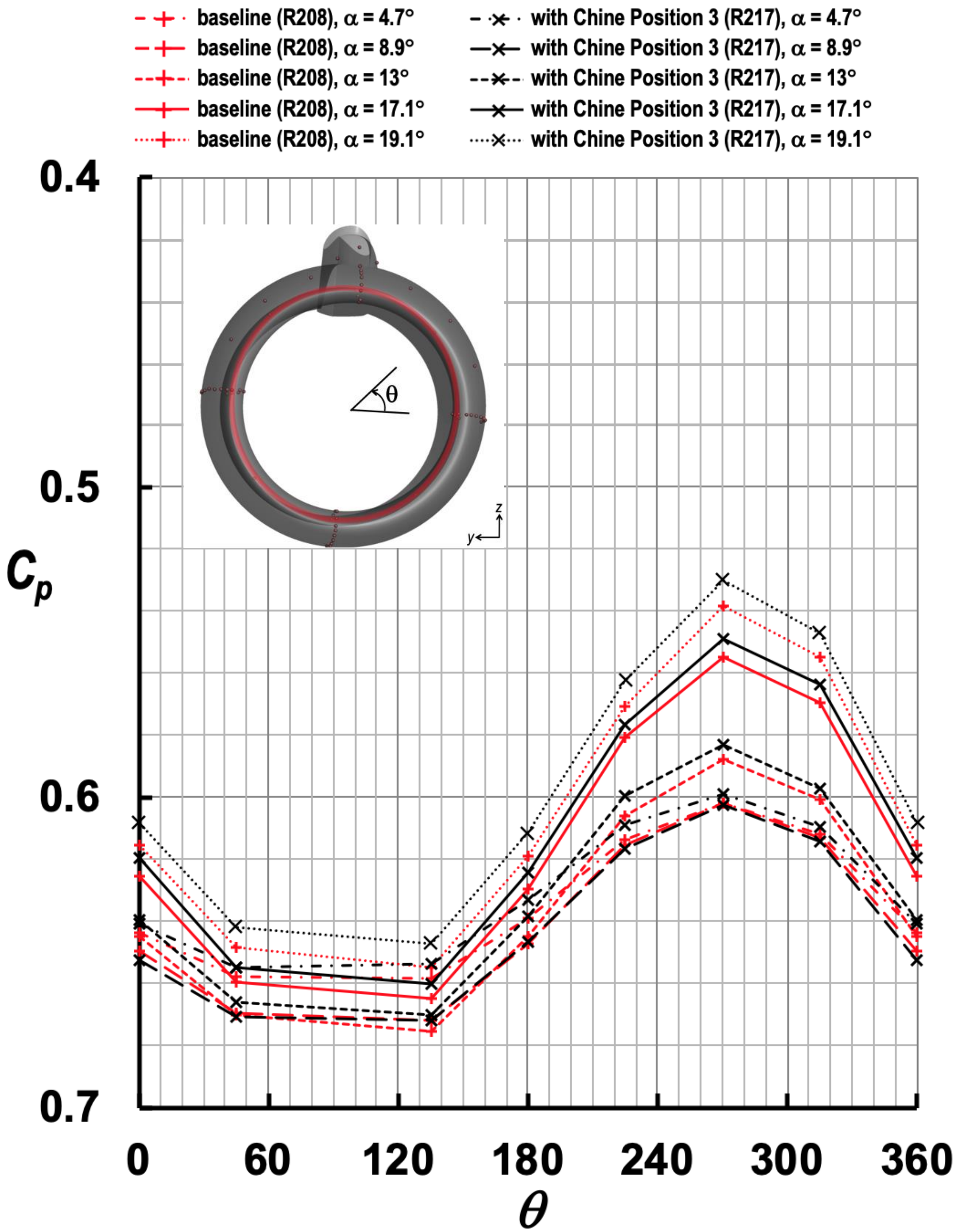

Figure 55. Circumferential C_p distributions at $x \approx 106.6$ inches on the nacelle interior for two variants of CRM-HL at five angles of attack ($M_\infty = 0.2$, with TWICS).

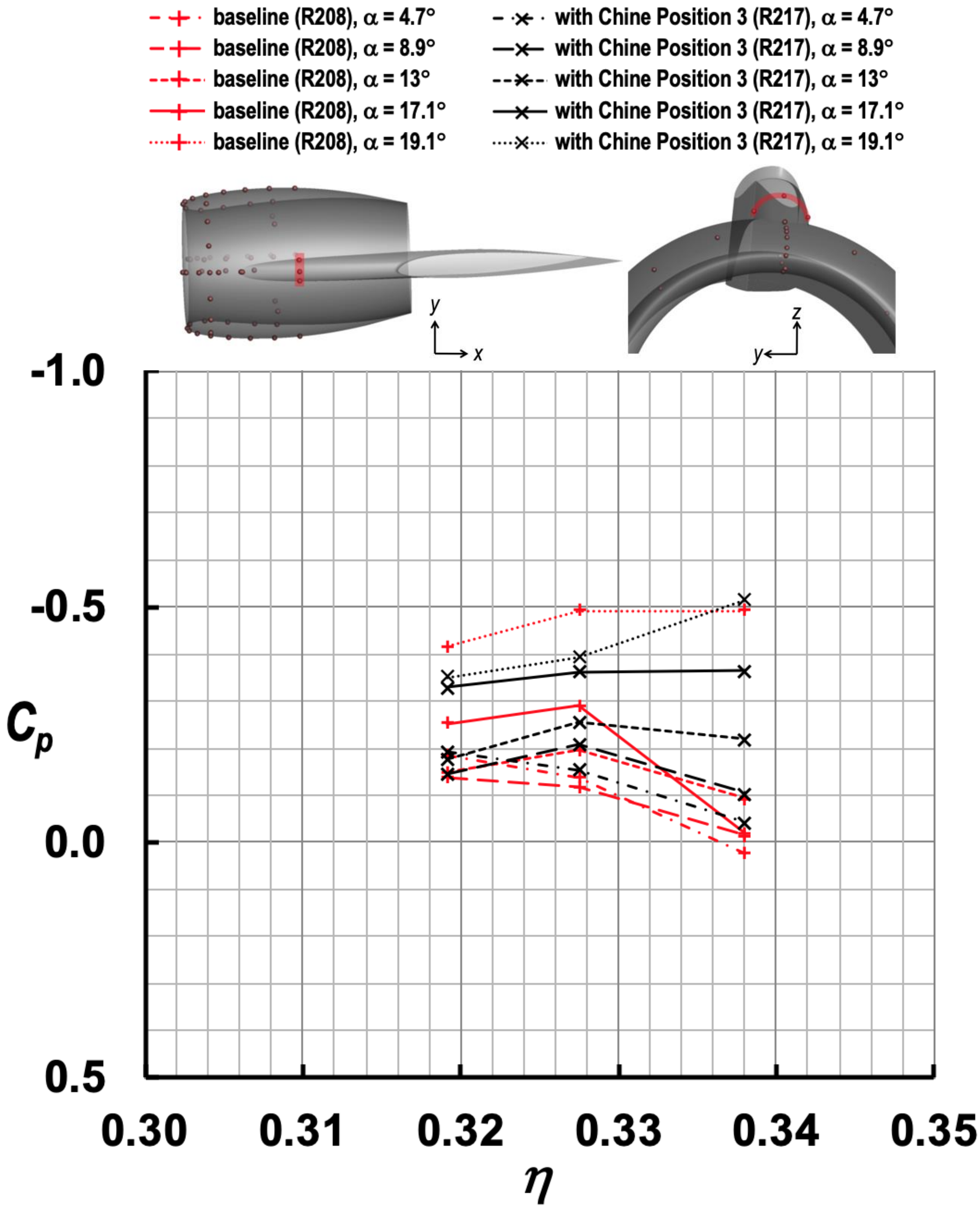

Figure 56. Spanwise C_p distributions at x = 109.2 inches on the nacelle pylon for two variants of CRM-HL at five angles of attack (M_∞ = 0.2, with TWICS).

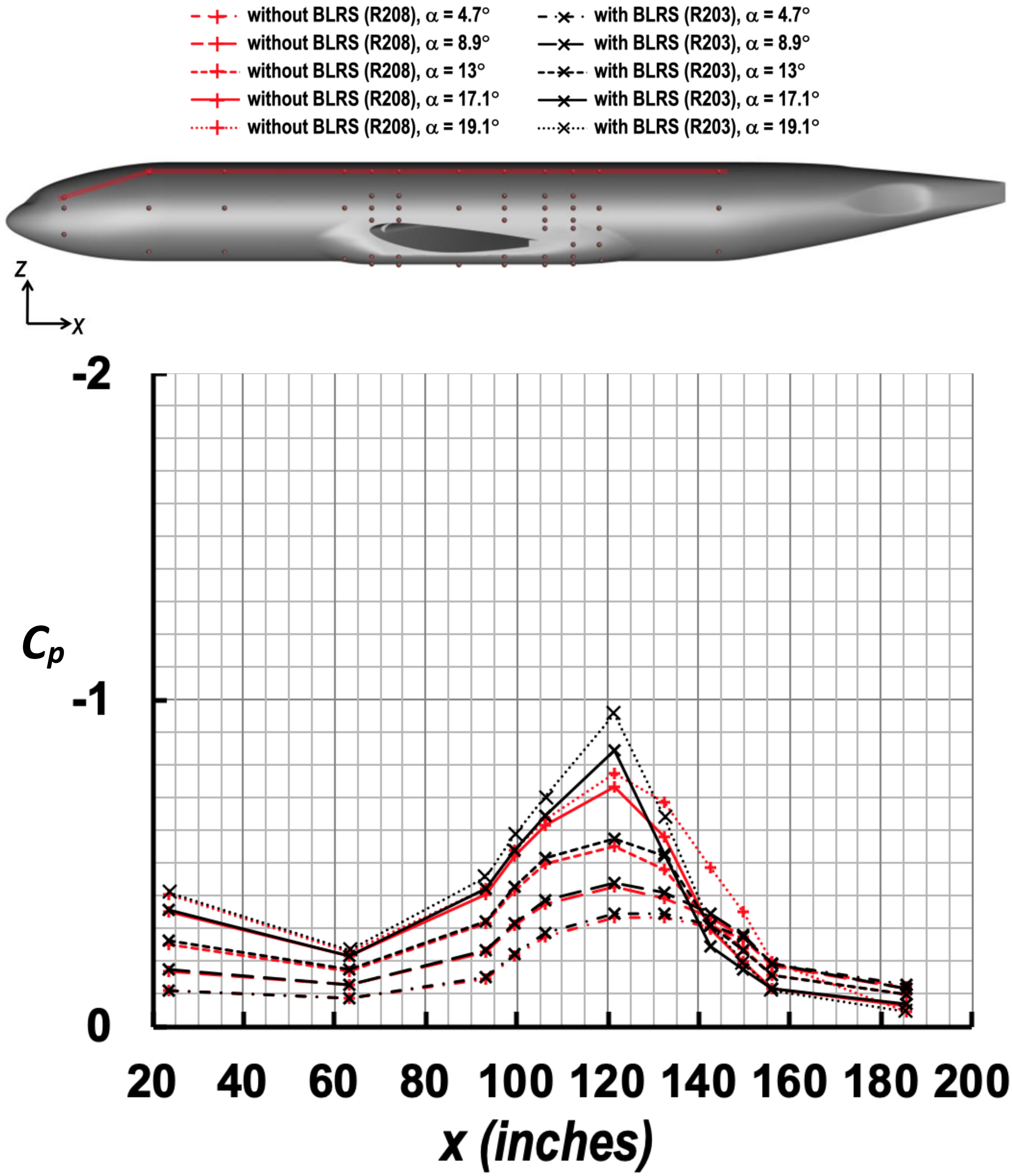

Figure 57. Streamwise C_p distributions at z = 32 inches (downstream of the x = 23.6 station) on the fuselage with and without activation of BLRS at five angles of attack (M_∞ = 0.2, with TWICS).

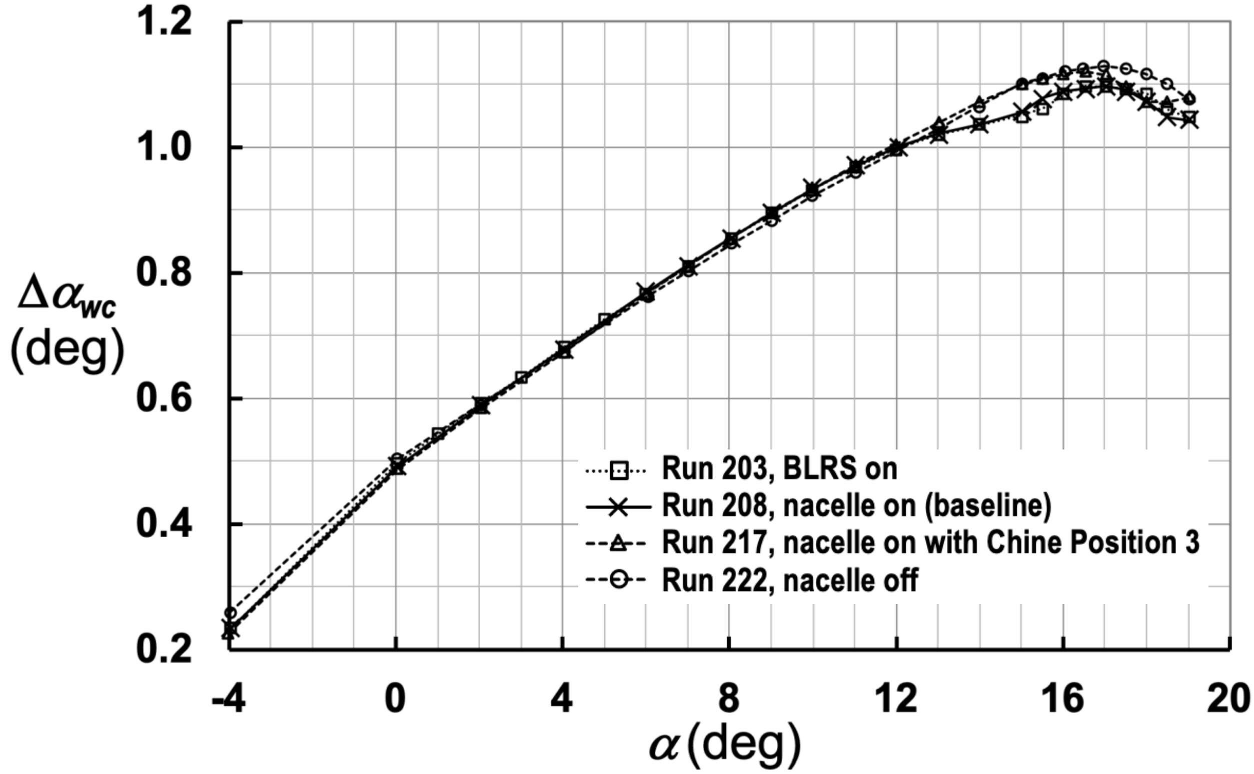

(a) $\Delta\alpha_{wc}$ vs. α

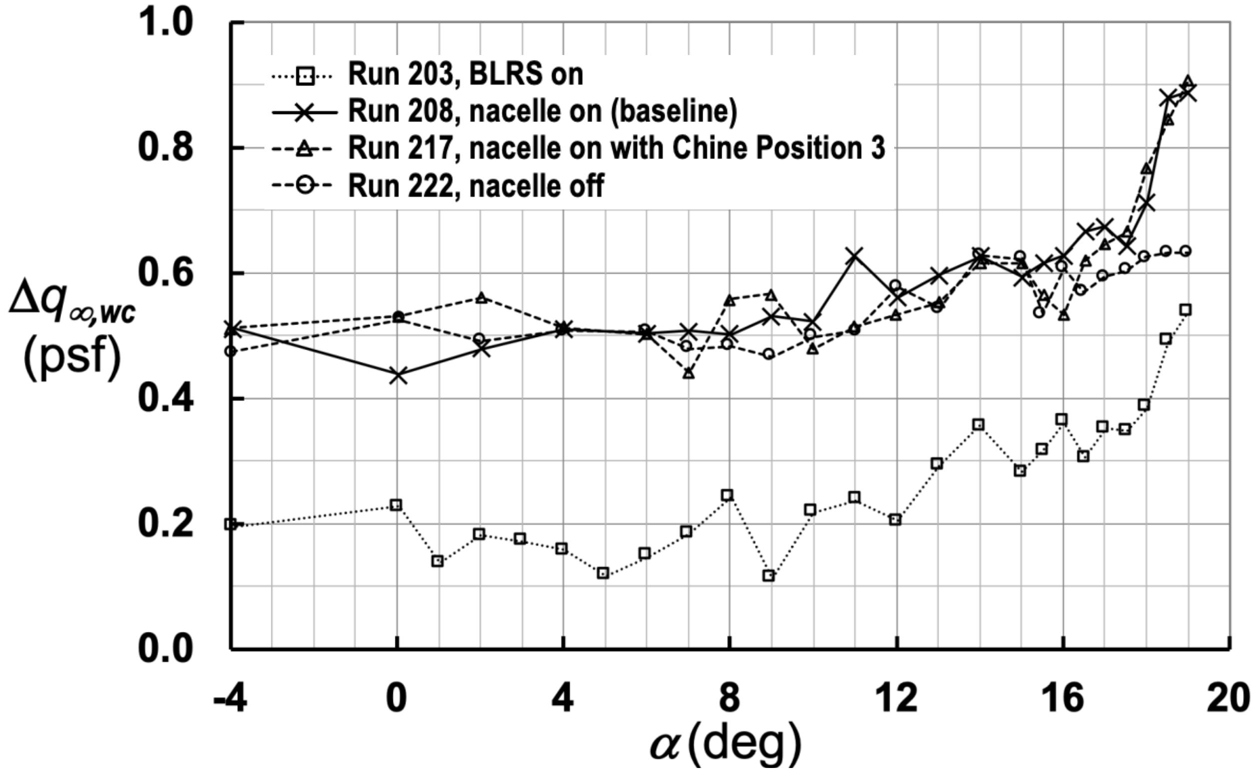

(b) $\Delta q_{\infty,wc}$ vs. α

Figure 58. Variations of $\Delta\alpha_{wc}$ and $\Delta q_{\infty,wc}$ as a function of uncorrected α due to TWICS ($M_\infty = 0.2$).

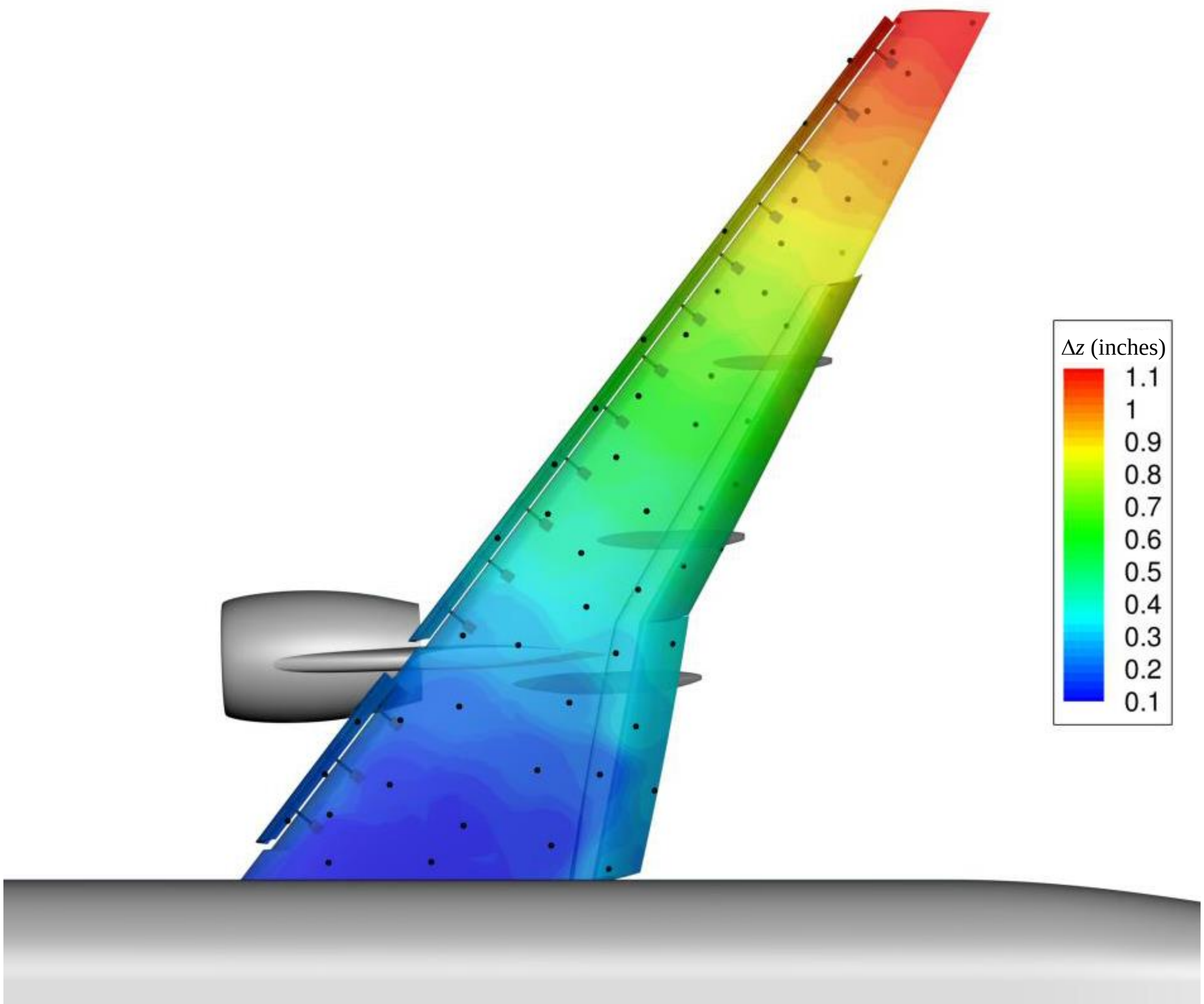

Figure 59. Contour plots of model deformation in *z* position (Δz, inches) at $\alpha = 19.1°$ with TWICS (or $\alpha = 18°$ without TWICS).

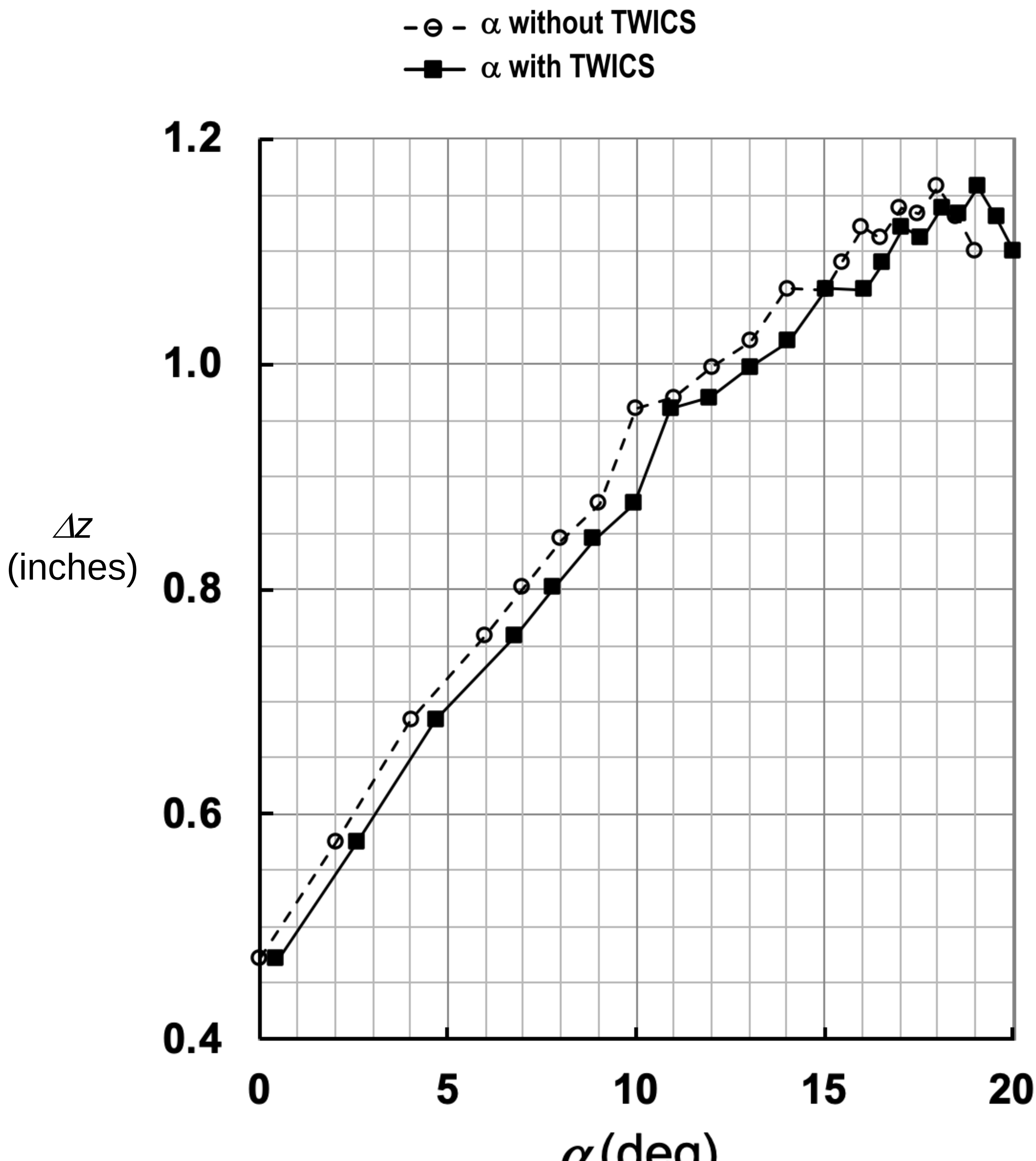

Figure 60. Model deformation in z position (Δz, inches) as a function of angle of attack at the wingtip (Target 1051, $M_\infty = 0.2$).

Appendix A.

CRM-HL Pressure Tap Coordinates

Table A1. CRM-HL Pressure Tap Coordinates on High-Lift Wing
(slat and flap coordinates given in both stowed and baseline deployed positions).

Location	Data file ID	Tap ID	Stowed Coordinates			Deployed Coordinates		
			x (inches)	*y* (inches)	*z* (inches)	*x* (inches)	*y* (inches)	*z* (inches)
Flap	CPP2108	1*	145.7415	12.3223	14.1272	147.0638	13.2756	10.1251
Flap	CPP2237	2	139.1916	12.3029	14.8816	142.2734	12.2700	14.5349
ME	CPP0256	3	140.5924	12.3021	15.2049	Same as stowed coordinates		
ME	CPP0242	4	121.1577	12.3000	18.0072			
ME		5**	100.7010	12.3160	18.6670			
ME		6**	99.3644	12.2990	17.5283			
Slat	CPP1041	7	106.1466	17.4501	19.4456	104.4566	18.8128	17.7752
Slat	CPP1021	8	105.6767	17.4499	19.3655	104.0608	18.7783	17.5117
Slat	CPP1034	9	105.1115	17.4496	19.2469	103.5937	18.7302	17.1756
Slat	CPP1019	10	104.4494	17.4499	19.0514	103.0692	18.6577	16.7326
Slat	CPP1011	11	103.9636	17.4495	18.8469	102.7088	18.5858	16.3548
Slat	CPP1039	12	103.6373	17.4501	18.6434	102.4933	18.5187	16.0434
Slat	CPP1023	13	103.4423	17.4488	18.4472	102.3942	18.4549	15.7932
Slat	CPP1035	14	103.3600	17.4497	18.3169	102.3715	18.4152	15.6460
Slat	CPP1013	15	103.3136	17.4515	18.2014	102.3757	18.3816	15.5262
Slat	CPP1030	16	103.2882	17.4513	18.0483	102.4139	18.3354	15.3830
Slat	CPP1012	17	103.3471	17.4505	17.8374	102.5519	18.2734	15.2247
Slat	CPP0724	18	103.5230	17.4490	17.6458	102.7886	18.2190	15.1317
Slat	CPP0743	19	103.8121	17.4493	17.4196	103.1424	18.1586	15.0549
Slat	CPP0841	20	104.1182	17.4491	17.2210	103.5007	18.1063	15.0092
Slat	CPP0809	21	104.2682	17.4489	17.1311	103.6732	18.0828	14.9933
Slat		22†	104.3101	17.4500	17.1440	103.7063	18.0886	15.0215
Slat	CPP0846	23	104.0707	17.4495	17.4630	103.3605	18.1775	15.1993
Slat	CPP0822	24	104.7970	17.4499	18.7138	103.5209	18.5653	16.5835
Slat	CPP0829	25	105.4736	17.4503	19.1400	103.9663	18.7073	17.2322
Slat	CPP1026	26	106.0820	17.4501	19.4365	104.4014	18.8086	17.7406
ME	CPP0255	27	141.6241	17.4520	16.3023	Same as stowed coordinates		
ME	CPP0257	28	140.4630	17.4521	16.4874			
ME	CPP0250	29	139.3013	17.4523	16.6721			
ME	CPP0149	30	138.1400	17.4503	16.8602			
ME	CPP0243	31	135.8089	17.4429	17.2155			
ME	CPP0244	32	132.3327	17.4499	17.7225			
ME	CPP0234	33	127.6833	17.4424	18.3212			
ME	CPP0221	34	123.9717	17.4494	18.7515			
ME	CPP0209	35	120.2496	17.4456	19.1343			
ME	CPP0217	36	116.5354	17.4487	19.4543			
ME	CPP0230	37	112.5771	17.4527	19.6756			
ME	CPP0205	38	110.4971	17.4492	19.7153			
ME	CPP0706	39	109.1857	17.4314	19.6900			
ME	CPP0543	40	108.2761	17.4353	19.6494			
ME	CPP0522	41	107.1059	17.4370	19.5589			
ME	CPP0709	42	106.0935	17.4310	19.3738			
ME	CPP0535	43	105.3730	17.4380	19.0598			
ME	CPP0519	44	104.8193	17.4347	18.6682			
ME	CPP0714	45	104.5030	17.4370	18.3309			

* Bad pressure ports due to leakage or blockage.
** Exist only on the non-strake piece and not on the strake piece tested.
† Not available.

Table A1. Continued

Location	Data file ID	Tap ID	Stowed Coordinates x (inches)	Stowed Coordinates y (inches)	Stowed Coordinates z (inches)	Deployed Coordinates x (inches)	Deployed Coordinates y (inches)	Deployed Coordinates z (inches)
ME	CPP0555	46	104.395	17.756	17.474	Same as stowed coordinates		
ME	CPP0836	47	104.4015	17.4600	17.0351			
ME	CPP0855	48*	105.8468	17.4545	16.3770			
ME	CPP0851	49	108.175	17.448	15.59			
ME	CPP2002	50	114.2195	17.4329	14.2075			
ME	CPP2015	51	120.2565	17.4324	13.6174			
ME	CPP2003	52*	126.2907	17.4252	13.6838			
ME	CPP0657	53*	132.3338	17.4514	14.1352			
ME	CPP0341	54	139.3768	17.4499	14.8951			
ME	CPP0317	55	139.3804	17.4507	15.4251			
ME	CPP0335	56	140.7240	17.4499	16.2129			
ME	CPP0336	57	142.0680	17.4500	16.1711			
ME	CPP0328	58	142.4033	17.4509	16.1395			
Flap	CPP2106	59	146.6511	17.4606	15.3657	148.1794	18.4014	11.3511
Flap	CPP2120	60	146.3405	17.4521	15.4445	147.9783	18.3419	11.5935
Flap	CPP2107	61	145.7417	17.4537	15.5768	147.5776	18.2465	12.0478
Flap	CPP2116	62	145.1391	17.4526	15.6988	147.1679	18.1487	12.4957
Flap	CPP2113	63	144.2399	17.4504	15.8664	146.5480	18.0034	13.1524
Flap	CPP2227	64	143.5176	17.4495	15.9924	146.0449	17.8882	13.6732
Flap	CPP2234	65	142.4389	17.4567	16.1334	145.2648	17.7282	14.4144
Flap	CPP2205	66	141.4878	17.4722	16.1696	144.5240	17.6031	14.9989
Flap	CPP2218	67	140.9819	17.4424	16.1385	144.1026	17.5031	15.2638
Flap	CPP2208	68	140.6364	17.4518	16.0997	143.8022	17.4654	15.4351
Flap	CPP2224	69	140.3356	17.4491	16.0413	143.5269	17.4239	15.5630
Flap	CPP2235	70	140.0347	17.4450	15.9531	143.2338	17.3832	15.6669
Flap	CPP2212	71	139.6735	17.4542	15.7717	142.8360	17.3543	15.7333
Flap	CPP2215	72	139.495	17.452	15.578	142.5780	17.3416	15.6819
Flap	CPP2222	73	139.431	17.455	15.391	142.4152	17.3500	15.5700
Flap	CPP2122	74	139.5354	17.4474	15.0704	142.3085	17.3828	15.2518
Flap	CPP2145	75	140.0361	17.4512	14.9658	142.6468	17.4671	14.8774
Flap	CPP2105	76	141.2306	17.4591	15.0912	143.6771	17.6378	14.2841
Flap	CPP2139	77	142.4346	17.4539	15.2018	144.7071	17.7980	13.6715
Flap	CPP2121	78	143.6390	17.4617	15.2913	145.7239	17.9728	13.0437
Flap	CPP2119	79	144.8421	17.4529	15.3490	146.7219	18.1336	12.3888
Flap	CPP2112	80	145.6308	17.4511	15.3642	147.3625	18.2446	11.9419
Slat	CPP0723	81	108.3778	22.5990	19.4835	107.0044	23.7894	17.2921
ME	CPP0258	82	142.6219	22.6014	17.3675	Same as stowed coordinates		
ME	CPP0232	83	126.3502	22.5966	19.5109			
ME	CPP0542	84	109.2145	22.5831	19.4369			
Flap	CPP2126	85	147.567	22.604	16.537	149.2502	23.5151	12.5213
Flap	CPP2223	86	140.898	22.598	16.975	144.1729	22.5105	16.7496
Slat	CPP0745	87	113.9890	27.7500	20.2466	112.3393	29.0586	18.8330
Slat	CPP0750	88	113.5218	27.7499	20.1750	111.9426	29.0268	18.5781
Slat	CPP0733	89	112.9594	27.7501	20.0724	111.4716	28.9840	18.2568
Slat	CPP0722	90	112.3032	27.7499	19.9121	110.9384	28.9216	17.8469

* Bad pressure ports due to leakage or blockage.

Table A1. Continued.

Location	Data file ID	Tap ID	Stowed Coordinates			Deployed Coordinates		
			x (inches)	*y* (inches)	*z* (inches)	*x* (inches)	*y* (inches)	*z* (inches)
Slat	CPP0758	91	111.8199	27.7491	19.7459	110.5648	28.8608	17.5034
Slat	CPP0760	92	111.4971	27.7490	19.5802	110.3373	28.8043	17.2265
Slat	CPP0747	93	111.2990	27.7503	19.4238	110.2197	28.7547	17.0088
Slat	CPP0739	94	111.2167	27.7514	19.3193	110.1867	28.7229	16.8839
Slat	CPP0757	95	111.1711	27.7521	19.2323	110.1801	28.6967	16.7894
Slat	CPP0749	96	111.1469	27.7520	19.1533	110.1897	28.6726	16.7110
Slat	CPP0902	97	111.2018	27.7510	18.8965	110.3424	28.5967	16.5113
Slat	CPP0752	98	111.3614	27.7500	18.7650	110.5403	28.5603	16.4635
Slat	CPP0756	99	111.6266	27.7489	18.6187	110.8402	28.5217	16.4465
Slat	CPP0808	100	111.9781	27.7489	18.4535	111.2264	28.4805	16.4485
Slat	CPP0804	101	112.1288	27.7482	18.3916	111.3884	28.4648	16.4572
Slat	CPP0802	102	111.9355	27.7459	18.6600	111.1046	28.5380	16.6107
Slat	CPP0845	103	112.1648	27.7492	19.2250	111.0875	28.7139	17.1943
Slat	CPP0850	104	112.6483	27.7497	19.5964	111.3790	28.8354	17.7158
Slat	CPP0824	105	113.3215	27.7495	19.9609	111.8459	28.9584	18.3099
Slat	CPP0840	106	113.9269	27.7499	20.1754	112.3112	29.0360	18.7457
ME	CPP0262	107	143.6291	27.7514	18.3841	Same as stowed coordinates		
ME	CPP0428	108	142.6488	27.7519	18.5258			
ME	CPP0401	109	141.6770	27.7499	18.6664			
ME	CPP0263	110	140.6896	27.7523	18.8123			
ME	CPP0248	111	138.7354	27.7386	19.0900			
ME	CPP0226	112	135.7859	27.7409	19.4732			
ME	CPP0213	113	131.8643	27.7508	19.8995			
ME	CPP0229	114	128.7225	27.7454	20.1795			
ME	CPP0201	115	125.5913	27.7445	20.3993			
ME	CPP0202	116	122.4606	27.7514	20.5341			
ME	CPP0218	117	119.1293	27.7487	20.5574			
ME	CPP0237	118	117.3648	27.7501	20.5185			
ME	CPP0541	119	116.2743	27.7257	20.4614			
ME	CPP0562	120	115.4816	27.7334	20.4032			
ME	CPP0704	121	114.5075	27.7293	20.3053			
ME	CPP0708	122	113.6448	27.7262	20.0804			
ME	CPP0561	123	113.0469	27.7356	19.7978			
ME	CPP0559	124	112.5792	27.7329	19.4935			
ME	CPP0524	125	112.2997	27.7312	19.2395			
ME	CPP0558	126	112.05	27.78	18.679			
ME	CPP0839	127	112.2339	27.7499	18.3494			
ME	CPP0848	128	113.4499	27.7491	17.9432			
ME	CPP0828	129	115.4090	27.7494	17.4252			
ME	CPP2004	130	120.5032	27.7370	16.5098			
ME	CPP2001	131	125.5975	27.7296	16.1241			
ME	CPP2018	132	130.6942	27.7335	16.1732			
ME	CPP2016	133	135.7838	27.7429	16.5541			
ME	CPP0342	134	141.1270	27.7497	17.1562			
ME	CPP0348	135	141.1391	27.7487	17.4094			

Table A1. Continued.

Location	Data file ID	Tap ID	Stowed Coordinates			Deployed Coordinates		
			x (inches)	*y* (inches)	*z* (inches)	*x* (inches)	*y* (inches)	*z* (inches)
ME	CPP0347	136	142.5061	27.7495	18.3088	Same as stowed coordinates		
ME	CPP0345	137	143.8821	27.7498	18.2864			
ME	CPP0327	138	144.2261	27.7496	18.2626			
Flap	CPP2101	139	148.4862	27.7686	17.5864	150.2496	28.6597	13.5952
Flap	CPP2137	140	148.1712	27.7493	17.6624	150.0441	28.5891	13.8363
Flap	CPP2135	141	147.5626	27.7458	17.7829	149.6289	28.4882	14.2862
Flap	CPP2117	142	146.9549	27.7478	17.8905	149.2063	28.3939	14.7260
Flap	CPP2133	143	146.0376	27.7415	18.0343	148.5580	28.2437	15.3736
Flap	CPP2214	144	145.3140	27.7394	18.1407	148.0423	28.1287	15.8792
Flap	CPP2216	145	144.2262	27.7401	18.2513	147.2373	27.9634	16.6005
Flap	CPP2238	146	143.2490	27.7534	18.2424	146.4488	27.8359	17.1637
Flap	CPP2229	147	142.7579	27.7531	18.1924	146.0260	27.7686	17.4093
Flap	CPP2203	148	142.4050	27.7520	18.1327	145.7080	27.7211	17.5667
Flap	CPP2210	149	142.0828	27.7581	18.0565	145.4043	27.6866	17.6941
Flap	CPP2230	150	141.7828	27.7534	17.9571	145.1053	27.6464	17.7884
Flap	CPP2233	151	141.4293	27.7548	17.7766	144.7148	27.6108	17.8498
Flap	CPP2232	152	141.2425	27.7384	17.6010	144.4619	27.5814	17.8156
Flap	CPP2202	153	141.177	27.751	17.395	144.2860	27.6006	17.6909
Flap	CPP2118	154	141.2949	27.7571	17.2015	144.2647	27.6388	17.4685
Flap	CPP2111	155	141.7892	27.7592	17.2273	144.6756	27.7104	17.2019
Flap	CPP2123	156	143.0098	27.7543	17.3640	145.7344	27.8713	16.6005
Flap	CPP2115	157	144.2175	27.7596	17.4853	146.7730	28.0416	15.9959
Flap	CPP2132	158	145.4415	27.7601	17.5787	147.8084	28.2117	15.3587
Flap	CPP2103	159	146.6512	27.7576	17.6351	148.8105	28.3797	14.6998
Flap	CPP2138	160	147.4727	27.7585	17.6360	149.4686	28.4993	14.2229
Slat	CPP0742	161	116.2198	32.8991	20.3327	114.8674	34.0497	18.3916
ME	CPP0416	162	144.6357	32.8995	19.3437	Same as stowed coordinates		
ME	CPP0247	163	131.1120	32.8987	20.8009			
ME	CPP0507	164*	116.8723	32.9378	20.1371			
Flap	CPP2141	165	149.3993	32.9106	18.5423	151.1901	33.7885	14.5946
Flap	CPP2226	166	142.721	32.901	18.897	146.0559	32.7856	18.7612
ME	CPP0402	167	145.6074	38.0507	20.1818	Same as stowed coordinates		
ME	CPP0448	168	144.7821	38.0512	20.2891			
ME	CPP0407	169	143.9567	38.0513	20.3962			
ME	CPP0423	170	143.1309	38.0517	20.5011			
ME	CPP0240	171	141.4753	38.0452	20.6985			
ME	CPP0211	172	139.0007	38.0424	20.9484			
ME	CPP0204	173	135.7127	38.0463	21.1981			
ME	CPP0225	174	133.0680	38.0501	21.3359			
ME	CPP0216	175	130.4219	38.0499	21.4058			
ME	CPP0223	176	127.7850	38.0424	21.4006			
ME	CPP0214	177	124.9740	38.0468	21.3125			
ME	CPP0527	178	123.4741	38.0294	21.2044			
ME	CPP0711	179	122.7050	38.0296	21.1359			
ME	CPP0727	180	122.5663	38.0287	21.1225			

* Bad pressure ports due to leakage or blockage.

Table A1. Continued.

Location	Data file ID	Tap ID	Stowed Coordinates			Deployed Coordinates		
			x (inches)	*y* (inches)	*z* (inches)	*x* (inches)	*y* (inches)	*z* (inches)
ME	CPP0763	181	121.0922	38.0504	20.9428	Same as stowed coordinates		
ME	CPP0735	182	120.3630	38.0494	20.8123			
ME	CPP0744	183	119.8543	38.0501	20.6758			
ME	CPP0753	184	119.4490	38.0495	20.5415			
ME	CPP0755	185	119.0685	38.0611	20.2629			
ME	CPP0734	186	118.9798	38.0570	20.0408			
Flap	CPP2114	187	150.3127	38.0585	19.3975	152.0704	38.9311	15.5141
Flap	CPP2104	188	150.0045	38.0491	19.4925	151.8809	38.8698	15.7679
Flap	CPP2130	189	149.4017	38.0531	19.6305	151.4802	38.7757	16.2295
Flap	CPP2128	190	148.7964	38.0477	19.7388	151.0605	38.6743	16.6674
Flap	CPP2131	191	147.8998	38.0480	19.8747	150.4237	38.5343	17.2976
Flap	CPP2231	192	147.1783	38.0462	19.9730	149.9048	38.4205	17.7956
Flap	CPP2225	193*	146.0896	38.0457	20.0696	149.0908	38.2550	18.5060
Flap	CPP2236	194	145.1261	38.0608	20.0443	148.3034	38.1326	19.0484
Flap	CPP2239	195	144.6470	38.0571	19.9838	147.8841	38.0644	19.2782
Flap	CPP2204	196	144.2739	38.0667	19.9148	147.5437	38.0254	19.4414
Flap	CPP2213	197	143.9488	38.0439	19.8255	147.2319	37.9629	19.5557
Flap	CPP2201	198	143.6612	38.0455	19.7232	146.9407	37.9309	19.6414
Flap	CPP2219	199	143.3073	38.0529	19.5330	146.5437	37.9020	19.6962
Flap	CPP2221	200	143.143	38.05	19.355	146.3064	37.8894	19.6490
Flap	CPP2207	201	143.081	38.057	19.205	146.1670	37.8991	19.5662
Flap	CPP2127	202	143.1764	38.0469	18.9766	146.1081	37.9209	19.3265
Flap	CPP2109	203	143.6750	38.0492	19.0102	146.5271	37.9926	19.0637
Flap	CPP2110	204	144.8823	38.0515	19.1632	147.5844	38.1574	18.4842
Flap	CPP2125	205	146.0950	38.0535	19.3083	148.6414	38.3233	17.8952
Flap	CPP2136	206	147.2972	38.0578	19.4217	149.6710	38.4925	17.2873
Flap	CPP2124	207	148.4972	38.0563	19.4964	150.6761	38.6586	16.6488
Flap	CPP2134	208	149.2864	38.0456	19.4931	151.3067	38.7624	16.1856
Slat	CPP0737	209	124.0416	43.1718	21.1436	122.7273	44.3047	19.3666
ME	CPP0430	210	146.7997	43.1890	20.9480	Same as stowed coordinates		
ME	CPP0235	211	135.9558	43.1992	21.8343			
ME	CPP0556	212	124.5433	43.1736	20.9104			
ME	CPP0751	213*	123.7028	43.1674	20.2161			
Flap	CPP0608	214	151.3864	43.1830	20.1297	152.9853	44.1448	16.4825
Flap	CPP0130	215	144.8378	43.2105	20.5324	147.8714	42.9078	20.4022
Slat	CPP0759	216	129.5677	48.3245	21.8186	128.0179	49.5755	20.6977
Slat	CPP0754	217	129.1164	48.3238	21.7540	127.6310	49.5420	20.4589
Slat	CPP0761	218	128.5685	48.3230	21.6631	127.1663	49.4976	20.1580
Slat	CPP0748	219	127.9363	48.3195	21.5312	126.6405	49.4357	19.7882
Slat	CPP0740	220	127.5154	48.3360	21.4741	126.2801	49.4217	19.5632
Slat	CPP0729	221	127.1549	48.3324	21.2629	126.0337	49.3434	19.2349
Slat	CPP0730	222*	126.9669	48.3263	21.1396	125.9100	49.2945	19.0536
Slat	CPP0725	223	126.8901	48.3284	21.0574	125.8725	49.2692	18.9506
Slat	CPP0732	224	126.8504	48.3207	21.0042	125.8565	49.2445	18.8906
Slat	CPP0738	225	126.8215	48.3215	20.9198	125.8635	49.2186	18.8055

* Bad pressure ports due to leakage or blockage.

Table A1. Continued.

Location	Data file ID	Tap ID	Stowed Coordinates			Deployed Coordinates		
			x (inches)	*y* (inches)	*z* (inches)	*x* (inches)	*y* (inches)	*z* (inches)
Slat	CPP0731	226	126.8851	48.3267	20.7392	125.9934	49.1703	18.6733
Slat	CPP0728	227	127.0166	48.3160	20.6504	126.1475	49.1368	18.6528
Slat	CPP0827	228	127.3030	48.3135	20.5350	126.4544	49.1075	18.6697
Slat	CPP0820	229	127.6537	48.3204	20.4340	126.8153	49.0934	18.7224
Slat	CPP0852	230	127.8010	48.3213	20.3973	126.9644	49.0873	18.7501
Slat	CPP0835	231	127.6459	48.2775	20.5016	126.7773	49.0730	18.7903
Slat	CPP0834	232	127.7975	48.3274	20.9939	126.7264	49.2752	19.2640
Slat	CPP0856	233	128.2537	48.3359	21.2661	127.0366	49.3796	19.6825
Slat	CPP0801	234	128.9083	48.3289	21.5675	127.5150	49.4839	20.2113
Slat	CPP0819	235	129.4941	48.3269	21.7591	127.9744	49.5575	20.6156
ME	CPP0432	236	149.6646	48.3363	21.5377	Same as stowed coordinates		
ME	CPP0414	237	148.9816	48.3393	21.6219			
ME	CPP0408	238	148.3010	48.3409	21.7037			
ME	CPP0406	239	147.6169	48.3372	21.7830			
ME	CPP0431	240	146.1962	48.3496	21.9366			
ME	CPP0246	241	144.2166	48.3494	22.0968			
ME	CPP0206	242	141.4721	48.2769	22.2859			
ME	CPP0220	243	139.2558	48.2922	22.3416			
ME	CPP0208	244	137.0691	48.3089	22.3431			
ME	CPP0210	245	134.8917	48.2994	22.2855			
ME	CPP0222	246	132.6360	48.3494	22.1132			
ME	CPP0551	247	131.3865	48.3202	22.0091			
ME	CPP0719	248	130.6416	48.3337	21.9391			
ME	CPP0718	249	130.1001	48.3270	21.8780			
ME	CPP0533	250	129.4269	48.3229	21.7242			
ME	CPP0526	251	128.8199	48.3385	21.4928			
ME	CPP0523	252	128.3971	48.3221	21.2912			
ME	CPP0717	253	128.0658	48.3321	21.0855			
ME	CPP0538	254	127.8656	48.3044	20.9365			
ME	CPP0547	255	127.4362	48.0029	20.5251			
ME	CPP0701	256	127.9747	48.5473	20.4258			
ME	CPP0812	257	128.6788	48.3502	20.2254			
ME	CPP0803	258	130.0416	48.3502	20.0168			
ME	CPP2013	259	133.5746	48.3393	19.6633			
ME	CPP2009	260	137.1158	48.3509	19.5305			
ME	CPP2012	261	140.6612	48.3384	19.6208			
ME	CPP2017	262	144.2137	48.3346	19.9522			
ME	CPP0332	263	147.092	48.351	20.375			
ME	CPP0337	264	147.1543	48.4515	20.5503			
ME	CPP0340	265	148.3829	48.3407	21.4650			
ME	CPP0302	266	149.5502	48.3343	21.4835			
ME	CPP0306	267	150.0025	48.3457	21.4637			
Flap	CPP0612	268	154.0784	48.3794	20.8357	155.7462	49.2855	17.3184
Flap	CPP0603	269	153.7743	48.3322	20.9320	155.5520	49.1596	17.5429
Flap	CPP0609	270	153.1967	48.3329	21.0715	155.1608	49.0181	17.9672

Table A1. Continued.

Location	Data file ID	Tap ID	Stowed Coordinates			Deployed Coordinates		
			x (inches)	*y* (inches)	*z* (inches)	*x* (inches)	*y* (inches)	*z* (inches)
Flap	CPP0613	271	152.6241	48.3337	21.1732	154.7520	48.8887	18.3600
Flap	CPP0139	272	151.7673	48.3304	21.2939	154.1219	48.7003	18.9223
Flap	CPP0137	273	151.0737	48.3270	21.3795	153.6048	48.5506	19.3680
Flap	CPP0141	274	150.0444	48.3351	21.4605	152.8113	48.3545	19.9989
Flap	CPP0133	275	149.1119	48.3231	21.4311	152.0326	48.1891	20.4855
Flap	CPP0135	276	148.6430	48.3468	21.3739	151.6175	48.1464	20.7081
Flap	CPP0138	277	148.3151	48.3300	21.3114	151.3132	48.0918	20.8352
Flap	CPP0128	278	148.0616	48.3329	21.2477	151.0696	48.0692	20.9272
Flap	CPP0134	279	147.7506	48.3191	21.1440	150.7555	48.0326	21.0146
Flap	CPP0129	280	147.3916	48.3469	20.9481	150.3502	48.0540	21.0725
Flap	CPP0140	281	147.212	48.351	20.787	150.1108	48.0742	21.0501
Flap	CPP0131	282	147.163	48.347	20.641	149.9865	48.1051	20.9645
Flap	CPP0602	283	147.3142	48.3590	20.4187	149.9821	48.2086	20.7161
Flap	CPP0607	284	147.7359	48.3382	20.4607	150.3501	48.2503	20.5089
Flap	CPP0611	285	148.8615	48.3130	20.6264	151.3639	48.3741	20.0071
Flap	CPP0601	286	150.0542	48.3462	20.7863	152.4309	48.5663	19.4839
Flap	CPP0605	287	151.1757	48.3607	20.9077	153.4171	48.7398	18.9641
Flap	CPP0604	288	152.311	48.351	20.97	154.3797	48.9105	18.3835
Flap	CPP0610	289	153.46	48.349	20.92	155.2890	49.1240	17.7125
Slat	CPP0741	290	131.7855	53.4487	21.9138	130.5122	54.5462	20.1924
ME	CPP0261	291	152.5317	53.4936	22.1148	Same as stowed coordinates		
ME	CPP0228	292	142.6726	53.4675	22.7449			
ME	CPP0549	293	132.2691	53.4822	21.6752			
Flap	CPP0606	294*	156.7282	53.5049	21.4466	158.4156	54.3805	18.0808
Flap	CPP0136	295	150.6350	53.4785	21.7180	153.5962	53.2112	21.6315
Slat	CPP0726	296	135.7292	58.6238	22.3113	134.4689	59.7077	20.6346
ME	CPP0259	297*	155.4051	58.6407	22.6405	Same as stowed coordinates		
ME	CPP0231	298	146.0147	58.6279	23.1724			
ME	CPP0560	299	136.1474	58.6516	22.0641			
Flap	CPP0620	300	159.29	58.641	21.999	160.9798	59.4873	18.8507
Flap	CPP0104	301	153.5547	58.6304	22.2484	156.4404	58.4019	22.1931
Slat	CPP1028	302	141.1719	63.7823	22.9882	139.6832	64.9822	21.9318
Slat	CPP1048	303	140.7463	63.7712	22.9228	139.3191	64.9393	21.7057
Slat	CPP1049	304	140.2318	63.7750	22.8322	138.8852	64.9004	21.4173
Slat	CPP1045	305	139.6326	63.7743	22.7015	138.3893	64.8424	21.0611
Slat	CPP1015	306	139.1901	63.7712	22.5727	138.0356	64.7873	20.7709
Slat	CPP0915	307	138.8944	63.7746	22.4477	137.8151	64.7438	20.5416
Slat	CPP0913	308	138.7086	63.7710	22.3323	137.6905	64.6998	20.3673
Slat	CPP0914	309	138.6334	63.7789	22.2516	137.6545	64.6805	20.2645
Slat	CPP0917	310	138.5907	63.7749	22.1891	137.6397	64.6564	20.1942
Slat	CPP0910	311	138.5718	63.7769	22.1127	137.6528	64.6344	20.1197
Slat	CPP0746	312	138.6248	63.7742	21.9643	137.7595	64.5881	20.0134
Slat	CPP0806	313	138.7319	63.7650	21.8941	137.8841	64.5610	19.9987
Slat	CPP0863	314	139.0235	63.7861	21.7887	138.1942	64.5574	20.0195
Slat	CPP0817	315	139.3695	63.7790	21.6988	138.5451	64.5332	20.0840

* Bad pressure ports due to leakage or blockage.

Table A1. Continued.

Location	Data file ID	Tap ID	Stowed Coordinates			Deployed Coordinates		
			x (inches)	*y* (inches)	*z* (inches)	*x* (inches)	*y* (inches)	*z* (inches)
Slat	CPP0813	316	139.5151	63.7862	21.6700	138.6902	64.5355	20.1160
Slat	CPP0821	317	139.3306	63.7121	21.9012	138.4231	64.5302	20.2631
Slat	CPP0823	318	139.5094	63.7851	22.2034	138.4744	64.6971	20.5763
Slat	CPP0857	319	139.9431	63.7873	22.4636	138.7681	64.7912	20.9772
Slat	CPP0825	320	140.5641	63.7770	22.7472	139.2225	64.8860	21.4779
Slat	CPP0844	321	141.1139	63.7881	22.9272	139.6549	64.9674	21.8537
ME	CPP0251	322	158.2597	63.7988	23.1184	Same as stowed coordinates		
ME	CPP0252	323	157.6679	63.7950	23.1842			
ME	CPP0260	324	157.1678	63.8001	23.0465			
ME	CPP0253	325	156.5108	63.7895	23.3050			
ME	CPP0249	326	155.3358	63.7893	23.4106			
ME	CPP0207	327	153.5897	63.7978	23.5213			
ME	CPP0236	328	151.2492	63.7152	23.6300			
ME	CPP0212	329	149.3142	63.7535	23.6267			
ME	CPP0203	330	147.4501	63.7432	23.5740			
ME	CPP0227	331	145.6085	63.7873	23.4202			
ME	CPP0521	332	143.6231	63.7742	23.2652			
ME	CPP0548	333*	142.5804	63.7804	23.1556			
ME	CPP0545	334	141.9395	63.7763	23.0815			
ME	CPP0516	335	141.4642	63.7786	23.0047			
ME	CPP0513	336	140.8890	63.7639	22.8384			
ME	CPP0506	337	140.3786	63.7758	22.6289			
ME	CPP0501	338	140.0144	63.7721	22.4476			
ME	CPP0517	339	139.7344	63.7744	22.2707			
ME	CPP0546	340	139.5568	63.7798	22.1169			
ME	CPP0515	341	139.3994	63.7805	21.8407			
ME	CPP0544	342	139.5065	63.7895	21.6860			
ME	CPP0861	343	140.2517	63.8021	21.5496			
ME	CPP0842	344	141.4256	63.7969	21.4361			
ME	CPP2006	345	144.4547	63.7977	21.2487			
ME	CPP2005	346	147.5049	63.7936	21.2273			
ME	CPP2008	347	150.5351	63.7970	21.3749			
ME	CPP2007	348	153.5815	63.7912	21.7037			
ME	CPP0308	349	155.951	63.803	22.085			
ME	CPP0323	350	155.9886	63.8799	22.2217			
ME	CPP0338	351	157.0944	63.7898	23.2461			
ME	CPP0316	352	158.1524	63.7998	23.0691			
ME	CPP0339	353	158.5205	63.7882	23.0520			
Flap	CPP0614	354	162.0366	63.7848	22.5158	163.6746	64.6442	19.4944
Flap	CPP0619	355	161.7954	63.7897	22.6080	163.5310	64.5793	19.6991
Flap	CPP0618	356	161.2838	63.7947	22.7347	163.1864	64.4572	20.0788
Flap	CPP0615	357	160.7831	63.7873	22.8204	162.8268	64.3374	20.4170
Flap	CPP0627	358	160.0162	63.7875	22.9248	162.2608	64.1728	20.9186
Flap	CPP0115	359	159.411	63.789	22.985	161.8014	64.0507	21.2980
Flap	CPP0126	360	158.5233	63.7826	23.0499	161.1138	63.8704	21.8338

* Bad pressure ports due to leakage or blockage.

Table A1. Continued.

Location	Data file ID	Tap ID	Stowed Coordinates x (inches)	Stowed Coordinates y (inches)	Stowed Coordinates z (inches)	Deployed Coordinates x (inches)	Deployed Coordinates y (inches)	Deployed Coordinates z (inches)
Flap	CPP0124	361	157.7059	63.7245	23.0100	160.4217	63.6849	22.2333
Flap	CPP0106	362	157.2962	63.7386	22.9526	160.0545	63.6436	22.4199
Flap	CPP0122	363	157.0392	63.7164	22.9042	159.8161	63.5922	22.5168
Flap	CPP0101	364	156.8121	63.7211	22.8474	159.5980	63.5738	22.6001
Flap	CPP0105	365	156.5337	63.7514	22.7538	159.3177	63.5813	22.6925
Flap	CPP0102	366	156.2563	63.7426	22.6187	159.0130	63.5647	22.7392
Flap	CPP0125	367	156.0689	63.7320	22.4754	158.7771	63.5644	22.7296
Flap	CPP0108	368	156.009	63.805	22.301	158.6298	63.6741	22.6547
Flap	CPP0624	369	156.1146	63.7612	22.1090	158.6040	63.7083	22.4354
Flap	CPP0622	370	156.5107	63.7667	22.1681	158.9617	63.7651	22.2643
Flap	CPP0616	371	157.5092	63.7845	22.3301	159.8709	63.9083	21.8443
Flap	CPP0621	372	158.5186	63.8004	22.4768	160.7801	64.0560	21.4060
Flap	CPP0617	373	159.5276	63.7838	22.5923	161.6701	64.1824	20.9330
Flap	CPP0623	374	160.5413	63.7687	22.6523	162.5319	64.3275	20.4157
Flap	CPP0625	375*	161.5150	63.8031	22.6127	163.3051	64.5416	19.8615
Slat	CPP1022	376	143.5401	68.9139	23.0943	142.3113	69.9677	21.4948
ME	CPP0420	377	161.1274	68.9391	23.5580	Same as stowed coordinates		
ME	CPP0238	378	152.7118	68.8859	24.0010			
ME	CPP0510	379	143.8765	68.9295	22.8274			
Flap	CPP0626	380	164.6855	68.9235	22.9833	166.2610	69.7938	20.1527
Flap	CPP0118	381	159.4805	68.9393	23.1891	162.1302	68.8387	23.1791
Slat	CPP1042	382	147.4370	74.0713	23.4892	146.2246	75.1102	21.9208
ME	CPP0411	383	163.9888	74.0945	23.9851	Same as stowed coordinates		
ME	CPP0241	384	156.0772	74.0804	24.3088			
ME	CPP0710	385	147.7512	74.0670	23.2271			
Flap	CPP0631	386	167.3394	74.0716	23.4445	168.8482	74.9550	20.8066
Flap	CPP0127	387	162.4664	74.0908	23.6307	164.9773	74.0669	23.6365
Slat	CPP1038	388	152.7944	79.2364	24.1541	151.3663	80.3848	23.1712
Slat	CPP1025	389	152.3908	79.2231	24.0907	151.0213	80.3411	22.9563
Slat	CPP1009	390	151.9042	79.2276	24.0028	150.6119	80.3044	22.6814
Slat	CPP1010	391	151.3325	79.2223	23.8778	150.1384	80.2446	22.3427
Slat	CPP1014	392	150.9029	79.2275	23.7526	149.7959	80.1989	22.0584
Slat	CPP0904	393	150.6249	79.2300	23.6398	149.5867	80.1588	21.8471
Slat	CPP0909	394	150.4424	79.2184	23.5382	149.4589	80.1114	21.6884
Slat	CPP0903	395	150.3774	79.2189	23.4662	149.4280	80.0881	21.5995
Slat	CPP0912	396	150.3433	79.2223	23.4020	149.4225	80.0707	21.5290
Slat	CPP0916	397	150.3258	79.2219	23.3090	149.4432	80.0414	21.4414
Slat	CPP0907	398	150.3871	79.2228	23.2163	149.5358	80.0158	21.3857
Slat	CPP1043	399	150.4847	79.2236	23.1474	149.6522	79.9983	21.3653
Slat	CPP1032	400	150.7791	79.2155	23.0418	149.9621	79.9669	21.3956
Slat	CPP0805	401	151.0882	79.2212	22.9744	150.2716	79.9607	21.4609
Slat	CPP0862	402	151.2336	79.2353	22.9531	150.4142	79.9719	21.4974
Slat	CPP0628	403	151.0264	79.2078	23.2186	150.1175	80.0207	21.6514
Slat	CPP0847	404	151.2029	79.2290	23.4117	150.2046	80.1050	21.8842
Slat	CPP0810	405	151.6297	79.2374	23.6656	150.4951	80.2028	22.2750

* Bad pressure ports due to leakage or blockage.

Table A1. Continued.

Location	Data file ID	Tap ID	Stowed Coordinates			Deployed Coordinates		
			x (inches)	*y* (inches)	*z* (inches)	*x* (inches)	*y* (inches)	*z* (inches)
Slat	CPP0837	406	152.2081	79.2369	23.9215	150.9225	80.2973	22.7316
Slat	CPP0816	407	152.7410	79.2279	24.0978	151.3389	80.3580	23.1032
ME	CPP0418	408	166.8605	79.2446	24.4050	Same as stowed coordinates		
ME	CPP0404	409	166.3664	79.2502	24.4534			
ME	CPP0403	410	165.8809	79.2460	24.4959			
ME	CPP0413	411	165.3933	79.2433	24.5371			
ME	CPP0412	412	164.4156	79.2469	24.6059			
ME	CPP0219	413	162.9655	79.2442	24.6652			
ME	CPP0224	414	161.0087	79.2455	24.6857			
ME	CPP0239	415	159.4537	79.2425	24.6648			
ME	CPP0215	416	157.8817	79.2479	24.6120			
ME	CPP0245	417	156.3218	79.2394	24.5215			
ME	CPP0530	418	154.6409	79.2294	24.3753			
ME	CPP0502	419	153.7753	79.2203	24.2791			
ME	CPP0505	420	153.2450	79.2192	24.2080			
ME	CPP0540	421	152.8552	79.2216	24.1193			
ME	CPP0557	422*	152.3630	79.2271	23.9543			
ME	CPP0525	423	151.9356	79.2147	23.7761			
ME	CPP0528	424	151.6337	79.2240	23.6178			
ME	CPP0702	425	151.3985	79.2200	23.4671			
ME	CPP0503	426	151.2552	79.2274	23.3406			
ME	CPP0553	427	151.1209	79.2326	23.1096			
ME	CPP0705	428	151.2070	79.2493	22.9806			
ME	CPP0843	429	151.8329	79.2492	22.8655			
ME	CPP0858	430	152.8105	79.2491	22.7805			
ME	CPP0838	431	155.3500	79.2492	22.6863			
ME	CPP2010	432	157.8773	79.2404	22.7379			
ME	CPP2011	433	160.4079	79.2442	22.8931			
ME	CPP2014	434	162.9619	79.2396	23.1782			
ME	CPP0305	435	165.011	79.247	23.514			
ME	CPP0303	436	165.032	79.3093	23.6483			
ME	CPP0333	437	165.9388	79.2346	24.3310			
ME	CPP0329	438	166.7451	79.2391	24.3646			
ME	CPP0301	439	167.0993	79.2415	24.3560			
Flap	CPP0633	440	170.0235	79.2778	23.8976	171.4571	80.1784	21.4576
Flap	CPP0646	441	169.8098	79.2458	23.9765	171.3271	80.0877	21.6243
Flap	CPP0642	442	169.4031	79.2436	24.0818	171.0557	79.9834	21.9275
Flap	CPP0630	443	168.9827	79.2416	24.1576	170.7561	79.8857	22.2159
Flap	CPP0639	444	168.3606	79.2386	24.2414	170.2964	79.7494	22.6210
Flap	CPP0634	445	167.8639	79.2443	24.2967	169.9229	79.6516	22.9384
Flap	CPP0635	446	167.1091	79.2505	24.3385	169.3308	79.5132	23.3877
Flap	CPP0110	447	166.4492	79.2658	24.3019	168.7714	79.4232	23.7282
Flap	CPP0112	448	166.1143	79.2531	24.2517	168.4686	79.3677	23.8700
Flap	CPP0111	449	165.8917	79.2511	24.2048	168.2598	79.3408	23.9561
Flap	CPP0121	450	165.6730	79.2599	24.1432	168.0459	79.3291	24.0325

Table A1. Continued.

Location	Data file ID	Tap ID	Stowed Coordinates			Deployed Coordinates		
			x (inches)	*y* (inches)	*z* (inches)	*x* (inches)	*y* (inches)	*z* (inches)
Flap	CPP0119	451	165.4860	79.2422	24.0785	167.8554	79.2990	24.0801
Flap	CPP0116	452*	165.2116	79.2520	23.9264	167.5440	79.3053	24.1186
Flap	CPP0113	453	165.0990	79.2548	23.8125	167.3864	79.3220	24.0948
Flap	CPP0117	454	165.0485	79.2527	23.6715	167.2638	79.3530	24.0145
Flap	CPP0640	455	165.1442	79.2511	23.5482	167.2708	79.4047	23.8674
Flap	CPP0647	456	165.4377	79.2247	23.5910	167.5344	79.4185	23.7294
Flap	CPP0637	457	166.2809	79.2497	23.7303	168.3039	79.5480	23.3801
Flap	CPP0632	458	167.1231	79.2341	23.8523	169.0615	79.6443	23.0042
Flap	CPP0641	459	167.9452	79.2305	23.9539	169.7912	79.7544	22.6279
Flap	CPP0643	460	168.7661	79.2346	24.0119	170.4950	79.8844	22.2217
Flap	CPP0638	461	169.5754	79.2451	23.9771	171.1361	80.0459	21.7535
Slat	CPP1020	462	155.2349	84.3781	24.2780	154.0545	85.3874	22.7760
ME	CPP0322	463	172.6750	84.3728	24.3149	Same as stowed coordinates		
ME	CPP0443	464	170.3531	84.4155	24.7281			
ME	CPP0437	465	167.5768	84.4093	24.9685			
ME	CPP0233	466	162.8903	84.3978	25.0229			
ME	CPP0508	467	155.5809	84.3789	24.0433			
Slat	CPP1002	468	159.1443	89.5195	24.6814	157.9742	90.5176	23.2191
ME	CPP0351	469	175.3344	89.5585	24.7541	Same as stowed coordinates		
ME	CPP0627	470	173.1724	89.5407	25.1322			
ME	CPP0426	471	170.6093	89.5366	25.3510			
ME	CPP0447	472	166.2400	89.5349	25.3820			
ME	CPP0537	473	159.4519	89.5272	24.4449			
Slat	CPP1016	474	164.4355	94.6716	25.3350	163.0586	95.7745	24.4366
Slat	CPP1037	475	164.0416	94.6722	25.2734	162.7231	95.7449	24.2232
Slat	CPP1027	476	163.5678	94.6721	25.1910	162.3228	95.7059	23.9596
Slat	CPP1008	477	163.0405	94.6716	25.0800	161.8848	95.6562	23.6496
Slat	CPP1046	478	162.6427	94.6694	24.9721	161.5638	95.6097	23.3953
Slat	CPP1024	479	162.3738	94.6668	24.8720	161.3574	95.5688	23.2002
Slat	CPP0911	480	162.2144	94.6730	24.7829	161.2475	95.5429	23.0565
Slat	CPP0905	481	162.1442	94.6733	24.7222	161.2074	95.5226	22.9754
Slat	CPP0906	482	162.1056	94.6706	24.6729	161.1913	95.5039	22.9178
Slat	CPP0908	483	162.0861	94.6745	24.6025	161.2017	95.4855	22.8477
Slat	CPP0736	484	162.1383	94.6752	24.4999	161.2899	95.4564	22.7798
Slat	CPP1029	485	162.2505	94.6872	24.4481	161.4140	95.4553	22.7769
Slat	CPP1040	486	162.5228	94.6722	24.3597	161.6962	95.4219	22.8151
Slat	CPP0807	487	162.8276	94.6790	24.3045	161.9971	95.4204	22.8890
Slat	CPP0831	488	162.9290	94.6772	24.2901	162.0952	95.4172	22.9181
Slat	CPP0814	489	162.7436	94.6505	24.5204	161.8323	95.4567	23.0503
Slat	CPP0832	490	162.9181	94.6814	24.6827	161.9308	95.5407	23.2528
Slat	CPP0811	491	163.3195	94.6856	24.9045	162.2104	95.6241	23.6066
Slat	CPP0629	492	163.8751	94.6886	25.1283	162.6299	95.7113	24.0251
Slat	CPP0818	493	164.3665	94.6868	25.2801	163.0187	95.7702	24.3566
ME	CPP0355	494	177.9936	94.7057	25.1968	Same as stowed coordinates		
ME	CPP0321	495	177.3752	94.6789	25.3558			

*   Bad pressure ports due to leakage or blockage.

Table A1. Continued.

Location	Data file ID	Tap ID	Stowed Coordinates			Deployed Coordinates		
			x (inches)	*y* (inches)	*z* (inches)	*x* (inches)	*y* (inches)	*z* (inches)
ME	CPP0363	496	176.7309	94.6987	25.4557	Same as stowed coordinates		
ME	CPP0318	497	175.9918	94.6869	25.5373			
ME	CPP0446	498	174.8445	94.6880	25.6479			
ME	CPP0405	499	173.6288	94.6843	25.7358			
ME	CPP0422	500	172.4390	94.6896	25.7801			
ME	CPP0421	501	170.8569	94.6943	25.7838			
ME	CPP0442	502	169.5783	94.6925	25.7519			
ME	CPP0438	503	168.3155	94.6859	25.6930			
ME	CPP0439	504	167.0549	94.6899	25.6082			
ME	CPP0529	505	166.1299	94.6842	25.5311			
ME	CPP0504	506	165.3148	94.6845	25.4421			
ME	CPP0536	507	164.8058	94.6811	25.3730			
ME	CPP0712	508	164.4573	94.6849	25.2902			
ME	CPP0511	509*	163.9924	94.6765	25.1418			
ME	CPP0509	510	163.5922	94.6743	24.9837			
ME	CPP0520	511	163.2992	94.6840	24.8393			
ME	CPP0518	512	163.0999	94.6719	24.7251			
ME	CPP0539	513	162.7174	94.3838	24.5729			
ME	CPP0720	514	162.7544	94.5815	24.3898			
ME	CPP0721	515	162.0863	94.6710	24.6295			
ME	CPP0849	516	163.5058	94.6979	24.2257			
ME	CPP0853	517	164.4177	94.6988	24.1652			
ME	CPP0833	518	166.2855	94.6883	24.1386			
ME	CPP0325	519	168.3277	94.6993	24.1934			
ME	CPP0330	520	170.3894	94.6977	24.3639			
ME	CPP0344	521	171.2581	94.6987	24.4666			
ME	CPP0315	522	172.4486	94.6988	24.6346			
ME	CPP0334	523	175.6183	94.6989	25.1482			
ME	CPP0360	524	176.6483	94.7010	25.2599			
ME	CPP0311	525	177.2670	94.7362	25.2962			
ME	CPP0310	526	177.7526	94.6925	25.2530			
Slat	CPP1033	527	166.9489	99.8187	25.4750	165.8076	100.7893	24.0834
ME	CPP0304	528*	180.6573	99.8640	25.6364	Same as stowed coordinates		
ME	CPP0320	529	178.8220	99.8405	25.9414			
ME	CPP0425	530	176.6507	99.8373	26.1217			
ME	CPP0419	531	172.9343	99.8463	26.1309			
ME	CPP0715	532	167.1695	99.8342	25.2378			
Slat	CPP1050	533	172.1826	104.9702	26.1334	170.8375	106.0454	25.2818
Slat	CPP1001	534	171.8118	104.9689	26.0722	170.5228	106.0147	25.0787
Slat	CPP1047	535	171.3631	104.9747	25.9889	170.1463	105.9818	24.8228
Slat	CPP1031	536	170.8538	104.9698	25.8801	169.7235	105.9292	24.5233
Slat	CPP1018	537	170.4587	104.9730	25.7749	169.4044	105.8886	24.2709
Slat	CPP1017	538	170.1999	104.9809	25.6801	169.2061	105.8597	24.0815
Slat	CPP1036	539	170.0418	104.9792	25.6056	169.0909	105.8308	23.9532
Slat	CPP1003	540	169.9725	104.9696	25.5562	169.0462	105.8045	23.8851

* Bad pressure ports due to leakage or blockage.

Table A1. Continued.

Location	Data file ID	Tap ID	Stowed Coordinates			Deployed Coordinates		
			x (inches)	*y* (inches)	*z* (inches)	*x* (inches)	*y* (inches)	*z* (inches)
Slat	CPP1004	541	169.9431	104.9741	25.5165	169.0354	105.7959	23.8375
Slat	CPP1007	542	169.9232	104.9784	25.4247	169.0539	105.7713	23.7486
Slat	CPP0762	543	169.9606	104.9657	25.3723	169.1075	105.7443	23.7220
Slat	CPP1005	544	170.1016	104.9698	25.3117	169.2606	105.7338	23.7255
Slat	CPP1044	545	170.3441	104.9758	25.2508	169.5067	105.7280	23.7694
Slat	CPP0815	546	171.1110	104.9850	25.7350	170.0172	105.9068	24.4975
Slat	CPP0826	547	171.6404	104.9866	25.9323	170.4231	105.9839	24.8828
Slat	CPP0859	548	172.1175	104.9818	26.0745	170.8024	106.0366	25.2010
ME	CPP0331	549	183.3129	105.0082	26.0920	Same as stowed coordinates		
ME	CPP0319	550	182.7855	104.9830	26.2067			
ME	CPP0312	551	182.2353	104.9784	26.2783			
ME	CPP0313	552	181.6461	104.9945	26.3446			
ME	CPP0349	553	180.6385	105.0233	26.4383			
ME	CPP0445	554	179.6669	104.9966	26.5002			
ME	CPP0429	555	178.6676	104.9921	26.5386			
ME	CPP0415	556	177.3542	104.9889	26.5404			
ME	CPP0434	557	176.2856	104.9910	26.5030			
ME	CPP0417	558	175.2337	104.9982	26.4421			
ME	CPP0707	559	174.1616	104.9845	26.3523			
ME	CPP0554	560	173.4032	104.9841	26.2724			
ME	CPP0563	561	172.7200	104.9825	26.1877			
ME	CPP0703	562	172.2962	104.9927	26.0987			
ME	CPP0713	563	172.0039	104.9829	26.0159			
ME	CPP0532	564	171.6066	104.9749	25.8827			
ME	CPP0550	565	171.2812	104.9737	25.7564			
ME	CPP0531	566	171.0426	104.9769	25.6455			
ME	CPP0512	567	170.8574	104.9801	25.5349			
ME	CPP0534	568	170.7438	104.9833	25.4467			
ME	CPP0552	569	170.6459	104.9847	25.2959			
		570	Not available					
ME	CPP0860	571	171.198	104.99	25.141			
ME	CPP0830	572	171.959	104.992	25.107			
ME	CPP0854	573	173.503	104.989	25.101			
ME	CPP0343	574	175.2267	104.9991	25.1910			
ME	CPP0324	575	176.9557	104.9853	25.3495			
ME	CPP0314	576	178.6687	104.9901	25.5909			
ME	CPP0326	577	179.8738	105.0215	25.8030			
ME	CPP0358	578	181.3111	105.0192	26.0214			
ME	CPP0352	579	182.1823	104.9894	26.1155			
ME	CPP0309	580	182.6602	104.9965	26.1354			
ME	CPP0361	581	183.0201	104.9839	26.1232			
Slat	CPP1006	582	174.7484	110.1282	26.2623	173.6397	111.0687	24.9371
ME	CPP0350	583	185.9568	110.1722	26.5816	Same as stowed coordinates		
ME	CPP0307	584	184.4675	110.1418	26.7329			
ME	CPP0435	585	182.6902	110.1466	26.8431			

Table A1. Concluded.

Location	Data file ID	Tap ID	Stowed Coordinates			Deployed Coordinates		
			x (inches)	*y* (inches)	*z* (inches)	*x* (inches)	*y* (inches)	*z* (inches)
ME	CPP0433	586	179.6336	110.1464	26.8337	Same as stowed coordinates		
ME	CPP0716	587	174.8920	110.1194	26.0332			
ME	CPP0440	588*	188.659	115.302	27.0463			
ME	CPP0441	589	187.281	115.299	27.076			
ME	CPP0424	590	185.664	115.298	27.107			
ME	CPP0444	591	182.887	115.299	27.062			
ME	CPP0436	592	178.322	115.301	26.537			
ME	CPP0901	593	177.778	115.296	26.307			
Flap	CPP2217	594	141.3907	12.2348	14.9974	144.1146	12.5152	13.3377
Flap	CPP2211	595	142.8039	12.2514	14.7910	145.1219	12.7522	12.3532
Flap	CPP2209	596	144.2368	12.2861	14.4969	146.0914	13.0167	11.2897
Flap	CPP2228	597	141.3864	11.9835	14.3570	143.7476	12.3171	12.7907
Flap	CPP2206	598	142.8149	12.0087	14.3116	144.8623	12.5520	11.9272
Flap	CPP2220	599	144.2441	12.0349	14.2152	145.9471	12.7921	11.0228
Flap	CPP2143	600	141.4181	12.2628	13.8760	143.4671	12.6349	12.4292
Flap	CPP2144	601	142.8498	12.2715	13.9956	144.6838	12.8411	11.6934
Flap	CPP2142	602	144.2810	12.2776	14.0783	145.8782	13.0476	10.9280
Flap	CPP0123	603	168.2056	82.7328	24.5440	170.4490	82.9139	24.1334
Flap	CPP0114	604	169.7129	82.9296	24.6016	171.7188	83.3449	23.4152
Flap	CPP0107	605	171.1395	83.0445	24.4222	172.7837	83.755	22.5329
Flap	CPP0120	606	168.2029	83.0040	24.3091	170.3195	83.2377	24.0489
Flap	CPP0103	607	169.7063	83.1914	24.4322	171.6236	83.6397	23.3795
Flap	CPP0109	608	171.2175	83.3914	24.4255	172.8597	84.0934	22.6113
Flap	CPP0644	609	168.2340	82.8059	24.0230	170.1740	83.1418	23.7461
Flap	CPP0636	610	169.7189	82.9564	24.2408	171.5165	83.4779	23.1464
Flap	CPP0645	611	171.2292	83.0964	24.3276	172.8039	83.8475	22.4293

* Bad pressure ports due to leakage or blockage.

Table A2. WUSS filler piece (for the full-span slat without nacelle/pylon).

Location	Data file ID	Tap ID	Stowed Coordinates			Deployed Coordinates		
			x (inches)	*y* (inches)	*z* (inches)	*x* (inches)	*y* (inches)	*z* (inches)
ME	CPP0727	180	122.3237	38.0458	21.0895	Same as stowed coordinates		
ME	CPP0763	181	121.5472	38.0579	20.8929			
ME	CPP0735	182	120.9405	38.0566	20.6360			
ME	CPP0744	183	120.4944	38.0532	20.3912			
ME	CPP0753	184	120.1790	38.0508	20.1678			
ME	CPP0755	185	119.9098	38.0500	19.8224			

Table A3. CRM-HL Pressure Tap Coordinates on Fuselage.

Data file ID	Tap ID	x (inches)	y (inches)	z (inches)
CPP1935	801	23.6144	6.9834	25.6164
CPP1934	802	23.6159	7.7770	22.9953
CPP1936	803	23.6189	6.9686	16.4741
CPP1933	804*	44.5985	7.0039	31.8566
CPP1937	805	44.6054	11.9910	22.9942
CPP1928	806*	44.5998	7.0011	12.1401
CPP1930	807	63.3022	7.0071	32.1335
CPP1931	808	63.3000	12.1679	23.0000
CPP1938	809	63.3005	7.0052	12.1141
CPP1940	810	93.0032	7.0088	32.1228
CPP1055	811	92.9894	12.2102	23.0116
CPP1929	812	92.9882	7.0034	10.4211
CPP1932	813	99.7004	7.0263	32.1395
CPP1054	814	99.6951	11.5956	26.0091
CPP1056	815	99.6928	12.1991	23.0029
CPP0462	816	99.6964	12.0998	19.9974
CPP1939	817	99.6809	11.0694	10.9564
CPP1927	818	99.6954	7.0003	9.2170
CPP1926	819	106.4071	7.0306	32.1432
CPP1061	820	106.4106	11.6076	26.0267
CPP1062	821	106.4049	12.2145	23.0223
CPP1063	822*	106.3990	12.0770	19.9967
CPP1921	823	106.3602	11.8235	10.9009
CPP1923	824	106.3792	6.9844	9.0148
CPP1949	825	121.2476	7.0165	32.1451
CPP1057	826	121.2490	12.1873	23.0041
CPP1922	827	121.2418	6.9999	9.0264
CPP0461	828	132.4962	7.0140	32.1326
CPP1060	829	132.5017	11.5843	26.0144
CPP1059	830	132.4993	12.1749	23.0003
CPP1058	831	132.4972	12.0305	20.0004
CPP1920	832	132.4834	11.7928	10.9380

Data file ID	Tap ID	x (inches)	y (inches)	z (inches)
CPP1924	833	132.4825	6.9923	9.0288
CPP1902	834	142.4950	7.0051	32.1347
CPP1912	835	142.5000	11.5589	25.9981
CPP1052	836	142.5007	12.1556	22.9982
CPP1051	837	142.5014	11.9980	20.0016
CPP1916	838	142.5024	11.8456	17.9947
CPP1053	839*	142.4857	11.4467	10.9334
CPP1925	840	142.4937	6.9568	9.0448
CPP1917	841	149.4970	7.0031	32.1127
CPP1906	842	149.4949	11.5737	26.0050
CPP1905	843	149.5028	12.1544	22.9972
CPP1904	844	149.5003	11.9997	20.0029
CPP1915	845	149.5044	11.9118	17.9962
CPP1908	846	149.5041	11.8693	14.0030
CPP1914	847	149.4997	10.5960	11.0105
CPP1909	848	149.5000	6.9863	9.2636
CPP1907	849	155.9282	6.9131	32.1536
CPP1913	850	155.9084	12.1436	22.9697
CPP1903	851	155.9286	11.4584	18.0249
CPP1910	852	155.9422	11.1256	13.9812
CPP1911	853	156.5016	6.9910	10.0130
CPP1918	854	185.4998	6.9979	32.0818
CPP1919	855	185.5158	12.0956	22.9829
CPP1901	856	185.5005	7.0004	12.1435

* Bad pressure ports due to leakage or blockage.

Table A4. CRM-HL Pressure Tap Coordinates on Nacelle/Pylon.

Data file ID	Tap ID	*x* (inches)	*y* (inches)	*z* (inches)
CPP1717	701	109.2734	36.9210	17.5800
CPP1719	702	109.2671	37.8850	18.4379
CPP1720	703	109.2055	39.1006	17.8244
CPP1744	704	99.9534	31.4993	11.8501
CPP1714	705	99.9631	32.8514	14.3588
CPP1733	706	99.9012	35.0511	16.1579
CPP1734	707	99.8458	37.7852	16.9982
CPP1743	708	99.7360	40.5749	16.7614
CPP1736	709	99.5987	43.1238	15.4704
CPP1737	710	99.4717	44.9971	13.3342
CPP1751	711†	106.8884	32.3704	8.9618
CPP1754	712†	106.9715	33.7346	13.7125
CPP1741	713†	106.6241	42.8616	14.7085
CPP1763	714†	106.4451	45.2210	10.3027
CPP1756	715†	106.3884	43.7071	5.6230
CPP1750	716†	106.5055	39.4364	3.3629
CPP1760	717†	106.6914	34.8013	4.7000
CPP1725	718	97.4939	31.9500	9.1497
CPP1715	719	97.6964	31.6932	9.1269
CPP1705	720	98.5318	31.4122	9.0710
CPP1732	721	99.9417	31.1652	9.0133
CPP1724	722	101.8312	30.9957	8.9291
CPP1757	723	104.0958	30.9181	8.8502
CPP1761	724	106.6374	30.9590	8.8040
CPP1758	725	109.2931	31.1362	8.7454
CPP1712	726	97.0143	37.8082	16.0370
CPP1710	727	97.3675	37.7705	16.3466
CPP1711	728	98.7128	37.7686	16.7713
CPP1742	729	100.7727	37.7991	17.1423
CPP1752	730	103.1242	37.8636	17.3843
CPP1735	731	97.0357	44.9569	10.5198
CPP1709	732	97.2278	45.2211	10.5467
CPP1730	733	98.0403	45.5616	10.5610
CPP1738	734	99.4264	45.9113	10.5600
CPP1722	735	101.2955	46.2214	10.5812
CPP1740	736	103.5440	46.4598	10.4934
CPP1755	737	106.0754	46.6071	10.4522
CPP1747	738	108.7654	46.6337	10.3785
CPP1728	739	97.5611	39.1967	2.9762
CPP1721	740	97.7371	39.2116	2.7314
CPP1723	741	98.5321	39.2798	2.4416
CPP1739	742	99.8713	39.3472	2.1898
CPP1716	743	101.6735	39.4327	1.9882
CPP1759	744	103.8265	39.4937	1.8570
CPP1748	745	106.2608	39.5999	1.8106
CPP1746	746	108.8149	39.6964	1.8561
CPP1708	747†	97.7527	32.3896	9.1906
CPP1706	748†	99.3125	32.7324	9.1873
CPP1729	749†	101.7329	32.6135	9.1164
CPP1762	750†	104.5514	32.4479	9.0263
CPP1701	751†	97.3242	37.8403	15.5212
CPP1703	752†	98.9930	37.9195	15.3924
CPP1707	753†	101.5170	37.9770	15.7413
CPP1753	754†	104.4984	38.0438	16.0299
CPP1727	755†	97.3150	44.5202	10.5118
CPP1702	756†	98.9055	44.2960	10.4291
CPP1731	757†	101.2798	44.5971	10.3774
CPP1745	758†	104.0827	44.9620	10.3524
CPP1704	759†	97.8222	39.1661	3.3871
CPP1713	760†	99.2508	39.1341	3.7841
CPP1726	761†	101.5151	39.2278	3.7860
CPP1749	762†	104.1611	39.3411	3.5706
CPP1718	763	103.2594	37.8437	17.4051

† Nacelle internal pressure ports.

Appendix B.

Aerodynamic Data Tables with Wall Correction (Runs 200 to 227)

Table B1. Aerodynamic Data Summary for Run 200 with TWICS.

Run No. (Configuration)	α (deg)	q_∞ (psf)	M_∞	Re (x 10^6)	C_L	C_m	C_D	L/D
200 (CRM-HL)	-3.76	58.29	0.2010	1.417	0.5235	-0.3166	0.1066	4.909
	0.46	58.29	0.2010	1.415	1.0863	-0.3881	0.1136	9.567
	2.61	57.73	0.2000	1.408	1.3044	-0.3854	0.1308	9.976
	4.69	57.72	0.2000	1.406	1.5069	-0.3778	0.1526	9.877
	6.77	58.03	0.2005	1.407	1.6906	-0.3644	0.1762	9.598
	7.81	58.24	0.2009	1.409	1.7885	-0.3594	0.1911	9.359
	8.87	58.16	0.2007	1.405	1.8818	-0.3555	0.2057	9.147
	9.90	58.25	0.2009	1.406	1.9693	-0.3511	0.2204	8.935
	10.93	58.26	0.2009	1.406	2.0504	-0.3441	0.2357	8.698
	11.96	58.67	0.2016	1.409	2.1258	-0.3359	0.2502	8.497
	13.01	57.96	0.2004	1.400	2.1919	-0.3254	0.2647	8.279
	14.02	58.37	0.2011	1.405	2.2356	-0.3119	0.2759	8.102
	15.03	58.35	0.2011	1.405	2.2656	-0.2962	0.2860	7.920
	16.06	58.28	0.2009	1.404	2.3062	-0.2826	0.2989	7.716
	16.56	58.23	0.2009	1.403	2.3313	-0.2767	0.3052	7.638
	17.10	58.29	0.2010	1.402	2.3716	-0.2702	0.3133	7.570
	17.58	58.28	0.2009	1.402	2.3865	-0.2644	0.3193	7.475
	18.12	58.54	0.2014	1.404	2.3949	-0.2578	0.3387	7.070
	18.60	58.40	0.2012	1.402	2.3853	-0.2486	0.3428	6.957
	19.08	58.41	0.2012	1.401	2.3386	-0.2502	0.3477	6.725
	19.54	58.37	0.2011	1.400	2.2678	-0.2883	0.3729	6.082
	20.04	58.34	0.2010	1.399	2.2613	-0.2896	0.3893	5.809

Table B2. Aerodynamic Data Summary for Run 201 with TWICS.

Run No. (Configuration)	α (deg)	q_∞ (psf)	M_∞	*Re*/ft (x 10^6)	C_L	C_m	C_D	*L/D*
201 (CRM-HL – increasing α)	-3.76	58.34	0.2010	1.406	0.5182	-0.3145	0.1064	4.869
	-3.28	58.29	0.2010	1.402	0.5902	-0.3228	0.1043	5.660
	-2.66	58.17	0.2007	1.400	0.6914	-0.3408	0.1030	6.714
	-2.16	58.18	0.2007	1.398	0.7663	-0.3535	0.1034	7.411
	-1.69	58.17	0.2007	1.397	0.8249	-0.3626	0.1042	7.914
	-1.13	58.29	0.2010	1.399	0.8960	-0.3715	0.1056	8.482
	-0.57	58.12	0.2006	1.396	0.9826	-0.3899	0.1075	9.137
	-0.07	58.22	0.2008	1.397	1.0359	-0.3905	0.1100	9.421
	0.55	58.24	0.2009	1.396	1.0953	-0.3884	0.1139	9.618
	1.02	58.14	0.2007	1.394	1.1464	-0.3879	0.1170	9.802
	1.53	58.40	0.2011	1.397	1.1994	-0.3880	0.1209	9.923
	2.07	58.13	0.2007	1.393	1.2526	-0.3877	0.1253	9.995
	2.59	58.27	0.2009	1.395	1.3046	-0.3866	0.1303	10.008
	3.10	57.69	0.1999	1.387	1.3537	-0.3843	0.1348	10.039
	3.64	58.19	0.2008	1.393	1.4035	-0.3820	0.1396	10.052
	4.17	58.51	0.2013	1.396	1.4526	-0.3803	0.1458	9.964
	4.67	58.18	0.2008	1.393	1.4986	-0.3777	0.1507	9.944
	6.77	58.05	0.2005	1.390	1.6900	-0.3648	0.1754	9.635
	7.81	58.00	0.2004	1.389	1.7842	-0.3595	0.1898	9.403
	8.86	58.44	0.2012	1.393	1.8774	-0.3554	0.2048	9.167
	9.89	58.38	0.2011	1.393	1.9660	-0.3503	0.2196	8.951
	10.93	58.06	0.2005	1.389	2.0484	-0.3434	0.2349	8.719
	11.96	58.27	0.2009	1.391	2.1239	-0.3361	0.2496	8.510
	12.99	58.37	0.2011	1.392	2.1897	-0.3257	0.2644	8.281
	14.02	58.49	0.2013	1.394	2.2366	-0.3120	0.2756	8.115
	15.02	58.41	0.2012	1.393	2.2648	-0.2972	0.2855	7.933
	16.04	58.40	0.2011	1.393	2.2984	-0.2826	0.2974	7.729
	16.56	58.32	0.2010	1.391	2.3351	-0.2766	0.3049	7.659
	17.08	58.42	0.2012	1.392	2.3697	-0.2705	0.3123	7.588
	17.61	58.46	0.2013	1.392	2.4008	-0.2671	0.3334	7.201
	18.10	58.25	0.2009	1.389	2.3947	-0.2588	0.3379	7.086
	18.61	58.40	0.2011	1.391	2.3783	-0.2487	0.3418	6.958
	19.06	58.61	0.2015	1.393	2.3351	-0.2504	0.3465	6.739
	19.57	58.62	0.2015	1.393	2.2703	-0.2890	0.3733	6.081
	20.04	58.65	0.2016	1.393	2.2627	-0.2900	0.3896	5.808
	20.56	58.67	0.2016	1.393	2.2675	-0.2806	0.4040	5.612
	21.05	58.66	0.2016	1.392	2.2790	-0.2829	0.4203	5.422
	21.54	58.64	0.2016	1.391	2.2748	-0.2681	0.4297	5.294

Table B3. Aerodynamic Data Summary for Run 202 with TWICS.

Run No. (Configuration)	α (deg)	q_∞ (psf)	M_∞	Re (x 10^6)	C_L	C_m	C_D	L/D
202 (CRM-HL – decreasing α)	21.54	58.85	0.2019	1.393	2.2719	-0.2655	0.4296	5.289
	21.04	58.79	0.2018	1.392	2.2794	-0.2873	0.4212	5.411
	20.54	58.80	0.2019	1.391	2.2691	-0.2851	0.4046	5.608
	20.04	58.76	0.2018	1.390	2.2625	-0.2866	0.3879	5.832
	19.52	58.68	0.2017	1.390	2.2696	-0.2905	0.3729	6.087
	19.06	58.45	0.2012	1.387	2.3354	-0.2500	0.3467	6.735
	18.57	58.61	0.2015	1.388	2.3801	-0.2491	0.3414	6.972
	18.08	58.14	0.2007	1.383	2.3946	-0.2588	0.3378	7.088
	17.59	58.58	0.2015	1.387	2.4035	-0.2676	0.3333	7.211
	17.07	58.50	0.2013	1.387	2.3838	-0.2735	0.3256	7.322
	16.57	58.42	0.2012	1.386	2.3546	-0.2775	0.3174	7.418
	16.05	58.34	0.2010	1.385	2.3189	-0.2832	0.3085	7.516
	15.03	58.40	0.2012	1.385	2.2703	-0.2961	0.2936	7.732
	14.00	58.40	0.2011	1.385	2.2258	-0.3107	0.2800	7.950
	12.98	58.17	0.2007	1.383	2.1750	-0.3241	0.2662	8.170
	11.97	58.32	0.2010	1.384	2.1118	-0.3342	0.2522	8.374
	10.93	58.47	0.2013	1.386	2.0379	-0.3431	0.2361	8.633
	9.85	58.07	0.2006	1.381	1.9583	-0.3498	0.2195	8.923
	8.84	58.41	0.2012	1.384	1.8755	-0.3555	0.2045	9.169
	7.81	58.24	0.2009	1.382	1.7826	-0.3588	0.1898	9.392
	6.75	58.21	0.2008	1.382	1.6869	-0.3646	0.1748	9.653
	4.65	58.45	0.2012	1.384	1.4977	-0.3777	0.1503	9.963
	4.15	57.83	0.2001	1.377	1.4487	-0.3800	0.1447	10.015
	3.61	58.55	0.2014	1.386	1.3883	-0.3814	0.1382	10.048
	3.12	58.36	0.2011	1.383	1.3462	-0.3838	0.1338	10.065
	2.58	58.50	0.2013	1.385	1.2942	-0.3859	0.1292	10.019
	2.07	58.29	0.2009	1.382	1.2481	-0.3877	0.1246	10.013
	1.53	58.30	0.2010	1.383	1.1944	-0.3881	0.1204	9.917
	1.02	58.11	0.2006	1.381	1.1370	-0.3874	0.1163	9.774
	0.52	58.41	0.2012	1.384	1.0857	-0.3888	0.1133	9.586
	-0.11	58.52	0.2014	1.385	1.0271	-0.3905	0.1092	9.407
	-0.62	58.25	0.2009	1.382	0.9648	-0.3881	0.1071	9.010
	-1.13	58.21	0.2008	1.382	0.8886	-0.3713	0.1054	8.430
	-1.65	58.38	0.2011	1.384	0.8253	-0.3631	0.1038	7.950
	-2.19	58.37	0.2011	1.383	0.7595	-0.3523	0.1034	7.345
	-2.71	58.37	0.2011	1.383	0.6772	-0.3378	0.1033	6.556
	-3.28	58.33	0.2010	1.382	0.5884	-0.3226	0.1043	5.643
	-3.78	58.36	0.2011	1.382	0.5139	-0.3147	0.1063	4.832

Table B4. Aerodynamic Data Summary for Run 203 with TWICS.

Run No. (Configuration)	α (deg)	q_∞ (psf)	M_∞	Re (x 10^6)	C_L	C_m	C_D	L/D
203 (CRM-HL with BLRS)	-3.76	58.10	0.2006	1.392	0.5192	-0.3172	0.1069	4.858
	0.53	57.92	0.2003	1.389	1.0971	-0.3857	0.1143	9.598
	1.55	57.82	0.2001	1.389	1.2037	-0.3853	0.1222	9.847
	2.60	57.72	0.1999	1.387	1.3062	-0.3820	0.1308	9.987
	3.63	57.77	0.2000	1.387	1.4013	-0.3767	0.1401	10.004
	4.69	57.95	0.2004	1.389	1.5035	-0.3715	0.1516	9.917
	5.74	58.13	0.2007	1.391	1.6070	-0.3657	0.1644	9.773
	6.77	57.57	0.1997	1.383	1.6965	-0.3576	0.1765	9.612
	7.81	57.50	0.1995	1.382	1.7929	-0.3506	0.1915	9.362
	8.87	58.40	0.2011	1.392	1.8881	-0.3458	0.2066	9.137
	9.89	57.81	0.2001	1.386	1.9783	-0.3410	0.2216	8.927
	10.93	57.98	0.2004	1.388	2.0592	-0.3338	0.2370	8.689
	11.98	57.86	0.2002	1.386	2.1330	-0.3248	0.2520	8.463
	13.01	58.00	0.2004	1.387	2.2034	-0.3128	0.2663	8.273
	14.02	58.31	0.2010	1.392	2.2477	-0.2993	0.2776	8.096
	15.03	58.20	0.2008	1.390	2.2791	-0.2822	0.2880	7.913
	16.06	58.18	0.2007	1.390	2.3152	-0.2686	0.3008	7.697
	16.57	58.02	0.2005	1.389	2.3411	-0.2614	0.3074	7.617
	17.09	58.17	0.2007	1.390	2.3844	-0.2560	0.3157	7.553
	17.61	58.13	0.2006	1.389	2.4177	-0.2520	0.3370	7.175
	18.12	58.11	0.2006	1.389	2.4120	-0.2430	0.3427	7.038
	18.61	57.98	0.2004	1.388	2.4067	-0.2342	0.3479	6.918
	19.10	58.11	0.2006	1.389	2.3858	-0.2234	0.3512	6.793
	19.56	58.38	0.2011	1.392	2.3219	-0.2460	0.3646	6.369
	20.05	58.15	0.2007	1.389	2.2884	-0.2578	0.3858	5.932

Table B5. Aerodynamic Data Summary for Run 208 with TWICS.

Run No. (Configuration)	α (deg)	q_∞ (psf)	M_∞	Re (x 10^6)	C_L	C_m	C_D	L/D
208 (CRM-HL, repeat run)	-3.74	58.80	0.2014	1.436	0.5251	-0.3159	0.1062	4.942
	0.52	58.33	0.2005	1.427	1.0857	-0.3875	0.1133	9.584
	2.61	58.40	0.2007	1.426	1.2950	-0.3849	0.1294	10.010
	4.69	58.53	0.2009	1.427	1.4920	-0.3765	0.1498	9.958
	6.77	58.41	0.2007	1.423	1.6903	-0.3640	0.1757	9.619
	7.81	58.70	0.2012	1.426	1.7851	-0.3586	0.1901	9.389
	8.87	58.53	0.2009	1.423	1.8805	-0.3550	0.2052	9.162
	9.90	58.58	0.2010	1.422	1.9672	-0.3503	0.2201	8.938
	10.93	58.50	0.2008	1.421	2.0498	-0.3441	0.2357	8.698
	11.96	58.80	0.2013	1.423	2.1244	-0.3360	0.2499	8.501
	13.01	58.67	0.2011	1.421	2.1937	-0.3251	0.2649	8.282
	14.02	58.63	0.2011	1.420	2.2376	-0.3125	0.2761	8.105
	15.05	58.85	0.2015	1.422	2.2689	-0.2967	0.2865	7.919
	16.07	58.54	0.2009	1.417	2.3109	-0.2829	0.2992	7.724
	16.59	58.61	0.2010	1.417	2.3594	-0.2774	0.3084	7.652
	17.09	58.38	0.2006	1.414	2.3802	-0.2711	0.3141	7.577
	17.60	58.86	0.2015	1.419	2.3889	-0.2645	0.3197	7.473
	18.10	58.80	0.2014	1.417	2.3977	-0.2580	0.3388	7.077
	18.59	58.44	0.2007	1.412	2.3809	-0.2484	0.3420	6.963
	19.08	59.08	0.2019	1.419	2.3401	-0.2478	0.3475	6.734
	19.55	58.79	0.2014	1.414	2.2704	-0.2844	0.3722	6.100
	20.04	59.14	0.2020	1.417	2.2586	-0.2860	0.3879	5.823

Table B6. Aerodynamic Data Summary for Run 209 with TWICS.

Run No. (Configuration)	α (deg)	q_∞ (psf)	M_∞	*Re* (x 10^6)	C_L	C_m	C_D	*L/D*
209 (CRM-HL – lower M_∞ run)	-3.76	23.44	0.1260	0.896	0.5179	-0.3194	0.1080	4.794
	0.48	23.13	0.1252	0.890	1.0724	-0.3813	0.1132	9.474
	2.60	23.21	0.1254	0.892	1.2887	-0.3821	0.1291	9.986
	4.68	23.12	0.1251	0.891	1.4853	-0.3748	0.1494	9.941
	6.79	23.25	0.1255	0.893	1.6898	-0.3624	0.1758	9.611
	7.81	23.41	0.1259	0.896	1.7802	-0.3595	0.1891	9.414
	8.86	23.17	0.1253	0.892	1.8710	-0.3543	0.2036	9.190
	9.89	23.32	0.1257	0.895	1.9577	-0.3480	0.2183	8.969
	10.93	23.28	0.1256	0.894	2.0390	-0.3418	0.2333	8.739
	11.97	23.23	0.1254	0.893	2.1118	-0.3344	0.2481	8.514
	13.00	23.17	0.1253	0.892	2.1743	-0.3238	0.2620	8.298
	14.01	23.22	0.1254	0.893	2.2227	-0.3096	0.2744	8.099
	15.04	23.23	0.1255	0.893	2.2587	-0.2952	0.2851	7.923
	16.07	23.38	0.1259	0.896	2.3283	-0.2827	0.3107	7.494
	16.57	23.27	0.1256	0.894	2.3562	-0.2781	0.3172	7.427
	17.11	23.31	0.1257	0.895	2.3843	-0.2730	0.3268	7.297
	17.59	23.36	0.1258	0.896	2.3953	-0.2640	0.3315	7.226
	18.09	23.32	0.1257	0.895	2.3886	-0.2521	0.3366	7.095
	18.59	23.33	0.1257	0.895	2.3689	-0.2388	0.3405	6.958
	19.08	23.39	0.1259	0.896	2.3343	-0.2320	0.3446	6.774
	19.54	23.43	0.1260	0.897	2.2667	-0.2643	0.3651	6.209
	20.04	23.38	0.1259	0.896	2.2544	-0.2720	0.3858	5.843

Table B7. Aerodynamic Data Summary for Run 210 with TWICS.

Run No. (Configuration)	α (deg)	q_∞ (psf)	M_∞	Re (x 10^6)	C_L	C_m	C_D	L/D
210 (CRM-HL – lower M_∞ run)	-3.78	33.58	0.1512	1.071	0.5148	-0.3140	0.1067	4.823
	0.48	33.15	0.1502	1.064	1.0779	-0.3834	0.1127	9.562
	2.61	33.24	0.1504	1.065	1.2927	-0.3828	0.1288	10.037
	4.69	33.19	0.1503	1.064	1.4876	-0.3762	0.1494	9.960
	6.77	33.28	0.1505	1.065	1.6901	-0.3637	0.1751	9.650
	7.81	33.27	0.1505	1.065	1.7837	-0.3585	0.1893	9.421
	8.86	33.23	0.1504	1.064	1.8753	-0.3543	0.2042	9.182
	9.89	33.39	0.1508	1.067	1.9613	-0.3485	0.2186	8.974
	10.95	33.07	0.1501	1.062	2.0429	-0.3425	0.2341	8.726
	11.98	33.29	0.1506	1.065	2.1186	-0.3353	0.2487	8.518
	13.00	33.39	0.1508	1.067	2.1815	-0.3247	0.2624	8.312
	14.01	33.29	0.1506	1.065	2.2259	-0.3103	0.2741	8.119
	15.04	33.39	0.1508	1.067	2.2655	-0.2949	0.2857	7.929
	16.07	33.26	0.1505	1.064	2.3200	-0.2835	0.2995	7.746
	16.56	33.45	0.1510	1.067	2.3453	-0.2768	0.3057	7.673
	17.09	33.28	0.1506	1.065	2.3894	-0.2739	0.3254	7.342
	17.59	33.21	0.1504	1.064	2.4062	-0.2664	0.3330	7.226
	18.10	33.42	0.1509	1.067	2.3981	-0.2569	0.3372	7.111
	18.59	33.50	0.1511	1.068	2.3804	-0.2458	0.3412	6.976
	19.08	33.47	0.1510	1.067	2.3371	-0.2439	0.3462	6.751
	19.54	33.49	0.1510	1.067	2.2684	-0.2793	0.3694	6.141
	20.05	33.60	0.1513	1.069	2.2718	-0.2822	0.3887	5.845

Table B8. Aerodynamic Data Summary for Run 211 with TWICS.

Run No. (Configuration)	***α* (deg)**	**q_∞ (psf)**	**M_∞**	***Re* (x 10^6)**	**C_L**	**C_m**	**C_D**	***L/D***
211 (CRM-HL – lower M_∞ run)	-3.76	45.25	0.1761	1.236	0.5154	-0.3136	0.1065	4.839
	0.48	45.00	0.1756	1.232	1.0778	-0.3861	0.1125	9.577
	2.61	44.91	0.1754	1.230	1.2937	-0.3846	0.1291	10.017
	4.69	45.16	0.1759	1.233	1.4908	-0.3761	0.1492	9.992
	6.79	45.05	0.1757	1.232	1.6886	-0.3641	0.1756	9.615
	7.81	45.24	0.1761	1.234	1.7823	-0.3594	0.1892	9.419
	8.86	44.93	0.1755	1.229	1.8760	-0.3551	0.2039	9.200
	9.91	45.00	0.1756	1.230	1.9619	-0.3489	0.2190	8.957
	10.93	45.35	0.1763	1.234	2.0446	-0.3439	0.2344	8.722
	11.98	44.98	0.1756	1.229	2.1203	-0.3362	0.2492	8.510
	13.01	45.17	0.1759	1.231	2.1813	-0.3247	0.2629	8.295
	14.00	45.27	0.1761	1.232	2.2263	-0.3116	0.2744	8.115
	15.04	45.23	0.1761	1.232	2.2616	-0.2956	0.2854	7.924
	16.06	45.04	0.1757	1.229	2.2959	-0.2818	0.2974	7.720
	16.56	45.18	0.1760	1.230	2.3393	-0.2767	0.3051	7.667
	17.08	45.22	0.1760	1.231	2.3684	-0.2705	0.3122	7.585
	17.59	45.29	0.1762	1.231	2.4029	-0.2673	0.3326	7.224
	18.10	45.19	0.1760	1.230	2.3946	-0.2582	0.3370	7.107
	18.59	45.11	0.1758	1.229	2.3786	-0.2482	0.3411	6.973
	19.09	45.46	0.1765	1.233	2.3391	-0.2463	0.3461	6.759
	19.55	45.15	0.1759	1.229	2.2693	-0.2869	0.3719	6.101
	20.05	45.45	0.1765	1.233	2.2659	-0.2866	0.3882	5.837

Table B9. Aerodynamic Data Summary for Run 212 with TWICS.

Run No. (Configuration)	α (deg)	q_∞ (psf)	M_∞	*Re* (x 10^6)	C_L	C_m	C_D	*L/D*
212 (CRM-HL, repeat run)	-3.76	58.72	0.2013	1.396	0.5158	-0.3157	0.1063	4.851
	0.48	58.33	0.2006	1.391	1.0775	-0.3883	0.1121	9.611
	2.60	58.30	0.2006	1.390	1.2917	-0.3856	0.1286	10.042
	4.69	58.44	0.2008	1.390	1.4887	-0.3775	0.1494	9.963
	6.77	58.53	0.2010	1.390	1.6873	-0.3649	0.1751	9.636
	7.81	58.29	0.2006	1.388	1.7832	-0.3604	0.1897	9.402
	8.86	58.53	0.2010	1.390	1.8779	-0.3559	0.2047	9.173
	9.92	58.61	0.2011	1.391	1.9664	-0.3513	0.2201	8.934
	10.91	58.34	0.2006	1.387	2.0453	-0.3453	0.2351	8.700
	11.98	58.66	0.2012	1.391	2.1237	-0.3368	0.2499	8.500
	13.01	58.33	0.2006	1.387	2.1892	-0.3265	0.2642	8.286
	14.04	58.48	0.2009	1.389	2.2361	-0.3130	0.2761	8.099
	15.04	58.53	0.2010	1.389	2.2639	-0.2972	0.2860	7.914
	16.06	58.49	0.2009	1.389	2.3047	-0.2837	0.2982	7.730
	16.56	58.64	0.2012	1.390	2.3349	-0.2777	0.3048	7.660
	17.08	58.58	0.2011	1.388	2.3682	-0.2709	0.3121	7.588
	17.59	58.45	0.2008	1.387	2.4018	-0.2679	0.3330	7.212
	18.12	58.65	0.2012	1.389	2.3928	-0.2597	0.3378	7.083
	18.59	58.81	0.2015	1.390	2.3787	-0.2496	0.3413	6.970
	19.08	58.88	0.2016	1.390	2.3295	-0.2514	0.3469	6.714
	19.54	58.98	0.2018	1.392	2.2585	-0.2930	0.3739	6.040
	20.04	58.60	0.2011	1.387	2.2572	-0.2874	0.3879	5.819

Table B10. Aerodynamic Data Summary for Run 215 with TWICS.

Run No. (Configuration)	α (deg)	q_∞ (psf)	M_∞	Re (x 10^6)	C_L	C_m	C_D	L/D
215 (with Chine Position 1)	-3.76	59.14	0.2016	1.478	0.5166	-0.3145	0.1066	4.847
	0.52	58.31	0.2001	1.465	1.0739	-0.3804	0.1126	9.539
	2.60	58.50	0.2005	1.467	1.2852	-0.3781	0.1292	9.944
	4.70	58.30	0.2001	1.463	1.4809	-0.3694	0.1500	9.873
	6.77	58.81	0.2010	1.466	1.6833	-0.3587	0.1758	9.574
	7.81	58.83	0.2010	1.466	1.7797	-0.3534	0.1904	9.348
	8.86	58.64	0.2007	1.463	1.8753	-0.3498	0.2058	9.111
	9.89	58.71	0.2008	1.462	1.9611	-0.3447	0.2202	8.906
	10.93	58.62	0.2007	1.460	2.0439	-0.3380	0.2355	8.680
	11.96	58.79	0.2010	1.461	2.1213	-0.3304	0.2504	8.471
	12.99	58.63	0.2007	1.459	2.1965	-0.3221	0.2666	8.239
	14.03	58.76	0.2009	1.458	2.2648	-0.3111	0.2815	8.047
	15.07	59.05	0.2014	1.462	2.3327	-0.2977	0.2966	7.864
	16.07	58.75	0.2009	1.457	2.3703	-0.2830	0.3083	7.688
	16.60	58.94	0.2012	1.459	2.3901	-0.2764	0.3151	7.585
	17.10	58.93	0.2012	1.459	2.4168	-0.2717	0.3223	7.500
	17.63	59.09	0.2015	1.460	2.4427	-0.2657	0.3300	7.403
	18.12	58.72	0.2008	1.454	2.4436	-0.2570	0.3343	7.310
	18.62	58.87	0.2011	1.455	2.4134	-0.2530	0.3387	7.125
	19.09	59.13	0.2016	1.458	2.3450	-0.2689	0.3540	6.623
	19.56	59.13	0.2016	1.457	2.3109	-0.2935	0.3795	6.089
	20.09	59.11	0.2015	1.457	2.3223	-0.2965	0.3989	5.822
	20.59	59.34	0.2019	1.455	2.3372	-0.2922	0.4136	5.651
	21.09	59.13	0.2016	1.452	2.3492	-0.2809	0.4253	5.524
	21.59	59.18	0.2017	1.452	2.3429	-0.2697	0.4358	5.376

Table B11. Aerodynamic Data Summary for Run 216 with TWICS.

Run No. (Configuration)	α (deg)	q_∞ (psf)	M_∞	Re (x 10^6)	C_L	C_m	C_D	L/D
216 (with Chine Position 2)	-3.78	59.13	0.2015	1.447	0.5093	-0.3132	0.1064	4.785
	0.50	58.34	0.2001	1.435	1.0721	-0.3807	0.1123	9.544
	2.59	58.80	0.2009	1.440	1.2818	-0.3776	0.1287	9.956
	4.68	58.54	0.2005	1.436	1.4784	-0.3697	0.1489	9.926
	6.77	58.89	0.2011	1.439	1.6850	-0.3581	0.1755	9.601
	7.81	58.83	0.2010	1.437	1.7822	-0.3528	0.1904	9.359
	8.87	59.02	0.2013	1.439	1.8762	-0.3490	0.2052	9.141
	9.89	58.76	0.2009	1.435	1.9633	-0.3436	0.2201	8.921
	10.93	59.02	0.2013	1.437	2.0469	-0.3367	0.2357	8.684
	11.98	58.63	0.2006	1.431	2.1253	-0.3302	0.2513	8.455
	13.01	58.77	0.2009	1.432	2.1994	-0.3208	0.2672	8.231
	14.04	58.98	0.2013	1.433	2.2708	-0.3108	0.2820	8.054
	15.06	58.67	0.2007	1.428	2.3441	-0.2977	0.2978	7.871
	16.09	58.70	0.2008	1.429	2.3937	-0.2838	0.3114	7.687
	16.59	58.73	0.2008	1.428	2.4129	-0.2766	0.3172	7.608
	17.13	58.73	0.2008	1.427	2.4314	-0.2702	0.3246	7.490
	17.61	58.60	0.2006	1.423	2.4459	-0.2648	0.3300	7.411
	18.14	58.77	0.2009	1.424	2.4380	-0.2553	0.3340	7.299
	18.60	58.72	0.2008	1.423	2.4057	-0.2528	0.3379	7.119
	19.07	59.04	0.2014	1.426	2.3407	-0.2749	0.3572	6.553
	19.59	59.07	0.2014	1.424	2.3252	-0.2901	0.3822	6.084
	20.08	59.06	0.2014	1.423	2.3328	-0.2884	0.3980	5.861

Table B12. Aerodynamic Data Summary for Run 217 with TWICS.

Run No. (Configuration)	α (deg)	q_∞ (psf)	M_∞	Re (x 10^6)	C_L	C_m	C_D	L/D
217 (with Chine Position 3)	-3.78	59.05	0.2015	1.419	0.5069	-0.3123	0.1067	4.752
	0.52	58.45	0.2004	1.410	1.0730	-0.3807	0.1126	9.528
	2.60	58.66	0.2008	1.412	1.2830	-0.3771	0.1291	9.940
	4.68	58.45	0.2004	1.408	1.4773	-0.3687	0.1493	9.897
	6.77	58.57	0.2007	1.408	1.6860	-0.3564	0.1761	9.576
	7.81	58.42	0.2004	1.405	1.7823	-0.3520	0.1906	9.350
	8.84	58.85	0.2011	1.409	1.8754	-0.3482	0.2054	9.129
	9.88	58.55	0.2006	1.405	1.9651	-0.3422	0.2205	8.912
	10.93	58.71	0.2009	1.406	2.0525	-0.3363	0.2370	8.660
	11.96	58.47	0.2005	1.402	2.1323	-0.3279	0.2530	8.428
	13.00	58.75	0.2010	1.405	2.2048	-0.3197	0.2689	8.199
	14.04	58.87	0.2012	1.404	2.2763	-0.3090	0.2843	8.007
	15.06	58.85	0.2012	1.404	2.3497	-0.2959	0.3006	7.816
	16.11	58.76	0.2010	1.401	2.4056	-0.2828	0.3157	7.621
	16.62	58.61	0.2007	1.399	2.4288	-0.2756	0.3221	7.540
	17.12	58.72	0.2009	1.400	2.4476	-0.2686	0.3282	7.458
	17.63	58.66	0.2008	1.398	2.4531	-0.2617	0.3333	7.361
	18.14	58.83	0.2011	1.400	2.4380	-0.2533	0.3365	7.246
	18.60	58.79	0.2010	1.398	2.3930	-0.2535	0.3474	6.888
	19.08	59.02	0.2015	1.400	2.3355	-0.2817	0.3646	6.405
	19.57	59.02	0.2014	1.400	2.3303	-0.2826	0.3823	6.096
	20.08	58.95	0.2013	1.398	2.3394	-0.2857	0.4002	5.845

Table B13. Aerodynamic Data Summary for Run 218 with TWICS.

Run No. (Configuration)	α (deg)	q_∞ (psf)	M_∞	*Re* (x 10^6)	C_L	C_m	C_D	*L/D*
218 (with Chine Position 3, repeat run)	-3.78	58.85	0.2011	1.395	0.5054	-0.3118	0.1062	4.757
	0.49	58.64	0.2008	1.392	1.0685	-0.3813	0.1124	9.505
	2.60	58.26	0.2001	1.387	1.2816	-0.3780	0.1287	9.957
	4.68	58.20	0.2000	1.385	1.4759	-0.3687	0.1493	9.883
	6.79	58.42	0.2004	1.386	1.6858	-0.3567	0.1761	9.573
	7.81	58.45	0.2004	1.386	1.7812	-0.3519	0.1903	9.358
	8.84	58.72	0.2009	1.388	1.8753	-0.3489	0.2050	9.146
	9.89	58.44	0.2004	1.384	1.9658	-0.3426	0.2210	8.896
	10.93	58.78	0.2010	1.388	2.0517	-0.3366	0.2369	8.659
	11.98	58.33	0.2002	1.382	2.1318	-0.3289	0.2530	8.427
	13.00	58.43	0.2004	1.383	2.2038	-0.3201	0.2681	8.221
	14.04	58.84	0.2011	1.387	2.2747	-0.3092	0.2838	8.016
	15.06	58.61	0.2007	1.384	2.3495	-0.2969	0.2998	7.838
	16.11	58.80	0.2010	1.386	2.4074	-0.2834	0.3152	7.637
	16.62	58.81	0.2011	1.385	2.4286	-0.2770	0.3218	7.548
	17.12	58.89	0.2012	1.385	2.4454	-0.2700	0.3276	7.464
	17.61	58.92	0.2012	1.386	2.4526	-0.2620	0.3325	7.375
	18.14	58.89	0.2012	1.385	2.4347	-0.2546	0.3354	7.258
	18.60	58.97	0.2013	1.386	2.3891	-0.2538	0.3465	6.895
	19.06	58.86	0.2012	1.383	2.3312	-0.2855	0.3659	6.371
	19.59	59.05	0.2015	1.385	2.3268	-0.2867	0.3836	6.066
	20.08	58.99	0.2014	1.384	2.3394	-0.2823	0.3984	5.872

Table B14. Aerodynamic Data Summary for Run 219 with TWICS.

Run No. (Configuration)	α (deg)	q_∞ (psf)	M_∞	Re (x 10^6)	C_L	C_m	C_D	L/D
219 (CRM-HL – with tufts)	-3.78	59.00	0.2014	1.391	0.5065	-0.3101	0.1070	4.734
	0.52	58.60	0.2007	1.385	1.0704	-0.3807	0.1126	9.508
	2.60	58.40	0.2003	1.382	1.2815	-0.3784	0.1286	9.966
	6.78	58.28	0.2001	1.378	1.6794	-0.3593	0.1753	9.579
	7.81	58.25	0.2000	1.375	1.7752	-0.3545	0.1894	9.374
	8.86	58.64	0.2007	1.379	1.8698	-0.3505	0.2043	9.154
	9.89	58.85	0.2011	1.381	1.9569	-0.3457	0.2189	8.938
	10.93	58.75	0.2009	1.379	2.0381	-0.3389	0.2341	8.707
	11.95	58.96	0.2013	1.382	2.1141	-0.3310	0.2488	8.497
	13.00	58.97	0.2013	1.381	2.1800	-0.3210	0.2631	8.286
	14.01	58.71	0.2008	1.378	2.2227	-0.3068	0.2741	8.108
	15.02	58.79	0.2010	1.378	2.2531	-0.2908	0.2844	7.923
	16.05	58.93	0.2012	1.380	2.2880	-0.2770	0.2964	7.720
	16.57	59.01	0.2014	1.380	2.3124	-0.2709	0.3034	7.622
	17.07	58.99	0.2013	1.379	2.3477	-0.2642	0.3103	7.566
	17.62	58.90	0.2012	1.379	2.3893	-0.2618	0.3321	7.194
	18.09	58.66	0.2008	1.375	2.3858	-0.2545	0.3371	7.078
	18.61	58.93	0.2012	1.378	2.3707	-0.2446	0.3405	6.963
	19.08	59.16	0.2016	1.380	2.3255	-0.2468	0.3463	6.715
	19.54	59.04	0.2014	1.378	2.2605	-0.2883	0.3734	6.054
	20.04	59.05	0.2014	1.377	2.2524	-0.2860	0.3875	5.813

Table B15. Aerodynamic Data Summary for Run 220 with TWICS.

Run No. (Configuration)	α (deg)	q_∞ (psf)	M_∞	Re (x 10^6)	C_L	C_m	C_D	L/D
220 (CRM-HL – with tufts, repeat run)	-3.76	59.10	0.2015	1.391	0.5087	-0.3109	0.1065	4.775
	0.52	58.52	0.2005	1.383	1.0705	-0.3813	0.1124	9.525
	2.59	58.59	0.2006	1.383	1.2793	-0.3790	0.1284	9.964
	4.66	58.74	0.2009	1.386	1.4751	-0.3706	0.1485	9.933
	6.78	58.47	0.2004	1.381	1.6809	-0.3589	0.1755	9.577
	7.81	58.58	0.2006	1.383	1.7741	-0.3543	0.1895	9.364
	8.84	58.63	0.2007	1.383	1.8687	-0.3506	0.2039	9.163
	9.89	58.63	0.2007	1.382	1.9565	-0.3453	0.2191	8.932
	10.93	58.95	0.2012	1.386	2.0386	-0.3393	0.2344	8.699
	11.95	58.91	0.2012	1.385	2.1144	-0.3315	0.2490	8.492
	13.00	58.83	0.2010	1.384	2.1802	-0.3204	0.2636	8.270
	14.01	58.75	0.2009	1.383	2.2254	-0.3071	0.2749	8.097
	15.02	58.77	0.2009	1.383	2.2525	-0.2914	0.2847	7.913
	16.06	58.92	0.2012	1.383	2.2914	-0.2778	0.2975	7.703
	16.55	58.90	0.2011	1.382	2.3180	-0.2710	0.3036	
	17.09	58.73	0.2009	1.381	2.3464	-0.2643	0.3107	7.551
	17.59	58.88	0.2011	1.382	2.3912	-0.2619	0.3321	7.201
	18.11	58.91	0.2012	1.381	2.3875	-0.2541	0.3374	7.076
	18.59	58.77	0.2009	1.379	2.3713	-0.2456	0.3408	6.958
	19.08	59.07	0.2015	1.382	2.3208	-0.2489	0.3462	6.704
	19.54	59.37	0.2020	1.386	2.2629	-0.2847	0.3710	6.100
	20.04	59.18	0.2016	1.384	2.2590	-0.2832	0.3874	5.831

Table B16. Aerodynamic Data Summary for Run 221 with TWICS.

Run No. (Configuration)	α (deg)	q_∞ (psf)	M_∞	Re (x 10^6)	C_L	C_m	C_D	L/D
221 (CRM-HL, repeat run)	-3.76	59.02	0.2014	1.398	0.5190	-0.3156	0.1063	4.880
	0.52	58.45	0.2003	1.389	1.0821	-0.3875	0.1128	9.594
	2.60	58.51	0.2005	1.389	1.2898	-0.3852	0.1288	10.014
	4.69	58.48	0.2004	1.388	1.4901	-0.3766	0.1494	9.973
	6.77	58.78	0.2009	1.391	1.6913	-0.3647	0.1759	9.617
	7.81	58.54	0.2005	1.387	1.7841	-0.3597	0.1901	9.385
	8.84	59.11	0.2015	1.393	1.8771	-0.3560	0.2045	9.178
	9.90	58.74	0.2008	1.388	1.9648	-0.3509	0.2196	8.947
	10.93	58.89	0.2011	1.390	2.0454	-0.3445	0.2347	8.715
	11.96	58.99	0.2013	1.392	2.1202	-0.3354	0.2495	8.499
	12.99	58.99	0.2013	1.391	2.1864	-0.3262	0.2638	8.287
	14.02	59.03	0.2014	1.391	2.2327	-0.3123	0.2753	8.109
	15.02	58.89	0.2011	1.389	2.2616	-0.2969	0.2852	7.929
	16.06	58.86	0.2011	1.389	2.2997	-0.2827	0.2982	7.712
	16.56	58.71	0.2008	1.387	2.3319	-0.2775	0.3048	7.651
	17.11	58.75	0.2009	1.387	2.3701	-0.2720	0.3132	7.567
	17.59	58.96	0.2012	1.389	2.4022	-0.2691	0.3331	7.211
	18.12	59.09	0.2015	1.390	2.3960	-0.2607	0.3385	7.079
	18.59	58.97	0.2013	1.389	2.3794	-0.2506	0.3417	6.963
	19.08	59.24	0.2017	1.391	2.3289	-0.2539	0.3475	6.702
	19.55	58.98	0.2013	1.388	2.2698	-0.2883	0.3724	6.095
	20.04	59.21	0.2017	1.390	2.2610	-0.2903	0.3892	5.810

Table B17. Aerodynamic Data Summary for Run 222 with TWICS.

Run No. (Configuration)	α (deg)	q_∞ (psf)	M_∞	Re (x 10^6)	C_L	C_m	C_D	L/D
222 (CRM-HL, nacelle off)	-3.73	59.21	0.2015	1.458	0.5773	-0.2958	0.1034	5.582
	0.55	58.49	0.2002	1.447	1.1079	-0.3962	0.1129	9.811
	2.60	58.85	0.2009	1.450	1.2990	-0.4040	0.1272	10.213
	4.69	58.62	0.2005	1.446	1.4835	-0.4042	0.1450	10.232
	6.78	58.68	0.2006	1.445	1.6765	-0.4017	0.1682	9.970
	7.80	58.63	0.2005	1.442	1.7647	-0.4018	0.1795	9.830
	8.85	59.00	0.2012	1.446	1.8546	-0.4027	0.1921	9.657
	9.88	59.01	0.2012	1.445	1.9401	-0.4029	0.2048	9.474
	10.92	58.69	0.2006	1.440	2.0229	-0.4033	0.2177	9.292
	11.97	58.55	0.2004	1.438	2.1032	-0.3994	0.2310	9.104
	13.00	58.70	0.2006	1.439	2.1771	-0.3954	0.2445	8.903
	14.05	58.79	0.2008	1.439	2.2546	-0.3917	0.2585	8.720
	15.06	59.27	0.2016	1.444	2.3291	-0.3910	0.2721	8.561
	16.11	58.92	0.2010	1.439	2.4054	-0.3929	0.2871	8.379
	16.60	58.88	0.2010	1.438	2.4303	-0.3861	0.2932	8.290
	17.14	59.01	0.2012	1.439	2.4485	-0.3776	0.2984	8.204
	17.62	58.85	0.2009	1.436	2.4604	-0.3682	0.3026	8.131
	18.11	58.93	0.2010	1.435	2.4650	-0.3562	0.3066	8.040
	18.63	59.00	0.2012	1.429	2.4553	-0.3412	0.3078	7.977
	19.11	58.72	0.2007	1.432	2.4345	-0.3278	0.3083	7.896
	19.60	58.50	0.2003	1.428	2.3980	-0.3176	0.3084	7.775
	20.08	58.98	0.2011	1.433	2.3443	-0.3183	0.3109	7.540

Table B18. Aerodynamic Data Summary for Run 224 with TWICS.

Run No. (Configuration)	α (deg)	q_∞ (psf)	M_∞	Re (x 10^6)	C_L	C_m	C_D	L/D
224 (CRM-HL, nacelle off – with tufts)	-3.74	58.90	0.2012	1.418	0.5682	-0.2938	0.1032	5.504
	0.55	58.63	0.2007	1.413	1.1056	-0.3967	0.1123	9.842
	2.58	58.91	0.2012	1.416	1.2963	-0.4045	0.1267	10.229
	4.66	58.53	0.2005	1.411	1.4830	-0.4046	0.1446	10.256
	6.78	59.01	0.2014	1.415	1.6737	-0.4025	0.1670	10.024
	7.80	58.63	0.2007	1.409	1.7619	-0.4016	0.1786	9.865
	8.85	58.97	0.2013	1.412	1.8502	-0.4032	0.1910	9.688
	9.88	58.55	0.2006	1.407	1.9378	-0.4038	0.2033	9.531
	10.92	58.62	0.2007	1.407	2.0195	-0.4028	0.2162	9.342
	11.95	58.86	0.2011	1.408	2.0959	-0.4002	0.2289	9.159
	13.00	58.64	0.2007	1.405	2.1739	-0.3963	0.2429	8.949
	14.03	58.66	0.2008	1.405	2.2494	-0.3923	0.2565	8.771
	15.05	58.58	0.2006	1.403	2.3248	-0.3909	0.2707	8.589
	16.09	58.68	0.2008	1.404	2.4000	-0.3924	0.2852	8.415
	16.62	58.86	0.2011	1.405	2.4239	-0.3854	0.2912	8.323
	17.12	58.95	0.2013	1.405	2.4407	-0.3766	0.2961	8.244
	17.63	58.71	0.2008	1.402	2.4526	-0.3659	0.3009	8.152
	18.15	59.05	0.2014	1.405	2.4571	-0.3534	0.3043	8.075
	18.62	58.88	0.2011	1.402	2.4523	-0.3390	0.3060	8.013
	19.12	58.77	0.2009	1.400	2.4262	-0.3252	0.3062	7.924
	19.62	58.98	0.2013	1.402	2.3882	-0.3150	0.3055	7.818
	20.07	58.57	0.2006	1.396	2.3314	-0.3163	0.3082	7.565

Table B19. Aerodynamic Data Summary for Run 225 with TWICS.

Run No. (Configuration)	α (deg)	q_∞ (psf)	M_∞	Re (x 10^6)	C_L	C_m	C_D	L/D
225 (CRM-HL, nacelle off, repeat)	-3.73	58.92	0.2012	1.409	0.5694	-0.2939	0.1032	5.519
	0.49	58.32	0.2002	1.400	1.1024	-0.3966	0.1117	9.868
	2.60	58.50	0.2005	1.401	1.2977	-0.4043	0.1266	10.251
	4.66	58.38	0.2003	1.399	1.4821	-0.4045	0.1445	10.258
	6.78	58.71	0.2009	1.403	1.6728	-0.4018	0.1669	10.022
	7.80	58.69	0.2008	1.401	1.7646	-0.4023	0.1789	9.864
	8.83	58.61	0.2007	1.400	1.8507	-0.4031	0.1907	9.707
	9.88	58.81	0.2011	1.401	1.9396	-0.4042	0.2036	9.525
	10.92	58.81	0.2011	1.401	2.0214	-0.4025	0.2167	9.327
	11.95	58.92	0.2012	1.402	2.1008	-0.4001	0.2295	9.156
	12.98	58.81	0.2011	1.401	2.1762	-0.3961	0.2434	8.942
	14.03	58.66	0.2008	1.399	2.2535	-0.3920	0.2570	8.768
	15.05	59.04	0.2015	1.402	2.3305	-0.3912	0.2715	8.584
	16.09	58.64	0.2008	1.397	2.4027	-0.3926	0.2861	8.398
	16.60	58.75	0.2009	1.398	2.4283	-0.3857	0.2917	8.325
	17.14	58.66	0.2008	1.397	2.4465	-0.3770	0.2975	8.223
	17.62	58.60	0.2007	1.396	2.4569	-0.3668	0.3014	8.152
	18.15	58.48	0.2005	1.394	2.4628	-0.3539	0.3053	8.068
	18.63	58.72	0.2009	1.397	2.4544	-0.3402	0.3068	8.000
	19.13	58.90	0.2012	1.399	2.4284	-0.3259	0.3066	7.920
	19.58	58.74	0.2009	1.396	2.3946	-0.3168	0.3062	7.820
	20.10	58.91	0.2012	1.398	2.3389	-0.3158	0.3095	7.558

Table B20. Aerodynamic Data Summary for Run 226 with TWICS.

Run No. (Configuration)	α (deg)	q_∞ (psf)	M_∞	*Re* (x 10^6)	C_L	C_m	C_D	*L/D*
226 (CRM-HL, nacelle off, repeat)	-3.74	58.93	0.2013	1.401	0.5667	-0.2944	0.1033	5.485
	0.49	58.35	0.2003	1.393	1.1006	-0.3971	0.1119	9.833
	2.60	58.53	0.2006	1.395	1.2960	-0.4050	0.1265	10.243
	4.67	58.68	0.2008	1.396	1.4836	-0.4047	0.1444	10.275
	6.78	58.92	0.2013	1.399	1.6745	-0.4020	0.1672	10.016
	7.80	58.73	0.2009	1.396	1.7623	-0.4031	0.1783	9.884
	8.83	58.85	0.2011	1.397	1.8525	-0.4039	0.1908	9.710
	9.88	58.56	0.2006	1.392	1.9389	-0.4041	0.2035	9.526
	10.92	58.71	0.2009	1.394	2.0209	-0.4034	0.2165	9.332
	11.95	58.78	0.2010	1.394	2.0986	-0.4003	0.2288	9.171
	12.98	58.98	0.2014	1.396	2.1748	-0.3961	0.2427	8.961
	14.03	58.71	0.2009	1.393	2.2519	-0.3923	0.2566	8.776
	15.05	58.69	0.2009	1.393	2.3295	-0.3911	0.2710	8.595
	16.09	58.93	0.2013	1.395	2.4018	-0.3928	0.2857	8.406
	16.60	58.87	0.2012	1.394	2.4280	-0.3862	0.2912	8.338
	17.14	58.78	0.2010	1.393	2.4461	-0.3770	0.2973	8.229
	17.62	58.86	0.2012	1.393	2.4557	-0.3668	0.3007	8.168
	18.13	58.96	0.2013	1.395	2.4610	-0.3544	0.3042	8.089
	18.62	58.96	0.2013	1.394	2.4524	-0.3403	0.3063	8.007
	19.13	58.64	0.2008	1.390	2.4287	-0.3264	0.3065	7.924
	19.60	58.80	0.2011	1.392	2.3906	-0.3158	0.3059	7.815
	20.08	58.84	0.2011	1.391	2.3389	-0.3169	0.3094	7.559

Table B21. Aerodynamic Data Summary for Run 227 with TWICS.

Run No. (Configuration)	α (deg)	q_∞ (psf)	M_∞	Re (x 10^6)	C_L	C_m	C_D	L/D
227 (CRM-HL, repeat run)	-3.76	58.88	0.2013	1.431	0.5154	-0.3136	0.1059	4.866
	0.52	58.77	0.2012	1.427	1.0866	-0.3879	0.1129	9.627
	2.61	58.73	0.2011	1.425	1.2968	-0.3857	0.1289	10.061
	4.67	58.56	0.2008	1.423	1.4909	-0.3766	0.1496	9.964
	6.79	58.68	0.2010	1.422	1.6925	-0.3641	0.1760	9.616
	7.81	58.77	0.2012	1.423	1.7846	-0.3593	0.1900	9.391
	8.84	58.65	0.2010	1.420	1.8767	-0.3555	0.2046	9.170
	9.90	58.55	0.2008	1.418	1.9650	-0.3501	0.2197	8.943
	10.93	58.76	0.2011	1.420	2.0467	-0.3437	0.2349	8.713
	11.96	58.54	0.2008	1.417	2.1230	-0.3352	0.2495	8.509
	12.99	58.97	0.2015	1.422	2.1881	-0.3248	0.2639	8.290
	14.02	58.89	0.2014	1.420	2.2365	-0.3118	0.2759	8.105
	15.03	58.64	0.2009	1.417	2.2676	-0.2958	0.2859	7.933
	16.05	58.57	0.2008	1.416	2.3218	-0.2834	0.2996	7.751
	16.58	58.46	0.2006	1.413	2.3763	-0.2792	0.3090	7.690
	17.12	58.77	0.2012	1.416	2.3963	-0.2722	0.3151	7.606
	17.59	58.73	0.2011	1.415	2.4039	-0.2662	0.3197	7.519
	18.10	58.78	0.2012	1.415	2.3963	-0.2593	0.3378	7.094
	18.61	58.61	0.2009	1.412	2.3778	-0.2491	0.3412	6.968
	19.06	58.83	0.2013	1.415	2.3358	-0.2487	0.3452	6.766
	19.53	58.74	0.2011	1.413	2.2677	-0.2879	0.3706	6.119
	20.04	59.13	0.2018	1.417	2.2621	-0.2824	0.3851	5.874

Appendix C.

Aerodynamic Data Summary Tables without Wall Correction (Runs 200 to 227)

Table C1. Aerodynamic Summary Data for Run 200 without TWICS.

Run No. (Configuration)	α_u (deg)	$q_{\infty,u}$ (psf)	$M_{\infty,u}$	$Re_{,u}$ (x 10^6)	$C_{L,u}$	$C_{m,u}$	$C_{D,u}$	$L/D_{,u}$
200 (CRM-HL)	-3.99	57.76	0.2000	1.411	0.5287	-0.3207	0.1060	4.990
	-0.03	57.78	0.2001	1.409	1.0968	-0.3939	0.1055	10.400
	2.02	57.29	0.1992	1.402	1.3158	-0.3913	0.1184	11.116
	4.01	57.31	0.1992	1.401	1.5194	-0.3838	0.1356	11.208
	6.00	57.49	0.1995	1.401	1.7087	-0.3715	0.1549	11.030
	7.00	57.83	0.2001	1.404	1.8037	-0.3658	0.1667	10.819
	8.01	57.67	0.1999	1.399	1.9007	-0.3626	0.1789	10.622
	9.00	57.74	0.2000	1.400	1.9899	-0.3584	0.1910	10.419
	10.00	57.70	0.1999	1.399	2.0739	-0.3518	0.2040	10.168
	10.99	58.12	0.2007	1.403	2.1497	-0.3436	0.2158	9.960
	12.01	57.41	0.1994	1.394	2.2172	-0.3332	0.2282	9.717
	13.00	57.80	0.2001	1.398	2.2620	-0.3197	0.2378	9.510
	13.99	57.75	0.2000	1.398	2.2940	-0.3041	0.2470	9.286
	15.01	57.67	0.1999	1.397	2.3357	-0.2905	0.2584	9.037
	15.49	57.65	0.1998	1.396	2.3599	-0.2844	0.2637	8.950
	16.02	57.72	0.1999	1.395	2.4009	-0.2779	0.2703	8.884
	16.49	57.68	0.1999	1.395	2.4173	-0.2722	0.2758	8.765
	17.02	57.87	0.2002	1.396	2.4286	-0.2658	0.2954	8.222
	17.50	57.66	0.1998	1.393	2.4221	-0.2567	0.3003	8.067
	18.01	57.71	0.1999	1.393	2.3733	-0.2582	0.3068	7.736
	18.50	57.55	0.1996	1.391	2.3066	-0.2971	0.3356	6.874
	19.00	57.49	0.1995	1.389	2.3012	-0.2985	0.3525	6.527

Table C2. Aerodynamic Summary Data for Run 201 without TWICS.

Run No. (Configuration)	α_u (deg)	$q_{\infty,u}$ (psf)	$M_{\infty,u}$	$Re_{,u}$ (x 10^6)	$C_{L,u}$	$C_{m,u}$	$C_{D,u}$	$L/D_{,u}$
201 (CRM-HL – increasing α)	-3.99	57.86	0.2002	1.400	0.5229	-0.3183	0.1056	4.949
	-3.54	57.75	0.2000	1.395	0.5962	-0.3271	0.1030	5.788
	-2.97	57.63	0.1998	1.393	0.6985	-0.3456	0.1007	6.939
	-2.51	57.66	0.1998	1.392	0.7738	-0.3584	0.1001	7.728
	-2.06	57.70	0.1999	1.392	0.8323	-0.3674	0.1001	8.317
	-1.53	57.81	0.2001	1.393	0.9042	-0.3766	0.1005	8.997
	-1.01	57.63	0.1998	1.390	0.9918	-0.3954	0.1011	9.807
	-0.54	57.72	0.1999	1.391	1.0458	-0.3962	0.1027	10.182
	0.05	57.77	0.2000	1.390	1.1053	-0.3941	0.1056	10.471
	0.50	57.65	0.1998	1.388	1.1571	-0.3938	0.1078	10.738
	0.99	57.89	0.2002	1.391	1.2111	-0.3941	0.1107	10.936
	1.50	57.63	0.1998	1.387	1.2646	-0.3938	0.1141	11.080
	2.00	57.83	0.2001	1.389	1.3158	-0.3924	0.1180	11.156
	2.49	57.23	0.1991	1.382	1.3658	-0.3904	0.1215	11.245
	3.00	57.71	0.1999	1.387	1.4167	-0.3882	0.1252	11.314
	3.51	58.01	0.2004	1.390	1.4668	-0.3868	0.1303	11.254
	3.99	57.77	0.2000	1.388	1.5110	-0.3837	0.1339	11.284
	6.00	57.60	0.1997	1.385	1.7055	-0.3714	0.1539	11.082
	7.00	57.53	0.1996	1.383	1.8013	-0.3663	0.1657	10.869
	8.01	57.91	0.2003	1.387	1.8974	-0.3627	0.1783	10.644
	9.00	57.88	0.2002	1.387	1.9862	-0.3576	0.1903	10.437
	10.00	57.51	0.1996	1.382	2.0714	-0.3510	0.2032	10.195
	10.99	57.74	0.2000	1.385	2.1474	-0.3437	0.2153	9.976
	11.99	57.87	0.2002	1.386	2.2130	-0.3332	0.2277	9.717
	13.00	57.91	0.2003	1.387	2.2637	-0.3199	0.2376	9.529
	13.99	57.86	0.2002	1.386	2.2913	-0.3048	0.2463	9.302
	14.99	57.78	0.2000	1.386	2.3281	-0.2905	0.2573	9.048
	15.49	57.76	0.2000	1.384	2.3628	-0.2842	0.2631	8.979
	16.00	57.78	0.2000	1.384	2.4014	-0.2785	0.2696	8.906
	16.51	57.78	0.2000	1.384	2.4353	-0.2753	0.2900	8.398
	17.00	57.58	0.1997	1.381	2.4288	-0.2669	0.2947	8.243
	17.52	57.68	0.1999	1.382	2.4141	-0.2567	0.2994	8.063
	17.99	57.89	0.2002	1.384	2.3701	-0.2583	0.3058	7.751
	18.52	57.79	0.2001	1.383	2.3093	-0.2979	0.3360	6.873
	19.00	57.79	0.2001	1.383	2.3031	-0.2990	0.3529	6.526
	19.51	57.77	0.2000	1.382	2.3097	-0.2897	0.3675	6.284
	20.00	57.71	0.1999	1.381	2.3241	-0.2924	0.3840	6.052
	20.49	57.64	0.1998	1.379	2.3221	-0.2775	0.3940	5.893

Table C3. Aerodynamic Data Summary for Run 202 without TWICS.

Run No. (Configuration)	α_u (deg)	$q_{\infty,u}$ (psf)	$M_{\infty,u}$	$Re_{,u}$ (x 10^6)	$C_{L,u}$	$C_{m,u}$	$C_{D,u}$	$L/D_{,u}$
202 (CRM-HL – decreasing α)	20.49	57.83	0.2001	1.381	2.3196	-0.2750	0.3941	5.886
	19.98	57.77	0.2000	1.380	2.3272	-0.2971	0.3854	6.039
	19.49	57.86	0.2002	1.380	2.3134	-0.2945	0.3684	6.279
	19.00	57.91	0.2003	1.380	2.3027	-0.2956	0.3512	6.557
	18.48	57.88	0.2002	1.380	2.3074	-0.2993	0.3354	6.880
	17.99	57.75	0.2000	1.378	2.3698	-0.2579	0.3059	7.747
	17.48	57.91	0.2003	1.380	2.4147	-0.2571	0.2988	8.082
	16.98	57.45	0.1995	1.375	2.4294	-0.2670	0.2947	8.245
	16.49	57.94	0.2003	1.380	2.4362	-0.2756	0.2896	8.413
	15.98	57.87	0.2002	1.379	2.4155	-0.2814	0.2825	8.551
	15.49	57.75	0.2000	1.378	2.3876	-0.2857	0.2756	8.663
	14.99	57.72	0.1999	1.377	2.3493	-0.2912	0.2678	8.773
	13.99	57.78	0.2000	1.378	2.2999	-0.3041	0.2547	9.030
	12.98	57.87	0.2002	1.379	2.2508	-0.3183	0.2422	9.294
	11.99	57.66	0.1998	1.377	2.1984	-0.3316	0.2301	9.554
	11.01	57.82	0.2001	1.378	2.1339	-0.3416	0.2182	9.780
	10.00	57.92	0.2003	1.379	2.0609	-0.3507	0.2047	10.068
	8.96	57.58	0.1997	1.375	1.9780	-0.3570	0.1904	10.391
	7.99	57.90	0.2002	1.378	1.8948	-0.3627	0.1780	10.644
	7.00	57.74	0.2000	1.376	1.8006	-0.3658	0.1659	10.851
	5.98	57.74	0.2000	1.376	1.7029	-0.3713	0.1534	11.101
	3.97	57.97	0.2004	1.379	1.5119	-0.3841	0.1338	11.303
	3.49	57.39	0.1993	1.372	1.4614	-0.3861	0.1291	11.318
	2.98	58.04	0.2005	1.380	1.4020	-0.3878	0.1242	11.290
	2.51	57.88	0.2002	1.378	1.3587	-0.3899	0.1206	11.268
	1.99	57.98	0.2004	1.379	1.3071	-0.3922	0.1172	11.151
	1.50	57.84	0.2002	1.377	1.2589	-0.3934	0.1134	11.101
	0.99	57.82	0.2001	1.377	1.2053	-0.3940	0.1103	10.925
	0.50	57.67	0.1998	1.375	1.1466	-0.3929	0.1072	10.699
	0.03	57.95	0.2003	1.379	1.0953	-0.3943	0.1051	10.424
	-0.58	58.04	0.2005	1.379	1.0365	-0.3960	0.1020	10.158
	-1.06	57.77	0.2000	1.377	0.9735	-0.3934	0.1009	9.647
	-1.53	57.70	0.1999	1.376	0.8971	-0.3765	0.1005	8.929
	-2.02	57.88	0.2002	1.378	0.8332	-0.3681	0.0997	8.353
	-2.53	57.84	0.2001	1.377	0.7671	-0.3572	0.1002	7.652
	-3.01	57.87	0.2002	1.377	0.6837	-0.3422	0.1010	6.766
	-3.54	57.82	0.2001	1.376	0.5941	-0.3268	0.1029	5.771
	-4.01	57.84	0.2001	1.376	0.5189	-0.3187	0.1057	4.908

Table C4. Aerodynamic Data Summary for Run 203 without TWICS.

Run No. (Configuration)	α_u (deg)	$q_{\infty,u}$ (psf)	$M_{\infty,u}$	$Re_{,u}$ (x 10^6)	$C_{L,u}$	$C_{m,u}$	$C_{D,u}$	$L/D_{,u}$
203 (CRM-HL with BLRS)	-3.99	57.90	0.2003	1.390	0.5213	-0.3194	0.1054	4.947
	0.03	57.69	0.1999	1.387	1.1024	-0.3897	0.1054	10.455
	1.01	57.68	0.1999	1.387	1.2077	-0.3888	0.1112	10.864
	2.01	57.54	0.1996	1.385	1.3116	-0.3861	0.1178	11.136
	3.00	57.60	0.1997	1.385	1.4069	-0.3809	0.1250	11.258
	4.01	57.80	0.2001	1.387	1.5093	-0.3758	0.1341	11.255
	5.01	58.02	0.2005	1.389	1.6122	-0.3700	0.1442	11.179
	6.00	57.43	0.1994	1.382	1.7031	-0.3622	0.1540	11.059
	7.00	57.31	0.1992	1.380	1.8011	-0.3556	0.1664	10.821
	8.01	58.16	0.2007	1.389	1.8988	-0.3513	0.1790	10.609
	9.00	57.70	0.1999	1.385	1.9854	-0.3459	0.1907	10.412
	10.00	57.76	0.2000	1.385	2.0705	-0.3394	0.2038	10.158
	11.01	57.62	0.1997	1.383	2.1457	-0.3307	0.2165	9.913
	12.01	57.79	0.2001	1.384	2.2155	-0.3186	0.2282	9.710
	13.00	58.01	0.2004	1.388	2.2636	-0.3056	0.2382	9.503
	13.99	57.85	0.2002	1.386	2.2980	-0.2888	0.2477	9.277
	15.01	57.89	0.2002	1.387	2.3316	-0.2748	0.2588	9.010
	15.51	57.71	0.1999	1.385	2.3593	-0.2678	0.2646	8.917
	16.01	57.81	0.2001	1.386	2.4049	-0.2626	0.2714	8.860
	16.51	57.82	0.2001	1.385	2.4365	-0.2584	0.2912	8.366
	17.02	57.76	0.2000	1.385	2.4329	-0.2496	0.2974	8.180
	17.52	57.64	0.1998	1.384	2.4274	-0.2406	0.3028	8.017
	18.01	57.73	0.1999	1.384	2.4079	-0.2298	0.3071	7.841
	18.50	57.89	0.2002	1.387	2.3479	-0.2529	0.3235	7.257
	19.00	57.61	0.1997	1.383	2.3164	-0.2650	0.3464	6.687

Table C5. Aerodynamic Data Summary for Run 208 without TWICS.

Run No. (Configuration)	α_u (deg)	$q_{\infty,u}$ (psf)	$M_{\infty,u}$	$Re_{,u}$ (x 10^6)	$C_{L,u}$	$C_{m,u}$	$C_{D,u}$	$L/D_{,u}$
208 (CRM-HL, repeat run)	-3.97	58.29	0.2005	1.430	0.5301	-0.3199	0.1055	5.026
	0.03	57.89	0.1997	1.421	1.0949	-0.3929	0.1050	10.427
	2.02	57.93	0.1998	1.420	1.3069	-0.3910	0.1172	11.148
	4.01	58.02	0.2000	1.420	1.5068	-0.3831	0.1334	11.292
	6.00	57.90	0.1998	1.417	1.7072	-0.3709	0.1544	11.060
	7.00	58.19	0.2003	1.420	1.8032	-0.3656	0.1662	10.852
	8.01	58.03	0.2000	1.417	1.8996	-0.3621	0.1785	10.642
	9.00	58.05	0.2000	1.416	1.9884	-0.3577	0.1908	10.420
	10.00	57.97	0.1999	1.414	2.0719	-0.3516	0.2038	10.169
	10.99	58.17	0.2002	1.416	2.1512	-0.3442	0.2159	9.964
	12.01	58.11	0.2001	1.414	2.2192	-0.3330	0.2283	9.722
	13.00	58.04	0.2000	1.413	2.2652	-0.3205	0.2381	9.515
	14.01	58.23	0.2003	1.414	2.2982	-0.3047	0.2475	9.287
	15.01	57.95	0.1999	1.410	2.3397	-0.2907	0.2585	9.052
	15.51	57.99	0.1999	1.409	2.3899	-0.2853	0.2660	8.986
	16.00	57.75	0.1995	1.406	2.4117	-0.2790	0.2710	8.899
	16.51	58.19	0.2003	1.411	2.4219	-0.2725	0.2764	8.763
	17.00	58.12	0.2002	1.409	2.4317	-0.2660	0.2954	8.232
	17.50	57.80	0.1996	1.404	2.4135	-0.2561	0.2990	8.071
	18.01	58.36	0.2006	1.410	2.3748	-0.2557	0.3065	7.748
	18.50	57.91	0.1998	1.404	2.3114	-0.2935	0.3351	6.898
	19.00	58.25	0.2004	1.407	2.2998	-0.2951	0.3514	6.544

Table C6. Aerodynamic Data Summary for Run 209 without TWICS.

Run No. (Configuration)	α_u (deg)	$q_{\infty,u}$ (psf)	$M_{\infty,u}$	$Re_{,u}$ (x 10^6)	$C_{L,u}$	$C_{m,u}$	$C_{D,u}$	$L/D_{,u}$
209 (CRM-HL – lower M_∞ run)	-3.99	23.23	0.1254	0.892	0.5230	-0.3234	0.1074	4.870
	-0.01	22.92	0.1246	0.886	1.0832	-0.3871	0.1054	10.275
	2.02	23.02	0.1249	0.888	1.3005	-0.3880	0.1171	11.109
	4.01	22.92	0.1246	0.887	1.4994	-0.3812	0.1332	11.260
	6.02	23.04	0.1249	0.889	1.7077	-0.3694	0.1546	11.045
	7.00	23.19	0.1253	0.892	1.7994	-0.3667	0.1654	10.877
	8.01	22.94	0.1247	0.888	1.8922	-0.3618	0.1774	10.665
	9.00	23.11	0.1251	0.891	1.9789	-0.3554	0.1893	10.452
	10.00	23.05	0.1249	0.890	2.0634	-0.3496	0.2021	10.212
	11.01	23.02	0.1249	0.889	2.1349	-0.3419	0.2141	9.970
	12.01	22.93	0.1246	0.887	2.2010	-0.3317	0.2263	9.727
	13.00	22.98	0.1248	0.888	2.2504	-0.3176	0.2370	9.495
	14.01	22.99	0.1248	0.888	2.2870	-0.3030	0.2464	9.282
	15.01	23.11	0.1251	0.891	2.3606	-0.2908	0.2699	8.747
	15.49	23.01	0.1248	0.889	2.3890	-0.2863	0.2754	8.675
	16.02	23.06	0.1250	0.890	2.4164	-0.2810	0.2837	8.517
	16.49	23.08	0.1251	0.890	2.4303	-0.2722	0.2883	8.429
	17.00	23.06	0.1250	0.890	2.4220	-0.2600	0.2936	8.250
	17.50	23.04	0.1249	0.889	2.4054	-0.2468	0.2986	8.057
	18.01	23.08	0.1250	0.890	2.3721	-0.2400	0.3042	7.797
	18.50	23.10	0.1251	0.890	2.3060	-0.2728	0.3278	7.034
	19.00	23.01	0.1249	0.889	2.2972	-0.2811	0.3498	6.567

Table C7. Aerodynamic Data Summary for Run 210 without TWICS.

Run No. (Configuration)	α_u (deg)	$q_{\infty,u}$ (psf)	$M_{\infty,u}$	$Re_{,u}$ (x 10^6)	$C_{L,u}$	$C_{m,u}$	$C_{D,u}$	$L/D_{,u}$
210 (CRM-HL – lower M_∞ run)	-4.01	33.28	0.1505	1.066	0.5198	-0.3180	0.1061	4.899
	-0.01	32.85	0.1496	1.059	1.0884	-0.3892	0.1048	10.386
	2.02	32.97	0.1498	1.061	1.3046	-0.3888	0.1167	11.177
	4.01	32.94	0.1498	1.060	1.5009	-0.3824	0.1329	11.290
	6.00	32.98	0.1499	1.061	1.7072	-0.3706	0.1538	11.099
	7.00	33.00	0.1499	1.061	1.8006	-0.3653	0.1653	10.893
	8.01	32.94	0.1498	1.060	1.8947	-0.3615	0.1777	10.662
	9.00	33.08	0.1501	1.062	1.9826	-0.3559	0.1895	10.462
	10.02	32.73	0.1493	1.056	2.0677	-0.3505	0.2027	10.199
	11.01	32.99	0.1499	1.060	2.1421	-0.3429	0.2146	9.981
	12.01	33.06	0.1501	1.061	2.2071	-0.3324	0.2263	9.753
	13.00	32.96	0.1498	1.060	2.2525	-0.3180	0.2365	9.525
	14.01	33.05	0.1500	1.061	2.2941	-0.3027	0.2468	9.297
	15.01	32.92	0.1497	1.059	2.3492	-0.2913	0.2585	9.087
	15.49	33.08	0.1501	1.061	2.3771	-0.2849	0.2640	9.005
	16.00	32.90	0.1497	1.058	2.4229	-0.2820	0.2823	8.582
	16.49	32.87	0.1496	1.058	2.4376	-0.2742	0.2890	8.435
	17.00	33.06	0.1500	1.061	2.4309	-0.2648	0.2937	8.276
	17.50	33.11	0.1502	1.062	2.4144	-0.2536	0.2986	8.087
	18.01	33.05	0.1500	1.060	2.3735	-0.2519	0.3056	7.768
	18.50	33.04	0.1500	1.060	2.3061	-0.2879	0.3319	6.949
	19.00	33.11	0.1502	1.061	2.3122	-0.2911	0.3516	6.576

Table C8. Aerodynamic Data Summary for Run 211 without TWICS.

Run No. (Configuration)	α_u (deg)	$q_{\infty,u}$ (psf)	$M_{\infty,u}$	$Re_{,u}$ (x 10^6)	$C_{L,u}$	$C_{m,u}$	$C_{D,u}$	$L/D_{,u}$
211 (CRM-HL – lower M_∞ run)	-3.99	44.83	0.1753	1.230	0.5207	-0.3177	0.1059	4.916
	-0.01	44.58	0.1748	1.226	1.0890	-0.3922	0.1047	10.400
	2.02	44.54	0.1747	1.225	1.3055	-0.3906	0.1171	11.154
	4.01	44.77	0.1751	1.228	1.5056	-0.3826	0.1329	11.331
	6.02	44.67	0.1749	1.226	1.7054	-0.3709	0.1543	11.051
	7.00	44.80	0.1752	1.228	1.8024	-0.3668	0.1656	10.885
	8.01	44.54	0.1747	1.224	1.8950	-0.3623	0.1773	10.687
	9.02	44.56	0.1747	1.224	1.9848	-0.3566	0.1901	10.438
	10.00	44.92	0.1754	1.228	2.0679	-0.3516	0.2028	10.196
	11.01	44.56	0.1747	1.223	2.1442	-0.3438	0.2150	9.972
	12.01	44.70	0.1750	1.225	2.2085	-0.3327	0.2270	9.730
	12.98	44.82	0.1752	1.226	2.2533	-0.3195	0.2367	9.519
	14.01	44.77	0.1751	1.225	2.2896	-0.3034	0.2465	9.288
	15.01	44.58	0.1748	1.223	2.3243	-0.2895	0.2573	9.034
	15.49	44.69	0.1750	1.224	2.3701	-0.2846	0.2636	8.992
	16.00	44.73	0.1751	1.224	2.3998	-0.2785	0.2696	8.902
	16.49	44.77	0.1751	1.224	2.4369	-0.2754	0.2890	8.431
	17.00	44.68	0.1750	1.223	2.4279	-0.2661	0.2936	8.269
	17.50	44.56	0.1747	1.221	2.4139	-0.2562	0.2986	8.083
	18.01	44.86	0.1753	1.225	2.3769	-0.2545	0.3055	7.780
	18.50	44.51	0.1746	1.220	2.3081	-0.2957	0.3346	6.899
	19.00	44.77	0.1751	1.223	2.3072	-0.2957	0.3515	6.564

Table C9. Aerodynamic Data Summary for Run 212 without TWICS.

Run No. (Configuration)	α_u (deg)	$q_{\infty,u}$ (psf)	$M_{\infty,u}$	$Re_{,u}$ (x 10^6)	$C_{L,u}$	$C_{m,u}$	$C_{D,u}$	$L/D_{,u}$
212 (CRM-HL, repeat run)	-3.99	58.21	0.2004	1.390	0.5208	-0.3196	0.1057	4.929
	-0.01	57.79	0.1997	1.384	1.0884	-0.3942	0.1042	10.440
	2.01	57.84	0.1997	1.385	1.3032	-0.3916	0.1165	11.183
	4.01	57.97	0.2000	1.384	1.5025	-0.3839	0.1330	11.294
	6.00	58.06	0.2001	1.385	1.7032	-0.3716	0.1537	11.081
	7.00	57.77	0.1996	1.381	1.8019	-0.3675	0.1658	10.866
	8.01	58.04	0.2001	1.384	1.8966	-0.3630	0.1780	10.653
	9.02	58.07	0.2002	1.385	1.9878	-0.3588	0.1909	10.413
	9.98	57.89	0.1998	1.382	2.0648	-0.3524	0.2031	10.168
	11.01	58.13	0.2003	1.385	2.1472	-0.3445	0.2155	9.962
	12.01	57.82	0.1997	1.381	2.2130	-0.3341	0.2276	9.724
	13.02	57.91	0.1999	1.382	2.2629	-0.3208	0.2381	9.504
	14.01	57.94	0.1999	1.382	2.2914	-0.3050	0.2470	9.276
	15.01	57.85	0.1998	1.381	2.3350	-0.2917	0.2579	9.055
	15.49	57.99	0.2000	1.382	2.3665	-0.2858	0.2635	8.980
	16.00	57.93	0.1999	1.380	2.4002	-0.2789	0.2695	8.905
	16.49	57.85	0.1998	1.379	2.4330	-0.2757	0.2892	8.414
	17.02	57.96	0.2000	1.380	2.4274	-0.2678	0.2947	8.237
	17.50	58.07	0.2002	1.381	2.4150	-0.2578	0.2989	8.079
	18.01	58.12	0.2003	1.381	2.3659	-0.2596	0.3066	7.717
	18.50	58.10	0.2002	1.381	2.2991	-0.3021	0.3373	6.816
	19.00	57.72	0.1995	1.377	2.2982	-0.2965	0.3516	6.537

Table C10. Aerodynamic Data Summary for Run 215 without TWICS.

Run No. (Configuration)	α_u (deg)	$q_{\infty,u}$ (psf)	$M_{\infty,u}$	$Re_{,u}$ (x 10^6)	$C_{L,u}$	$C_{m,u}$	$C_{D,u}$	$L/D_{,u}$
215 (with Chine Position 1)	-3.99	58.65	0.2007	1.471	0.5213	-0.3183	0.1058	4.927
	0.03	57.76	0.1992	1.458	1.0850	-0.3864	0.1048	10.356
	2.02	58.04	0.1997	1.461	1.2966	-0.3840	0.1172	11.059
	4.03	57.80	0.1992	1.457	1.4955	-0.3758	0.1339	11.172
	6.00	58.25	0.2000	1.459	1.7016	-0.3658	0.1548	10.994
	7.00	58.26	0.2000	1.459	1.7994	-0.3607	0.1667	10.791
	8.01	58.16	0.1999	1.457	1.8936	-0.3567	0.1791	10.570
	9.00	58.16	0.1998	1.456	1.9830	-0.3522	0.1912	10.371
	10.00	58.07	0.1997	1.453	2.0667	-0.3456	0.2038	10.141
	10.99	58.24	0.2000	1.455	2.1452	-0.3380	0.2162	9.922
	11.99	58.09	0.1997	1.452	2.2213	-0.3298	0.2298	9.666
	13.00	58.28	0.2001	1.453	2.2880	-0.3184	0.2420	9.457
	14.01	58.45	0.2004	1.454	2.3616	-0.3056	0.2552	9.256
	14.99	58.17	0.1999	1.450	2.3992	-0.2908	0.2654	9.042
	15.51	58.34	0.2002	1.452	2.4200	-0.2842	0.2714	8.916
	16.00	58.31	0.2001	1.451	2.4485	-0.2797	0.2777	8.817
	16.51	58.43	0.2003	1.451	2.4761	-0.2738	0.2846	8.700
	17.00	58.12	0.1998	1.446	2.4750	-0.2648	0.2886	8.575
	17.52	58.25	0.2000	1.448	2.4454	-0.2607	0.2943	8.308
	18.01	58.37	0.2002	1.449	2.3818	-0.2773	0.3132	7.606
	18.50	58.30	0.2001	1.447	2.3505	-0.3025	0.3406	6.900
	19.02	58.24	0.2000	1.446	2.3643	-0.3058	0.3601	6.566
	19.51	58.46	0.2004	1.444	2.3800	-0.3015	0.3744	6.356
	20.00	58.18	0.1999	1.440	2.3951	-0.2904	0.3862	6.202
	20.50	58.21	0.1999	1.440	2.3902	-0.2791	0.3972	6.017

Table C11. Aerodynamic Data Summary for Run 216 without TWICS.

Run No. (Configuration)	α_u (deg)	$q_{\infty,u}$ (psf)	$M_{\infty,u}$	$Re_{,u}$ (x 10^6)	$C_{L,u}$	$C_{m,u}$	$C_{D,u}$	$L/D_{,u}$
216 (with Chine Position 2)	-4.01	58.64	0.2007	1.441	0.5140	-0.3169	0.1057	4.862
	0.01	57.75	0.1991	1.428	1.0840	-0.3870	0.1047	10.354
	2.01	58.27	0.2000	1.433	1.2947	-0.3839	0.1170	11.064
	4.01	58.07	0.1997	1.430	1.4918	-0.3759	0.1327	11.240
	6.00	58.37	0.2002	1.433	1.7023	-0.3650	0.1543	11.032
	7.00	58.28	0.2000	1.431	1.8014	-0.3599	0.1667	10.809
	8.01	58.42	0.2003	1.432	1.8986	-0.3567	0.1790	10.607
	9.00	58.18	0.1999	1.428	1.9861	-0.3512	0.1911	10.394
	10.00	58.43	0.2003	1.430	2.0712	-0.3445	0.2041	10.148
	11.01	58.09	0.1997	1.425	2.1489	-0.3378	0.2170	9.903
	12.01	58.20	0.1999	1.425	2.2255	-0.3286	0.2305	9.656
	13.00	58.41	0.2003	1.426	2.2977	-0.3187	0.2426	9.470
	13.99	58.13	0.1998	1.422	2.3709	-0.3054	0.2557	9.273
	15.00	58.12	0.1997	1.421	2.4235	-0.2917	0.2676	9.056
	15.49	58.14	0.1998	1.421	2.4427	-0.2845	0.2726	8.961
	16.02	58.14	0.1998	1.420	2.4622	-0.2781	0.2794	8.812
	16.49	57.98	0.1995	1.416	2.4780	-0.2727	0.2844	8.713
	17.02	58.15	0.1998	1.417	2.4701	-0.2631	0.2887	8.557
	17.50	58.13	0.1998	1.415	2.4362	-0.2604	0.2937	8.294
	17.99	58.28	0.2000	1.417	2.3776	-0.2833	0.3166	7.510
	18.52	58.26	0.2000	1.414	2.3644	-0.2990	0.3427	6.899
	19.00	58.16	0.1998	1.412	2.3759	-0.2977	0.3590	6.619

Table C12. Aerodynamic Data Summary for Run 217 without TWICS.

Run No. (Configuration)	α_u (deg)	$q_{\infty,u}$ (psf)	$M_{\infty,u}$	$Re_{,u}$ (x 10^6)	$C_{L,u}$	$C_{m,u}$	$C_{D,u}$	$L/D_{,u}$
217 (with Chine Position 3)	-4.01	58.54	0.2006	1.413	0.5117	-0.3161	0.1061	4.825
	0.03	57.92	0.1995	1.404	1.0837	-0.3865	0.1048	10.341
	2.02	58.10	0.1998	1.405	1.2966	-0.3836	0.1174	11.041
	4.01	57.93	0.1995	1.402	1.4920	-0.3752	0.1333	11.196
	6.00	58.07	0.1998	1.402	1.7028	-0.3632	0.1548	11.000
	7.00	57.98	0.1996	1.400	1.7984	-0.3586	0.1665	10.799
	7.99	58.29	0.2002	1.402	1.8963	-0.3556	0.1790	10.591
	8.98	57.98	0.1996	1.398	1.9875	-0.3498	0.1915	10.381
	10.00	58.24	0.2001	1.400	2.0730	-0.3435	0.2048	10.120
	10.99	57.96	0.1996	1.396	2.1552	-0.3353	0.2183	9.871
	11.99	58.22	0.2000	1.398	2.2294	-0.3273	0.2318	9.618
	13.00	58.32	0.2002	1.398	2.3027	-0.3168	0.2447	9.409
	13.99	58.24	0.2001	1.396	2.3798	-0.3041	0.2587	9.199
	15.01	58.15	0.1999	1.394	2.4367	-0.2909	0.2716	8.971
	15.51	58.05	0.1997	1.392	2.4582	-0.2834	0.2770	8.876
	16.00	58.19	0.2000	1.393	2.4760	-0.2762	0.2821	8.776
	16.51	58.04	0.1997	1.391	2.4854	-0.2697	0.2874	8.648
	17.02	58.18	0.2000	1.392	2.4713	-0.2612	0.2913	8.483
	17.50	58.13	0.1999	1.390	2.4266	-0.2614	0.3042	7.977
	18.01	58.25	0.2001	1.391	2.3728	-0.2903	0.3243	7.316
	18.50	58.18	0.2000	1.390	2.3709	-0.2916	0.3428	6.916
	19.00	58.05	0.1997	1.388	2.3831	-0.2951	0.3611	6.600

Table C13. Aerodynamic Data Summary for Run 218 without TWICS.

Run No. (Configuration)	α_u (deg)	$q_{\infty,u}$ (psf)	$M_{\infty,u}$	$Re_{,u}$ (x 10^6)	$C_{L,u}$	$C_{m,u}$	$C_{D,u}$	$L/D_{,u}$
218 (with Chine Position 3, repeat run)	-4.01	58.32	0.2002	1.389	0.5104	-0.3158	0.1057	4.828
	0.01	58.17	0.1999	1.386	1.0782	-0.3868	0.1046	10.312
	2.02	57.80	0.1993	1.381	1.2930	-0.3838	0.1168	11.067
	4.01	57.75	0.1992	1.380	1.4890	-0.3748	0.1332	11.180
	6.02	57.94	0.1995	1.380	1.7019	-0.3633	0.1548	10.994
	7.00	57.95	0.1995	1.380	1.7994	-0.3588	0.1665	10.805
	7.99	58.19	0.2000	1.382	1.8952	-0.3561	0.1786	10.612
	9.00	57.98	0.1996	1.379	1.9847	-0.3496	0.1915	10.362
	10.00	58.30	0.2002	1.382	2.0721	-0.3438	0.2048	10.117
	11.01	57.86	0.1994	1.376	2.1532	-0.3361	0.2182	9.869
	11.99	57.89	0.1994	1.376	2.2289	-0.3278	0.2311	9.646
	13.00	58.29	0.2001	1.381	2.3008	-0.3169	0.2443	9.418
	13.99	58.07	0.1997	1.378	2.3767	-0.3047	0.2575	9.229
	15.01	58.22	0.2000	1.379	2.4368	-0.2913	0.2709	8.995
	15.51	58.20	0.2000	1.378	2.4598	-0.2850	0.2768	8.886
	16.00	58.25	0.2001	1.378	2.4782	-0.2781	0.2822	8.783
	16.49	58.31	0.2002	1.378	2.4842	-0.2699	0.2866	8.668
	17.02	58.19	0.2000	1.377	2.4701	-0.2627	0.2907	8.498
	17.50	58.28	0.2001	1.377	2.4237	-0.2618	0.3035	7.985
	17.99	58.12	0.1999	1.374	2.3673	-0.2940	0.3257	7.269
	18.52	58.16	0.1999	1.375	2.3691	-0.2959	0.3445	6.876
	19.00	58.15	0.1999	1.374	2.3801	-0.2913	0.3588	6.634

Table C14. Aerodynamic Data Summary for Run 219 without TWICS.

Run No. (Configuration)	α_u (deg)	$q_{\infty,u}$ (psf)	$M_{\infty,u}$	$Re_{,u}$ (x 10^6)	$C_{L,u}$	$C_{m,u}$	$C_{D,u}$	$L/D_{,u}$
219 (CRM-HL – with tufts, repeat run)	-4.01	58.50	0.2005	1.386	0.5112	-0.3139	0.1064	4.806
	0.03	58.11	0.1998	1.379	1.0805	-0.3864	0.1048	10.315
	2.02	57.91	0.1994	1.376	1.2937	-0.3844	0.1168	11.075
	6.02	57.75	0.1992	1.372	1.6967	-0.3663	0.1543	10.993
	7.00	57.80	0.1992	1.370	1.7915	-0.3611	0.1655	10.822
	8.01	58.16	0.1999	1.373	1.8882	-0.3574	0.1778	10.619
	9.00	58.37	0.2002	1.375	1.9759	-0.3527	0.1898	10.410
	10.00	58.26	0.2000	1.373	2.0589	-0.3461	0.2025	10.170
	10.99	58.46	0.2004	1.376	2.1362	-0.3384	0.2147	9.950
	12.01	58.37	0.2002	1.374	2.2067	-0.3290	0.2271	9.715
	13.00	58.14	0.1998	1.371	2.2490	-0.3145	0.2366	9.507
	13.99	58.16	0.1999	1.371	2.2823	-0.2987	0.2460	9.279
	15.01	58.37	0.2002	1.373	2.3152	-0.2845	0.2564	9.028
	15.51	58.37	0.2002	1.373	2.3427	-0.2788	0.2628	8.913
	16.00	58.34	0.2002	1.372	2.3794	-0.2721	0.2685	8.862
	16.53	58.16	0.1999	1.370	2.4254	-0.2702	0.2893	8.383
	17.00	58.02	0.1996	1.367	2.4183	-0.2623	0.2940	8.225
	17.52	58.22	0.2000	1.369	2.4058	-0.2525	0.2983	8.065
	18.01	58.41	0.2003	1.371	2.3617	-0.2549	0.3061	7.715
	18.50	58.20	0.1999	1.368	2.2997	-0.2972	0.3365	6.834
	19.00	58.16	0.1999	1.367	2.2935	-0.2950	0.3513	6.528

Table C15. Aerodynamic Data Summary for Run 220 without TWICS.

Run No. (Configuration)	α_u (deg)	$q_{\infty,u}$ (psf)	$M_{\infty,u}$	$Re_{,u}$ (x 10^6)	$C_{L,u}$	$C_{m,u}$	$C_{D,u}$	$L/D_{,u}$
220 (CRM-HL – with tufts, repeat run)	-3.99	58.60	0.2006	1.385	0.5135	-0.3147	0.1059	4.849
	0.03	58.00	0.1996	1.377	1.0811	-0.3871	0.1046	10.333
	2.01	58.12	0.1998	1.378	1.2909	-0.3849	0.1166	11.072
	3.99	58.19	0.1999	1.379	1.4908	-0.3774	0.1327	11.236
	6.02	58.01	0.1996	1.376	1.6966	-0.3655	0.1543	10.995
	7.00	58.13	0.1998	1.377	1.7903	-0.3609	0.1657	10.808
	7.99	58.14	0.1998	1.377	1.8874	-0.3576	0.1776	10.629
	9.00	58.06	0.1997	1.375	1.9789	-0.3529	0.1903	10.400
	10.00	58.42	0.2003	1.379	2.0609	-0.3468	0.2029	10.159
	10.99	58.40	0.2003	1.379	2.1368	-0.3390	0.2149	9.943
	12.01	58.27	0.2000	1.377	2.2054	-0.3281	0.2275	9.694
	13.00	58.19	0.1999	1.377	2.2512	-0.3147	0.2371	9.494
	13.99	58.13	0.1998	1.375	2.2818	-0.2993	0.2463	9.265
	15.01	58.32	0.2001	1.376	2.3203	-0.2855	0.2576	9.009
	15.49	58.30	0.2001	1.376	2.3468	-0.2786	0.2627	8.934
	16.02	58.11	0.1998	1.373	2.3766	-0.2721	0.2689	8.839
	16.49	58.19	0.1999	1.374	2.4254	-0.2700	0.2890	8.393
	17.02	58.23	0.2000	1.373	2.4214	-0.2621	0.2944	8.224
	17.50	58.02	0.1996	1.371	2.4077	-0.2537	0.2988	8.058
	18.01	58.27	0.2000	1.372	2.3588	-0.2571	0.3064	7.698
	18.49	58.49	0.2004	1.376	2.3036	-0.2938	0.3341	6.894
	19.00	58.29	0.2001	1.373	2.3003	-0.2923	0.3510	6.553

Table C16. Aerodynamic Data Summary for Run 221 without TWICS.

Run No. (Configuration)	α_u (deg)	$q_{\infty,u}$ (psf)	$M_{\infty,u}$	$Re_{,u}$ (x 10^6)	$C_{L,u}$	$C_{m,u}$	$C_{D,u}$	$L/D_{,u}$
221 (CRM-HL, repeat run)	-3.99	58.52	0.2005	1.392	0.5239	-0.3194	0.1056	4.960
	0.03	57.91	0.1994	1.382	1.0930	-0.3935	0.1048	10.425
	2.01	57.99	0.1995	1.383	1.3026	-0.3915	0.1169	11.141
	4.01	57.94	0.1994	1.382	1.5057	-0.3834	0.1332	11.303
	6.00	58.27	0.2000	1.385	1.7083	-0.3716	0.1545	11.057
	7.00	58.01	0.1996	1.381	1.8029	-0.3668	0.1663	10.843
	7.99	58.56	0.2005	1.386	1.8976	-0.3634	0.1781	10.657
	9.00	58.19	0.1999	1.382	1.9866	-0.3585	0.1905	10.428
	10.00	58.29	0.2000	1.383	2.0700	-0.3525	0.2032	10.186
	10.99	58.43	0.2003	1.385	2.1445	-0.3431	0.2154	9.957
	11.99	58.49	0.2004	1.385	2.2093	-0.3336	0.2272	9.723
	13.00	58.45	0.2003	1.384	2.2596	-0.3201	0.2374	9.517
	13.99	58.30	0.2001	1.382	2.2891	-0.3047	0.2463	9.293
	15.01	58.23	0.1999	1.382	2.3299	-0.2906	0.2581	9.026
	15.49	58.12	0.1997	1.380	2.3610	-0.2852	0.2633	8.965
	16.02	58.08	0.1997	1.379	2.4028	-0.2801	0.2706	8.879
	16.49	58.31	0.2001	1.381	2.4351	-0.2772	0.2894	8.413
	17.02	58.37	0.2002	1.382	2.4316	-0.2689	0.2953	8.233
	17.50	58.25	0.2000	1.380	2.4151	-0.2587	0.2993	8.069
	18.01	58.47	0.2004	1.382	2.3656	-0.2620	0.3072	7.701
	18.50	58.09	0.1997	1.378	2.3112	-0.2974	0.3354	6.891
	19.00	58.28	0.2000	1.379	2.3037	-0.2997	0.3529	6.528

Table C17. Aerodynamic Data Summary for Run 222 without TWICS.

Run No. (Configuration)	α_u (deg)	$q_{\infty,u}$ (psf)	$M_{\infty,u}$	$Re_{,u}$ (x 10^6)	$C_{L,u}$	$C_{m,u}$	$C_{D,u}$	$L/D_{,u}$
222 (CRM-HL, nacelle off)	-3.99	58.73	0.2007	1.453	0.5824	-0.2995	0.1021	5.707
	0.05	57.96	0.1993	1.441	1.1188	-0.4023	0.1045	10.712
	2.01	58.36	0.2000	1.444	1.3112	-0.4103	0.1150	11.406
	4.01	58.12	0.1996	1.440	1.4981	-0.4110	0.1287	11.638
	6.02	58.17	0.1997	1.438	1.6932	-0.4088	0.1470	11.515
	7.00	58.15	0.1997	1.437	1.7816	-0.4090	0.1559	11.428
	8.01	58.52	0.2003	1.440	1.8726	-0.4100	0.1658	11.291
	9.00	58.54	0.2004	1.439	1.9585	-0.4103	0.1759	11.133
	10.00	58.19	0.1997	1.434	2.0434	-0.4111	0.1863	10.966
	11.01	58.04	0.1995	1.431	2.1252	-0.4074	0.1970	10.786
	12.01	58.13	0.1996	1.432	2.2027	-0.4040	0.2083	10.576
	13.02	58.25	0.1998	1.432	2.2799	-0.4001	0.2194	10.393
	13.99	58.64	0.2005	1.436	2.3587	-0.4001	0.2305	10.235
	15.01	58.30	0.1999	1.431	2.4362	-0.4022	0.2426	10.043
	15.49	58.34	0.2000	1.431	2.4578	-0.3948	0.2474	9.936
	16.02	58.41	0.2001	1.432	2.4794	-0.3867	0.2522	9.832
	16.49	58.29	0.1999	1.429	2.4899	-0.3769	0.2557	9.737
	16.98	58.34	0.2000	1.428	2.4957	-0.3649	0.2596	9.612
	17.50	58.40	0.2001	1.422	2.4862	-0.3498	0.2612	9.520
	17.99	58.09	0.1996	1.424	2.4663	-0.3364	0.2626	9.392
	18.50	57.87	0.1992	1.420	2.4297	-0.3260	0.2642	9.198
	19.00	58.35	0.2000	1.426	2.3752	-0.3266	0.2687	8.841

Table C18. Aerodynamic Data Summary for Run 224 without TWICS.

Run No. (Configuration)	α_u (deg)	$q_{\infty,u}$ (psf)	$M_{\infty,u}$	$Re_{,u}$ (x 10^6)	$C_{L,u}$	$C_{m,u}$	$C_{D,u}$	$L/D_{,u}$
224 (CRM-HL, nacelle off – with tufts)	-3.99	58.39	0.2003	1.411	0.5736	-0.2977	0.1021	5.620
	0.05	58.12	0.1998	1.407	1.1162	-0.4026	0.1039	10.746
	1.99	58.44	0.2004	1.410	1.3080	-0.4106	0.1145	11.424
	3.99	58.04	0.1996	1.405	1.4970	-0.4113	0.1283	11.669
	6.02	58.56	0.2006	1.409	1.6886	-0.4093	0.1458	11.585
	7.00	58.14	0.1998	1.403	1.7791	-0.4088	0.1551	11.470
	8.01	58.42	0.2003	1.406	1.8704	-0.4110	0.1651	11.326
	9.00	58.06	0.1997	1.401	1.9569	-0.4114	0.1746	11.208
	10.00	58.10	0.1998	1.401	2.0406	-0.4107	0.1850	11.031
	10.99	58.25	0.2000	1.401	2.1212	-0.4088	0.1954	10.853
	12.01	58.15	0.1998	1.399	2.1965	-0.4043	0.2065	10.636
	13.00	58.18	0.1999	1.399	2.2724	-0.4003	0.2173	10.458
	13.99	58.05	0.1997	1.397	2.3507	-0.3993	0.2289	10.270
	14.99	58.15	0.1998	1.397	2.4271	-0.4010	0.2406	10.087
	15.51	58.32	0.2001	1.399	2.4517	-0.3940	0.2457	9.979
	16.00	58.36	0.2002	1.398	2.4705	-0.3855	0.2500	9.881
	16.51	58.08	0.1997	1.395	2.4844	-0.3750	0.2545	9.762
	17.02	58.46	0.2004	1.398	2.4874	-0.3621	0.2576	9.657
	17.50	58.30	0.2001	1.395	2.4821	-0.3474	0.2594	9.568
	18.01	58.16	0.1999	1.393	2.4572	-0.3336	0.2607	9.425
	18.52	58.31	0.2001	1.394	2.4210	-0.3235	0.2617	9.251
	19.00	57.91	0.1994	1.389	2.3633	-0.3247	0.2665	8.868

Table C19. Aerodynamic Data Summary for Run 225 without TWICS.

Run No. (Configuration)	α_u (deg)	$q_{\infty,u}$ (psf)	$M_{\infty,u}$	$Re_{,u}$ (x 10^6)	$C_{L,u}$	$C_{m,u}$	$C_{D,u}$	$L/D_{,u}$
225 (CRM-HL, nacelle off, repeat)	-3.99	58.46	0.2004	1.403	0.5744	-0.2975	0.1019	5.639
	-0.01	57.81	0.1993	1.394	1.1130	-0.4026	0.1033	10.773
	2.01	57.99	0.1996	1.395	1.3104	-0.4107	0.1145	11.446
	3.99	57.96	0.1996	1.394	1.4945	-0.4107	0.1280	11.673
	6.02	58.19	0.2000	1.396	1.6898	-0.4090	0.1460	11.577
	7.00	58.23	0.2000	1.396	1.7808	-0.4093	0.1552	11.472
	7.99	58.09	0.1998	1.393	1.8701	-0.4108	0.1647	11.352
	9.00	58.35	0.2002	1.396	1.9579	-0.4116	0.1748	11.201
	10.00	58.29	0.2001	1.395	2.0429	-0.4105	0.1855	11.012
	10.99	58.41	0.2003	1.396	2.1228	-0.4081	0.1956	10.854
	11.99	58.32	0.2002	1.395	2.1986	-0.4041	0.2068	10.629
	13.00	58.17	0.1999	1.393	2.2768	-0.4001	0.2177	10.457
	13.99	58.55	0.2006	1.396	2.3548	-0.3995	0.2294	10.266
	14.99	58.10	0.1998	1.391	2.4302	-0.4013	0.2414	10.067
	15.49	58.14	0.1999	1.391	2.4588	-0.3948	0.2463	9.984
	16.02	58.11	0.1998	1.391	2.4747	-0.3856	0.2511	9.854
	16.49	57.99	0.1996	1.389	2.4881	-0.3758	0.2548	9.764
	17.02	57.89	0.1994	1.387	2.4933	-0.3626	0.2584	9.650
	17.50	58.08	0.1998	1.389	2.4872	-0.3491	0.2604	9.551
	18.01	58.25	0.2001	1.391	2.4613	-0.3346	0.2612	9.421
	18.48	58.13	0.1999	1.389	2.4250	-0.3250	0.2619	9.257
	19.02	58.25	0.2001	1.390	2.3708	-0.3242	0.2675	8.861

Table C20. Aerodynamic Data Summary for Run 226 without TWICS.

Run No. (Configuration)	α_u (deg)	$q_{\infty,u}$ (psf)	$M_{\infty,u}$	$Re_{,u}$ (x 10^6)	$C_{L,u}$	$C_{m,u}$	$C_{D,u}$	$L/D_{,u}$
226 (CRM-HL, nacelle off, repeat)	-3.99	58.49	0.2005	1.395	0.5714	-0.2978	0.1020	5.603
	-0.01	57.85	0.1994	1.387	1.1111	-0.4030	0.1036	10.730
	2.01	58.07	0.1998	1.390	1.3073	-0.4110	0.1143	11.439
	3.99	58.19	0.2000	1.391	1.4977	-0.4113	0.1281	11.692
	6.02	58.45	0.2004	1.393	1.6898	-0.4088	0.1460	11.573
	7.00	58.22	0.2000	1.390	1.7802	-0.4105	0.1549	11.494
	7.99	58.45	0.2004	1.392	1.8679	-0.4107	0.1644	11.362
	9.00	58.12	0.1999	1.387	1.9564	-0.4114	0.1747	11.201
	10.00	58.25	0.2001	1.389	2.0402	-0.4109	0.1852	11.019
	10.99	58.24	0.2001	1.388	2.1218	-0.4085	0.1951	10.873
	11.99	58.40	0.2003	1.389	2.2003	-0.4047	0.2065	10.654
	13.00	58.17	0.1999	1.386	2.2773	-0.4007	0.2175	10.468
	13.99	58.14	0.1999	1.386	2.3563	-0.3998	0.2292	10.281
	14.99	58.39	0.2003	1.389	2.4290	-0.4015	0.2411	10.076
	15.49	58.30	0.2002	1.388	2.4573	-0.3951	0.2457	10.002
	16.02	58.22	0.2000	1.386	2.4747	-0.3856	0.2509	9.863
	16.49	58.21	0.2000	1.386	2.4885	-0.3760	0.2543	9.787
	17.00	58.39	0.2003	1.388	2.4907	-0.3630	0.2573	9.679
	17.50	58.35	0.2003	1.387	2.4837	-0.3489	0.2598	9.559
	18.01	58.00	0.1996	1.383	2.4611	-0.3351	0.2611	9.427
	18.50	58.12	0.1999	1.384	2.4241	-0.3245	0.2621	9.250
	19.00	58.19	0.2000	1.384	2.3704	-0.3252	0.2674	8.863

Table C21. Aerodynamic Data Summary for Run 227 without TWICS.

Run No. (Configuration)	α_u (deg)	$q_{\infty,u}$ (psf)	$M_{\infty,u}$	$Re_{,u}$ (x 10^6)	$C_{L,u}$	$C_{m,u}$	$C_{D,u}$	$L/D_{,u}$
227 (CRM-HL, repeat run)	-3.99	58.31	0.2003	1.424	0.5208	-0.3178	0.1054	4.943
	0.03	58.24	0.2002	1.421	1.0975	-0.3939	0.1048	10.472
	2.02	58.22	0.2002	1.419	1.3095	-0.3920	0.1168	11.212
	3.99	58.03	0.1998	1.416	1.5064	-0.3834	0.1333	11.297
	6.02	58.18	0.2001	1.416	1.7095	-0.3710	0.1546	11.060
	7.00	58.20	0.2002	1.416	1.8046	-0.3667	0.1663	10.852
	7.99	58.15	0.2001	1.414	1.8957	-0.3626	0.1780	10.651
	9.00	57.99	0.1998	1.411	1.9872	-0.3578	0.1906	10.425
	10.00	58.18	0.2001	1.413	2.0707	-0.3515	0.2033	10.187
	10.99	58.02	0.1998	1.410	2.1461	-0.3428	0.2151	9.975
	11.99	58.39	0.2005	1.415	2.2142	-0.3327	0.2276	9.730
	13.00	58.28	0.2003	1.413	2.2643	-0.3198	0.2380	9.515
	13.99	58.06	0.1999	1.410	2.2952	-0.3036	0.2467	9.305
	14.99	57.94	0.1997	1.408	2.3521	-0.2914	0.2586	9.095
	15.49	57.81	0.1995	1.405	2.4086	-0.2873	0.2661	9.050
	16.02	58.14	0.2000	1.409	2.4281	-0.2802	0.2713	8.950
	16.49	58.07	0.1999	1.408	2.4369	-0.2742	0.2758	8.836
	17.00	58.07	0.1999	1.407	2.4318	-0.2675	0.2946	8.255
	17.52	57.89	0.1996	1.403	2.4134	-0.2572	0.2988	8.077
	17.99	58.07	0.1999	1.405	2.3724	-0.2568	0.3046	7.789
	18.48	57.83	0.1995	1.402	2.3098	-0.2972	0.3337	6.922
	19.00	58.25	0.2002	1.406	2.3032	-0.2914	0.3484	6.610

Appendix D.

Aerodynamic Comparison Plots for Data without Wall Correction

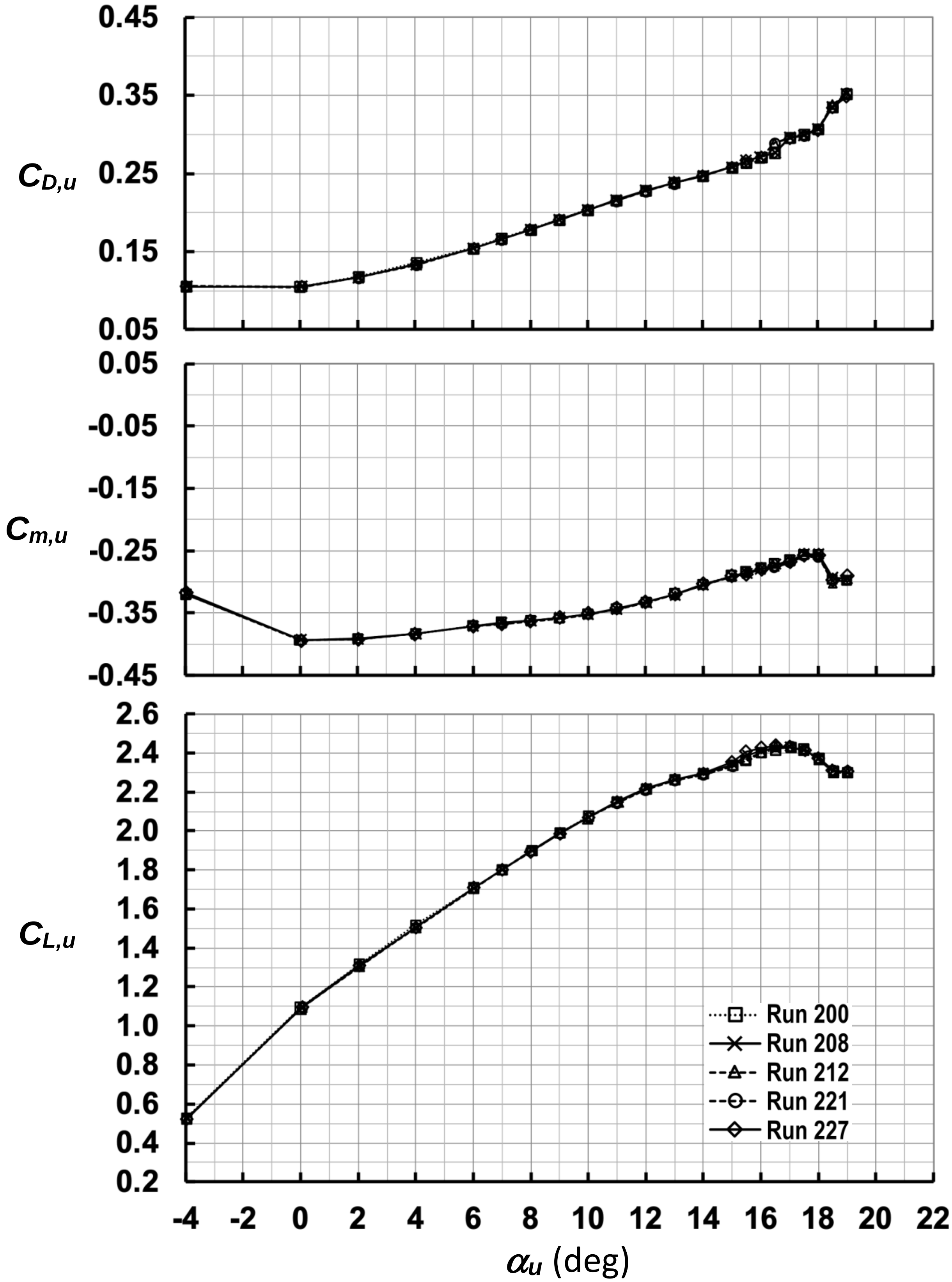

Figure D1. $C_{D,u}$, $C_{m,u}$ and $C_{L,u}$ vs. α_u plots for CRM-HL baseline repeat runs ($M_\infty = 0.2$, without TWICS).

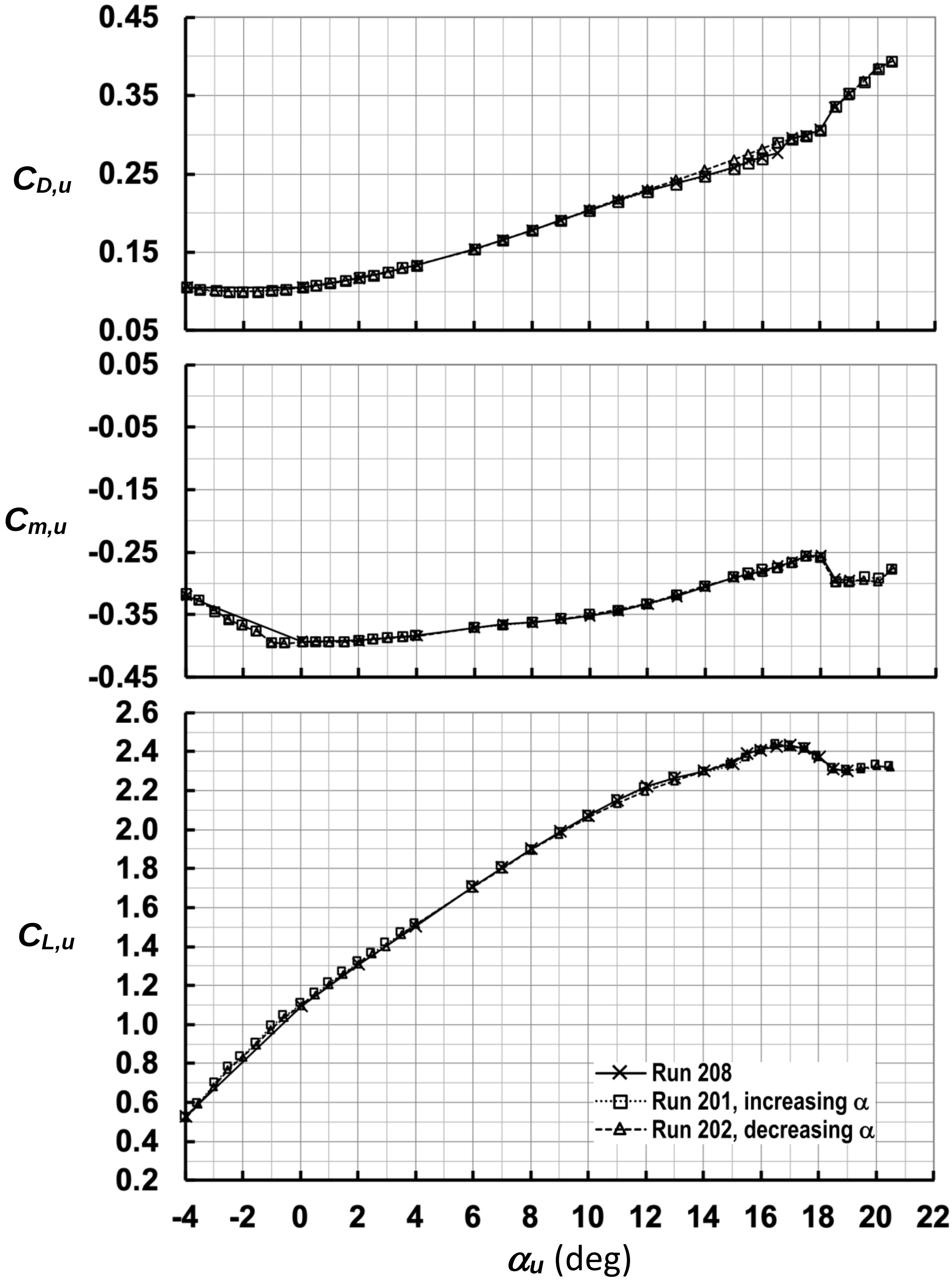

Figure D2. $C_{D,u}$, $C_{m,u}$ and $C_{L,u}$ vs. α_u plots for increasing/decreasing α ($M_\infty = 0.2$, without TWICS).

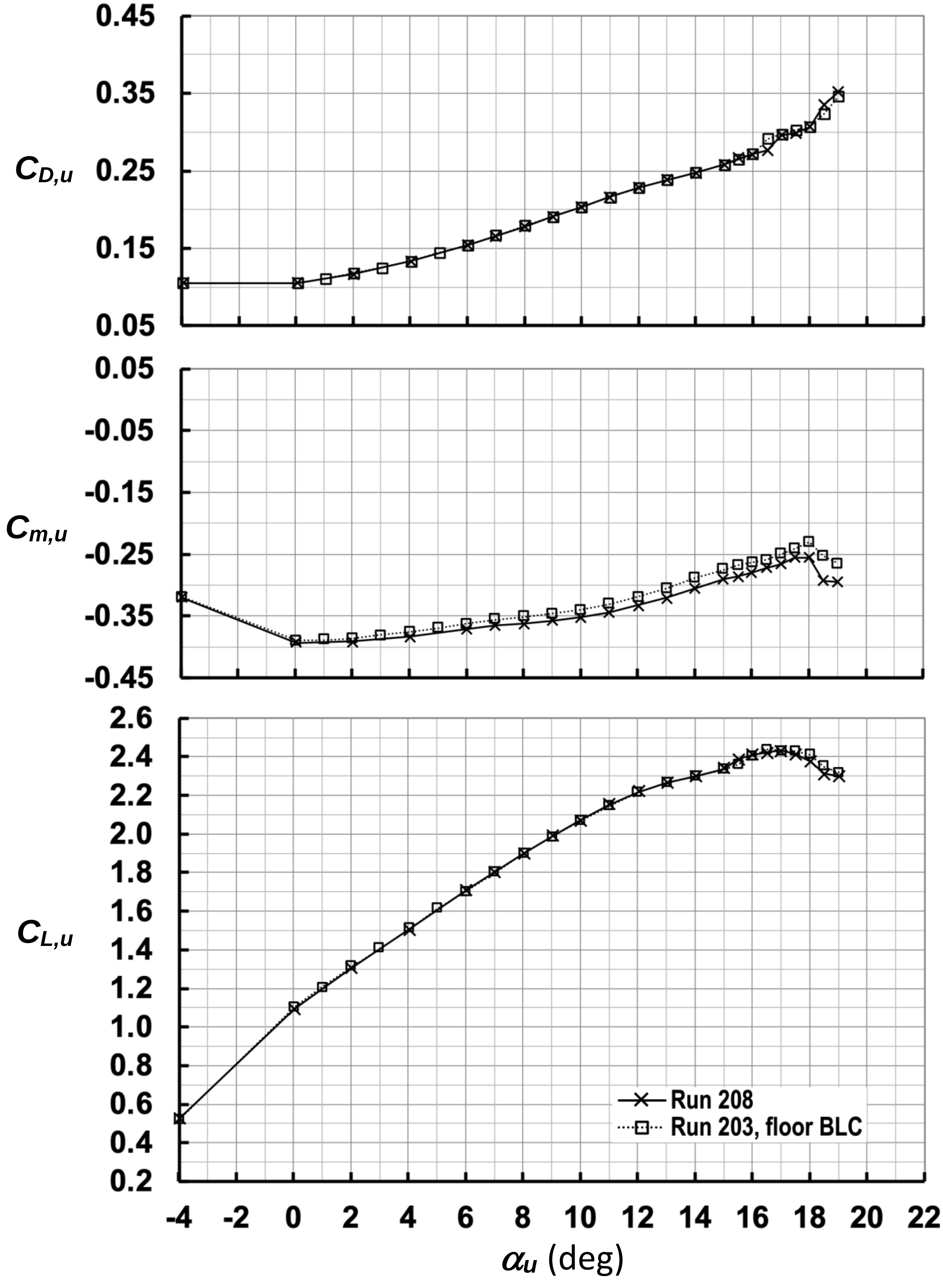

Figure D3. Effects of BLRS on $C_{D,u}$, $C_{m,u}$ and $C_{L,u}$ vs. α_u plots ($M_\infty = 0.2$, without TWICS).

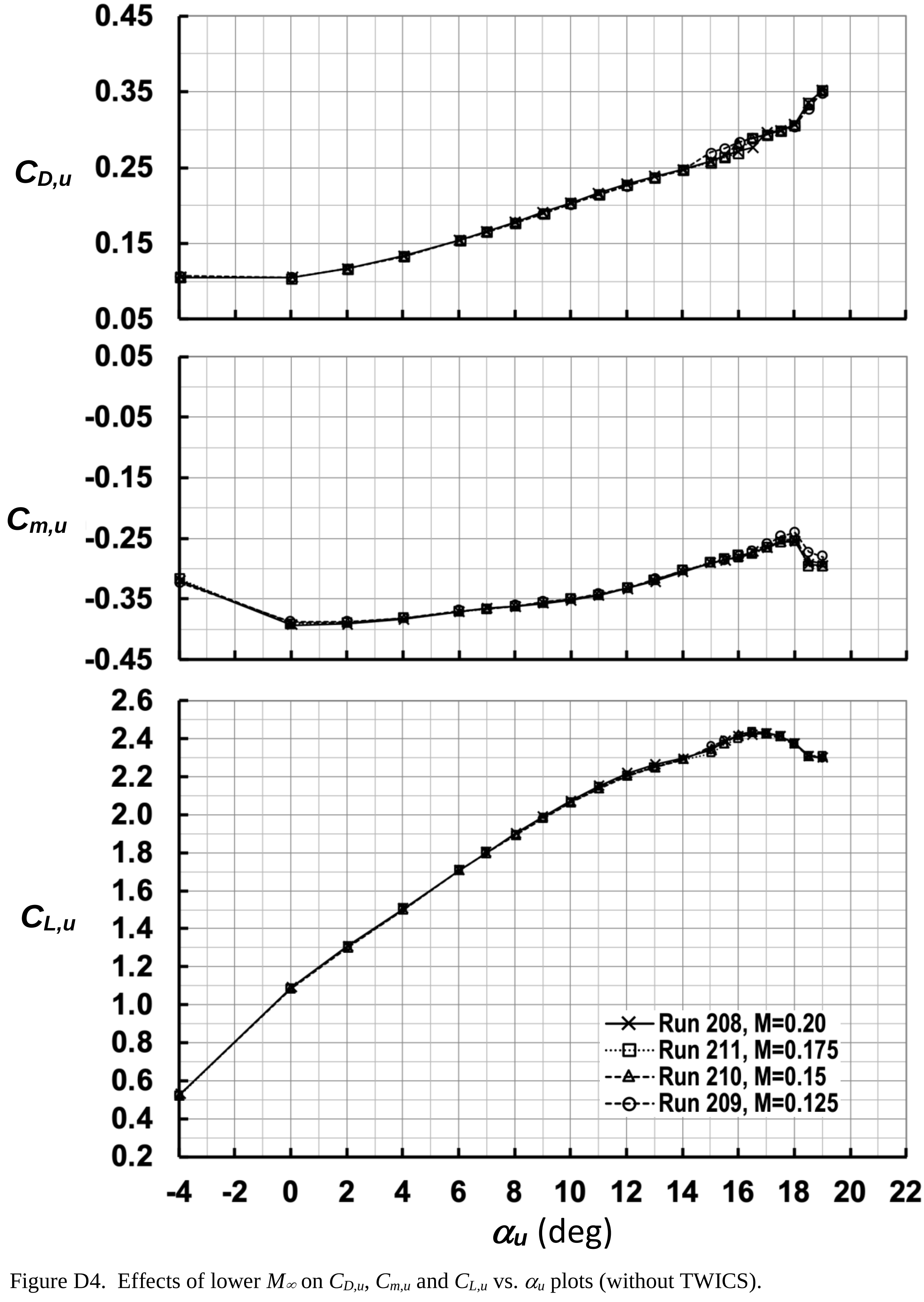

Figure D4. Effects of lower M_∞ on $C_{D,u}$, $C_{m,u}$ and $C_{L,u}$ vs. α_u plots (without TWICS).

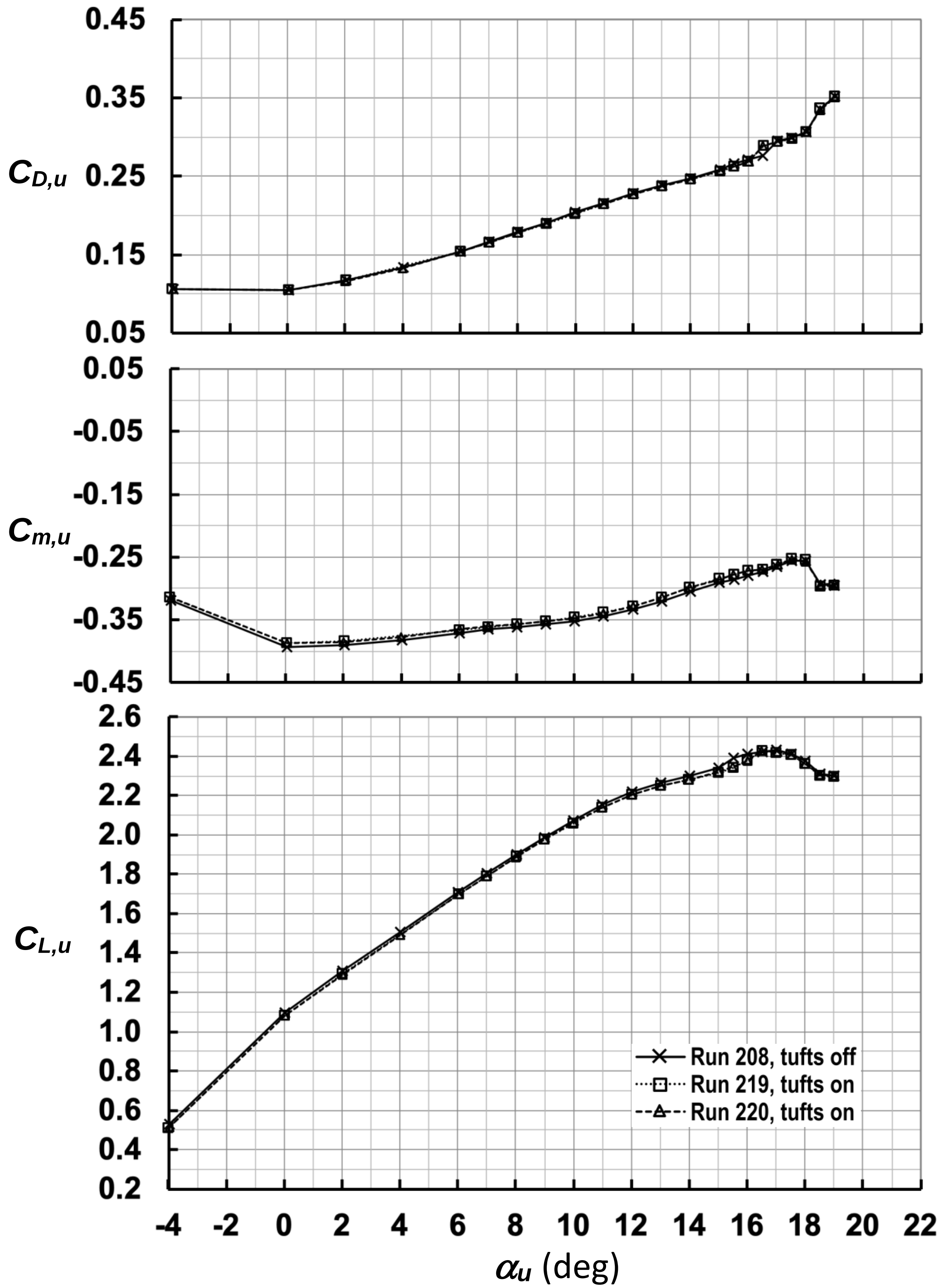

Figure D5. Effects of tufts on $C_{D,u}$, $C_{m,u}$ and $C_{L,u}$ vs. α_u plots ($M_\infty = 0.2$, without TWICS).

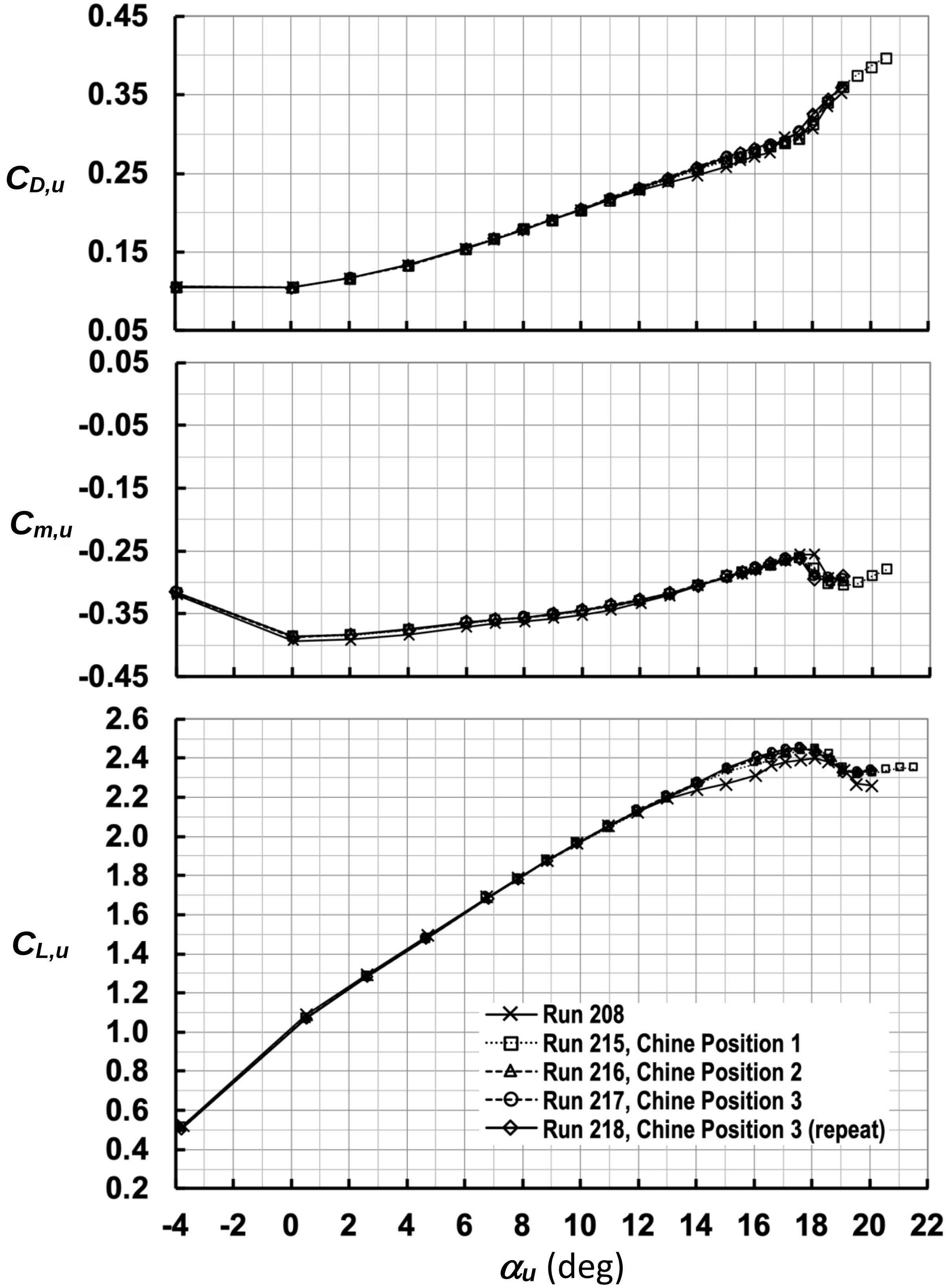

Figure D6. Effects of nacelle chines on $C_{D,u}$, $C_{m,u}$ and $C_{L,u}$ vs. α_u plots ($M_\infty = 0.2$, without TWICS).

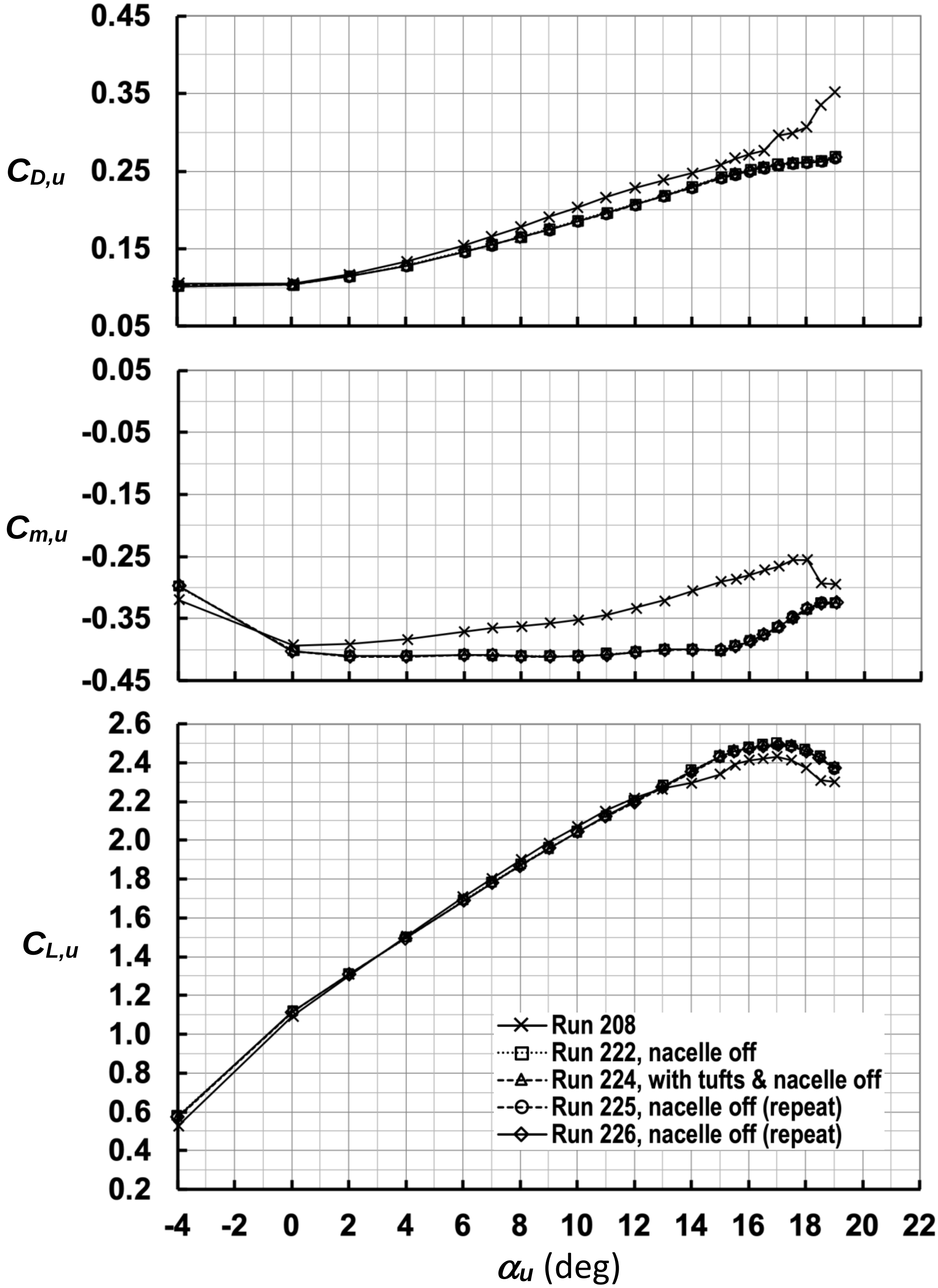

Figure D7. Effects of nacelle on $C_{D,u}$, $C_{m,u}$ and $C_{L,u}$ vs. α_u plots ($M_\infty = 0.2$, without TWICS).